Rheology and Microstructure of Complex Fluids: Dispersions, Emulsions and Polymer Solutions

Thesis by

Michael Vicic

In Partial Fulfillment of the Requirements

for the Degree of

Doctor of Philosophy

California Institute of Technology

Pasadena, California

1999

(Submitted 22 February 1999)

Acknowledgments

First of all, I would like to thank John Brady for allowing me to pursue my own interests in rheology during my last year of graduate school. These projects were unfunded, yet I was able to continue for a full year, with the help of a SURF for one summer, to complete the emulsion and polymer solution projects presented here. John always says that if a student proposes a project that he finds interesting and important, that he will find funding. I'm living proof that he follows through on this promise. Prior to that, John arranged for my visit to The University of Queensland to learn about experimental rheology so that I could return to Caltech to setup and maintain a rheology lab. The experience of starting and maintaining a lab has provided me with invaluable experience for which I am grateful.

While working in the Brady group, I've shared time, work and some laughs with many people—Phil L., Thanh, Jeff, Yvette, Yevgeny, Douglas, Dave, Saud, Mina, Ganesh, Denis, Merzhad, Phil W., Kengo, Johan, Sofiane, and Panos. I would especially like to thank Dave for his friendship through the years and Denis for his excellent work as a SURF.

In addition to the Brady group, I am indebted to Julie Kornfield's group. They allowed me to renovate part of one of their labs for the rheology lab, let me work in their labs as one of the group, and adhered to my annoying, closed-door policy for the rheology lab during my last, very focused year. I would especially like to thank Jagdish who has shown a genuine interest in my work and life, especially during times of failure.

Many others at Caltech made the time pass more quickly than it should have at times. Whether it was flag football, soccer, volleyball or softball, the people on these teams were always fun to play and compete with. I would like to thank Margie, Kathy and Anne for always being there to talk, listen and help as friends, as well as secretaries. I would also like to thank Cheryl for helping to make the first year of

graduate school bearable and for her continued friendship.

In addition to my time at Caltech, I had the good fortune to work in Michael Mackay's labs at The University of Queensland during part of 1996. I shall forever be grateful to Michael for allowing me to pick his brain about experimental rheology and life as a scientist, as well as for his suggestion for the project about stress jumps of polymer solutions. While in Michael's labs, I had the privilege of working, learning and playing with a number of people—Peter, Camilla, Vince, Stu M., Grant, Justin, Babak, Brenton, Ollie, Yoosip, Eric, Steve, and John. I hope that we can maintain our friendships across the ocean.

But without the support of my family, I never would have reached this point of my life. It started with my Dad preaching the importance of education after a long, tiring day of construction work when I was young. Their support continued during my 12 years of Catholic elementary and high school through which they provided a loving environment and many rides, while suffering some financial hardship. During the last 12 years of graduate and undergraduate work, they have been overly understanding about school-related obligations, my move to California, missed trips for Christmas, and sometimes infrequent phone calls. Thank you for your continued understanding and support; they mean more to me than you can ever know.

Most of all, I would like to thank the love of my life, Nikki. She endured my mood swings, failures, successes, foibles, work ethic, and many lonely vacations over the last five years. Through it all, Nikki is still the one person who can always put a smile on my face, regardless of my mood. Thank you for being my eternal source of joy. I hope that one day we can fondly look back at my graduate school experience as we stay young together.

Abstract

The rheology and microstructure of complex fluids are intimately related, and this relationship is explored to gain a deeper understanding of the physics of colloidal dispersions, emulsions and polymer solutions.

The nonequilibrium microstructure and rheological properties of dispersions in steady, simple shear flow are calculated by solving the Smoluchowski equation as a function of dimensionless shear rate. The particles have a purely repulsive interaction with an hydrodynamic radius, a, and a thermodynamic radius, b. For hard spheres, $b/a \to 1$, shear thinning is caused by a decrease in the Brownian contribution since Brownian motion becomes less important with increasing shear. Shear thickening occurs because of an increase in the hydrodynamic viscosity caused by the increased probability of finding particles near contact with increasing shear when particles hydrodynamically interact. The first normal stress difference changes sign since Brownian and hydrodynamic contributions have opposite signs, while the second normal stress difference is always negative. Scaling arguments are made to extend these dilute results for concentrated dispersions. Similar calculations and analyses are performed to study the effects of hydrodynamic interactions and varying b/a ratios on rheology and microstructure.

Scaling arguments for the volume-fraction dependence of the bulk stress of emulsions at the critical capillary number are presented along with experimental evidence using an unstabilized emulsion of polymerized castor oil dispersed in polydimethylsiloxane. It is shown that the droplet contribution to both the relative shear viscosity and first normal stress difference is linear in volume fraction for a given viscosity ratio for dilute to moderately-concentrated emulsions in steady, simple shear flow.

Stress jump measurements are performed for the first time for (i) shear startup and (ii) polymer solutions in shear. The startup viscosity of a polymer solution of polyacrylamide in fructose-water at equilibrium is equal to the measured high-

frequency dynamic viscosity, as expected, since both methods measure the viscous contribution to the viscosity associated with the equilibrium microstructure. Since polymer solutions exhibit stress jumps different from the solvent viscosity, effects of shear on the hydrodynamic viscosity can be investigated.

Contents

List of Figures

List of Tables

Chapter 1

Introduction

Complex fluids are multicomponent systems in which there are at least two different length scales. Often these different length scales are inherent in the components, where, for example, colloidal dispersions consist of small particles suspended in a fluid, where the particles have a characteristic length $\sim O(10^{-7}$ m) and the suspending fluid molecules are $\sim O(10^{-10}$ m). Alternatively, all components can have the same characteristic length, but at least one of these components interacts in such a way that structures with larger length scales are formed. An emulsion of two immiscible Newtonian fluids has components that both have the characteristic length of a molecule, $\sim O(10^{-10}$ m), but droplets are formed having a characteristic length $\sim O(10^{-5}$ m) because the fluids are immiscible.

When flowing, a complex fluid may be shear thinning and/or shear thickening, where shear thinning (thickening) is a decrease (increase) in the steady viscosity with an increase in the applied rate. Complex fluids may also exhibit interesting physical behavior during flow, such as rod climbing when a single rod spins in a reservoir of fluid and/or die swell when a complex fluid flows through and exits a die. Phenomena such as rod climbing and die swell are results of normal stress differences.

The main theme of this thesis is the exploration of the relationship between the microstructure of a complex fluid and the macroscopic rheological properties in simple shear flow. These rheological properties include shear viscosity, first and second normal stress differences and the nonequilibrium osmotic pressure.

Colloidal dispersions are analyzed in Chapters 2 and 3, where the microstructure is found by solving the two-particle Smoluchowski equation and then used to calculate the macroscopic rheological properties. In Chapter 2 the analysis focuses on behavior at small shear rates while the analysis of Chapter 3 is valid for arbitrary shear rates. In both chapters, the colloidal dispersions consist of spherical particles with a hydrodynamic radius, a, and a thermodynamic radius, b. Three different cases are studied: (1) $b/a = 1$ and hydrodynamic interactions are neglected, (2) hard sphere particles, where $b/a \to 1$ and two particle hydrodynamic interactions are included, and (3) steric or charged stabilized particles, where b/a is varied and two particle hydrodynamic interactions are included. For hard sphere dispersions, shear thinning

is caused by a decrease in the Brownian stress due to the decreasing importance of Brownian motion with increasing shear rate. Shear thickening occurs at high shear rate because there is a large probability of finding two particles near contact and these particles hydrodynamically interact, resulting in an increase of the hydrodynamic contribution to the viscosity. The first normal stress difference, N_1, is positive at small shear rates, passes through zero, and is negative at high shear rates since the Brownian and hydrodynamic contributions have opposite signs. At low shear rates the positive Brownian contribution dominates while the negative hydrodynamic contribution dominates at high shear rates. The second normal stress difference, N_2, is negative for all shear rates. Lastly, since $|N_1/N_2| \sim O(1)$ and $N_2 < 0$, there is only negative rod climbing. The effects of hydrodynamic interactions on rheology and microstructure are studied by changing b/a. There are only minor effects on the microstructure, but rheology is quite sensitive to the value of b/a.

Next, in Chapter 4, emulsions of two immiscible Newtonian fluids are studied. A scaling argument is presented for the volume-fraction dependence of the bulk stress of an emulsion at the critical capillary number. At the critical capillary number, the droplets are just about to burst and a small increase in the shear rate should cause droplet breakup. This scaling argument relies on the hypotheses that the size, shape and orientation of the droplets are relatively insensitive to changes in volume fraction for dilute to moderately-concentrated emulsions at a given shear rate. Experiments are performed on an unstabilized emulsion in simple shear flow using a constant stress rheometer, and the scaling argument for the volume-fraction dependence for viscosity and first normal stress difference is confirmed; thus, $\eta_r - 1 \sim O(\phi)$ and $N_1 \sim O(\eta_s \dot{\gamma} \phi)$ for any value of applied stress (or rate) and for dilute to moderately-concentrated emulsions, where $\eta_r = \eta/\eta_s$ is the relative viscosity, η is the emulsion viscosity, η_s is the suspending fluid viscosity, $\dot{\gamma}$ is the shear rate, and ϕ is the volume fraction of the dispersed phase.

Finally, polymer solutions are discussed in Chapter 5. Linear viscoelastic and stress jump measurements at flow startup are completed for polymer solutions of polyacrylamide in fructose-water. Stress jumps at startup are made for the first time,

confirming the relationship $\eta^+(t=0;\dot{\gamma}) = \eta'_\infty$, where $\eta^+(t;\dot{\gamma})$ is the viscosity growth function after flow startup at time t and shear rate $\dot{\gamma}$, and η'_∞ is the high-frequency dynamic viscosity. This relationship is valid simply because both measurements yield the viscous contribution to the viscosity associated with the equilibrium microstructure. Furthermore, it is shown that stress jumps at startup also yield $G(t=0)$, where $G(t)$ is the linear viscoelastic relaxation modulus; thus, startup stress jumps can be used to test predictions of η'_∞ and $G(t=0)$ of different rheological models.

Chapter 2

Normal stresses in colloidal dispersions

2.1 Introduction

Colloidal dispersions — suspensions of small particles dispersed in a fluid medium — occur in a wide variety of situations, including slurries, paints, pastes, dyes, polymers, protein solutions, many foodstuffs and ceramic sols. In these "microstructured" materials the suspended particles interact through hydrodynamic, interparticle and Brownian (or thermal) forces. The balance between thermal and interparticle forces determines the equilibrium behavior, which can give rise to a variety of states, from dispersed amorphous gas- or liquid-like microstructures with a relatively low shear viscosity to highly ordered crystalline dispersions with elastic moduli and yield stresses. Under the action of an external driving force such as shear, hydrodynamic forces come into play and compete with thermal and interparticle forces to set the structure and determine properties. An even richer variety of microstructures is now possible, with flow-induced melting or ordering, etc., and transport properties in these highly nonequilibrium states can be vastly different from those at equilibrium.

Our understanding of colloidal dispersions has increased markedly in the last decade. This has resulted from three developments: 1) The excellent experiments on well-characterized model systems [van der Werff & de Kruif (1989); van der Werff *et al.* (1989); van der Werff (1990)], 2) the invention of Stokesian Dynamics as a technique to numerically simulate suspension behavior [Bossis & Brady (1984, 1987, 1989); Brady & Bossis (1985, 1988); Phung & Brady (1992); Phung (1993)], and 3) a new scaling theory capable of predicting behavior near maximum solids fractions [Brady (1993a, 1993b, 1994)]. The scaling theory successfully predicts the near-equilibrium behavior of colloidal dispersions, specifically to first order in the perturbation of the microstructure caused by flow. This first order perturbation is sufficient to determine the shear viscosity, but in order to determine normal stresses, perturbations to second order in the shear rate are required. The purpose of this paper is to extend the perturbation theories to second order, and thereby predict normal stresses and the shear-rate dependence of the osmotic pressure of colloidal dispersions.

To our knowledge the only analysis of normal stresses in colloidal dispersions is

that of Blawzdziewicz & Szamel (1993), where they considered the dilute limit of Brownian hard spheres in simple shear flow in the absence of hydrodynamic interactions. By using an eigenfunction expansion they were able to compute the microstructural deformation and resultant rheology up to Peclet numbers of 12.5. The Peclet number, $Pe = \dot{\gamma}a^2/D_0$, measures the relative importance of hydrodynamic shear and Brownian forces. Here, a is the particle size, $\dot{\gamma}$ the magnitude of the shear rate, and D_0 the Brownian diffusivity of an isolated particle; $D_0 = kT/6\pi\eta a$, with kT the thermal energy and η the viscosity of the suspending fluid.

On the experimental side there have been numerous measurements of normal stresses in polymeric fluids, and of suspensions dispersed in polymeric liquids, but there have been very few measurements of suspensions in Newtonian fluids. Indeed, we have found only three such studies: Al-Hadithi, Barnes & Walters (1992), Jomha & Reynolds (1993), and Laun (1994). A very limited range of conditions were covered in these studies and, in particular, the shear rates were too large to extract the low-shear-limit behavior considered here.

The only other results on normal stresses in colloidal dispersions are the Stokesian Dynamics simulations of Phung (1993) for suspensions of Brownian hard spheres. Phung has simulation results for both the first and second normal stress differences for volume fractions ranging from 0.316 to 0.51 and for Peclet numbers from 10^{-2} to 10^4. We shall compare our theoretical predictions with his simulation results below.

Several recent papers in the literature have pointed out that the perturbation to the suspension microstructure by flow is singular rather than regular [Ronis (1984); Dhont (1989)]. In a linear flow there is always a region far from a particle where the effects of convection and diffusion balance regardless how small the Peclet number [Leal (1992)]. This "outer" region occurs at a distance of $O(aPe^{-1/2})$ from a test particle and renders the perturbation singular with the appearance of fractional powers and logarithms of the Peclet number. However, the perturbation of the pair-distribution function by a linear flow has the character of a quadrupole, which is weak in the outer region, and it is possible to proceed as a regular perturbation expansion up to $O(Pe^2)$. Thus, the low shear limit of the normal stresses can be obtained as a

regular perturbation expansion for a general linear flow.

In section 2.2 we introduce the N—particle Smoluchowski equation and reduce it down to the equation for a pair. We show explicitly that the perturbation to the microstructure proceeds as a regular expansion up to $O(Pe^2)$ and determine the form of this expansion for a general linear flow. We also show that the next correction to the microstructure is $O(Pe^{5/2})$ and that this term can be obtained by simply matching with the lowest order outer solution. In the next section we discuss the separate Brownian, hydrodynamic and interparticle force contributions to the stress and determine the general form of the rheological behavior to second order. We also show that the $O(Pe^{5/2})$ correction to the microstructure gives an $O(Pe^{3/2})$ contribution only to the osmotic pressure. The next term in the deviatoric stress is $O(Pe^2)$.

In section 2.4 we present the exact results for the dilute $O(\phi^2)$ contribution to the stress, where ϕ is the volume fraction of the suspended particles. We also introduce the scaling theory of Brady (1993b) which shows that the dominant contribution to the stress as maximum packing is approached comes from the Brownian stress. Further, this scaling theory shows that the appropriate Peclet number is that based on the short-time self-diffusivity, $D_0^s(\phi)$, at the volume fraction of interest, not on the infinite dilution or "bare" diffusion coefficient D_0. The perturbation expansion now proceeds in powers of $Pe \equiv \dot{\gamma}a^2/D_0^s(\phi)$. This theory predicts that the normal stresses scale as $\bar{P}e\, g(2;\phi)/\hat{D}_0^s(\phi)$ as ϕ approaches maximum packing, ϕ_m (and as $Pe \to 0$). Here, $\hat{D}_0^s(\phi) = D_0^s(\phi)/D_0$. At random close packing, $\phi_m \approx 0.63$, the equilibrium radial-distribution function diverges as $g(2;\phi) \sim (1-\phi/\phi_m)^{-1}$ and the short-time self-diffusivity vanishes as $D_0^s(\phi) \sim D_0(1-\phi/\phi_m)$, so that the normal stresses diverge as $(1-\phi/\phi_m)^{-2}Pe$ or as $(1-\phi/\phi_m)^{-3}Pe$. This scaling prediction is shown to be in reasonable agreement with the available simulation data. This dependence of the rheological response on Pe also explains why suspensions at higher concentrations shear thin at corresponding lower shear rates (*c.f.* Brady 1993b).

We conclude in section 2.5 with a discussion of how the results we have obtained for Brownian hard spheres can be used to predict the normal stresses in suspensions

where the particles interact through repulsive interparticle forces. If the interparticle forces are short-ranged, then there is only a slight quantitative change in the normal stresses; the scaling relations at maximum packing still apply. For long-range repulsive forces characterized by a length b ($\gg a$), the scaling changes as the suspension is now hydrodynamically dilute but "thermodynamically" concentrated. The relevant Peclet number is now based on the length scale b, $Pe_b = \dot{\gamma}b^2/D_0$, with the short-time self-diffusivity, which is a function of the hydrodynamic or true volume fraction, given by the infinite dilution or bare diffusivity, D_0. The equilibrium radial-distribution function now depends on the "thermodynamic" volume fraction $\phi_b = 4\pi nb^3/3$, and diverges at random close packing based on b, ϕ_{bm}. Thus, the normal stress differences are predicted to scale as $(1-\phi/\phi_{bm})^{-1}Pe_b$, as $\phi \to \phi_{bm}$.

Finally, we also show how this perturbation approach can be extended to higher shear rates (or Peclet numbers) to give the complete rheological response as a function of shear rate. We also remark on a singular limit at high Peclet numbers that has recently been worked out [Morris & Brady (1994)] which predicts finite normal stresses in the hydrodynamic limit.

2.2 Perturbation to the microstructure

We consider a suspension of identical spherical particles of radii a subjected to Brownian, interparticle and hydrodynamic forces at low Reynolds number ($\rho\dot{\gamma}a^2/\eta \ll 1$). The equation governing the distribution of particles — the microstructure — is the well-known N–particle Smoluchowski equation:

$$\frac{\partial P_N}{\partial t} + \nabla\cdot\boldsymbol{j}_N = 0, \tag{2.1}$$

where P_N is the probability density for the N particles to be in configuration $\boldsymbol{x}$. The probability flux $\boldsymbol{j}_N$ is given by

$$\boldsymbol{j}_N = \mathbf{U}P_N + \mathbf{R}_{FU}^{-1}\cdot(\mathbf{F}^P - kT\nabla\ln P_N)P_N. \tag{2.2}$$

In (2.2) $\mathbf{U}$ is the velocity of the particles due to the shear flow, and in writing this we have combined the individual particle velocity vectors (for spherical particles only the translational velocities and the positions of the centers of each particle need be considered) into a single 3–N vector $\mathbf{U}$. The colloidal interparticle forces are denoted by $\mathbf{F}^P$, and the Brownian forces are given by kT times the gradient with respect to the configuration vector $\boldsymbol{x}$ of the log of the probability density, $-kT\nabla \ln P_N$. The $3N \times 3N$ hydrodynamic resistance tensor $\mathbf{R}_{FU}$ relates the hydrodynamic force exerted on the particles to their velocities, and its inverse, $\mathbf{R}_{FU}^{-1}$, is the N-particle mobility giving the velocities in terms of the forces. From the Stokes-Einstein relation this mobility multiplied by kT is the N–particle diffusivity tensor:

$$\mathbf{D} = kT\mathbf{R}_{FU}^{-1}. \tag{2.3}$$

With interparticle forces derivable from a potential,

$$\mathbf{F}^P = -\nabla V,$$

the equilibrium distribution ($\mathbf{U} \equiv 0$) is given by

$$\boldsymbol{j}_N = 0,$$

which, since $\mathbf{D}$ is positive definite, requires that

$$\mathbf{F}^P = kT\nabla \ln P_N,$$

whose solution is the Boltzmann distribution

$$P_N^0 \sim \exp(-V/kT), \tag{2.4}$$

where the superscript ^{0} denotes equilibrium. For the case of Brownian hard spheres, the potential is infinite if the particles were to overlap and zero elsewhere, and (2.4)

gives the well-known hard-sphere distribution.

In the presence of a shearing motion, $\mathbf{U} \neq 0$, the particle velocities are given by

$$\mathbf{U} = \langle \mathbf{\Gamma} \rangle \cdot \boldsymbol{x} + \mathbf{R}_{FU}^{-1} \cdot \mathbf{R}_{FE} : \langle \mathbf{E} \rangle, \tag{2.5}$$

where $\langle \mathbf{\Gamma} \rangle = \langle \mathbf{E} \rangle + \langle \mathbf{\Omega} \rangle$, and $\langle \mathbf{E} \rangle$ and $\langle \mathbf{\Omega} \rangle$ are the bulk or macroscopic rate of strain and vorticity tensors of the imposed linear flow, respectively. The hydrodynamic resistance tensor $\mathbf{R}_{FE}$ gives the hydrodynamic forces on the particles due to the imposed flow. In the absence of hydrodynamic interactions (*i.e.*, $\mathbf{R}_{FE} \equiv 0$), the particles would simply be advected by the imposed linear flow: $\mathbf{U} = \langle \mathbf{\Gamma} \rangle \cdot \boldsymbol{x}$.

The flow causes a departure of the microstructure from equilibrium, which we write as

$$P_N = P_N^0 [1 + f_N]. \tag{2.6}$$

The determination of f_N and the resulting rheological response is the central point of this work.

We nondimensionalize all lengths by the particle size a, all velocities by $\dot{\gamma} a$, where $\dot{\gamma} = |\mathbf{\Gamma}|$, and the diffusivity by $D_0 = kT/6\pi\eta a$, the isolated single particle diffusivity, and integrate the N–particle Smoluchowski equation over $N-2$ particles. Neglecting direct coupling to a third particle (which is necessary for analytical progress, but does not affect the form of the Peclet expansion), the equation governing the perturbation to the pair distribution, f, becomes

$$\nabla_r \cdot g(r) \langle \mathbf{D}_r \rangle_2^0 \cdot \nabla_r f = Pe \nabla_r \cdot g(r) \langle \mathbf{U}_r \rangle_2^0 (1 + f), \tag{2.7}$$

with boundary conditions of no flux at the surface of contact of the two particles:

$$\hat{\boldsymbol{r}} \cdot \langle \mathbf{D}_r \rangle_2^0 \cdot \nabla_r f = Pe\, \hat{\boldsymbol{r}} \cdot \langle \mathbf{U}_r \rangle_2^0 (1 + f) \quad @ \quad r = 2, \tag{2.8}$$

and no perturbation at large distances

$$f \sim 0 \quad \text{as} \quad r \to \infty. \tag{2.9}$$

In (2.7) and (2.8) $\mathbf{U}_r = \mathbf{U}_2 - \mathbf{U}_1$ is the relative velocity of two particles arising from the imposed shearing motion, $\mathbf{D}_r$ is their relative diffusivity: $\mathbf{D}_r = \mathbf{D}_{22} + \mathbf{D}_{11} - \mathbf{D}_{12} - \mathbf{D}_{21}$, and ∇_r is the gradient with respect to $\boldsymbol{r} = \boldsymbol{r}_2 - \boldsymbol{r}_1$. The unit vector along the line of centers of the two particles is denoted $\hat{\boldsymbol{r}}$.

The angle brackets $\langle\ \rangle_2^0$ denote a conditional average over the equilibrium distribution with two particles fixed:

$$\langle \mathbf{U}_r(\boldsymbol{r}_1, \boldsymbol{r}_2) \rangle_2^0 \equiv \frac{1}{(N-2)!} \int \mathbf{U}_r(\boldsymbol{r}_1, \boldsymbol{r}_2, \ldots, \boldsymbol{r}_N) \times P^0_{N-2/2}(\boldsymbol{r}_3, \ldots, \boldsymbol{r}_N | \boldsymbol{r}_1, \boldsymbol{r}_2) d\boldsymbol{r}_3 \cdots \boldsymbol{r}_N,$$

where $P^0_{N-2/2}$ is the conditional probability for finding particles at $\boldsymbol{r}_3, \ldots, \boldsymbol{r}_N$ given that there are two particles at $\boldsymbol{r}_1$ and $\boldsymbol{r}_2$. The normalization factor $(N-2)!$ arises because the particles are indistinguishable. We have also introduced the equilibrium pair-distribution function $P_2^0 = n^2 g(r)$, with $g(r)$ the radial-distribution function.

Before proceeding with the perturbation expansion, we must first understand the singular nature of the problem. This is simplest if we consider the limiting form of (2.7) in the absence of hydrodynamic interactions because the singular region is far from contact where hydrodynamic interactions are weak. Without hydrodynamic interactions (2.7)–(2.9) become

$$2\nabla_r^2 f = Pe\langle \hat{\boldsymbol{\Gamma}} \rangle \cdot \boldsymbol{r} \cdot \nabla_r f, \tag{2.10a}$$

$$\hat{\boldsymbol{r}} \cdot \nabla_r f = Pe \hat{\boldsymbol{r}} \cdot \langle \hat{\mathbf{E}} \rangle \cdot \hat{\boldsymbol{r}} (1 + f) \quad @ \quad r = 2, \tag{2.10b}$$

$$f \sim 0 \quad \text{as} \quad r \to \infty, \tag{2.10c}$$

where the factor of 2 in front of diffusive term comes from the fact that the relative diffusivity is twice the single particle diffusivity, and the $\hat{}$ denotes a nondimensional

quantity. It is well known [Leal (1992)] that even though the Peclet number is small, at distances $r \sim O(Pe^{-1/2})$ convection is as important as diffusion in (2.10). Thus, there is an "outer" region where $r = \rho Pe^{-1/2}$, and in outer variables (2.10) becomes

$$2\nabla_\rho^2 f = \langle\hat{\mathbf{\Gamma}}\rangle\cdot\boldsymbol{\rho}\cdot\nabla_\rho f. \tag{2.11}$$

The solution to this outer equation must satisfy the outer boundary condition $f \sim 0$ and match the "inner" solution as $\rho \to 0$.

In the "inner" region with $r \sim O(1)$, we see that departure of f from unity is forced by the boundary condition at contact. This boundary condition has the character of a quadrupole forcing — forced by the second order rate of strain tensor $\langle\hat{\mathbf{E}}\rangle$ — of magnitude $O(Pe)$, and thus the leading inner solution is

$$f = -Pe\,\frac{16}{3}\frac{1}{r^3}(\hat{\mathbf{r}}\cdot\langle\hat{\mathbf{E}}\rangle\cdot\hat{\mathbf{r}}), \tag{2.12}$$

which satisfies the inner boundary condition and asymptotes to 0 at large r.

Now the inner solution (2.12) will be the leading term that must be matched with the outer solution. Rewriting (2.12) in outer variables gives

$$f = -Pe^{5/2}\,\frac{16}{3}\frac{1}{\rho^3}(\hat{\boldsymbol{\rho}}\cdot\langle\hat{\mathbf{E}}\rangle\cdot\hat{\boldsymbol{\rho}}), \tag{2.13}$$

which shows that the leading outer solution must be of $O(Pe^{5/2})$ in order to match with the inner solution. Since this is of lower order than the next *regular* — $O(Pe^2)$ — term in the inner region, the perturbation expansion can be written as a regular series up to $O(Pe^{5/2})$. Specifically, we write

$$f = Pef_1 + Pe^2 f_2 + O(Pe^{5/2}). \tag{2.14}$$

To determine the normal stresses, it is sufficient to solve the regular perturbation problem for f_2. The next term in the expansion is singular and its form is determined by matching with the $O(Pe^{5/2})$ outer solution, which we shall do below.

The first-order perturbation f_1 is a scalar and must be linear in the imposed flow, so we may write

$$f_1 = -h_1(r)\hat{\boldsymbol{r}}\cdot\langle\hat{\mathbf{E}}\rangle\cdot\hat{\boldsymbol{r}}. \tag{2.15}$$

Batchelor (1977) was the first to derive the equation for h_1 and determine the shear viscosity at low shear rates for dilute dispersions.

In a similar manner, the second order perturbation f_2 is also a scalar and must be quadratic in the imposed flow. Thus, f_2 has the form

$$\begin{aligned} f_2 \;=\; & -h_2(r)(\hat{\boldsymbol{r}}\cdot\langle\hat{\mathbf{E}}\rangle\cdot\hat{\boldsymbol{r}})^2 - h_3(r)\hat{\boldsymbol{r}}\cdot\langle\hat{\mathbf{E}}\rangle\cdot\langle\hat{\boldsymbol{\Omega}}\rangle\cdot\hat{\boldsymbol{r}} \\ & -h_4(r)\hat{\boldsymbol{r}}\cdot\langle\hat{\mathbf{E}}\rangle\cdot\langle\hat{\mathbf{E}}\rangle\cdot\hat{\boldsymbol{r}} - h_5(r)\langle\hat{\mathbf{E}}\rangle:\langle\hat{\mathbf{E}}\rangle. \end{aligned} \tag{2.16}$$

The ordinary differential equations governing h_1 through h_5 found by substituting (2.15) and (2.16) in (2.7)–(2.9) are listed in the appendix. Note that because of the normalization of the pair-distribution function, from (2.6) we have the solvability condition

$$\int g(\boldsymbol{r})f(\boldsymbol{r})d\boldsymbol{r} = 0. \tag{2.17}$$

Carrying out the angular integrations shows that f_1 satisfies the requirement, and for f_2 we have

$$\int_2^\infty g(r)\left(\tfrac{2}{15}h_2(r) + \tfrac{1}{3}h_4(r) + h_5(r)\right)r^2dr = 0. \tag{2.18}$$

2.3 Macroscopic stress

The bulk or macroscopic stress of a suspension at low Reynolds numbers can be written as

$$\langle\boldsymbol{\Sigma}\rangle = -\langle p\rangle\mathbf{I} + 2\eta\langle\mathbf{E}\rangle + \langle\boldsymbol{\Sigma}_P\rangle, \tag{2.19}$$

where $\langle p\rangle$ is a constant setting the level of the pressure, and $2\eta\langle\mathbf{E}\rangle$ is the deviatoric stress contribution from the fluid. The particle contribution to the stress $\langle\boldsymbol{\Sigma}_P\rangle$ is given by

$$\langle\boldsymbol{\Sigma}_P\rangle = -nkT\mathbf{I} + n[\langle\mathbf{S}^H\rangle + \langle\mathbf{S}^B\rangle + \langle\mathbf{S}^P\rangle]. \tag{2.20}$$

Here, $-nkT\mathbf{I}$ is the isotropic stress associated with the thermal kinetic energy of the Brownian particles. $\mathbf{I}$ is the isotropic tensor and n is the number density of particles. The hydrodynamic, $\mathbf{S}^H$, Brownian, $\mathbf{S}^B$, and interparticle, $\mathbf{S}^P$, contributions to the stress are given by

$$\langle \mathbf{S}^H \rangle = -\langle \mathbf{R}_{SU} \cdot \mathbf{R}_{FU}^{-1} \cdot \mathbf{R}_{FE} - \mathbf{R}_{SE} \rangle : \langle \mathbf{E} \rangle, \tag{2.21a}$$

$$\langle \mathbf{S}^B \rangle = -kT \langle \nabla \cdot (\mathbf{R}_{SU} \cdot \mathbf{R}_{FU}^{-1}) \rangle, \tag{2.21b}$$

$$\langle \mathbf{S}^P \rangle = -\langle (\mathbf{x}\mathbf{I} + \mathbf{R}_{SU} \cdot \mathbf{R}_{FU}^{-1}) \cdot \mathbf{F}^P \rangle. \tag{2.21c}$$

The additional hydrodynamic resistance tensors, $\mathbf{R}_{SU}$ and $\mathbf{R}_{SE}$, relate the particle stresslets (symmetric first moment of the force distribution integrated over the particle surface, which gives the stress) to the particles' velocities and the rate of strain, respectively. The tensors $\mathbf{R}_{SU}$ and $\mathbf{R}_{SE}$ here are *not* taken to be traceless in their first two indices as has been the convention in the past. The trace of these functions can be used to determine the osmotic pressure. From the symmetry of the low-Reynolds number resistance tensors, $\mathbf{R}_{SU}$ is equal to the transpose of $\mathbf{R}_{FE}$. The angle brackets $\langle\ \rangle$ denote an average over the distribution P_N.

Brady (1993b) showed that the particle contribution to the bulk stress could be rewritten into the more convenient form

$$\begin{aligned} \langle \boldsymbol{\Sigma}_P \rangle = & -nkT\mathbf{I} - nkTa \oint \boldsymbol{n}_2 \boldsymbol{n}_2 P_{1/1}(\boldsymbol{r}_2|\boldsymbol{r}_1) dS_2 - n\langle \boldsymbol{x}\mathbf{F}^P \rangle \\ & -n\langle \mathbf{R}_{SU} \cdot \mathbf{R}_{FU}^{-1} \cdot \mathbf{R}_{FE} - \mathbf{R}_{SE} \rangle : \langle \mathbf{E} \rangle \\ & -n\langle \mathbf{R}_{SU} \cdot \mathbf{R}_{FU}^{-1} \cdot [\mathbf{F}^P - kT\nabla \ln P_N] \rangle, \end{aligned} \tag{2.22}$$

where $P_{1/1}(\boldsymbol{r}_2|\boldsymbol{r}_1)$ is the probability density for finding a particle at $\boldsymbol{r}_2$ given that there is a particle at $\boldsymbol{r}_1$, and the integral is over the surface of contact of the two touching particles; $\boldsymbol{n}_2$ is the unit normal along the line of centers from particle 1 to 2.

Equation (2.22) is identical to (2.20) and is the exact form for the particle stress both in and out of equilibrium. At equilibrium, $\langle \mathbf{E} \rangle = \langle \boldsymbol{\Omega} \rangle = 0$, $\mathbf{F}^P = kT\nabla \ln P_N$,

and (2.22) reduces to the osmotic pressure of a colloidal dispersion. The osmotic pressure, Π, is defined, *mechanically*, to be minus one third the trace of $\langle \boldsymbol{\Sigma}_P \rangle$:

$$\Pi \equiv -\frac{1}{3}\mathbf{I}:\langle \boldsymbol{\Sigma}_P \rangle, \tag{2.23}$$

and at equilibrium

$$\frac{\Pi^0}{nkT} = 1 + 4\phi g(2a) + \tfrac{1}{3}\langle \boldsymbol{x}\cdot\mathbf{F}^P/kT \rangle, \tag{2.24}$$

where $\phi = 4\pi a^3 n/3$ is the volume fraction of particles. The Brownian contribution to the osmotic pressure is given by the equilibrium radial-distribution function at contact $g(r = 2a)$, and the interparticle forces give the familiar $\langle \boldsymbol{x}\cdot\mathbf{F}^P \rangle$ pressure.

Introducing the perturbation to the structure (2.6) the particle stress becomes

$$\begin{aligned} \langle \boldsymbol{\Sigma}_P \rangle \;=\; & -\Pi^0\mathbf{I} + 2\eta\eta'_\infty\langle \mathbf{E} \rangle - n^2 kT 4a^3 g(2a) \oint \hat{\boldsymbol{r}}\hat{\boldsymbol{r}} f(\boldsymbol{r}) d\Omega \\ & -n^2 a^4 \int \hat{\boldsymbol{r}}\hat{\boldsymbol{r}} r F_{12}(r) g(r) f(\boldsymbol{r}) d\boldsymbol{r} \\ & -n\langle (\mathbf{R}_{SU}\cdot\mathbf{R}_{FU}^{-1}\cdot\mathbf{R}_{FE} - \mathbf{R}_{SE}) f_N \rangle_0^0 : \langle \mathbf{E} \rangle \\ & -nkT\langle \mathbf{R}_{SU}\cdot\mathbf{R}_{FU}^{-1}\cdot\nabla f_N \rangle_0^0. \end{aligned} \tag{2.25}$$

In (2.25) Π^0 is the equilibrium osmotic pressure of (2.24), and we have assumed that the interparticle forces are central and pairwise additive:

$$\mathbf{F}_2^P = -\mathbf{F}_1^P = \hat{\boldsymbol{r}} F_{12}(r).$$

The high frequency dynamic viscosity, η'_∞, is defined as the equilibrium average of the hydrodynamic contribution to the stress:

$$2\eta\eta'_\infty\langle \hat{\mathbf{E}} \rangle \equiv -n\langle \mathbf{R}_{SU}\cdot\mathbf{R}_{FU}^{-1}\cdot\mathbf{R}_{FE} - \mathbf{R}_{SE} \rangle_0^0 : \langle \hat{\mathbf{E}} \rangle. \tag{2.26}$$

Note that in the surface and volume integrals from Brownian motion and interparticle forces, knowledge of the perturbation to the pair-distribution function, f, is required, while the other two contributions involving hydrodynamics require knowledge of the

full N–particle distribution f_N. In (2.25) $d\Omega$ denotes the solid angle: $dS_2 = (2a)^2 d\Omega$.

In order to understand the origin of the different contributions to the stress, we shall denote the separate contributions to the stress in (2.25) that depend on the deformation to the structure as $\langle \boldsymbol{\Sigma}_P^{B1} \rangle$, $\langle \boldsymbol{\Sigma}_P^{XF} \rangle$, $\langle \boldsymbol{\Sigma}_P^{H} \rangle$, and $\langle \boldsymbol{\Sigma}_P^{B2} \rangle$, respectively. Introducing the general form for the perturbation expansion for f, neglecting couplings to a third particle arising from many-body hydrodynamics in $\langle \boldsymbol{\Sigma}_P^{H} \rangle$ and $\langle \boldsymbol{\Sigma}_P^{B2} \rangle$, and carrying out the necessary integrations we have to $O(Pe)$

$$\begin{aligned}
\frac{\langle \boldsymbol{\Sigma}_P^{B1} \rangle}{\eta\dot{\gamma}} &= \frac{36}{5}\phi^2 g(2) \times \Big\{ h_1(2)\langle \hat{\mathbf{E}} \rangle \\
&+ Pe\left(\tfrac{1}{3}h_2(2) + \tfrac{5}{6}h_4(2) + \tfrac{5}{2}h_5(2)\right)(\langle \hat{\mathbf{E}} \rangle : \langle \hat{\mathbf{E}} \rangle)\mathbf{I} \\
&+ Pe\left(\tfrac{4}{7}h_2(2) + h_4(2)\right)[\langle \hat{\mathbf{E}} \rangle \cdot \langle \hat{\mathbf{E}} \rangle - \tfrac{1}{3}(\langle \hat{\mathbf{E}} \rangle : \langle \hat{\mathbf{E}} \rangle)\mathbf{I}] \\
&+ Pe\tfrac{1}{2}h_3(2)(\langle \hat{\mathbf{E}} \rangle \cdot \langle \hat{\boldsymbol{\Omega}} \rangle + \langle \hat{\boldsymbol{\Omega}} \rangle^T \cdot \langle \hat{\mathbf{E}} \rangle)\Big\}, \qquad (2.27)
\end{aligned}$$

$$\begin{aligned}
\frac{\langle \boldsymbol{\Sigma}_P^{XF} \rangle}{\eta\dot{\gamma}} &= \frac{9}{5}\phi^2 \times \Big\{ I_1^P \langle \hat{\mathbf{E}} \rangle \\
&+ Pe\left(\tfrac{1}{3}I_2^P + \tfrac{5}{6}I_4^P + \tfrac{5}{2}I_5^P\right)(\langle \hat{\mathbf{E}} \rangle : \langle \hat{\mathbf{E}} \rangle)\mathbf{I} \\
&+ Pe\left(\tfrac{4}{7}I_2^P + I_4^P\right)[\langle \hat{\mathbf{E}} \rangle \cdot \langle \hat{\mathbf{E}} \rangle - \tfrac{1}{3}(\langle \hat{\mathbf{E}} \rangle : \langle \hat{\mathbf{E}} \rangle)\mathbf{I}] \\
&+ Pe\tfrac{1}{2}I_3^P(\langle \hat{\mathbf{E}} \rangle \cdot \langle \hat{\boldsymbol{\Omega}} \rangle + \langle \hat{\boldsymbol{\Omega}} \rangle^T \cdot langle\hat{\mathbf{E}}\rangle)\Big\}, \qquad (2.28)
\end{aligned}$$

$$\begin{aligned}
\frac{\langle \boldsymbol{\Sigma}_P^{H} \rangle}{\eta\dot{\gamma}} &= 4\phi^2 Pe \times \Big\{ \frac{1}{5}\int_2^\infty \mathcal{B}(r)h_1(r)g(r)r^2 dr(\langle \hat{\mathbf{E}} \rangle \cdot \langle \hat{\mathbf{E}} \rangle)\mathbf{I} \qquad (2.29) \\
&- \int_2^\infty \left(\langle L(r) \rangle_2^0 + \tfrac{2}{7}\langle M(r) \rangle_2^0\right) h_1(r)g(r)r^2 dr[\langle \hat{\mathbf{E}} \rangle \cdot \langle \hat{\mathbf{E}} \rangle - \tfrac{1}{3}(\langle \hat{\mathbf{E}} \rangle : \langle \hat{\mathbf{E}} \rangle)\mathbf{I}]\Big\},
\end{aligned}$$

$$\begin{aligned}
\frac{\langle \boldsymbol{\Sigma}_P^{B2} \rangle}{\eta\dot{\gamma}} &= \frac{9}{10}\phi^2 \times \Big\{ I_1^{B2}(3)\langle \hat{\mathbf{E}} \rangle \\
&+ Pe\left(\tfrac{1}{3}I_2^{B2}(0) + \tfrac{5}{6}I_4^{B2}(0) + \tfrac{5}{2}I_5^{B2}(0)\right)(\langle \hat{\mathbf{E}} \rangle : \langle \hat{\mathbf{E}} \rangle)\mathbf{I} \\
&+ Pe\left(\tfrac{4}{7}I_2^{B2}(3) + I_4^{B2}(3)\right)[\langle \hat{\mathbf{E}} \rangle \cdot \langle \hat{\mathbf{E}} \rangle - \tfrac{1}{3}(\langle \hat{\mathbf{E}} \rangle : \langle \hat{\mathbf{E}} \rangle)\mathbf{I}] \\
&+ Pe\tfrac{1}{2}I_3^{B2}(3)(\langle \hat{\mathbf{E}} \rangle \cdot \langle \hat{\boldsymbol{\Omega}} \rangle + \langle \hat{\boldsymbol{\Omega}} \rangle^T \cdot \langle \hat{\mathbf{E}} \rangle)\Big\}, \qquad (2.30)
\end{aligned}$$

where

$$I_i^P = \int_2^\infty F_{12}(r) h_i(r) g(r) r^3 dr, \tag{2.31}$$

$\mathcal{B}(r)$ is a pressure moment function introduced by Jeffrey *et al.* (1993), $\langle L(r)\rangle_2^0$ and $\langle M(r)\rangle_2^0$ are the conditionally averaged hydrodynamic functions associated with the hydrodynamic stress, and $I_i^{B2}(\alpha)$ are given by

$$I_i^{B2}(\alpha) = \int_2^\infty \left(r \frac{dh_i(r)}{dr} \langle A(r)\rangle_2^0 + \alpha h_i(r) \langle B(r)\rangle_2^0 \right) g(r) r^2 dr. \tag{2.32}$$

Before we present results for the stress contributions, we first discuss the order of the next correction in Peclet number to the stress. From the regular perturbation expansion for f, (2.14), we see there will be an $O(Pe^2)$ contribution from the hydrodynamic stress, $\langle \boldsymbol{\Sigma}_P^H \rangle$, involving the perturbation functions h_2–h_4. For simple shear flow this hydrodynamic stress does not contribute to normal stress differences; it only changes the shear viscosity. Although we could present this correction now, we shall see that the Brownian (or interparticle force) contribution to the stress will also have a correction of $O(Pe^2)$ which we have not determined.

The contributions presented above are all from the "inner" region where $r \sim O(1)$, and we must determine the magnitude of the contributions from the "outer" region with $r \sim \rho Pe^{-1/2}$. At large distances, the hydrodynamic contribution to the stress behaves as

$$\frac{|\langle \boldsymbol{\Sigma}_P^H \rangle|}{\eta\dot{\gamma}} \sim \int \frac{1}{r^3} f g r^2 dr \sim O(Pe^{5/2}) \tag{2.33}$$

since $f \sim O(Pe^{5/2})$ in the outer region. The two Brownian contributions can be combined and from the form given in (2.21), we know that at large r

$$\frac{|\langle \boldsymbol{\Sigma}_P^B \rangle|}{\eta\dot{\gamma}} \sim \frac{1}{Pe} \int \frac{1}{r^6} f g r^2 dr \sim O(Pe^3). \tag{2.34}$$

Similar arguments would apply for the interparticle force contribution; a detailed estimate requires knowledge of how F_{12} decays with r. (This is discussed further in section 2.5.) Thus, all contributions from the outer region are at most $O(Pe^{5/2})$.

The next contribution to the stress will come from the next term in the inner region, which is $O(Pe^{5/2})$. This term will generate an $O(Pe^{3/2})$ correction to both the Brownian and interparticle force contributions to the stress. However, as we now show this next term will only contribute to the isotropic stress. The next inner term of $O(Pe^{5/2})$, denoted by f_3, satisfies a homogeneous differential equation with homogeneous inner boundary condition. The solution is forced by matching to the outer problem. The leading outer term satisfies (2.11) and behaves as the quadrupole (2.13) as $\rho \to 0$. Examination of this solution as $\rho \to 0$ shows that the first mismatched term of $O(Pe^{5/2})$ is simply a constant $CPe^{5/2}$. The inner solution at $O(Pe^{5/2})$ must asymptote to a constant at large r; thus, f_3 must be proportional to C and therefore it has no angular dependence — it is a purely radial function. A disturbance in the structure that is purely radial only generates an isotropic macroscopic stress from the Brownian or interparticle force contributions. Thus, the $O(Pe^{5/2})$ correction to the structure contributes only to the osmotic pressure; this contribution being $O(Pe^{5/2})$. The next correction to the deviatoric stress is therefore of $O(Pe^2)$. This $O(Pe^2)$ contribution comes from two sources: the $O(Pe^2)$ deformation to the structure through the hydrodynamic stress contribution discussed above, and the $O(Pe^3)$ correction to the structure through the Brownian and interparticle force contributions. (Note that the $O(Pe^{5/2})$ perturbation to the structure will generate a deviatoric contribution from the hydrodynamic stress of $O(Pe^{5/2})$.)

2.4 Results

2.4.1 Dilute suspensions: $O(\phi^2)$

The ordinary differential equations governing h_1 through h_5 in the appendix have been solved numerically in the dilute limit in the absence of interparticle forces. The two-body hydrodynamic functions are used, and we solve the equations for h_1 through h_5 by the following method: far-field asymptotic results are used to numerically integrate inward to $r = 2$ using a sixth-order Adams-Bashforth integrator, supplemented with

the proper near-field form given by an asymptotic analysis. This solution method follows in the same spirit as that used by Batchelor (1977) to solve for h_1.

Thus, correct to $O(\phi^2 Pe)$, the bulk stress in a general linear flow is given by

$$\begin{aligned}\frac{\langle \boldsymbol{\Sigma}_P^H \rangle}{\eta\dot{\gamma}} &= (5\phi + 9.86\phi^2)\langle \hat{\mathbf{E}} \rangle + 0.940\phi^2 Pe(\langle \hat{\mathbf{E}} \rangle : \langle \hat{\mathbf{E}} \rangle)\mathbf{I} \\ &\quad -1.62\phi^2 Pe[\langle \hat{\mathbf{E}} \rangle \cdot \langle \hat{\mathbf{E}} \rangle - \tfrac{1}{3}(\langle \hat{\mathbf{E}} \rangle : \langle \hat{\mathbf{E}} \rangle)\mathbf{I}] - O(\phi^2 Pe^2, \phi^3), \qquad (2.35)\end{aligned}$$

and

$$\begin{aligned}\frac{\langle \boldsymbol{\Sigma}_P^B \rangle}{\eta\dot{\gamma}} &= 1.96\phi^2\langle \hat{\mathbf{E}} \rangle - 0.532\phi^2 Pe(\langle \hat{\mathbf{E}} \rangle : \langle \hat{\mathbf{E}} \rangle)\mathbf{I} \\ &\quad +0.378\phi^2 Pe[\langle \hat{\mathbf{E}} \rangle \cdot \langle \hat{\mathbf{E}} \rangle - \tfrac{1}{3}(\langle \hat{\mathbf{E}} \rangle : \langle \hat{\mathbf{E}} \rangle)\mathbf{I}] \\ &\quad -0.899\phi^2 Pe(\langle \hat{\mathbf{E}} \rangle \cdot \langle \hat{\mathbf{\Omega}} \rangle + \langle \hat{\mathbf{\Omega}} \rangle^T \cdot \langle \hat{\mathbf{E}} \rangle) + O(\phi^2 Pe^{3/2}, \phi^3), \qquad (2.36)\end{aligned}$$

where we have combined the Brownian contributions into a single expression and have included the $O(\phi)$ and $O(\phi^2)$ contributions from η'_∞ in $\langle \boldsymbol{\Sigma}_P^H \rangle$. Note that the $O(\phi^2 Pe^{3/2})$ error in the Brownian stress is only to the isotropic part; the deviatoric stress is correct to $O(Pe^2)$.

For a simple shear flow with velocity in the 1 direction, velocity gradient in the 2 direction and vorticity 3, the relative viscosity, first and second normal stress differences and the osmotic pressure are:

$$\eta_r = 1 + \frac{5}{2}\phi + 5.91\phi^2 + O(\phi^2 Pe^2), \qquad (2.37)$$

$$\frac{N_1}{\eta\dot{\gamma}} = 0.899\phi^2 Pe + O(\phi^2 Pe^2), \qquad (2.38)$$

$$\frac{N_2}{\eta\dot{\gamma}} = -0.788\phi^2 Pe + O(\phi^2 Pe^2), \qquad (2.39)$$

$$\frac{\Pi}{nkT} = 1 + 4\phi + 0.156\phi Pe^2 + O(\phi Pe^{5/2}). \qquad (2.40)$$

It is important to note that there are no contributions to the relative viscosity from the $O(Pe^2)$ distortion of the equilibrium microstructure through the Brownian stress, nor from the $O(Pe)$ distortion to the structure through the hydrodynamic

stress; so there is no $O(Pe)$ correction to the relative shear viscosity. A second-order analysis is not sufficient to predict a shear-thinning viscosity. The viscosity thus shear thins in simple shear flow at $O(Pe^2)$. Note also that the hydrodynamic stress does not contribute to the first normal stress difference for simple shear flow — only terms proportional to $\langle \hat{\mathbf{E}} \rangle : \langle \hat{\mathbf{\Omega}} \rangle$ contribute.

At present, there are no experimental nor simulation data available to compare with the theoretical predictions for the normal stress differences for dilute suspensions at low Peclet number. Note, however, that at low shear rates,

$$N_1, N_2 \sim \dot{\gamma}^2,$$

as expected. It is encouraging that N_1 is positive and N_2 negative at small Peclet numbers, in agreement with the results of Phung (1993) for more concentrated suspensions.

As discussed by Jeffrey *et al.* (1993), we see that the $O(Pe^2)$ deformation of the microstructure contributes an $O(\phi Pe^2)$ term to the osmotic pressure. There is no $O(\phi Pe)$ correction since $\mathbf{I} : \langle \hat{\mathbf{E}} \rangle = 0$ for an incompressible material.

We should also note that the solvability requirement, (2.17) and (2.18), is satisfied by the solution for f_2 when matching to the outer solution is taken into account.

2.4.2 Scaling theory as $\phi \to \phi_m$

Brady (1993b) has shown that as maximum packing is approached, the dominant contribution to the macroscopic stress comes from the contact integral of the Brownian stress:

$$\langle \mathbf{\Sigma}_P^{B1} \rangle = -n^2 kT 4a^3 g(2a) \oint \hat{\boldsymbol{r}} \hat{\boldsymbol{r}} f(\boldsymbol{r}) d\Omega. \tag{2.41}$$

This result immediately shows that the stress will be proportional to the equilibrium radial-distribution function at contact $g(2a)$.

Now, in the pair-evolution equation (2.7), the relative diffusivity which balances the convective motion, $\langle \mathbf{D}_r \rangle_2^0$, is not simply the infinite dilution value $2\mathbf{I}$ (in dimen-

sionless form), but rather twice the short-time self diffusivity at the volume fraction of interest. That is

$$\langle \mathbf{D}_r \rangle_2^0 \sim 2\hat{D}_0^s(\phi)\mathbf{I},$$

where $\hat{D}_0^s(\phi)$ is the nondimensional short-time self-diffusivity at the volume fraction ϕ. Thus, we see the appropriate Peclet number for the asymptotic expansion is

$$\bar{Pe} = \dot{\gamma}a^2/D_0^s(\phi). \tag{2.42}$$

The perturbation expansion proceeds in powers of $\bar{Pe}$, and we have for $\langle \boldsymbol{\Sigma}_P^{B1} \rangle$

$$\begin{aligned}\frac{\langle \boldsymbol{\Sigma}_P \rangle}{\eta\dot{\gamma}} \sim \frac{\langle \boldsymbol{\Sigma}_P^{B1} \rangle}{\eta\dot{\gamma}} \sim\ & \frac{36}{5}\phi^2 \frac{g(2)}{\hat{D}_0^s(\phi)} \times \Big\{ h_1(2)\langle \hat{\mathbf{E}} \rangle \\ & + \bar{Pe}\left(\tfrac{1}{3}h_2(2) + \tfrac{5}{6}h_4(2) + \tfrac{5}{2}h_5(2)\right)(\langle \hat{\mathbf{E}} \rangle : \langle \hat{\mathbf{E}} \rangle)\mathbf{I} \\ & + \bar{Pe}\left(\tfrac{4}{7}h_2(2) + h_4(2)\right)[\langle \hat{\mathbf{E}} \rangle \cdot \langle \hat{\mathbf{E}} \rangle - \tfrac{1}{3}(\langle \hat{\mathbf{E}} \rangle : \langle \hat{\mathbf{E}} \rangle)\mathbf{I}] \\ & + \bar{Pe}\tfrac{1}{2}h_3(2)(\langle \hat{\mathbf{E}} \rangle \cdot \langle \hat{\boldsymbol{\Omega}} \rangle + \langle \hat{\boldsymbol{\Omega}} \rangle^T \cdot \langle \hat{\mathbf{E}} \rangle)\Big\}. \end{aligned} \tag{2.43}$$

This scaling analysis predicts that the stress scales as $g(2;\phi)/\hat{D}_0^s(\phi) \times \mathcal{F}(\bar{Pe})$, where in (2.43) we have given the result for a general linear flow for $\mathcal{F}$ to $O(\bar{Pe})$.

As random close packing is approached, $\phi \to \phi_m \approx 0.63$, the radial distribution function at contact diverges as [Woodcock (1981)]

$$g(2;\phi) \sim 1.2(1 - \phi/\phi_m)^{-1},$$

and the short-time self diffusivity vanishes as [Brady (1993b); Phung (1993)]

$$\hat{D}_0^s(\phi) \sim 0.85(1 - \phi/\phi_m).$$

Thus, the theory predicts the stress to diverge as $(1 - \phi/\phi_m)^{-2}$. This prediction for the shear viscosity was shown to be in excellent accord with experiment [Brady (1993b)].

To obtain a numerical prediction for the behavior near maximum packing, we need

an estimate for $h_i(2)$. Here we shall use the simple approximation of Brady (1993b) and estimate $h_i(2)$ by neglecting hydrodynamic interactions. The contact values of h_i are listed in the appendix.

For simple shear flow we have as $\phi \to \phi_m$:

$$\eta_r \sim 1.3(1-\phi/\phi_m)^{-2} + O(\bar{Pe}^2), \tag{2.44}$$

$$\frac{N_1}{\eta\dot{\gamma}} \sim 0.51(1-\phi/\phi_m)^{-2}\bar{Pe} + O(\bar{Pe}^2), \tag{2.45}$$

$$\frac{N_2}{\eta\dot{\gamma}} = -0.36(1-\phi/\phi_m)^{-2}\bar{Pe} + O(\bar{Pe}^2), \tag{2.46}$$

$$\frac{\Pi}{nkT} \sim 2.9(1-\phi/\phi_m)^{-1} + 0.27(1-\phi/\phi_m)^{-1}\bar{Pe}^2 + O(Pe^{5/2}). \tag{2.47}$$

Unlike the dilute limit, we can test our theoretical predictions for the normal stress differences using the simulation data of Phung (1993). At this point it is useful to introduce dimensionless normal stress difference coefficients,

$$\chi_1 = \frac{N_1}{\eta\dot{\gamma}Pe}, \tag{2.48}$$

and

$$\chi_2 = \frac{N_2}{\eta\dot{\gamma}Pe}. \tag{2.49}$$

These coefficients are constant at low Peclet number for a given volume fraction. In Figures 2.1a and 2.1b we see very good agreement for χ_1 and χ_2 between our theoretical predictions and the simulation results at $Pe = 0.01$, the smallest value of the Peclet number for which results are available. We also see that the results at $Pe = 0.1$ are substantially less than those at $Pe = 0.01$, so it is not certain that the low $\bar{Pe}$ asymptote has been reached. Note also that in terms of the "bare" Peclet number $\dot{\gamma}a^2/D_0$, the normal stress differences are predicted to diverge as $(1-\phi/\phi_m)^{-3}Pe$. The requirement for the perturbation expansion is now that $\bar{Pe} \ll 1$, which is a very severe requirement as $\phi \to \phi_m$.

2.4.3 Structural deformation

With the solution of the ordinary differential equations for h_1 through h_5 in the dilute limit in the absence of interparticle forces, the microstructure of the suspension in a given flow can be determined. In this section we analyze the microstructure in simple shear flow to determine how the microstructure affects macroscopic properties and to discuss the effects of hydrodynamic interactions on the microstructure.

Figures 2.2a–2.2c are density plots of f for a dilute suspension in simple shear flow at $Pe = 0.1$ neglecting interparticle forces; shown are plots in the velocity-gradient, vorticity-gradient, and velocity-vorticity planes, respectively. These density plots are created so that the test particle at the center of each picture has a value of $f = 0$ and is 50% black. The regions that are greater than 50% black are regions in which f is positive, and the regions lighter than 50% black are regions of negative f.

In Figure 2.2a we see a slight asymmetry with respect to the extensional and compressional axes. This asymmetry is due solely to the $h_3(r)\hat{\mathbf{r}}\cdot\langle\hat{\mathbf{E}}\rangle:\langle\hat{\boldsymbol{\Omega}}\rangle\cdot\hat{\mathbf{r}}$ contribution to f because this contribution is symmetric with respect to the axes in the velocity/gradient directions. All other contributions are either symmetric with respect to the extensional/compressional axes or have an isotropic contribution in the 1-2 plane. Thus, the first normal stress difference is determined solely by $h_3(r)$, as remarked in section 2.4.1.

Also in Figure 2.2a we see a slight distortion of the microstructure along the gradient axis. Previous investigators have been concerned with the deformation of the structure along this axis [Ronis (1984); Schwarzl & Hess (1986); Dhont (1989); Blawzdziewicz & Szamel (1993)], but only the theory of Blawzdziewicz & Szamel (1993) predicts a distortion of the microstructure along the gradient axis. They show that the deformation is small for shear rates up to $Pe = 0.5$. From our analysis we find the deformation along the gradient axis in simple shear flow to be

$$f(r; 2-axis) = \frac{1}{4}\left(h_3(r) - h_4(r) - 2h_5(r)\right) Pe^2.$$

We see that the deformation is $O(Pe^2)$ which explains why Blawzdziewicz & Szamel

(1993) report only a small distortion for small Pe.

Since the $O(Pe)$ deformation only distorts the structure in the velocity-gradient plane, the structural changes in the vorticity-gradient, Figure 2.2b, and velocity-vorticity, Figure 2.2c, planes are $O(Pe^2)$. Although there is an $O(Pe^2)$ deformation to the microstructure in the vorticity-gradient plane, this contribution does not lead to a shear-thinning viscosity in the absence of hydrodynamic interactions, as was postulated by Blawzdziewicz & Szamel (1993). As discussed earlier, it is the $O(Pe^3)$ deformation to the structure that leads to a shear-thinning viscosity. It should be no surprise that structural changes in the vorticity-gradient plane are not correlated with shear-thinning since Bossis & Brady (1989) report a shear-thinning viscosity in monolayer dispersions.

Since we have solved for the structure of a dilute suspension at low Peclet number both with and without hydrodynamic interactions, we can assess the contribution to the structure solely due to hydrodynamic interactions. These contributions are plotted in Figures 2.3a–2.3c at $Pe = 0.1$ for the velocity-gradient, vorticity-gradient and velocity-vorticity planes, respectively. As before we use the test particle in the middle at 50% black; so hydrodynamics have a negative effect in lighter regions and a positive effect in darker regions.

In the velocity-gradient plane (Figure 2.3a) at large distances, we see that hydrodynamic interactions increase the particle density along the extensional axis and decrease the density along the compressional axis, but the opposite occurs very near the particle surface. This sign change is an $O(Pe)$ effect given by h_1 (*c.f.*, (2.14) and (2.15)), as shown below. The value of h_1 at contact is $h_{1,H}(2) = 0.71$ and $h_{1,NH}(2) = 0.67$ for the cases of two-particle hydrodynamics and no-hydrodynamic interactions, respectively; therefore, $h_{1,H} - h_{1,NH} > 0$ very near the particle surface. Far away from the particle, $h_{1,H}(r) \sim 4.46/r^3$ and $h_{1,NH}(r) \sim 5.33/r^3$; thus, $h_{1,H} - h_{1,NH} < 0$ as $r \to \infty$ and hydrodynamic interactions have opposite effects on the microstructure in these two limiting cases.

We shall first analyze the compressional axis to describe why this sign change occurs. Far from the test particle, hydrodynamic interactions tend to hinder a second

particle from approaching; so we expect a negative contribution from hydrodynamic interactions along the compressional axis at large distances. Close to the test particle, however, the second particle is trying to diffuse away from the test particle while the external flow tends to push the particles together; external flow dominates near the particle, resulting in a build-up of particles near the surface along the compressional axis. Along the extensional axis the situation is reversed: hydrodynamic interactions tend to stop the particles from moving apart at large distances, leading to a positive hydrodynamic contribution far from the test particle. Near the test particle, the second particle is diffusing away and the external flow is pulling the particles apart, and there is a negative hydrodynamic contribution near the particle along the extensional axis.

We can confirm this physical picture by solving the differential equation for h_1 for a suspension of particles that interact with a hard-sphere potential characterized by a length b ($> a$). The appropriate length scale for the pair-evolution equation (2.7) is now b, and the no-flux boundary condition (2.8) is applied at a distance $2b$ from the particle, while all hydrodynamic interactions remain scaled by the particle size, a. As a result of this scaling, we can solve the differential equation for h_1, as it is presented in the appendix with Pe replaced by $Pe_b = \dot{\gamma}b^2/D_0$, and we simply apply the no-flux boundary condition at $r = 2b/a$. Since $b/a > 1$, lubrication effects are eliminated but both the far-field hydrodynamic interactions and the balance between convective and diffusive fluxes at the hard-sphere surface are retained; therefore, the effects of hydrodynamic interactions near the hard-sphere surface are a result only of the no-flux boundary condition. The results of this study are valid for $Pe_b \ll 1$ and for suspensions that are dilute based on the thermodynamic volume fraction, ϕ_b.

Before presenting the results of this study, we analyze two limiting cases, $b/a \to 1$ and $b/a \to \infty$. For the case of $b/a \to 1$, both the hydrodynamic and thermodynamic length scales are identical, and we recover our previous results for Brownian hard spheres in the absence of interparticle forces. If $b/a \to \infty$, hydrodynamic interactions are negligible and we recover the solution for the case in which hydrodynamics is neglected with Pe replaced by Pe_b; thus, hydrodynamic interactions have a negligible

effect on the microstructure as $b/a \to \infty$. When $b/a \sim O(1)$, we find that $h_{1,H} - h_{1,NH}$ is positive near $r = 2b/a$ and negative at large distances for $1.25 < b/a < 9$, and we see that the sign change in $h_{1,H} - h_{1,NH}$ is caused by the balance of the convective flux and diffusive flux at $r = 2b/a$ and *not* lubrication. It is interesting to note that there is a maximum value of $h_{1,H} - h_{1,NH}$ at $r = 2b/a$ for $b/a \approx 4$, and we conclude that lubrication has the expected effect — a reduction in the particle density near the test particle along the compressional axis, but the effect is quantitative rather than qualitative.

2.5 Conclusions

In this paper normal stresses in a suspension of Brownian hard spheres at low shear rate have been determined theoretically. An evolution equation for the pair-distribution function was developed, and it was shown that the perturbation to the microstructure is regular to $O(Pe^2)$ for a general linear flow with the next term being $O(Pe^{5/2})$. The bulk stress for a dilute suspension in a general linear flow was determined to $O(\phi^2 Pe)$, and normal stresses in simple shear flow were determined to be: $N_1/\eta\dot{\gamma} = 0.899\phi^2 Pe$ and $N_2/\eta\dot{\gamma} = -0.788\phi^2 Pe$ for $Pe \ll 1$.

A scaling theory was presented for concentrated suspensions using the corrected time scale, $a^2/D_0^s(\phi)$, and the appropriate Peclet number, $Pe = \dot{\gamma}a^2/D_0^s(\phi)$, replacing $Pe = \dot{\gamma}a^2/D_0$. This scaling theory predicted that the stress diverges near maximum packing, ϕ_m, as $g(2;\phi)/\hat{D}_0^s(\phi)$ because the dominant contribution to the stress comes from the Brownian stress. Hence, normal stress differences in simple shear flow diverge as $N_i/\eta\dot{\gamma} \sim \bar{P}e\ g(2;\phi)/\hat{D}_0^s(\phi) \sim (1-\phi/\phi_m)^{-2}\bar{P}e$ as $\phi \to \phi_m$ and $\bar{P}e \ll 1$. This scaling theory does not rely on any of the assumptions made in deriving the evolution equation for the pair-distribution function (*e.g.*, neglect of third-body interactions) and relies on the use of the appropriate time scale, $a^2/D_0^s(\phi)$. In addition, the scaling theory emphasizes the importance of both thermodynamic and hydrodynamic effects on rheology since both contribute to the divergence of the normal stresses — there is a thermodynamic contribution of $(1-\phi/\phi_m)^{-1}$ through the divergence of $g(2;\phi)$ and

a hydrodynamic contribution of $(1-\phi/\phi_m)^{-1}$ since $\hat{D}_0^s(\phi)$ vanishes as $\phi \to \phi_m$.

With knowledge of this scaling theory and the similarity between the Brownian and interparticle force contributions to the stress, we can analyze Brownian particles that interact through interparticle forces. If the range of the colloidal force is comparable to the particle size, both hydrodynamics and thermodynamics are important, the scaling does not change near maximum packing, and the normal stress differences diverge as $N_i/\eta\dot{\gamma} \sim (1-\phi/\phi_m)^{-2}\bar{P}e$ as $\phi \to \phi_m$. On the other hand, if the particles interact through long-range repulsive forces, the thermodynamic volume fraction, $\phi_b = 4\pi b^3 n/3$, is much greater than the hydrodynamic volume fraction, the stress diverges only through $g(2;\phi_b)$ as random close packing of the thermodynamic volume fraction is approached, and the normal stress differences diverge as $N_i/\eta\dot{\gamma} \sim (1-\phi_b/\phi_{bm})^{-1}Pe_b$ as $\phi \to \phi_{bm}$, where $Pe_b = \dot{\gamma}b^2/D_0$.

A natural extension of this work would be to include conditionally averaged hydrodynamic interactions to extend the results to mildly concentrated suspensions at low Peclet number. The conditionally averaged hydrodynamic quantities can be obtained quite simply from Stokesian Dynamics because they depend only on the equilibrium distribution of particles at a given volume fraction, ϕ, and the separation between two particles. Despite the simplicity of these functions, this approach may prove to be inadequate because the evolution equation for the pair-distribution may no longer capture the proper physics due to one or more of the closure assumptions (*e.g.*, neglect of third-body interactions and/or breaking of non-linear averages, $\langle fg\rangle = \langle f\rangle\langle g\rangle$).

This work may also form a starting point for an extension to higher Peclet numbers by expressing the pair-distribution function in terms of an eigenfunction expansion. A similar method was used by Blawzdziewicz & Szamel (1993) for the case of a dilute suspension in simple shear flow in the absence of hydrodynamic interactions where the pair-distribution function is expressed as a linear combination of multipoles using the Elrick solution. Although the Elrick solution provides the correct eigenfunctions for this particular system, an expansion that uses general eigenfunctions may be required to include hydrodynamic interactions, external flows other than simple shear flow, and mildly concentrated suspensions. For suspensions near maximum pack-

ing, the expansion used by Blawzdziewicz & Szamel (1993) should give reasonable approximations by using the scaling theory presented here.

One important rheological feature that we would like to predict through an eigenfunction expansion is the sign change in the first normal stress difference. It has been found by Phung (1993) and Laun (1994) for simple shear flow, that at low Peclet number $N_1 > 0$ and at high Peclet number $N_1 < 0$ with the sign change occurring around $Pe \approx 1 - 10$. From the data of Phung (1993), there is a positive Brownian contribution that decays $\sim 1/Pe$, and a hydrodynamic contribution that is negative and approaches a constant value as $Pe \to \infty$. At low Peclet number the Brownian contribution dominates, yielding a positive N_1; while at high Peclet number, the hydrodynamic contribution dominates and $N_1 < 0$. Thus, the hydrodynamic contribution must be predicted.

We would also like to use this method to confirm the theoretical findings of Morris and Brady (1994) for normal stress differences at high Peclet number. By performing an asymptotic analysis of the microstructure of a suspension as $Pe \to \infty$, they have been able to determine that N_1 and $N_2 \sim \eta\dot{\gamma}$ as $Pe \to \infty$. This scaling has been numerically confirmed by Phung (1993).

References

Al-Hadithi, T.S.R., H.A. Barnes, & K. Walters, "The relationship between the linear (oscillatory) and nonlinear (steady-state) flow properties of a series of polymer and colloidal systems." Colloid Polym. Sci. **270**, 40–46 (1992).

Batchelor, G.K., "The effect of Brownian motion on the bulk stress in a suspension of spherical particles." J. Fluid Mech. **83**, 97–117 (1977).

Batchelor, G.K. & J.T. Green, "The hydrodynamic interaction of two small freely moving spheres in a linear flow field." J. Fluid Mech. **56**, 375–400 (1972).

Blawzdziewicz, J. & G. Szamel, "Structure and rheology of semidilute suspension under shear." Phys. Rev. E **48**, 4632–4636 (1993).

Bossis, G. & J.F. Brady, "Dynamic simulation of sheared suspensions. I. General method." J. Chem. Phys. **80**, 5141–5154 (1984).

Bossis, G. & J.F. Brady, "Self-diffusion of brownian particles in concentrated suspensions under shear." J. Chem. Phys. **87**, 5437–5448 (1987).

Bossis, G. & J.F. Brady, "The rheology of brownian suspensions." J. Chem. Phys. **91**, 1866–1874 (1989).

Brady, J.F. & G. Bossis, "The rheology of concentrated suspensions of spheres in simple shear flow by numerical simulation." J. Fluid Mech. **155**, 105–129 (1985).

Brady, J.F. & G. Bossis, "Stokesian dynamics." Ann. Rev. Fluid Mech. **20**, 111–157 (1988).

Brady, J.F., "Brownian motion, hydrodynamics, and the osmotic pressure." J. Chem. Phys. **98**, 3335–3341 (1993a).

Brady, J.F., "The rheological behavior of concentrated colloidal dispersions." J. Chem. Phys. **99**, 567–581 (1993b).

Brady, J.F., "The long-time self-diffusivity in concentrated colloidal dispersions." J. Fluid Mech. **272**, 109–133 (1994).

Dhont, J.K.G., "On the distortion of the static structure factor of colloidal fluids in shear flow." J. Fluid Mech. **204**, 421–431 (1989).

Jeffrey, D.J., J.F. Morris, & J.F. Brady, "The pressure moments for two rigid spheres in low-Reynolds-number flow." Phys. Fluids A **5**, 2317-2325 (1993).

Johma, A.I. & P.A. Reynolds, "An experimental study of the first normal stress difference-- shear stress relationship in simple shear flow for concentrated shear thickening suspensions." Rheol. Acta. **32**, 457–464 (1993).

Kim, S. & S.J. Karrila, *Microhydrodynamics: Principles and selected applications.* (Butterworth-Heinemann, Boston, 1991).

Kim, S. & R.T. Mifflin, "The resistance and mobility functions of two equal spheres in low Reynolds number flow." Phys. Fluids **28**, 2033 2045 (1985).

Laun, H.M., "Normal stresses in extremely shear thickening polymer dispersions." J. Non-Newt. Fluid Mech. **54**, 87–108 (1994).

Leal, L.G., *Laminar flow and convective transport processes: Scaling principles and asymptotic analysis.* (Butterworth-Heinemann, Boston, 1992).

Morris, J.F. & J.F. Brady (to be submitted).

Phung, T.N., Ph.D. thesis, California Institute of Technology, 1993.

Phung, T.N. & J.F. Brady, "Microstructured fluids: structure, diffusion and rheology of colloidal dispersions." in *Slow Dynamics in Condensed Matter*, edited by Kawasaki, Tokuyama and Kawakatsu, AIP Conference Proc. 256 (Am. Inst. of Phys., New York, 1992), pp. 391-400.

Ronis, D., "Theory of fluctuations in colloidal suspensions undergoing steady shear flow." Phys. Rev. A **29**, 1453–1460 (1984).

Schwarzl, J.F. & S. Hess, "Shear-flow induced distortion of the structure of a fluid—application of a simple kinetic equation." Phys. Rev. A **33**, 4277-4283 (1986).

van der Werff, J.C. & C.G. de Kruif, "Hard-sphere colloidal dispersions: the scaling of rheological properties with particle size, volume fraction, and shear rate." J. Rheol. **33**, 421-454 (1989).

van der Werff, J.C., C.G. de Kruif, & J.K.G. Dhont, "The shear-thinning behaviour of colloidal dispersions. II. Experiments." Physica A **160**, 205–212 (1989).

van der Werff, J.C, Ph.D. thesis, University of Utrecht, 1990.

Woodcock, L.V., "Glass transition in the hard sphere model and Kauzman's paradox." Ann. N.Y. Acad. Sci. **37**, 274 (1981).

Yoon, B.J. & S. Kim, "Note on the direct calculation of mobility functions for two equal spheres in Stokes flow." J. Fluid Mech. **185**, 437–446 (1987).

Appendix A

The equations governing the perturbation functions h_i defined in (2.15) and (2.16) are found by substituting f from (2.14) into the steady pair-evolution equation (2.7). We make use of the following definitions for the relative diffusivity and velocity:

$$\langle \mathbf{D}_r \rangle_2^0 = 2\left(\langle G(r)\rangle_2^0 \hat{\boldsymbol{r}}\hat{\boldsymbol{r}} + \langle H(r)\rangle_2^0 (\mathbf{I} - \hat{\boldsymbol{r}}\hat{\boldsymbol{r}})\right), \tag{2.50}$$

$$\langle \mathbf{U}_r \rangle_2^0 = r\hat{\boldsymbol{r}}\cdot\left(\langle \hat{\mathbf{E}}\rangle + \langle \hat{\boldsymbol{\Omega}}\rangle\right) - r\hat{\boldsymbol{r}}\cdot\langle \hat{\mathbf{E}}\rangle \left(\langle A(r)\rangle_2^0 \hat{\boldsymbol{r}}\hat{\boldsymbol{r}} + \langle B(r)\rangle_2^0 (\mathbf{I} - \hat{\boldsymbol{r}}\hat{\boldsymbol{r}})\right). \tag{2.51}$$

The ordinary differential equations for $h_i(r)$ are:

$$L_2 h_1(r) = -\tfrac{1}{2} g(r)\langle W(r)\rangle_2^0 - \tfrac{1}{2} r\left(1 - \langle A(r)\rangle_2^0\right)\frac{dg(r)}{dr}, \tag{2.52}$$

$$L_4 h_2(r) = \left(\tfrac{1}{2}\langle W(r)\rangle_2^0 - 1 + \langle B(r)\rangle_2^0\right) g(r) h_1(r) + \tfrac{1}{2} r\left(1 - \langle A(r)\rangle_2^0\right)\frac{dg(r)h_1(r)}{dr}, \tag{2.53}$$

$$L_2 h_3(r) = -h_1(r), \tag{2.54}$$

$$L_2 h_4(r) = -8\frac{\langle H(r)\rangle_2^0}{r^2} h_3(r) + \left(1 - \langle B(r)\rangle_2^0\right) h_1(r), \tag{2.55}$$

$$L_0 h_5(r) = -2\frac{\langle H(r)\rangle_2^0}{r^2} h_4(r), \tag{2.56}$$

with the operator, L_α, defined by

$$L_\alpha = \frac{1}{r^2}\frac{d}{dr}\left(r^2 g(r)\langle G(r)\rangle_2^0 \frac{d}{dr}\right) - \alpha(\alpha+1)\frac{g(r)\langle H(r)\rangle_2^0}{r^2}, \tag{2.57}$$

and with $\langle W(r)\rangle_2^0$ given by

$$\langle W(r)\rangle_2^0 = 3\left(\langle B(r)\rangle_2^0 - \langle A(r)\rangle_2^0\right) - r\frac{d\langle A(r)\rangle_2^0}{dr}. \tag{2.58}$$

All five ordinary differential equations have the same boundary condition at large r,

$$h_i(r) \sim 0 \quad \text{as} \quad r \to \infty, \tag{2.59}$$

but they have different inner boundary conditions @ $r = 2$:

$$\langle G(r)\rangle_2^0 h_1'(r) = -\left(1 - \langle A(r)\rangle_2^0\right), \tag{2.60}$$

$$\langle G(r)\rangle_2^0 h_2'(r) = h_1(r)\left(1 - \langle A(r)\rangle_2^0\right), \tag{2.61}$$

$$\langle G(r)\rangle_2^0 h_3'(r) = 0, \tag{2.62}$$

$$\langle G(r)\rangle_2^0 h_4'(r) = 0, \tag{2.63}$$

$$\langle G(r)\rangle_2^0 h_5'(r) = 0. \tag{2.64}$$

Note that when complete hydrodynamic interactions are used, the inner boundary conditions are all the same:

$$\langle G(r)\rangle_2^0 h_i'(r) = 0 \quad @ \quad r = 2. \tag{2.65}$$

The functions $\langle A(r)\rangle_2^0$, $\langle B(r)\rangle_2^0$, $\langle G(r)\rangle_2^0$, and $\langle H(r)\rangle_2^0$, are nondimensional effective hydrodynamic functions between two particles in the suspension. These functions depend only on the equilibrium distribution and the relative separation between two particles. In the dilute limit, the effective hydrodynamic functions are simply equal to their two-particle values (*i.e.*, $\langle A(r)\rangle_2^0 = A(r)$) and have been well-studied [Batchelor & Green (1972); Kim & Mifflin (1985); Yoon & Kim (1987); Kim & Karrila (1991)].

For future use, we record here the solution to h_1–h_5 in the absence of hydrodynamic interactions:

$$h_1(r) = \frac{16}{3}\frac{1}{r^3}; \quad h_1(2) = \frac{2}{3} \tag{2.66}$$

$$h_2(r) = \frac{2}{3}\left(\frac{1}{r} - \frac{16}{r^5}\right); \quad h_2(2) = 0, \tag{2.67}$$

$$h_3(r) = \frac{8}{27}\left(\frac{3}{r} - \frac{4}{r^3}\right); \quad h_3(2) = \frac{8}{27}, \tag{2.68}$$

$$h_4(r) = -\frac{32}{63}\left(\frac{5}{r^3} - \frac{12}{r^5}\right); \quad h_4(2) = -\frac{8}{63}, \tag{2.69}$$

$$h_5(r) = -\frac{4}{945}\left(\frac{105}{r} - \frac{200}{r^3} + \frac{144}{r^5}\right); \quad h_5(2) = -\frac{128}{945}. \tag{2.70}$$

From the above solutions for h_2-h_5, we see that the solvability condition (2.18)

is apparently not satisfied by the $1/r$ terms in h_2-h_5. This slowly decaying function must be matched to an outer solution, and when this is done, the full uniformly valid expansion for f satisfies the solvability condition (2.17).

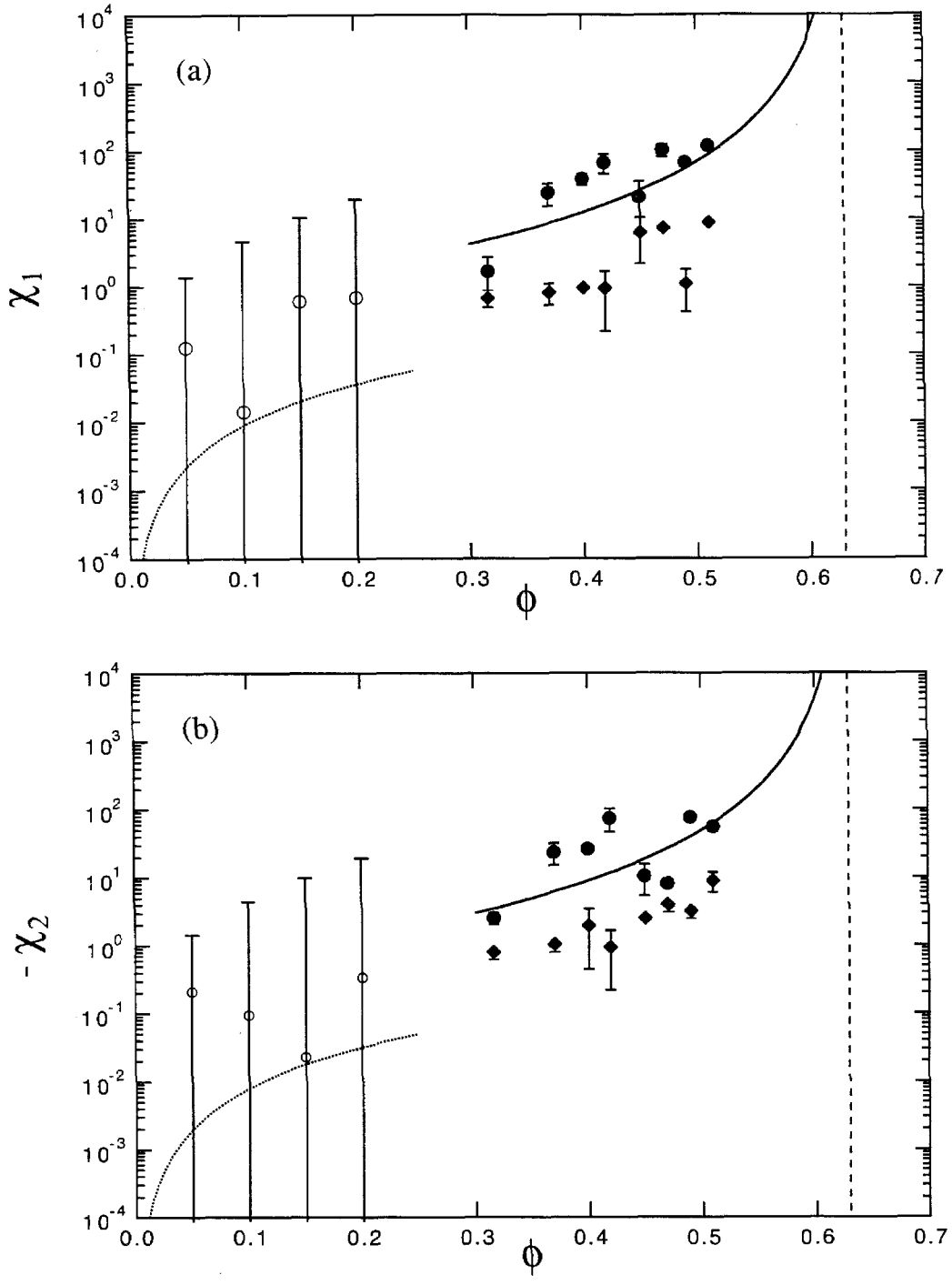

Figure 2.1: Comparison of the theoretical predictions for the dimensionless normal stress coefficients, (a) χ_1 and (b) $-\chi_2$, for Brownian hard spheres in simple shear flow with the Stokesian Dynamics results of Phung (1993), where $\chi_i = N_i/\eta\dot{\gamma}Pe$. The dotted lines are the theoretical predictions for dilute suspensions, Equations (38) and (39), and the solid lines are the scaling theories, Equations (45) and (46), as random close packing, $\phi_m \approx 0.63$, is approached. The symbols are the results of Phung (1993) for $N = 27$ at: $Pe = 0.01$ (solid circles) and $Pe = 0.1$ (solid diamonds).

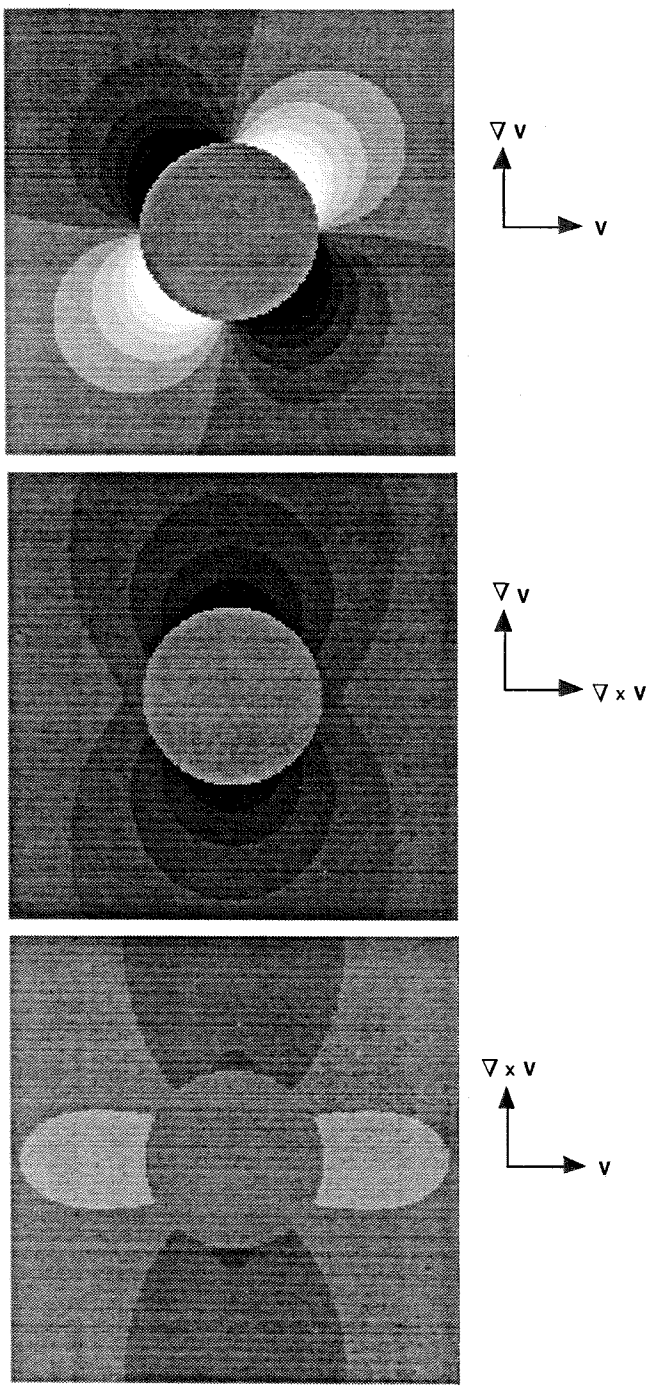

Figure 2.2: Density plots of the perturbation quantity f in the (a) velocity-gradient, (b) vorticity-gradient and (c) velocity-vorticity planes for a dilute suspension in simple shear flow with two-particle hydrodynamic interactions in the absence of interparticle forces at $Pe = 0.1$. The test particle at the center is at 50 percent black, darker regions have positive f while lighter regions have negative f.

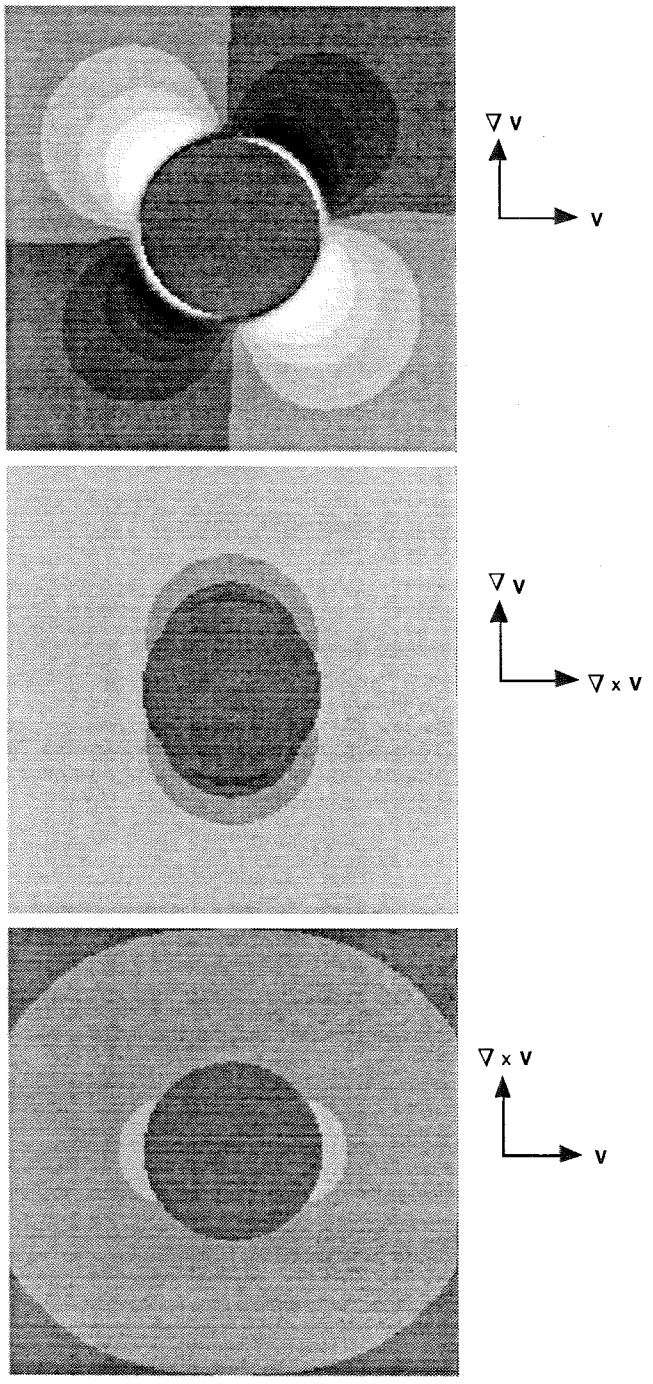

Figure 2.3: Density plots of the contribution to the perturbation quantity f from two-particle hydrodynamic interactions in the (a) velocity-gradient, (b) vorticity-gradient and (c) velocity-vorticity planes for a dilute suspension in simple shear flow in the absence of interparticle forces at $Pe = 0.1$. The test particle at the center is at 50 percent black, where there is no effect from hydrodynamic interactions; hydrodynamics has a positive effect in darker regions and a negative effect in lighter regions.

Chapter 3
Colloidal dispersions at arbitrary Peclet number in simple shear flow

3.1 Introduction

The nonequilibrium microstructure and macroscopic properties of hard-sphere colloidal dispersions in simple shear flow are predicted by solving the two-particle Smoluchowski equation for a range of Peclet numbers and evaluating the bulk stress. Dilute results are extended to higher concentrations by using the scaling theory of Brady (1993b). The colloidal particles have a hydrodynamic radius, a, and a thermodynamic (or effective hard sphere) radius, b, allowing hard sphere ($b/a \to 1$), sterically stabilized ($b/a < 1.1$), and charge stabilized ($b/a > 2$) systems to be studied while including two-particle hydrodynamic interactions. The Peclet number associated with such systems is $Pe_b = 6\pi\eta_s\dot{\gamma}ab^2/kT$, where η_s is the Newtonian viscosity of the suspending fluid, $\dot{\gamma}$ is the shear rate, k is the Boltzmann constant, and T is the absolute temperature.

In section 3.2, the nonequilibrium microstructure is expanded in terms of surface spherical harmonics and the resulting two-particle Smoluchowksi equation and its boundary conditions are derived in a form that can be used for any linear flow. Symmetry arguments are made for simple shear flow to reduce the number of coupled ordinary differential equations. The solution method is discussed and compared and contrasted with the work of Lionberger (1998), who uses approximations for the outer boundary condition. These approximations are not used in the current work.

After finding the nonequilibrium microstructure, the macroscopic properties are calculated by using the equations for the bulk stress in section 3.3. The equations for the hydrodynamic, Brownian and interparticle force contributions to the bulk stress are valid to $O(\phi_b^2)$, where $\phi_b = 4\pi nb^3/3$ and n is the particle density, and are derived in a general form for arbitrary values of b/a for spherical particles. The bulk stress is not traceless and the nonequilibrium osmotic pressure is calculated.

Section 3.4 is split into three parts. In part 3.4.1 the particles have $b/a = 1$ and hydrodynamic interactions are neglected. In the next part, part 3.4.2, the particles hydrodynamically interact with $b/a \to 1$. Finally, in part 3.4.3 sterically stabilized and charge stabilized dispersions are studied by varying the value of b/a while keeping

two-particle hydrodynamic interactions.

When hydrodynamic interactions are neglected and $b/a = 1$ (section 3.4.1), numerical results are obtained for $Pe \leq 20$. At large Peclet number, the interparticle force stress has a viscous scaling, $\sim O(\eta_s \dot{\gamma})$, and the viscosity, normal stress differences and osmotic pressure all have non-zero asymptotes in the limit $Pe \to \infty$. These non-zero asymptotes are caused by the formation of a boundary layer at particle contact in the compressional zone in which the probability of finding a second particle is $\sim O(Pe)$. At low Peclet number, the relative shear viscosity is constant and then shear thins with a term that is $\sim O(\phi^2 Pe^2)$. Dilute results for viscosity are extended to higher concentrations and compared with Brownian Dynamics [Foss & Brady (1999)] with reasonable agreement at small volume fractions but poor agreement at high volume fractions. The poor agreement is caused by a relaxation time that is dependent on the volume fraction [Bergenholtz (1999)], while the scaling theory of Brady (1993b) predicts a single relaxation time for Brownian Dynamics, independent of volume fraction. A Cox-Merz rule is shown to be valid over the range volume fractions for which the relaxation time is independent of volume fraction, and a Padé approximate is formed for the numerical results of this study. Normal stress differences at low Peclet number have the form, $N_i/\eta_s\dot{\gamma} \sim O(Pe) + O(Pe^{5/2})$. The $O(Pe^{5/2})$ comes from the $O(Pe^{7/2})$ deformation of the microstructure since the $O(Pe^3)$ deformation yields contributions only to the isotropic and shear stresses. The scaling theory of Brady (1993b) is used and the dilute results qualitatively predict the behavior of Brownian Dynamics simulations [Foss & Brady (1999)]. Furthermore, the normal stress differences only cause negative rod climbing, as shown by using the heuristic argument of Lodge, Schieber & Bird (1988), since $|N_1/N_2| \sim O(1)$. Finally, the osmotic pressure has the form, $\Pi/nkT - 1 - 4\phi - (16/45)\phi Pe^2 + O(Pe^{5/2})$, at low Peclet number, as shown by Brady & Vicic (1995). The coefficient of the $O(Pe^{5/2})$ term is predicted by matching the $O(Pe^{5/2})$ isotropic term of the inner expansion with the first mismatched term of the outer expansion, and the coefficient is in excellent agreement with the numerical results. The results are extended to higher concentrations by a scaling theory [Brady (1993b)] and are in reasonable agreement with

Brownian Dynamics simulation data [Foss & Brady (1999)].

In section 3.4.2 two particles hydrodynamically interact and $b/a \to 1$. The limit of $b/a \to 1$ is used instead of $b/a = 1$ to avoid closed streamlines, to account for surface roughness or the presence of a steric stabilizer, and to avoid a singularity in the problem since the radial component of the relative diffusivity vanishes at particle contact when $b/a = 1$. The shear viscosity is constant at low Peclet number, shear thins, reaches a constant value and then shear thickens at high Peclet number. Shear thinning is caused by a decrease in the Brownian viscosity due to the reduced importance of Brownian motion as Peclet number increases in agreement with experiments [Kaffashi *et al.* (1997)] and simulations [Foss *et al.* (1999)]. Shear thickening occurs because of an increase in the hydrodynamic viscosity, again in agreement with experiments [Bender & Wagner (1995); O'Brien & Mackay (1996)] and simulations [Foss *et al.* (1999)]. The root cause of hydrodynamic shear thickening is the formation of a boundary layer in the compressional zone at particle contact and the presence of hydrodynamic interactions, resulting in an increase in the hydrodynamic contribution to the viscosity with increasing rate. The constant viscosity at intermediate Peclet numbers occurs simply because the hydrodynamic viscosity is increasing at the same rate that the Brownian viscosity is decreasing. Scaling theory [Brady (1993b)] is used to extend these results to finite concentrations. The scaling theory collapses experimental and simulation data to a single master curve, but the dilute results are in only qualitative agreement.

The same interplay between the Brownian and hydrodynamic contributions is also evident for the first normal stress difference. At low Peclet number the first normal stress difference is positive, but it is negative at high Peclet number. The sign change occurs because the Brownian and hydrodynamic contributions have different signs, and the Brownian contribution dominates for $Pe \ll 1$ while the hydrodynamic contribution dominates at $Pe \gg 1$. The sign change occurs near $Pe\eta'_\infty \approx 10$, where η'_∞ is the nondimensional high-frequency dynamic viscosity, and the dilute theory properly predicts the sign change for Stokesian Dynamics simulation data [Foss *et al.* (1999)] after using the scaling theory [Brady (1993b)]. The hydrodynamic contribution to

the first normal stress difference is $O(Pe^{5/2})$ at low Peclet number and arises from the $O(Pe^{5/2})$ term of the outer expansion. Also, the first normal stress difference at high Peclet number is negative because the boundary layer extends into the extensional zone with a relatively small downstream shift of the maximum contact value in the boundary layer.

Since both the hydrodynamic and Brownian contributions are negative for all Peclet number, the second normal stress difference is always negative. The dilute results correctly predict a maximum near $Pe\eta'_\infty \approx 4$ when compared to scaled Stokesian Dynamics results [Foss *et al.* (1999); Brady (1993b)]. This dilute theory also predicts that only negative rod climbing should occur, and this fact has been experimentally confirmed by Leighton (1997) in the high Peclet limit.

Next, in section 3.4.3 the value of b/a is varied. Shear thickening occurs at larger values of Pe_b as b/a increases, and the degree of shear thickening decreases since lubrication interactions are eliminated and the effects of far-field hydrodynamic interactions are reduced as b/a increases. At some large value of b/a, the hydrodynamic viscosity will appear only as a small constant value for all Peclet numbers since hydrodynamic shear thickening is slight. The shear viscosity decreases with a decrease in the thermodynamic radius, b, for a system in which the particle radius, a, and particle volume fraction, ϕ_a, are kept constant. Physically, this situation is achieved by adding salt to a charge stabilized system; thus, reducing the Debye length. The theory predicts the same behavior as seen in experimental systems [Mallamace, Micali & Vasi (1990)]. The shear viscosity increases as the hydrodynamic radius, a, decreases for a system in which the Debye length and the hydrodynamic volume fraction, ϕ_a, are held constant; thus, shear viscosity increases as b/a increases when ϕ_a is constant. Experiments [Ogawa *et al.* (1997)] confirm this behavior.

Not only does shear thickening occur at higher Peclet numbers as b/a increases, but the sign change in the first normal stress difference also occurs at higher Peclet numbers as b/a increases. The Brownian and interparticle force contributions have the same sign, different from the sign of the hydrodynamic contribution. As b/a increases, the effects of hydrodynamic interactions are reduced and the hydrodynamic

contribution to the first normal stress difference decreases. At some large value of b/a, there will no longer be a sign change in the first normal stress difference since the hydrodynamic contribution will be nearly zero.

Finally, in section 3.5 it is shown how the method presented here can be extended to other flows, other interparticle forces, and other spherical bodies, such as droplets.

3.2 Nonequilibrium microstructure

The microstructure of a dispersion of equal-sized, spherical particles subjected to Brownian, interparticle and hydrodynamic forces with small particle Reynolds number, $\rho\dot{\gamma}a^2/\eta_s \ll 1$, is governed by the N-particle Smoluchowski equation,

$$\frac{\partial P_N}{\partial t} + \nabla\cdot\boldsymbol{j}_N = 0, \tag{3.1}$$

where P_N is the probability density for the N particles to be in configuration $\boldsymbol{x}$, and ρ is the fluid density.

The probability flux $\boldsymbol{j}_N$ is given by

$$\boldsymbol{j}_N = \mathbf{U}P_N + \mathbf{R}_{FU}^{-1}\cdot(\mathbf{F}^P - kT\nabla\ln P_N)P_N, \tag{3.2}$$

where $\mathbf{U}$ is the velocity of the particles due to the external flow, $\mathbf{F}^P$ is the total nonhydrodynamic interparticle force, and $kT\nabla\ln P_N$ is the Brownian force. In addition, $\mathbf{R}_{FU}$ is the hydrodynamic resistance tensor that relates the hydrodynamic force exerted on the particles to the particle velocities. Its inverse, $\mathbf{R}_{FU}^{-1}$, is the mobility tensor relating the velocities to the forces. By multiplying the mobility by kT, the Stokes-Einstein relation yields the particle diffusivity,

$$\mathbf{D} = kT\mathbf{R}_{FU}^{-1}. \tag{3.3}$$

The particle velocities are non-zero in the presence of an imposed flow, and

$$\mathbf{U} = \boldsymbol{x}\cdot\langle\boldsymbol{\Gamma}\rangle + \mathbf{R}_{FU}^{-1}\cdot\mathbf{R}_{FE}:\langle\mathbf{E}\rangle, \tag{3.4}$$

where $\langle\boldsymbol{\Gamma}\rangle = \langle\mathbf{E}\rangle + \langle\boldsymbol{\Omega}\rangle$, and $\langle\mathbf{E}\rangle$ and $\langle\boldsymbol{\Omega}\rangle$ are the bulk rate of strain and vorticity tensors of the external flow, respectively. The hydrodynamic resistance tensor $\mathbf{R}_{FE}$ gives the hydrodynamic forces on the particles due to the imposed flow. In the absence of hydrodynamic interactions (*i.e.*, $\mathbf{R}_{FE} \equiv 0$), the particles would simply be advected by the imposed linear flow: $\mathbf{U} = \boldsymbol{x}\cdot\langle\boldsymbol{\Gamma}\rangle$.

The N–particle Smoluchowski equation, integrated over $N-2$ particles and neglecting three-body effects, becomes

$$\nabla_r\cdot\mathbf{D}_r\cdot\nabla_r g(\mathbf{r}) = Pe_b\nabla_r\cdot(\mathbf{U}_r g(\mathbf{r})), \tag{3.5}$$

where $g(\mathbf{r})$ is the nonequilibrium pair-distribution function. In equation (3.5) we nondimensionalize all lengths by the effective hard-sphere radius, b, the relative velocity, $\mathbf{U}_r$, by $b\dot{\gamma}$, the relative diffusivity, $\mathbf{D}_r$, by $D_0 = kT/6\pi\eta_s a$, the bare-particle diffusivity. The Peclet number, $Pe_b = (b^2/D_0)/(1/\dot{\gamma}) = 6\pi\eta_s\dot{\gamma}ab^2/kT$, is the ratio of the diffusive and convective time scales. In terms of two-particle hydrodynamic functions, the relative diffusivity and relative velocity are written,

$$\mathbf{D}_r = 2\left(G\left(r\tfrac{b}{a}\right)\hat{\mathbf{r}}\hat{\mathbf{r}} + H\left(r\tfrac{b}{a}\right)(\mathbf{I}-\hat{\mathbf{r}}\hat{\mathbf{r}})\right), \tag{3.6}$$

$$\mathbf{U}_r = \mathbf{r}\cdot\langle\boldsymbol{\Gamma}\rangle - \mathbf{r}\cdot\langle\mathbf{E}\rangle\cdot\left(A\left(r\tfrac{b}{a}\right)\hat{\mathbf{r}}\hat{\mathbf{r}} + B\left(r\tfrac{b}{a}\right)(\mathbf{I}-\hat{\mathbf{r}}\hat{\mathbf{r}})\right), \tag{3.7}$$

where ∇_r is the gradient with respect to the interparticle separation, $\mathbf{r} = \mathbf{r}_2 - \mathbf{r}_1$, $\hat{\mathbf{r}}$ is the unit vector along the line of centers between the two particles, $\mathbf{I}$ is the isotropic tensor, $G\left(r\frac{b}{a}\right)$ and $H\left(r\frac{b}{a}\right)$ are the radial and tangential components of the relative diffusivity, $\mathbf{D}_r = \mathbf{D}_{22} + \mathbf{D}_{11} - \mathbf{D}_{12} - \mathbf{D}_{21}$, and $A\left(r\frac{b}{a}\right)$ and $B\left(r\frac{b}{a}\right)$ are radial and tangential components of the relative velocity, $\mathbf{U}_r = \mathbf{U}_2 - \mathbf{U}_1$, due to the imposed flow [Batchelor & Green (1972a); Batchelor (1976)]. Note that *all* of the two-particle hydrodynamic functions include b/a in the argument because r is nondimensionalized

by the thermodynamic radius, b, but the hydrodynamic functions are evaluated based on the hydrodynamic radius, a.

The no-flux boundary condition for two particles at contact is

$$\hat{\mathbf{r}}\cdot\mathbf{D}_r\cdot\nabla_r g(\mathbf{r}) = Pe_b\,\hat{\mathbf{r}}\cdot\mathbf{U}_r g(\mathbf{r}) \quad @ \quad r=2, \tag{3.8}$$

and there is no deformation of the equilibrium structure at large distances,

$$g(\mathbf{r}) \sim 1 \quad \text{as} \quad r\to\infty. \tag{3.9}$$

Since the nonequilibrium microstructure decays to unity at large separations, this behavior is subtracted so that the deformation function, f, decays to zero for large values of $|\mathbf{r}|$. In addition, the deformation function, f, is a convenient choice for reporting results for the microstructure since the surface value of f scales with Pe_b for both $Pe_b \ll 1$ [Brady & Vicic (1995)] and $Pe_b \gg 1$ [Brady & Morris (1997)]. We introduce the deformation of the equilibrium microstructure,

$$g(\mathbf{r};Pe_b) = 1 + f(\mathbf{r};Pe_b), \tag{3.10}$$

and expand f in terms of surface spherical harmonics,

$$f(\mathbf{r};Pe_b) = \sum_{\substack{\ell \\ |m|\le\ell}} B_{\ell,m}(r;Pe_b)\,Y_{\ell,m}(\theta,\varphi), \tag{3.11}$$

where the surface spherical harmonic, $Y_{\ell,m}(\theta,\varphi)$, is defined [McQuarrie (1983)],

$$Y_{\ell,m}(\theta,\varphi) = \left(\frac{2\ell+1}{4\pi}\frac{(\ell-|m|)!}{(\ell+|m|)!}\right)^{1/2} P_\ell^{|m|}(\cos[\theta])\exp[im\varphi], \tag{3.12}$$

and $P_\ell^m(\cos[\theta])$ is the Associated Legendre Polynomial [McQuarrie (1983)],

$$P_\ell^{|m|}(x) = \left(1-x^2\right)^{m/2}\frac{d^m P_\ell(x)}{dx^m}, \tag{3.13}$$

where $P_\ell(x)$ is the ℓ^{th} Legendre Polynomial. The expansion for f, equation (3.11), is substituted into the Smoluchowski equation, equation (3.5), and boundary conditions, equations (3.8) and (3.9), to obtain a series of coupled, ordinary differential equations by using the orthogonality property of surface spherical harmonics,

$$\int Y_{\ell,m} Y^*_{p,q} d\Omega = \delta_{\ell p}\delta_{mq}, \tag{3.14}$$

where $Y^*_{p,q}$ is the complex conjugate of the surface spherical harmonic $Y_{p,q}$, $d\Omega$ is the differential surface area and δ_{ij} is the Kronecker delta function,

$$\delta_{ij} = \begin{cases} 1, & \text{if } i = j; \\ 0, & \text{otherwise.} \end{cases} \tag{3.15}$$

The resulting ordinary differential equation for $B_{p,q}(r; Pe_b)$ can be written for a general linear flow,

$$\begin{aligned} &G\left(r\tfrac{b}{a}\right)\frac{d^2B_{p,q}}{dr^2} + \left(2\frac{G\left(r\frac{b}{a}\right)}{r} + \frac{dG\left(r\frac{b}{a}\right)}{dr}\right)\frac{dB_{p,q}}{dr} - \frac{p(p+1)}{r^2}H\left(r\tfrac{b}{a}\right)B_{p,q} \\ &\quad = \frac{1}{2}Pe_b W\left(r\tfrac{b}{a}\right)\beta_1 \\ &\quad + \frac{1}{2}Pe_b \sum_{\ell,|m|\le\ell}\left[\left(W\left(r\tfrac{b}{a}\right)B_{\ell,m} + r\left(1 - A\left(r\tfrac{b}{a}\right)\right)\frac{dB_{\ell,m}}{dr}\right)\beta_2\right. \\ &\qquad \left. + \left(1 - B\left(r\tfrac{b}{a}\right)\right)(\beta_3+\beta_4)B_{\ell,m} + (\beta_5+\beta_6)B_{\ell,m}\right], \end{aligned} \tag{3.16}$$

with the no-flux boundary condition at particle contact,

$$G\left(2\tfrac{b}{a}\right)\frac{dB_{p,q}}{dr} = Pe_b\left(1 - A\left(2\tfrac{b}{a}\right)\right)\left[\beta_1 + \sum_{\ell,|m|\le\ell} B_{\ell,m}\beta_2\right] \quad @ \quad r = 2, \tag{3.17}$$

and the boundary condition of no deformation at large distances,

$$B_{p,q} \sim 0 \quad \text{as} \quad r \to \infty. \tag{3.18}$$

The constants, β_i, in these equations are dependent on ℓ, m, p, and q and cause the ordinary differential equations for $B_{p,q}$ to be coupled,

$$\beta_1 = \int (\hat{\mathbf{r}}\cdot\langle\mathbf{E}\rangle\cdot\hat{\mathbf{r}})\, Y^*_{p,q} d\Omega, \tag{3.19}$$

$$\beta_2 = \int (\hat{\mathbf{r}}\cdot\langle\mathbf{E}\rangle\cdot\hat{\mathbf{r}})\, Y_{\ell,m} Y^*_{p,q} d\Omega, \tag{3.20}$$

$$\beta_3 = \int \left(\hat{\mathbf{r}}\cdot\langle\mathbf{E}\rangle\cdot\hat{\theta}\right) \frac{\partial Y_{\ell,m}}{\partial\theta} Y^*_{p,q} d\Omega, \tag{3.21}$$

$$\beta_4 = \int (\hat{\mathbf{r}}\cdot\langle\mathbf{E}\rangle\cdot\hat{\varphi}) \frac{1}{\sin[\theta]} \frac{\partial Y_{\ell,m}}{\partial\varphi} Y^*_{p,q} d\Omega, \tag{3.22}$$

$$\beta_5 = \int \left(\hat{\mathbf{r}}\cdot\langle\mathbf{\Omega}\rangle\cdot\hat{\theta}\right) \frac{\partial Y_{\ell,m}}{\partial\theta} Y^*_{p,q} d\Omega, \tag{3.23}$$

$$\beta_6 = \int (\hat{\mathbf{r}}\cdot\langle\mathbf{\Omega}\rangle\cdot\hat{\varphi}) \frac{1}{\sin[\theta]} \frac{\partial Y_{\ell,m}}{\partial\varphi} Y^*_{p,q} d\Omega. \tag{3.24}$$

In these integrals $\hat{\theta}$ and $\hat{\varphi}$ are the unit vectors in the θ- and φ-directions for spherical coordinates, and the partial derivatives of the surface spherical harmonics are evaluated using

$$\frac{\partial Y_{\ell,m}}{\partial\theta} = imY_{\ell,m}, \tag{3.25}$$

where $i = \sqrt{-1}$ and

$$\begin{aligned}\frac{\partial Y_{\ell,m}}{\partial\varphi} &= |m|\cot[\theta] Y_{\ell,m} \\ &- ([\ell-|m|][\ell+|m|+1])^{1/2} \left(\frac{2\ell+1}{4\pi}\frac{(\ell-|m|-1)!}{(\ell+|m|+1)!}\right)^{1/2} \\ &\times P_\ell^{|m|+1}(\cos[\theta]) \exp[im\varphi].\end{aligned} \tag{3.26}$$

We can immediately reduce the number of equations in (3.16) by using the fact that f is real as well as using symmetry arguments for different linear flows after choosing a coordinate system. For all flows, the deformation function, f, must be real,

$$B_{\ell,m}(r; Pe_b) = B_{\ell,-m}(r; Pe_b), \tag{3.27}$$

reducing the number of equations by approximately half. Furthermore, for simple

shear flow, if $\langle \mathbf{\Gamma} \rangle = \hat{\mathbf{x}}\hat{\mathbf{z}}$, then

$$B_{\ell,m}(r; Pe_b) = 0 \text{ when } \ell \text{ is odd}, \tag{3.28}$$

based on symmetry of the imposed flow. Similar arguments can be made for planar, uniaxial and biaxial extensional flows. For uniaxial and biaxial extensional flows, if the coordinate system is chosen so that f is independent of the φ-coordinate, then

$$B_{\ell,m} = 0 \text{ when } |m| > 0, \tag{3.29}$$

and the number of equations in (3.16) is drastically reduced. In addition for extensional flows, $\beta_4 = \beta_6 = 0$ since $\langle \mathbf{\Omega} \rangle = \mathbf{0}$.

The integrals for β_i, equations (3.19)-(3.24), are numerically evaluated using the rate of strain and vorticity tensors for the given external flow field. The integrals with respect to φ are simple and are completed by hand using orthogonality. The integrals with respect to θ are numerically evaluated using the equation in Appendix A for integrals of the product of two Associated Legendre Polynomials and most powers of $\sin[\theta]$ and $\cos[\theta]$.

To numerically solve the ordinary differential equations, the domain is transformed from $r \in [2, \infty)$ to $t \in [0, 1]$ by using the transformation variable $t = 2/r$. By using this transformation, the outer boundary condition, equation (3.18), is exactly applied since the infinite r-domain is transformed to a finite t-domain. The ordinary differential equations are transformed into finite difference equations using an $O(h^4)$ scheme and equal-spaced intervals in the t-domain. By using equal-spaced intervals in t-space, a greater density of points occurs near $r = 2$ than at $r \to \infty$. Stretched coordinates were used with little success—memory requirements dictated the number of total intervals and placing more intervals near particle contact within the boundary layer didn't allow accurate calculation of $O(1)$ variations of f far from particle contact. The local behavior of the finite difference scheme is used to form a band diagonal matrix for an arbitrary choice of the maximum value of ℓ, ℓ_{max}, in the expansion for

f. The band diagonal matrix is then solved using a direct, LU-decomposition method [Press *et al.* (1992)].

The main disadvantage of this method is the large, internal memory requirement for storage of the band diagonal matrix. The band diagonal matrix, as constructed, includes a large percentage of zeroes, but no direct scheme could be found to further reduce the memory requirement for matrix storage. This disadvantage means that there is a maximum value for ℓ_{max}, which is dependent on the spacing in the finite difference scheme, for which the internal memory is fully utilized. The main advantage of this scheme is that the method is direct. A number of indirect methods were tested with limited success for $Pe_b > 1$ and with no success for $Pe_b > 5$. These indirect methods relied on an iterative scheme, but did not converge for $Pe_b > 5$ even with an excellent initial guess by using the boot-strapping method. Since the current method is direct, a solution can be obtained for the truncated set of equations for any value of the Peclet number. Of course, as $Pe_b \to \infty$, the truncated set of equations no longer provides a meaningful approximation to the real solution of the Smoluchowski equation since $\ell_{max} \to \infty$ as $Pe_b \to \infty$.

Because of the limitation on ℓ_{max}, it is necessary to define a convergence criterion that must be satisfied in order for the solution to be accepted as a good approximation to the real solution. Ideally, one would like to extrapolate to $\ell_{max} \to \infty$ using the results for different levels of truncation, but a meaningful method of extrapolation could not be found. Plots of $B_{2,1}(r = 2; Pe_b)$ versus ℓ_{max} for a given number of intervals did not yield power law nor exponential behavior for $Pe_b \sim O(1)$. Instead, the solution is accepted at ℓ_{max} if the solution at the next highest level of truncation in ℓ provides a solution for which the rheological properties do not vary by more than 0.1%.

The numerical technique of Lionberger (1998) is similar to the method independently developed in this study, but with some major differences which are discussed here. Lionberger (1998) does not transform the unbounded domain to a bounded one and uses the outer boundary condition, equation (3.9), at some value of r rather than at $r \to \infty$. He realizes that an outer solution exists and chooses the value of r based on $r = Pe_b^{-1/2}$, the proper scaling for the outer region where convection and diffusion are both important for $Pe_b \ll 1$. He compares solutions from this method to a second solution method in which the pair-distribution function is matched to the outer solution of Elrick (1962) to first order and finds insignificant differences between the two methods in this limit. But by applying the solution at finite r or matching the solution to the outer solution to first order, an approximation is introduced into the system of equations. No such approximation is made in the current study since the transformed domain is bounded and the outer boundary condition can be exactly applied. Even though the approximation for the outer boundary condition in the work of Lionberger (1998) is valid for $Pe_b \ll 1$, it fails at high Peclet numbers in the extensional zone. For $Pe_b \gg 1$, Brady & Morris (1997) show that the boundary layer length scales as $\sim O(Pe_b^{-1})$. Thus, $r = Pe_b^{-1/2}$ is larger than $\sim O(Pe_b^{-1})$ when $Pe_b \gg 1$, and Lionberger's outer boundary condition is valid in the compressional zone where the boundary layer forms. Outside the compressional zone the boundary layer separates and the probability density is convected downstream forming a wake on the downstream side of the test particle. In the extensional zone the length of the wake region, L_1, is $\sim O(Pe_b)$ since

$$
\begin{aligned}
&L_1/U_1 \sim L_2^2/D_{22}, \\
&\frac{L_1}{b} \sim \left(\frac{L_2}{b}\right)^2 \left(\frac{bU_1}{D_{22}}\right), \\
&\frac{L_1}{b} \sim \left(\frac{L_2}{b}\right)^2 Pe_b \text{ with } \frac{L_2}{b} \sim O(1),
\end{aligned}
$$

where 1 is the velocity direction and 2 is the gradient direction in simple shear flow. Immediately, we see that $r = Pe_b^{-1/2}$ is much smaller than $\sim O(Pe_b)$ when $Pe_b \gg 1$,

and Lionberger's method fails to properly calculate the microstructure in the extensional zone because of the approximate boundary condition. Based on this analysis, Lionberger's results for the microstructure and rheology are valid for $Pe_b \leq 1$ but not for $Pe_b \gg 1$. The approximate boundary condition has a greater effect on the bulk stress at high Peclet numbers for the case of two-particle hydrodynamic interactions than for the case of no hydrodynamic interactions. For the case of two-particle hydrodynamics, $O(1)$ variations in the nonequilibrium microstructure result in an $O(1)$ contribution to the bulk stress; whereas, for the case of no hydrodynamic interactions, only the surface values of the nonequilibrium microstructure are required to calculate the bulk stress. Note that these surface values are still affected by the approximate boundary condition, but the effect is not expected to be as great. Finally, Lionberger (1998) uses s shooting method, an indirect method, and apparently finds that no solution can be found for $Pe_b > 8$ since that is the largest value for which data is reported.

3.3 Bulk stress

The bulk stress of a suspension at low Reynolds numbers can be written as,

$$\langle \boldsymbol{\Sigma} \rangle = -\langle p \rangle_f \mathbf{I} + 2\eta_s \langle \mathbf{E} \rangle + \langle \boldsymbol{\Sigma}_P \rangle, \tag{3.30}$$

where $\langle p \rangle_f$ is the average pressure in the fluid, which is arbitrary if the fluid is incompressible, and $2\eta_s \langle \mathbf{E} \rangle$ is the contribution to the deviatoric stress from the Newtonian suspending fluid. The particle stress, $\langle \boldsymbol{\Sigma}_P \rangle$, is written [Brady (1993a)] as,

$$\langle \boldsymbol{\Sigma}_P \rangle = -nkT\mathbf{I} + n[\langle \mathbf{S}^H \rangle + \langle \mathbf{S}^B \rangle + \langle \mathbf{S}^P \rangle], \tag{3.31}$$

where $nkT\mathbf{I}$ is the isotropic, kinetic contribution to the particle stress and n is the number density of particles. The remaining contributions to the stress are the hydrodynamic, Brownian and interparticle force stresslets, respectively,

$$\langle \mathbf{S}^H \rangle = -\langle \mathbf{R}_{SU} \cdot \mathbf{R}_{FU}^{-1} \cdot \mathbf{R}_{FE} - \mathbf{R}_{SE} \rangle : \langle \mathbf{E} \rangle, \tag{3.32a}$$

$$\langle \mathbf{S}^B \rangle = -kT \langle \nabla \cdot (\mathbf{R}_{SU} \cdot \mathbf{R}_{FU}^{-1}) \rangle, \tag{3.32b}$$

$$\langle \mathbf{S}^P \rangle = -\langle (x\mathbf{I} + \mathbf{R}_{SU} \cdot \mathbf{R}_{FU}^{-1}) \cdot \mathbf{F}^P \rangle, \tag{3.32c}$$

where $\mathbf{R}_{SU}$ and $\mathbf{R}_{SE}$ are hydrodynamic resistance tensors relating the stress to the velocity and rate of strain, respectively. These two hydrodynamic tensors are not traceless, and the contribution to the osmotic pressure due to hydrodynamic interactions are calculated [Jeffrey, Morris & Brady (1993)].

The particle stress contributions can be rewritten in a form that is valid for a system of two particles,

$$\begin{aligned} n\langle \mathbf{S}^H \rangle = {} & 5\phi_a \eta_s \dot{\gamma} \langle \mathbf{E} \rangle + 5\phi_a^2 \eta_s \dot{\gamma} \langle \mathbf{E} \rangle \\ & + \frac{15}{4\pi} \phi_b^2 \left(\frac{a}{b} \right)^3 \eta_s \dot{\gamma} \int \Big(K\left(r\tfrac{b}{a}\right) \langle \mathbf{E} \rangle \\ & \quad + L\left(r\tfrac{b}{a}\right) \left(\hat{\mathbf{r}} \cdot \langle \mathbf{E} \rangle \hat{\mathbf{r}} + \langle \mathbf{E} \rangle \cdot \hat{\mathbf{r}}\hat{\mathbf{r}} - \tfrac{2}{3}\mathbf{I} \left(\hat{\mathbf{r}} \cdot \langle \mathbf{E} \rangle \cdot \hat{\mathbf{r}} \right) \right) \\ & \quad + M\left(r\tfrac{b}{a}\right) \left(\hat{\mathbf{r}} \cdot \langle \mathbf{E} \rangle \cdot \hat{\mathbf{r}} \right) \left(\hat{\mathbf{r}}\hat{\mathbf{r}} - \tfrac{1}{3}\mathbf{I} \right) \\ & \quad - \frac{2}{5} \mathcal{B}\left(r\tfrac{b}{a}\right) \left(\left(\hat{\mathbf{r}}\hat{\mathbf{r}} - \tfrac{1}{3}\mathbf{I} \right) : \langle \mathbf{E} \rangle \right) \mathbf{I} \Big) \, g(\mathbf{r}) \, d\mathbf{r}, \end{aligned} \tag{3.33a}$$

$$\begin{aligned} n\langle \mathbf{S}^B \rangle = {} & -\frac{27}{16\pi} \phi_b^2 \eta_s \dot{\gamma} \frac{a}{b} \frac{1}{Pe_b} \int W\left(r\tfrac{b}{a}\right) \left(\hat{\mathbf{r}}\hat{\mathbf{r}} - \tfrac{1}{3}\mathbf{I} \right) g(\mathbf{r}) \, d\mathbf{r} \\ & - \frac{1}{\pi} \phi_b nkT \frac{2}{3} \frac{a}{b} \mathcal{A}\left(2\tfrac{b}{a}\right) \mathbf{I} \int g(\mathbf{2}) \, d\Omega, \end{aligned} \tag{3.33b}$$

$$\begin{aligned} n\langle \mathbf{S}^P \rangle = {} & -\frac{3}{\pi} \phi_b nkT \left(1 - A\left(2\tfrac{b}{a}\right) \right) \int \hat{\mathbf{r}}\hat{\mathbf{r}} g(\mathbf{2}) \, d\Omega \\ & - \frac{1}{\pi} \phi_b nkT \left(A\left(2\tfrac{b}{a}\right) - \frac{2}{3} \frac{a}{b} \mathcal{A}\left(2\tfrac{b}{a}\right) \right) \mathbf{I} \int g(\mathbf{2}) \, d\Omega. \end{aligned} \tag{3.33c}$$

The interparticle force is taken as the hard-sphere force, $\mathbf{F}^P = \frac{1}{2} kT \delta(r-2)$, where

$\delta(r-2)$ is the delta function and the factor of $1/2$ is required to give the proper value for the equilibrium osmotic pressure. This set of equations for the bulk stress, when nondimensionalized by $\eta_s\dot{\gamma}$, is correct to $O(\phi_b^2)$, where $\phi_b = 4\pi nb^3/3$, and the equations are valid for arbitrary values of b/a. In these equations, $K(r\frac{b}{a})$, $L(r\frac{b}{a})$ and $M(r\frac{b}{a})$ are the two-particle hydrodynamic functions associated with the hydrodynamic stress [Kim & Mifflin (1985); Kim & Karrila (1991)] and $\mathcal{A}(r\frac{b}{a})$ and $\mathcal{B}(r\frac{b}{a})$ are pressure moment functions used to calculate osmotic pressure [Jeffrey, Morris & Brady (1993)].

As a check on the set of equations for the bulk stress, we first calculate the equilibrium osmotic pressure and then briefly analyze the behavior of the different contributions to the bulk stress for varying b/a ratios. The osmotic pressure, Π, is mechanically defined [Brady (1993a)],

$$\Pi \equiv -\frac{1}{3}\mathbf{I}:\langle \boldsymbol{\Sigma}_P \rangle. \tag{3.34}$$

Jeffrey, Morris & Brady (1993) show that there is no contribution to the equilibrium osmotic pressure from the hydrodynamic stress since the material is incompressible. Furthermore, by applying equation (3.34) to equations (3.33)–(3.33),

$$\frac{\Pi^0}{nkT} = 1 + 4\phi_b g_{eq}\left(2;\phi_b\right), \tag{3.35}$$

where $g_{eq}\left(2;\phi_b\right)$ is the contact value of the equilibrium radial-distribution function. The equilibrium osmotic pressure always has this simple form since the contributions from $\mathcal{A}(r\frac{b}{a})$ exactly cancel for all values of b/a.

If the particles have thermodynamic and hydrodynamic radii that are nearly equal, $b/a \to 1$, then the contribution to the bulk stress from interparticle forces vanishes and is transferred to the Brownian stress since $A(2) \to 1$ and $\mathcal{A}(2) \to 3/2$, and the contributions from the interparticle force to the traceless stress and osmotic pressure both tend to zero. Furthermore, if the system has $b/a \gg 1$, the hydrodynamic stress decays quite quickly since the particle acts like a point particle in a hydrodynamic

sense, and we see that the hydrodynamic stress scales as $(a/b)^3$ if the integral remains $O(1)$ with respect to changes in b/a, but the integral is actually $O(a/b)^3$ and the hydrodynamic stress scales as $O(a/b)^6$. Finally, the interparticle force contribution to the bulk stress, nondimensionalized by $\eta_s\dot{\gamma}$, retains a factor of a/b in front of the surface integral when the proper Peclet number, $Pe_b = 6\pi\eta_s\dot{\gamma}ab^2/kT$, is used, in agreement with previous work [Brady (1993b); Brady & Morris (1997)].

3.4 Results

For simple shear flow $\langle\mathbf{\Gamma}\rangle = \hat{\mathbf{x}}\hat{\mathbf{z}}$ is used as the rate of strain tensor. Rheological properties and the osmotic pressure are defined,

$$\Sigma_{21} = \Sigma_{xz} = 2\eta\langle E_{21}\rangle = 2\eta\langle E_{xz}\rangle, \tag{3.36}$$

$$\eta_r = \eta/\eta_s, \tag{3.37}$$

$$N_1 = \Sigma_{11} - \Sigma_{22} = \Sigma_{zz} - \Sigma_{xx}, \tag{3.38}$$

$$N_2 = \Sigma_{22} - \Sigma_{33} = \Sigma_{xx} - \Sigma_{yy}, \tag{3.39}$$

$$\Pi \equiv -\frac{1}{3}\mathbf{I}:\langle\mathbf{\Sigma}_P\rangle, \tag{3.40}$$

where Σ_{ij} is the ij^{th}-component of the bulk stress, E_{ij} is the ij^{th}-component of the rate of strain tensor, and the subscripts used for $\mathbf{\Sigma}$ and $\langle\mathbf{E}\rangle$ denote the flow direction (1), the gradient direction (2) and the vorticity direction (3). In addition, η is the shear viscosity, η_r is the relative shear viscosity, N_1 is the first normal stress difference, and N_2 is the second normal stress difference.

This section is broken into three parts with each part addressing the following cases: (i) the thermodynamic and hydrodynamic radii are the same, $b/a = 1$, and hydrodynamic interactions are neglected or, alternatively, $b/a \to \infty$ with two-particle hydrodynamic interactions, (ii) the thermodynamic and hydrodynamic radii are nearly equal, $b/a \to 1$, and two-particle hydrodynamic interactions are included, (iii) the ratio of the thermodynamic and hydrodynamic radii is varied, $1.01 < b/a < 5.00$, and two-particle hydrodynamic interactions are included. For each case, previous in-

vestigations in theory, simulations and experiments are first discussed, then a few general notes about the solution procedure are made. Finally, the results of this study are presented for the microstructure, relative shear viscosity, normal stress differences and osmotic pressure. During the discussion of the individual rheological properties, a scaling argument for the volume-fraction dependence of the bulk stress is used to extend the results for the rheology of dilute dispersions to concentrated dispersions and comparisons are made to existing data, if available.

3.4.1 No hydrodynamic interactions, $b/a = 1$

In this section the Smoluchowski equation, equation (3.16), and its boundary conditions, equations (3.17) and (3.18), are solved with $b/a = 1$ while neglecting hydrodynamic interactions, $G(r)=H(r)=1$ and $A(r)=B(r)=0$. Since $b/a = 1$, then $\phi_b=\phi_a=\phi$ and $Pe_b = Pe$. When calculating the particle stress to $O(\phi^2)$ using equations (3.33)–(3.33), $K(r)=L(r)=M(r)=\mathcal{A}(r)=\mathcal{B}(r)=0$ since hydrodynamic interactions are neglected.

There are a number of theoretical works in which the microstructure and/or rheology are predicted for colloidal dispersions when hydrodynamic interactions are neglected. Most of these analyses focus on solving the Smoluchowski equation in the low Peclet limit [Dhont (1989); Brady & Vicic (1995)], the high Peclet limit [Brady & Morris (1997)], or for arbitrary Peclet numbers [Blawzdziewicz & Szamel (1993); Lionberger (1998)], while other works solve a fluctuating convective-diffusion equation instead of the Smoluchowski equation [Ronis (1984, 1986)]. Ronis (1984, 1986) and Dhont (1989), solving different equations, both argue that the structure factor, and hence the viscosity, is nonanalytic in shear rate in the limit of vanishing shear rate. They predict a first correction to the low shear Newtonian viscosity scales as $\sim O(\dot{\gamma}^{-1/2})$. The nonanalytic character of the perturbation expansion for low shear rates is correct [Brady & Vicic (1995)], but the first nonanalytic term in the inner expansion is shown to occur at $O(Pe^{5/2})$. The expansion is regular to $O(Pe^2)$ and Brady & Vicic (1995) show that the $O(Pe)$ deformation yields the low shear Newtonian vis-

cosity while the $O(Pe^2)$ deformation yields normal stress differences and the first correction to the equilibrium osmotic pressure. At high Peclet numbers, where Brownian motion is weak, Brady & Morris (1997) show that the surface value of the nonequilibrium radial-distribution function scales with the Peclet number, $g(\mathbf{2}) \sim O(Pe)$. Since only the surface value is required to calculate the bulk stress for a system in which hydrodynamic interactions are neglected, it is shown that the particle stress has a viscous scaling, $|\boldsymbol{\Sigma}_P| \sim O(\eta_s \dot{\gamma})$. Furthermore, Brady & Morris (1997) show that the perturbation expansion for the nonequilibrium radial-distribution functions proceeds in powers of Pe^{-1} and they solve the Smoluchowski equation in the limit $Pe \to \infty$ by neglecting the angular velocity terms within the boundary layer. At arbitrary Peclet number Blawzdziewicz & Szamel (1993) and Lionberger (1998) both solve the Smoluchowski equation and find the resulting rheological properties for $Pe \leq 12.5$ and $Pe \leq 5$, respectively. The rheological results of Blawzdziewicz & Szamel (1993) and Lionberger (1998) are used to as a check on some of the results of this work.

All of the theoretical results discussed thus far focus on dilute dispersions. Brady (1993b) and Brady & Morris (1997) show how the results of the two-particle problem can be used to predict the rheology of concentrated dispersions for all values of Peclet number. The scaling argument is simplified when hydrodynamic interactions are neglected since the particle stress scales simply with the contact value of the equilibrium radial-distribution function, $g_{eq}(2;\phi)$,

$$\frac{\langle \boldsymbol{\Sigma}_P \rangle}{\eta_s \dot{\gamma}} \sim \phi^2 g_{eq}\left(2;\phi\right), \tag{3.41}$$

and the Peclet number remains the proper parameter for the scaling since the nondimensional short-time self-diffusivity, $D_0^s\left(\phi\right)$, is unity when hydrodynamic interactions are neglected. Brady (1993b) further shows that the particle stress diverges near close packing since the equilibrium radial-distribution function diverges near close packing [Woodcock (1981)],

$$g\left(2;\phi\right) \sim \left(1 - \phi/\phi_m\right)^{-1}, \tag{3.42}$$

where ϕ_m is the maximum packing fraction and $\phi_m \approx 0.64$ for hard spheres [Nolan &

Kavanagh (1992)].

There are no experimental conditions which can be directly related to complete neglect of hydrodynamic interactions. For charged colloidal dispersions, the ratio of the thermodynamic radius to the hydrodynamic radius can be greater than one (i.e., $b/a > 1$), but analysis of these experiments is delayed to the subsection in which b/a is varied.

Even though no experiments exist, Brownian Dynamics simulations are plentiful. In Brownian Dynamics simulations, hydrodynamic interactions are neglected but the hydrodynamic drag on a single particle is included in the simulations through the bare-particle diffusivity, D_0. This assumption is the same as the assumption used in this section when solving the Smoluchowski equation. The majority of these simulations were performed by Heyes' group [Heyes & Melrose (1993); Heyes *et al.* (1994); Mitchell, Heyes & Melrose (1995)] and more recently by Rastogi, Wagner & Lustig (1996) and Foss & Brady (1999). There are two problems with Brownian Dynamics simulations. First, the signal-to-noise ratio at low Peclet number is small and rheological properties are difficult to measure for $Pe \ll 1$. Secondly, at high Peclet numbers, the dispersion undergoes a shear-induced phase transition into a hexagonal shear-string phase. The predictions made in this section are only valid for a well-dispersed Brownian suspension and, thus, disagreement between theoretical predictions and Brownian Dynamics simulations are expected for $Pe > 30$.

Results for the nonequilibrium microstructure are numerically calculated by solving the Smoluchowski equation for a range of Peclet numbers to $Pe = 20$. The macroscopic properties at higher Peclet numbers do not meet the convergence criterion, but all macroscopic properties converge at lower Peclet numbers by using 60 intervals with $\ell_{max} = 10$ for $Pe \leq 1$ and $\ell_{max} = 18$ for $1 < Pe \leq 20$.

Microstructure

In Figure 3.1 the deformation parameter is scaled by the Peclet number, f/Pe, and plotted in the velocity-gradient plane for different Peclet numbers. Since there is no change in the equilibrium microstructure for $r < 2$ (i.e., $g(r < 2) = g_{eq}(r < 2) = 0$),

the excluded volume region sets the color for regions where there is no deformation of the equilibrium microstructure, $f=0$. As the color tends from cyan to red to yellow, the value of f/Pe increases. The spectrum of green denotes $f/Pe < 0$. At small Peclet numbers, the quadrupole structure of the $O(Pe)$ perturbation to the microstructure is distorted by the $O(Pe^2)$ deformation, as shown by Brady & Vicic (1995). As the Peclet number increases, the region with $f > 0$ is compressed toward particle contact and a boundary layer forms in the compressional zone at high Peclet numbers. Also at high Peclet numbers, a wake region downstream of the test particle is formed, similar to that seen in uniform flow past a sphere at high Reynolds number. In this wake region, $f \to -1$ since the probability of finding the second particle in the wake region tends toward zero, $g \to 0$. In the density plots the size of the wake is deceivingly small at high Peclet numbers since $f/Pe \sim O(Pe^{-1})$ in this region. The scaling f/Pe is maintained though because the main feature of these density plots is the formation of a boundary layer with increasing Peclet number. For the largest Peclet number, $Pe = 20$, there are two important features near the surface of the particle — the value of f inside the boundary layer is not symmetric with respect to the compressional axis and the point of separation occurs within the extensional zone.

The asymmetry and point of separation can better be seen in Figure 3.2, in which the contact value of f/Pe is plotted in the velocity-gradient plane. The numerical data in Figure 3.2 is the same as the upper part of the plots in Figure 3.1 with the angle θ measured from the velocity direction, $\hat{\mathbf{z}}$, and $\varphi = 0$. The compressional axis is at $\theta = 3\pi/4$, but the maximum value of f/Pe is at $\theta_{max} \approx 2.26$-radians for $Pe \gg 1$, slightly lower than $\theta = 3\pi/4$; thus, the structure at the particle surface is slightly asymmetric. This asymmetry leads to a non-zero first normal stress difference, as seen later. In addition, the point of separation occurs approximately at $\theta \approx 1.26$-radians instead of $\theta = \pi/2$, where $\hat{\mathbf{r}}\cdot\langle\mathbf{E}\rangle\cdot\hat{\mathbf{r}} = 0$ [Brady & Morris (1997)]. The point of separation occurs at a point further downstream than $\pi/2$ because of the angular velocity within the boundary layer caused by the rotational component of simple shear flow. Since the point of separation is in the extensional zone, a non-zero, first

normal stress difference develops. Finally, the prediction of Brady & Morris (1997) is included in Figure 3.2 in the compressional zone to emphasize the difference in symmetry and the point of separation between the numerical results of this work and the high Peclet, approximate asymptotic analysis when the angular velocity within the boundary layer is neglected [Brady & Morris (1997)].

Even though the results of Brady & Morris (1997) are only approximate, the results are in excellent agreement with the numerical results along the compressional axis, as shown in Figure 3.3b, where f/Pe is plotted as a function of the boundary layer coordinate,

$$2 + (r - 2)Pe. \tag{3.43}$$

Based on the collapse of the numerical data, it appears that the high Peclet asymptote has been nearly reached and the extrapolation of rheological properties to $Pe \to \infty$ might be warranted. But recent results of Bergenholtz (1999) show that extrapolation of these results to high Peclet numbers, especially the first normal stress difference, yield incorrect asymptotes. The formation of the boundary layer is better seen in Figure 3.3a, where the numerical results for f/Pe are plotted as a function of particle separation, r, along the compressional axis. It is seen that the surface value of f/Pe is fairly insensitive to Peclet number, but the formation of the boundary layer is evident as the Peclet number increases.

Finally, Figure 3.4a shows that the wake region includes points for which $f \to -1$ as $Pe \to \infty$ and that a large region in the extensional zone exists for which $f > 0$. At small Peclet numbers the value of f along the extensional axis is always negative, and there is always a smaller probability of finding a second particle along this axis than at equilibrium. At high Peclet numbers the surface value of f along the extensional axis tends toward -1, and there is nearly zero probability of finding a second particle at this point. But at larger particle separations, $r > 2.8$, for $Pe = 20$, the value of f is always positive along the extensional axis. The fact that $f > 0$ for $r > 2.8$ can be understood by analyzing the two-body problem in the limit of weak Brownian motion, as shown in Figure 3.4b. A test particle with unit radius is placed at the origin and a

second particle of unit radius is placed upstream in the velocity-gradient (z-x) plane at $(x, 0, -\infty)$ with $0 < x < 2$ in simple shear flow. The upstream particle is advected toward the test particle, makes contact with and is swept over the test particle, and is advected downstream where it passes the extensional axis at $r = 2\sqrt{2} \approx 2.83$, which is approximately the value of r at which $f > 0$ for $Pe = 20$ in the numerical results of this work.

Shear viscosity

In Figure 3.5 the $O(\phi^2)$ contribution to the relative shear viscosity is plotted as a function of Peclet number. The numerical results are in excellent agreement with the low Peclet asymptotic result, $\eta_r - 1 - 2.5\phi = (12/5)\phi^2$, of Brady & Vicic (1995). The high Peclet asymptotic result of Brady & Morris (1997) provides a good approximation to the numerical results despite the fact that Brady & Morris (1997) neglect the angular velocity within the boundary layer in their analysis. But the most striking feature of Figure 3.5 is the fact that there is a residual contribution to the shear viscosity at infinite Peclet number. As Brady & Morris (1997) discuss, there is an $O(1)$ contribution to the shear viscosity because the surface value of the nonequilibrium microstructure grows as $O(Pe)$ and the integral for the particle stress, equation (3.33), is preceded by a factor of Pe^{-1}. The numerical results are compared with the results of Blawzdziewicz & Szamel (1993) and found to be in excellent agreement over the whole range for which they obtain results, $Pe \leq 12.5$. The numerical results are also compared to the results of Lionberger (1998) and are in excellent agreement at low Peclet numbers, but the results of Lionberger are uniformly smaller than the results of this study at intermediate Peclet numbers. This difference in results is most likely caused by the approximation Lionberger (1998) used for the outer boundary condition.

There is some debate about the first correction to the zero-shear, Newtonian viscosity. Ronis (1984, 1986) and Dhont (1989) both predict an $O(Pe^{1/2})$ correction while Brady & Vicic (1995) show that the $O(Pe^3)$ deformation of the equilibrium microstructure yields an $O(\phi^2 Pe^2)$ contribution to the relative shear viscosity. In Figure

3.6, the value of the relative viscosity is subtracted from the zero-shear, Newtonian value to find that $\eta_r = 1 + 2.5\phi + (12/5)\phi^2 - 0.62\phi^2 Pe^2$ for $Pe \ll 1$. The $O(\phi^2 Pe^2)$ contribution is in agreement with the prediction of Brady & Vicic (1995). In the Brownian Dynamics simulations of Rastogi, Wagner & Lustig (1996), a Yukawa potential is used with $\phi_b/\phi_a \approx 0.50/0.267$ or $b/a \approx 1.23$. Even though $b/a \neq 1$, the results are qualitatively analyzed since hydrodynamic interactions are neglected and there is only an interparticle force contribution to the stress. Rastogi, Wagner & Lustig (1996) claim that the first correction to the low shear viscosity is not $O(\phi^2 Pe^2)$ based on their results, but instead they fit a Ree-Eyring model,

$$\eta_r - 1 - 2.5\phi = 12.84 \frac{\sinh^{-1}[12.86 Pe]}{12.86 Pe}, \tag{3.44}$$

to the data for the interparticle force contribution to the viscosity. There are two problems with their conclusion that the next correction is *not* $O(\phi^2 Pe^2)$: (i) the Peclet numbers are not small enough to accurately determine the correction and the error for data at small Peclet numbers is quite large and (ii) the Ree-Eyring model asymptotes to,

$$\eta_r - 1 - 2.5\phi_a = 12.84 - \frac{1}{6} 12.84 (12.86 Pe)^2, \tag{3.45}$$

and the model used to fit their data does, in fact, have an $O(\phi^2 Pe^2)$ term as the first correction to the Newtonian, low-shear viscosity.

The scaling argument of Brady (1993b) predicts that

$$\eta_r - 1 - \frac{5}{2}\phi \sim \phi^2 g_{eq}(2;\phi). \tag{3.46}$$

This scaling argument is applied to the results of the Brownian Dynamics simulations of Foss & Brady (1999) and compared to the numerical results of this study in Figure 3.7. The Carnahan-Starling equation [Carnahan & Starling (1969)],

$$g_{eq}(2;\phi) = \frac{1 - \frac{1}{2}\phi}{(1-\phi)^3}, \tag{3.47}$$

is used to approximate the value of $g_{eq}(2;\phi)$. There is reasonable agreement between the simulations and the numerical results at intermediate Peclet numbers. At low Peclet numbers, there is reasonable agreement for smaller volume fractions, but the low-shear viscosity appears to increase faster than predicted by the scaling argument of Brady (1993b). At high Peclet numbers, the system undergoes a shear-induced phase transition for $Pe > 30$ and the lack of agreement is not surprising since the theory is only valid for well-dispersed systems. In a recent analysis by Foss & Brady (1999) of startup flow using Brownian Dynamics, it appears that a metastable state appears at approximately one strain unit where the system is still well-dispersed and reaches a constant value for the stress before the dispersion undergoes a shear-induced phase transition. Results of this analysis of Foss & Brady (1999) show that there is a residual viscosity at high Peclet numbers, as predicted by the numerical results of this work. Foss & Brady (1999) have not yet completed the full analysis, but a sample of these results is included in Figure 3.7.

One reason for the failure of the scaling theory of Brady (1993b) at large volume fractions is that the characteristic relaxation time is no longer independent of volume fraction as it is at smaller volume fractions. Brady (1993b) predicts that the relaxation time is $b^2/\hat{D}_0^s(\phi)$, but for Brownian Dynamics simulations the short-time self-diffusivity is simply equal to the bare-particle diffusivity, $\hat{D}_0^s(\phi) = D_0$, since hydrodynamic interactions are neglected. Thus, Brady (1993b) predicts a relaxation time that is independent of volume fraction. If the relaxation time is independent of volume fraction, then a plot of the reduced dynamic viscosity versus nondimensional frequency should have the same behavior for all volume fractions. In Figure 3.8, the results of Bergenholtz (1999) for the frequency response of a Brownian dispersion is plotted. Bergenholtz (1999) calculated the frequency response by using the Green-Kubo method and the Brownian Dynamics algorithm of Foss (1999). The most striking feature about Figure 3.8 is that there is a single relaxation time for volume fractions less than $\phi = 0.40$, but the relaxation time increases for larger volume fractions. These results show that the scaling theory of Brady (1993b) fails at large volume fractions.

Next, the existence of a Cox-Merz rule is investigated. It has been proposed for other systems, such as polymer melts, that the shear viscosity in steady flow is equal to the dynamic shear viscosity in oscillatory flow when $\dot{\gamma}=\omega$. One would not expect such a relationship to be valid since the microstructure changes with shear rate for steady flow, but only the equilibrium microstructure is probed in dynamic measurements. But there is one common thread for steady and oscillatory data — as $\dot{\gamma}$ and ω increase, the relative importance of Brownian motion decreases. A Cox-Merz rule for colloidal dispersions has been verified using Brownian Dynamics simulations [Heyes *et al.* (1994), Heyes & Mitchell (1995)] in steady and oscillatory shear flows as well as using the Green-Kubo method for $\phi = 0.300$, 0.400, and 0.472. Theoretically, a Cox-Merz rule is also verified, as shown in Figure 3.9, by plotting reduced viscosity versus Peclet number. The reduced viscosity is defined,

$$\eta^* = \frac{\eta(Pe) - \eta(Pe \to \infty)}{\eta(Pe = 0) - \eta(Pe \to \infty)}. \tag{3.48}$$

The results of this study are compared to the theoretical prediction of Brady (1993b) for the dynamic shear viscosity and found to be in excellent agreement despite the fact that the reduced steady viscosity is $\sim O(Pe^{-1})$ but the reduced dynamic viscosity is $\sim O(Pe^{-1/2})$ for $Pe \gg 1$. As an aid for future use, the results for the reduced steady viscosity are fit to a Padé approximate to capture the first correction to the zero-shear Newtonian viscosity which is $O(Pe^2)$ and the $O(Pe^{-1})$ behavior for large Peclet numbers,

$$\eta^* = \frac{1 + 2.22Pe}{1 + 2.22Pe + 0.62Pe^2}. \tag{3.49}$$

This Padé approximate is included in Figure 3.9 and is an excellent approximation to the shear thinning curve for the reduced steady shear viscosity.

Normal stress differences

In Figures 3.10 and 3.11, the $O(\phi^2)$ contribution to the nondimensional first and second normal stress differences are plotted as a function of Peclet number. The numerical results are in excellent agreement with the low Peclet asymptotic results,

$N_1/\eta_s\dot{\gamma} = (16/15)\phi^2 Pe$ and $N_2/\eta_s\dot{\gamma} = -(16/21)\phi^2 Pe$, of Brady & Vicic (1995). For the second normal stress difference, the high Peclet asymptotic result of Brady & Morris (1997) provides a good approximation to the numerical value. But Brady & Morris (1997) predict that $N_1 = 0$ as $Pe \to \infty$ since the angular velocity terms in the boundary layer are neglected and the resulting microstructure is symmetric with respect to the compressional axis. The importance of the rotational component of the external flow is even seen at low Peclet numbers where Brady & Vicic (1995) show that only the $\langle \mathbf{E} \rangle : \langle \mathbf{\Omega} \rangle$ term is responsible for a non-zero, first normal stress difference. But even when the angular velocity terms are kept in the analysis at high Peclet number, the first normal stress difference is nearly zero as $Pe \to \infty$ [Bergenholtz (1999)]. The numerical results of Blawzdziewicz & Szamel (1993) and Lionberger (1998) are found to be in excellent agreement with the results here. The maximum in the nondimensional first normal stress difference is not seen in the results of Lionberger (1998) since the calculations were terminated at a Peclet number lower than the Peclet number at which the maximum in N_1 occurs; thus, Lionberger's extrapolation to $Pe \to \infty$ is incorrect and his use of the Ree-Eyring model is invalid.

In the work of Brady & Vicic (1995), it is predicted that the next correction to $N_i/\eta_s\dot{\gamma}$ is $O(\phi^2 Pe^2)$, arising from the $O(Pe^3)$ deformation of the microstructure. In Figures 3.12 and 3.13, the next corrections are numerically calculated and found to be $O(\phi^2 Pe^{5/2})$ instead of $O(\phi^2 Pe^2)$. The fact that the $O(Pe^3)$ deformation contributes to the shear viscosity but not the normal stress differences can be explained by analyzing the vector invariant form for the $O(Pe^3)$ perturbation for the inner solution.

The inner expansion for the deformation to the equilibrium microstructure can be written,

$$f = f_1 Pe + f_2 Pe^2 + f_3 Pe^{5/2} + f_4 Pe^3 \ln[Pe] + f_5 Pe^3 + f_6 Pe^{7/2} + O(Pe^4 \ln[Pe]), \quad (3.50)$$

where f_1 and f_2 can be written in a vector invariant form and f_3 is simply a constant for a general linear flow [Brady & Vicic (1995)]. If we assume that the next term in the inner expansion is $O(Pe^3)$, we find that f_5 has a particular solution that includes a term proportional to $\ln[r]$. If f_5 is expressed in terms of the outer variable, $\rho = rPe^{1/2}$, then $f_5 Pe^3$ includes a term that is $O(Pe^3 \ln[Pe])$. Since no part of the outer solution matches such a term, an $O(Pe^3 \ln[Pe])$ term is required in the inner expansion and $f_4 \neq 0$. The $O(Pe^3 \ln[Pe])$ term of the inner expansion yields only a contribution to the osmotic pressure since f_4 satisfies a homogeneous differential equation with a homogeneous boundary condition at particle contact. To completely specify the general solution, the result for f_4 is matched with the portion of f_5 that contains $\ln[r]$, just as for the case of mass transfer from a single sphere [Acrivos & Taylor (1962)]. The $O(Pe^3)$ perturbation, f_5, must be a scalar quantity that is cubic in the imposed flow and must vanish for pure rotation, and the quantity may only include combinations of $\hat{\mathbf{r}}$, $\langle \mathbf{E} \rangle$ and $\langle \mathbf{\Omega} \rangle$. There are only 14 linearly independent, non-zero terms for an incompressible system,

$$
\begin{gathered}
\left(E_{ij}E_{jk}E_{ki}\right), \left(E_{ij}E_{jk}\Omega_{ki}\right), \left(E_{ij}\Omega_{jk}\Omega_{ki}\right), \left(\Omega_{ij}E_{jk}\Omega_{ki}\right), \\
\left(\hat{r}_i E_{ij}\hat{r}_j\right)^3, \left(\hat{r}_i E_{ij}E_{jk}\hat{r}_k\right)\left(\hat{r}_i E_{ij}\hat{r}_j\right), \left(\hat{r}_i E_{ij}\Omega_{jk}\hat{r}_k\right)\left(\hat{r}_i E_{ij}\hat{r}_j\right), \\
\left(\hat{r}_i \Omega_{ij}\Omega_{jk}\hat{r}_k\right)\left(\hat{r}_i E_{ij}\hat{r}_j\right), \left(E_{ij}E_{ji}\right)\left(\hat{r}_i E_{ij}\hat{r}_j\right), \left(\Omega_{ij}\Omega_{ji}\right)\left(\hat{r}_i E_{ij}\hat{r}_j\right), \\
\left(\hat{r}_i E_{ij}E_{jk}E_{kl}\hat{r}_l\right), \left(\hat{r}_i \Omega_{ij}E_{jk}E_{kl}\hat{r}_l\right), \left(\hat{r}_i \Omega_{ij}\Omega_{jk}E_{kl}\hat{r}_l\right), \left(\hat{r}_i \Omega_{ij}E_{jk}\Omega_{kl}\hat{r}_l\right).
\end{gathered}
$$

The first four of these terms contribute only to the isotropic pressure and are of no consequence for normal stress differences. It can be shown that the remaining 10 terms, when substituted into equation (3.33), yield contributions only to the isotropic stress or to the shear viscosity; thus, the $O(Pe^3)$ deformation of the equilibrium microstructure does not contribute to the normal stress differences. The $O(Pe^{7/2})$ deformation does contribute to normal stress differences and yields an $O(Pe^{5/2})$ contribution.

Once again, the scaling argument of Brady (1993b),

$$\frac{N_i}{\eta_s \dot{\gamma}} \sim \phi^2 g_{eq}(2;\phi), \tag{3.51}$$

is used with the Carnahan-Starling equation, equation (3.47), and the Brownian Dynamics simulations of Foss & Brady (1999). The scaling argument collapses the data of Foss & Brady (1999) quite nicely, as shown in Figures 3.14 and 3.15, but there is only qualitative agreement between the theoretical prediction of this work and the data of Foss & Brady (1999) for the scaled first normal stress difference. The theory overpredicts the maximum value of the nondimensional first normal stress difference by a factor of two and the theoretical curve is shifted toward slightly higher values of Peclet number. Note that the Brownian Dynamics simulations do show a maximum value for the nondimensional first normal stress difference at a Peclet number smaller than Peclet numbers for which the dispersion exhibits a shear-induced phase transition. The agreement between the simulations and the theoretical prediction is more quantitative for the nondimensional second normal stress difference. It is difficult to ascertain whether the simulation data exhibit a maximum value or not because the maximum occurs at a Peclet number at which shear-induced phase transitions occur.

One of the more traditional measures of the effect of normal stress differences is the Weissenberg effect, or rod climbing. In this experiment a cylindrical rod, with its axis parallel to the direction of gravity, is submerged in a fluid contained in a coaxial cylinder. The radius of the rod is much smaller than the radius of the container so that wall effects are eliminated. Lodge, Schieber & Bird (1988) present a heuristic argument for such a system when the effects of surface tension and centrifugal force are negligible in the absence of secondary flows,

$$r\frac{\partial p_{zz}}{\partial r} = N_1 + 2\Sigma_{12}\frac{dN_2}{d\Sigma_{12}}. \tag{3.52}$$

In their analysis there is a frictionless horizontal plate above the fluid. If this plate is removed and $r\frac{\partial p_{zz}}{\partial r} > 0$, then the fluid will climb the rod since $r > 0$ and the pressure

on the plate, $-p_{zz}$, increases as the radius decreases. Equation (3.52) tends to agree with the results of most, but not all, experiments and is rewritten for this work,

$$r\frac{\partial p_{zz}/\partial r}{\eta_s\dot{\gamma}\phi_b^2} = \frac{N_1}{\eta_s\dot{\gamma}\phi_b^2} - 2\frac{N_2}{\eta_s\dot{\gamma}\phi_b^2} - 2Pe_b\frac{d\left(N_2/\left(\eta_s\dot{\gamma}\phi_b^2\right)\right)}{dPe_b}. \tag{3.53}$$

If the left-hand side of equation (3.53) is positive, then rod climbing should occur. If the left-hand side is negative, then negative rod climbing—depression of the surface of the fluid that is not caused by centrifugal forces—occurs. The left-hand side of equation (3.53) is plotted as a function of Peclet number in Figure 3.16 and only negative rod climbing is found for all values of Peclet number for a dispersion in which hydrodynamic interactions are neglected and $b/a = 1$. Negative rod climbing occurs because the value of the first normal stress difference is the same magnitude as the second normal stress difference for dispersions, which is different from many other systems, such as polymer solutions, for which $-N_2/N_1 < 0.25$ at small shear rates and rod climbing occurs [Lodge, Schieber & Bird (1988)].

Osmotic pressure

The $O(\phi Pe)$ contribution to the osmotic pressure is shown in Figure 3.17. There is excellent agreement between the theoretical results and the low Peclet asymptotic result, $\Pi/nkT - 1 - 4\phi = (16/45)\phi Pe^2$, of Brady & Vicic (1995). Even though the angular velocity terms in the boundary layer are neglected by Brady & Morris (1997) in the high Peclet limit, the asymptotics provide an excellent approximation to the numerical results as $Pe \to \infty$. Neither of the other two numerical investigations [Blawzdziewicz & Szamel (1993); Lionberger (1998)] predict the shear-rate dependence of the osmotic pressure.

The next correction to the nondimensional osmotic pressure is predicted to be $O(\phi Pe^{5/2})$, arising from the first mismatched term of the outer solution [Brady & Vicic (1995)]. When the $O(Pe^{5/2})$ term of the expansion in the inner region is matched with the Elrick (1962) solution for the outer region [Leal (1992)], the next correction to the nondimensional osmotic pressure is found to be $0.286\phi Pe^{5/2}$. This prediction

is numerically confirmed in Figure 3.18 where the correction to the osmotic pressure exhibits oscillatory behavior with respect to Peclet number at small Peclet numbers due to numerical error.

Brownian Dynamics simulation data [Foss & Brady (1999)] are compared with the results of this work in Figure 3.19 by using the scaling theory of Brady (1993b),

$$\Pi/nkT - (\Pi/nkT)_0 \sim \phi Pe g_{eq}(2;\phi), \tag{3.54}$$

where $(\Pi/nkT)_0$ is the equilibrium value of the nondimensional osmotic pressure. For simulations, data is only included for volume fractions for which the osmotic pressure is measured at equilibrium. The scaling argument collapses the simulation data quite nicely and the numerical results are in reasonable agreement.

3.4.2 Two particle hydrodynamic interactions, $b/a \to 1$

In this section the Smoluchowski equation, equation (3.16), and its boundary conditions, equations (3.17) and (3.18), are solved with the thermodynamic and hydrodynamic radii nearly equal. Since $b/a \to 1$, then $Pe_b = Pe$ and $\phi_a = \phi_b = \phi$. Even though the Peclet number and volume fraction take their limiting form, the two-particle hydrodynamic functions are evaluated at $r\frac{b}{a}$.

There are four reasons why the limit $b/a \to 1$ is taken rather than simply letting $b \equiv a$. Physically, closed streamlines form at large Peclet numbers if $b = a$ [Batchelor & Green (1972b), but if $b/a > 1.0001$, then closed streamlines are destroyed [Brady & Morris (1997)]. From a practical point of view, Smart & Leighton (1989) show that for noncolloidal particles, $b/a > 1.001$ in most cases because of surface roughness. For colloidal particles, a similar phenomenon occurs when the particles are sterically-stabilized, where the stabilizer acts like a porous medium and only a finite force is required for the particles to thermodynamically contact. We take the minimum value for b/a as 1.001 for colloidal particles as well. From a numerical point of view, the tangential components of the radial velocity and the radial mobility, $B(r\frac{b}{a})$ and $H(r\frac{b}{a})$, have slow decaying $1/\ln[r\frac{b}{a}-2]$ behavior as $r\frac{b}{a} \to 2$. For example,

$B(2)=0.4056$ but $B(2.002)=0.2792$ and $B(2.004)=0.2662$; thus, the surface value of the tangential component of the relative velocity changes very little as $r \to 2$ when $\frac{b}{a} \approx 1.001$ compared to its variation when $b \equiv a$. Note that two of the hydrodynamic functions, $L(r\frac{b}{a})$ and $M(r\frac{b}{a})$, in the hydrodynamic contribution to the stress also have $1/\ln[r\frac{b}{a}-2]$ behavior. Finally, if $b \equiv a$, then a singularity is introduced into the Smoluchowski equation, equation (3.16), through the relative radial mobility of the two particles since

$$G(r\frac{b}{a}) \sim 2\left(r\frac{b}{a}-2\right) \text{ as } r \to 2, \tag{3.55}$$

the coefficient in front of the second derivative is exactly zero and LU-decomposition fails. There are methods to eliminate the singularity, but in view of the above evidence regarding b/a ratios, these are not pursued. All of the results in this section are obtained by using $b/a = 1.001$.

Most of the theoretical descriptions are concerned with the case of $b/a = 1$, and these theories are described here. At zero Peclet number, Batchelor & Green (1972b) show that the equilibrium microstructure yields an $O(1)$ contribution to the hydrodynamic stress, resulting a nonzero viscosity but no normal stress differences. At low Peclet number, Batchelor (1977) extends these calculations to include the first order perturbation to the equilibrium microstructure and calculates the $O(1)$ contribution to the Brownian stress, yielding the total low-shear, Newtonian viscosity for colloidal dispersions. Continuing the work at low Peclet number, Brady & Vicic (1995) calculate the hydrodynamic normal stresses from the $O(Pe)$ deformation of the microstructure, determine the $O(Pe^2)$ deformation of the microstructure, and calculate the Brownian normal stresses from the $O(Pe^2)$ deformation, yielding the low-shear normal stress difference coefficients and osmotic pressure at small Peclet numbers. Additionally, it can be shown that the $O(Pe^2)$ deformation yields an $O(Pe^2)$ contribution to the hydrodynamic stress, resulting in an $O(Pe^2)$ contribution to the hydrodynamic viscosity. For $Pe \sim O(1)$ Lionberger (1998) solves the Smoluchowski Equation in the singular limit, $b/a = 1$, for $Pe \leq 8$ using an approximation for the boundary condition at large separations, calculates only viscosity and normal stress

differences, and predicts a shear thinning hydrodynamic viscosity for $Pe \approx 1$ in contrast to the monotonic increasing hydrodynamic viscosity with respect to increasing rate, as calculated in Stokesian Dynamics simulations [Foss *et al.* (1999)]. At high Peclet numbers, Batchelor & Green (1972b) show that in the limit of no Brownian motion, the nonequilibrium microstructure is isotropic and calculate the viscosity for pure straining flow. Results for simple shear flow cannot be obtained in this limit, and Brownian motion or three particle interactions are required to eliminate closed streamlines. By including Brownian motion, Brady & Morris (1997) analyze the boundary layer in the compressional zone in which Brownian motion and hydrodynamic shearing forces balance, resulting in an anisotropic microstructure. The boundary layer has a length that is $\sim O(1/Pe)$. Furthermore, Brady & Morris (1997) show that the case $b/a = 1$ is a singular limit when $Pe \gg 1$ since the nonequilibrium microstructure drastically changes its scaling with respect to Peclet number for small changes in b/a, $g \sim O(Pe^{0.78})$ when $b/a = 1$ but $g \sim O(Pe)$ when $b/a \to 1$. One main effect on rheology is that the nondimensional Brownian stresses are $\sim O(Pe^{-0.22})$ for $b/a = 1$ but $\sim O(1)$ for $b/a \to 1$. As discussed earlier, the singular limit is not investigated and we investigate the limit $b/a \to 1$.

These predictions for dilute dispersions can be extended to higher concentrations by using the scaling argument of Brady (1993b) as shown by Brady & Vicic (1995), Brady (1996), and Brady & Morris (1997). Since there are hydrodynamic interactions, a particle does not diffuse with its bare-particle diffusivity. Rather, it diffuses with the short-time self-diffusivity, and the scaled Peclet number is

$$\overline{Pe} = \frac{Pe}{D_0^s(\phi)}. \tag{3.56}$$

Additionally, the particle stress no longer has just a simple scaling with the equilibrium radial-distribution function, as shown in the previous section. The Brownian stress,

$$\frac{\langle \boldsymbol{\Sigma}_B \rangle}{\eta_s \dot{\gamma}} \sim \phi^2 \frac{g_{eq}(2;\phi)}{D_0^s(\phi)}, \tag{3.57}$$

and the nonequilibrium hydrodynamic stress,

$$\frac{\langle \boldsymbol{\Sigma}_H \rangle}{\eta_s \dot{\gamma}} + 1 - \eta'_\infty \sim \phi^2 \frac{g_{eq}(2;\phi)}{D_0^s(\phi)}, \tag{3.58}$$

include factors from both the structure, the radial-distribution function, and particle dynamics, the short-time self-diffusivity, where η'_∞ is the nondimensional high-frequency dynamic viscosity. A value of unity from the nondimensional contribution of the solvent viscosity to the bulk stress is included on the left-hand side of equation (3.58) since η'_∞ also includes a contribution from the solvent viscosity.

The short-time self-diffusivity is not a rheological quantity, and ideally, for a rheological model, all quantities should be able to be measured or deduced simply from rheometry. Since the short-time self-diffusivity is only a function of hydrodynamic interactions of the equilibrium microstructure, it should be somehow related to the high-frequency dynamic viscosity which is also a function of hydrodynamic interactions for an equilibrium microstructure. A relationship was first proposed by Beenakker (1984) and later shown by Brady (1994). More recently, Bergenholtz *et al.* (1998) measured both the short-time self-diffusivity and the high-frequency dynamic viscosity for the same dispersion to confirm that,

$$D_0^s(\phi) \approx 1/\eta'_\infty(\phi). \tag{3.59}$$

Using this relationship, we find that the scaled Peclet number can be written,

$$\overline{Pe} = Pe\eta'_\infty(\phi), \tag{3.60}$$

and the Brownian and nonequilibrium hydrodynamic stresses scale,

$$\sim \phi^2 g_{eq}(2;\phi)\,\eta'_\infty(\phi). \tag{3.61}$$

As a supplement to the first of these theoretical investigations, a number of numerical simulation techniques have been developed to study the microstructure and

rheological properties of colloidal dispersions at finite concentrations in flow while including hydrodynamic interactions between particles. These methods include Stokesian Dynamics [Brady & Bossis (1987)], dissipative particle dynamics [Boek *et al.* (1997)], discretized Boltzmann methods [Ladd (1993, 1994a, 1994b)], and Brownian Dynamics with approximate methods of including mean-field hydrodynamic interactions [Rastogi & Wagner (1997); Heyes & Mitchell (1997)]. Only results from the Stokesian Dynamics method [Foss *et al.* (1999)] are analyzed here since the method fully accounts for hydrodynamic interactions *and* calculates both the hydrodynamic and Brownian contributions to the particle stress separately. Stokesian Dynamics results [Foss *et al.* (1999)] show that the Brownian viscosity shear thins for all Peclet numbers, qualitatively like the interparticle force viscosity for Brownian Dynamics. In addition, the hydrodynamic viscosity is constant at small Peclet numbers, appears to be a monotonic increasing function with respect to Peclet number, and increases rapidly for large Peclet numbers. These Brownian and hydrodynamic contributions yield a total viscosity which is constant at low Peclet numbers, then shear thins due to the decrease in the Brownian viscosity, reaches a constant value when the rate of decrease of the Brownian viscosity equals the rate of increase of the hydrodynamic viscosity, and shear thickens at high Peclet numbers as the hydrodynamic viscosity increases. Stokesian Dynamics results further show that the first normal stress difference is positive at small Peclet numbers, zero at intermediate Peclet numbers and negative at large Peclet numbers. The sign change in the first normal stress difference occurs since the Brownian contribution is positive and the hydrodynamic contribution is negative. At low Peclet number, the Brownian contribution dominates, yielding a positive first normal stress difference; whereas, at high Peclet number the hydrodynamic contribution is dominant and the first normal stress difference is negative. Furthermore, Stokesian Dynamics shows that the second normal stress difference is negative for all values of the Peclet number. The full stress tensor is not yet calculated in Stokesian Dynamics since the pressure moments [Jeffrey, Morris & Brady (1993)] have not yet been included, and the osmotic pressure is not calculated.

Some of the rheological behavior observed in Stokesian Dynamics simulations is

experimentally confirmed. Shear thinning [Krieger (1971); de Kruif *et al.* (1985); Jones *et al.* (1991)] and shear thickening [Boersma, Laven & Stein (1990); D'Haene (1992); Laun (1994)] of the total viscosity of hard-sphere colloidal dispersions have been observed for years, but recent advances in rheology allow the individual contributions to the shear viscosity to be determined. Optical dichroism is related to the thermodynamic contribution to the total shear viscosity for hard-sphere colloidal dispersions through a system-specific, stress-optic coefficient [Bender & Wagner (1995)]. In the case of colloidal hard spheres, the thermodynamic contribution is simply the Brownian contribution. (For a general system, the thermodynamic contribution is the sum of the interparticle force and Brownian contributions.) Simultaneous measurement of optical dichroism and total shear viscosity allows the same microstructure to be probed by both techniques, and these measurements confirm that shear thickening is related to an increase in the hydrodynamic contribution to the shear viscosity [Bender & Wagner (1996)]. Additionally, stress jumps—mechanical measurements using a conventional rheometer equipped with a torque rebalance transducer—can be used to measure the viscous contribution to the shear viscosity for the microstructure at the time of flow cessation since the viscous contribution immediately decays when the flow is stopped [Mackay, Liang & Halley (1992)]. The viscous contribution is simply the sum of the hydrodynamic and solvent contributions to the total shear viscosity. The total viscosity is also mechanically measured and is simply the value of the viscosity just prior to cessation; thus, the total viscosity and its viscous contribution are both measured for the same microstructure. Stress jump measurements confirm that shear thinning is caused by a decrease in the Brownian viscosity [Kaffashi *et al.* (1997)]. Additional stress jump measurements show that shear thickening is caused by an increase in the hydrodynamic viscosity, at least for the case of continuous shear thickening [O'Brien & Mackay (1996)]. There is at least one measurement for which the thermodynamic contribution discontinuously increases and causes discontinuous shear thickening of the total viscosity [O'Brien & Mackay (1996)].

Even though much progress has been made in measuring the shear viscosity, and its individual contributions, for a hard-sphere colloidal dispersion, little progress has

been made in the measurement of normal stress differences. There are few measurements of the first normal stress difference for a well-characterized, hard-sphere colloidal dispersion dispersed in a Newtonian fluid [Laun (1994); Aral & Kalyon (1997)] even though there are a number of measurements for other particulate systems [Willey & Macosko (1978); Chan & Powell (1984); Poslinski *et al.* (1988); Ohl & Gleissle (1993); Jomha & Reynolds (1993)]. Additionally, the first normal stress difference measurements that are available are only in the limit when $Pe \gg 1$. In this case it is found that the first normal stress difference is negative and approximately scales with $\eta_s\dot{\gamma}$, as expected. The main difficulty in measuring the first normal stress difference is the fact that $N_1 \approx 0$ when $Pe \sim O(1)$ due to the difference in signs of the hydrodynamic and Brownian contributions. $N_1 \approx 0$ is a problem in mechanical measurements because the total thrust on the upper tool in a cone-and-plate geometry is directly related to the first normal stress difference, and forces near zero must be measured. Measurements at small rates, where $N_1 > 0$ are difficult for two reasons—the force is small, $\sim O(\eta_s\dot{\gamma}Pe)$, and the required rates are often smaller than the lower limit of a standard motor for a rheometer. Since the Brownian contribution to the first normal stress difference is always positive, regardless of the value of Peclet number, one would expect optical measurements to be useful to at least measure one of the contributions to the first normal stress difference. An additional advantage of an optical measurement is the increased sensitivity compared to a mechanical measurement. Wagner (1998) finds that it is difficult to make optical measurements of the Brownian contribution to the first normal stress difference since a stable and meaningful signal cannot be obtained for concentrated dispersions.

There are no measurements of the second normal stress difference for a well-characterized hard-sphere suspension in the literature, but Leighton (1997) approximates the values of the second normal stress difference for non-Brownian suspensions. Leighton uses viscous resuspension data in Couette flow [Acrivos, Mauri & Fan (1993)], normal force measurements in parallel disk flow [Gadala-Maria (1979); Leighton (1997)], and the fact that there is no particle migration in parallel disk flow [Chow *et al.* (1994)] to determine the individual normal stress differences. Leighton

(1997) finds that $N_i \sim O(\eta_s \dot{\gamma})$, $N_2 < 0$, $N_1 < 0$, and $N_2/N_1 \approx 3$ for $Pe \gg 1$.

Another way to measure the effect of normal stress differences is to perform rod climbing experiments, which are commonly done for polymer solutions. There are no published data for rod climbing experiments for well-characterized hard-sphere suspensions, but Leighton (1997) has performed rod climbing experiments on non-Brownian particles in a Newtonian suspending fluid. He finds that there is negative rod climbing, as expected, since $N_1 < 0$ for $Pe \gg 1$.

There are no measurement of the nonequilibrium osmotic pressure for any system, but recently Kalogrianitis & van Egmond (1997) developed a system to optically determine the full stress tensor for the thermodynamic contribution to the particle stress.

In this section the Smoluchowski equation is solved using $\ell_{max} = 10$ and 400 intervals for each ordinary differential equation when $Pe \leq 1$. The value of ℓ_{max} is the same as that used for the case of no hydrodynamic interactions when $Pe \leq 1$, but the number of required intervals is much larger for the case of two-particle hydrodynamic interactions. A greater number of intervals is required since rheological properties are dependent on values of the nonequilibrium microstructure far from particle contact; whereas, only the surface values are required to calculate the rheology when hydrodynamic interactions are neglected.

All macroscopic properties, except for the hydrodynamic contribution to the osmotic pressure when $Pe > 1$, meet the convergence criterion. The fact that more moments in the expansion and a finer grid resolution are required to achieve accurate calculation of the osmotic pressure, as compared to other rheological properties, is also seen at low Peclet numbers. For $Pe > 1$ the Smoluchowski equation is solved with $\ell_{max} = 16$ and 160 intervals, but only the viscosity and normal stress differences are reported since the hydrodynamic contribution to the osmotic pressure does not converge. Calculations are completed for $Pe \leq 10$.

Microstructure

The descriptions of the meaning of all microstructure plots in the previous section apply to this set of microstructure plots as well.

Qualitatively, the density plots in Figure 3.20 for the case of $b/a \to 1$ look remarkably similar to the density plots for the case of no hydrodynamic interactions, Figure 3.1, when comparing plots at the same Peclet number; thus, qualitative analysis of the plots is not necessary. Note that the legend for the colors is identical for both figures. There are only two noticeable differences—the red portion in the compressional zone is slightly smaller and the downstream portion of $f > 0$ near particle contact more closely follows an undisturbed streamline than the extensional axis in Figure 3.20. The slightly smaller portion of red is indicative of smaller values of f in the boundary layer when hydrodynamic interactions are present. This observation is consistent with the concept that lubrication forces tend to keep two particles apart in the compressional zone, and one would expect that there is a lower probability of finding the second particle in the boundary layer when hydrodynamic interactions are present than when they are neglected. Additionally, the presence of hydrodynamic interactions makes it more difficult for two particles to separate in the extensional zone and one expects a higher probability of finding a second particle along the extensional axis when hydrodynamic interactions are present than when they are neglected.

This effect of hydrodynamic interactions is better seen in Figure 3.21, where the contact value of f/Pe is plotted in the velocity-gradient plane. We see that the separation point, $f = 0$, occurs at an angle less than $\theta \approx 1.12$-radians. It's difficult to ascertain whether this is the true separation point since higher Peclet numbers are not included, but this value is a maximum value for the separation point. Note that the angle of the separation point, $\theta_{max} \approx 1.12$-radians, occurs more downstream when including hydrodynamic interactions than when hydrodynamic interactions are neglected, where $\theta_{max} \approx 1.26$-radians. The point of separation is further downstream because lubrication forces tend to keep the two particles together in the extensional zone and a second particle can more easily move tangentially than radially with re-

spect to the test particle. Additionally, the maximum contact value occurs slightly more downstream within the boundary layer for the case when hydrodynamic interactions are present, but the actual value of the maximum is quite similar for the two cases.

At first glance the fact that the maximum contact values are approximately equal for both cases seems to contradict the observation of the smaller region of red in the density plot for the case in which hydrodynamic interactions are present. But, in fact, the smaller region of red indicates that the probability decreases more rapidly with respect to particle separation along the compressional axis, and this fact is seen in Figure 3.22b when comparing to Figure 3.3b.

In the previous section, a simple geometric argument was used to predict the value at which $f = 0$ along the extensional axis, and it was found that $f = 0$ at $r \approx 2.83$. In Figure 3.23 we see that at $Pe = 10$, $f = 0$ at $r \approx 2.41$, closer to particle contact than the case of no hydrodynamic interactions. There are two reasons for the smaller value of r—the separation point is further downstream and hydrodynamic interactions. Since the separation point is further downstream, the region of $f > 0$ would cross the extensional axis at a smaller value of r if the particle is simply advected by the external flow as in the case of no hydrodynamic interactions. But the second particle does not follow an undisturbed streamline and the presence of hydrodynamic interactions reduces the velocity of the second particle along the extensional axis.

Shear viscosity

All three contributions to the $O(\phi^2)$ contribution to the relative shear viscosity are shown in Figure 3.24. As expected, the interparticle force contribution is negligible since the interparticle stress is $\sim O(b/a - 1)$. The total viscosity is constant at low Peclet number, shear thins, has a constant value near $Pe = 6$ and shear thickens at high Peclet numbers, in qualitative agreement with simulation and experimental results. Furthermore, shear thinning occurs because of a decrease in the Brownian contribution, and shear thickening occurs because of an increases in the hydrodynamic contribution, agreeing with experiments and simulations. It is difficult to see in the

figure, but the hydrodynamic contribution is a monotonic increasing function of Peclet number, in agreement with the results of Foss *et al.* (1999), but in disagreement with the results of Lionberger (1998). Lionberger (1998) calculates an initial decrease in the hydrodynamic contribution to the shear viscosity with a minimum at $Pe \sim O(1)$ and shows excellent agreement with the Stokesian Dynamics results of Phung, Brady & Bossis (1996). Unfortunately, the results of Phung, Brady & Bossis (1996) predict a minimum in the hydrodynamic viscosity only because of structure formation which is caused by an error in the code, as corrected by Foss *et al.* (1999). The data from the correct simulation conditions do not show a minimum in the hydrodynamic contribution to the viscosity since long-range structure no longer forms.

Shear thinning of the hydrodynamic viscosity, as calculated by Lionberger (1998), could be due to one or more miscalculations. In equation (27) of Lionberger (1998), the coefficients preceding the integrals do not have the same power of π for integrals with similar integrands. Additionally in equation (27), there are two integrals for $H_{2,2}$ (and $H_{2,0}$)—one integral with M in the integrand and another with L in the integrand. The two integrands should combine to $L + \frac{2}{7}M$ as seen in equation (29) of Lionberger, equation (29) of Brady & Vicic (1995) and the results of this work. Finally, the effect of the approximate outer boundary condition cannot be tested because of these errors, but the monopole of the spherical harmonic expansion, $B_{0,0}$, should be affected most by the outer boundary condition, as seen for osmotic pressure when hydrodynamic interactions are neglected. Since the calculation of the hydrodynamic viscosity includes an integral using the monopole, this calculations is sensitive to the behavior of $B_{0,0}$ at large separations.

The actual cause of shear thickening is currently a controversial subject in the literature [Hoffman (1998)]. There are two schools of thought—shear thickening is caused by cluster formation and the resulting increase in the hydrodynamic stress [Bossis & Brady (1984); Phung, Brady & Bossis (1996); Bender & Wagner (1996)] or shear thickening is caused by destruction of order [Hoffman (1998)]. Both mechanisms may lead to shear thickening, but the results of this work show that destruction of shear-induced order is *not* required for shear thickening to occur, as has been suggested. In

fact, shear thickening occurs in this case because of the formation of the boundary layer in the compressional zone in the presence of hydrodynamic interactions. There is an $O(Pe)$ probability of finding two particles near contact and the values of the hydrodynamic functions reach their maxima near particle contact because of lubrication; thus, it seems that the hydrodynamic stress can be calculated solely from the boundary layer. This hypothesis is tested for $Pe = 10$ by calculating the hydrodynamic viscosity in two parts. The first part is simply the contribution over all space from the equilibrium microstructure. The second part is the contribution from the nonequilibrium microstructure near particle contact, within the boundary layer. I used an outer limit of $(r-2)Pe < 6$ for the boundary layer calculation. The result of this calculation is shown in Figure 3.24 and is in close agreement with the value that is correctly calculated by using the nonequilibrium microstructure throughout all space. Even though $O(1)$ variations of f contribute to the hydrodynamic viscosity, this contribution appears to be negligible when calculating the hydrodynamic shear viscosity.

The corrections to the low-shear, Newtonian viscosity contributions are shown in Figure 3.25. As expected, based on the analysis of the previous section, the first correction for the Brownian and interparticle force contributions to the shear viscosity is $O(Pe^2)$ at low Peclet number, arising from the $O(Pe^3)$ deformation of the microstructure. As shown by Brady & Vicic (1995), the first correction to the hydrodynamic viscosity is also $O(Pe^2)$, but arising from the $O(Pe^2)$ deformation rather than the $O(Pe^3)$ deformation.

These results can be extended to higher concentrations by using the scaling theory of Brady (1993b). Since the Brownian and nonequilibrium hydrodynamic stresses have the same scaling, equations (3.57) and (3.58), a scaled viscosity, η^*, is formed.

$$\begin{aligned}
\eta_r &= 1 + \eta_H + \eta_B, \\
\eta_r - \eta'_\infty &= 1 + \eta_H - \eta'_\infty + \eta_B, \\
\eta_r - \eta'_\infty &\sim \phi^2 g_{eq}(2;\phi)\,\eta'_\infty(\phi)\,. \\
\eta^* &= \frac{\eta_r - \eta'_\infty}{\phi^2 g_{eq}(2;\phi)\,\eta'_\infty(\phi)}.
\end{aligned} \tag{3.62}$$

By plotting the scaled viscosity, η^*, versus the scaled Peclet number, $Pe\eta'_\infty(\phi)$, a universal curve for the shear thinning behavior of a dispersion should be found. Such a plot is made and compared with the Stokesian Dynamics results of Foss *et al.* (1999) in Figure 3.26. The value of $\eta'_\infty(\phi)$ is approximated by taking the low Peclet limit for the hydrodynamic contribution to the shear viscosity. The value of $g_{eq}(2;\phi)$ is approximated by using the Carnahan-Starling equation, (3.47). The collapse of the data to a single master curve is remarkable for all values of Peclet number. The theoretical curve of this work compares poorly with the master curve of data since the value of the low Peclet limit is too small and the value of the scaled Peclet number at which shear thickening occurs is also too small. The error in the simulation data is too large to comment on the value of the Peclet for which shear thinning begins. At low Peclet number, the theory underpredicts the value of the master curve. The theory predicts that the value should be slightly less than unity, but the master curve passes through a value between 2.0 and 2.5. The low-shear value of the master curve is not a surprise since Brady (1993b) showed that a value of 12/5 for the coefficient compared quite well to experimental and simulation data.

Since the simulation data collapses so nicely to a master curve, a second figure, Figure 3.27, is made which includes both experiments [van der Werff, de Kruif & Dhont (1989); D'Haene, Mewis & Fuller (1993); Bender & Wagner (1995)] and simulations [Foss *et al.* (1999)]. The Carnahan-Starling and Woodcock equations for the equilibrium radial-distribution function are used for $\phi < 0.52$ and $0.52 \leq \phi \leq 0.64$, respec-

tively with $\phi_m = 0.64$ used for maximum packing [Nolan & Kavanagh (1992)]. There is fair agreement between the experimental data and simulation data, but considering the sources of error when plotting the experimental data, the agreement is quite good. There are three main sources of error in the experimental data--measurement of volume fraction, polydispersity and deviations from hard-sphere behavior. Small deviations in volume fraction have quite large effects on physical properties since the dispersions are near close-packing where physical properties either diverge or vanish.

Normal stress differences

In Figure 3.28 the $O(\phi^2)$ contributions to the nondimensional first normal stress differences, $N_1/\eta_s\dot{\gamma}$, are shown. The first normal stress difference is positive at small Peclet numbers, changes sign near $Pe = 9$ and is negative at high Peclet numbers.

The first normal stress difference changes sign since the Brownian and hydrodynamic contributions have opposite signs, but the surprising feature in Figure 3.28 is the small magnitude of the hydrodynamic contribution to the first normal stress difference at small Peclet numbers. To better observe the behavior for $Pe \ll 1$, the magnitudes of these contributions are shown on a log-log plot in Figure 3.29a and the next correction to the contributions to the first normal stress difference are shown in Figure 3.29b. The hydrodynamic contribution is so small that it is even smaller than the interparticle force contribution at small Peclet numbers. Even more surprising is the $O(Pe^{5/2})$ scaling for $Pe \ll 1$. Brady & Vicic (1995) show that the hydrodynamic contribution to the first normal stress difference is $o(Pe)$ since the $O(Pe)$ deformation does not contribute. Additionally, it can be shown that the $O(Pe^2)$ deformation does not yield hydrodynamic normal stress differences. Furthermore, Brady & Vicic (1995) show that the next term for the inner expansion, the $O(Pe^{5/2})$ term, is isotropic and does not contribute to normal stress differences. One expects that the next term in the inner expansion, $O(Pe^3)$, might yield an $O(Pe^3)$ contribution to the nondimensional first normal stress difference. In Figure 3.30a one of the moments used in the calculation of the first normal stress difference is shown to scale with $O(Pe^3)$ at small Peclet numbers. Both moments used in the calculation of the first

normal stress difference, $B_{4,1}$ and $B_{4,3}$, have this same scaling, resulting in an $O(Pe^3)$ term for the hydrodynamic contribution to the first normal stress difference. But $N_1/\eta_s\dot{\gamma} \sim O(Pe^{5/2})$ and not $O(Pe^3)$. In this analysis, the effects of the outer solution, where $rPe^{1/2} \sim O(1)$, have not yet been included. Brady & Vicic (1995) show that the $O(Pe^{5/2})$ term of the outer expansion yields an $O(Pe^{5/2})$ contribution to the hydrodynamic stress, and it is this contribution which yields the $O(Pe^{5/2})$ term of the nondimensional first normal stress difference. The far-field behavior for $B_{4,3}$ is shown in Figure 3.30b where $B_{4,3}/Pe^{5/2}$ is plotted versus $rPe^{1/2}$ and all curves collapse for $rPe^{1/2} > 4$ when $Pe \leq 0.20$.

Both the Brownian and interparticle contributions are $O(Pe)$ for small Peclet number and are caused by the $O(Pe^2)$ deformation of the microstructure. The next correction to both contributions at low Peclet number is $O(Pe^{5/2})$ due to the $O(Pe^{7/2})$ deformation of the microstructure, as already shown for the case in which hydrodynamic interactions are neglected.

At high Peclet number, the first normal stress difference cannot be extrapolated to its infinite plateau value, but the hydrodynamic contribution to N_1 should not equal zero, as predicted by Brady & Morris (1997). $N_1 = 0$ in their approximate analysis since the angular velocity in the boundary layer is neglected, resulting in a structure at particle contact [Brady & Morris (1997)],

$$f_{BM}(2) \sim \begin{cases} -\sin[\theta]\cos[\theta]\cos[\varphi], & \text{if } > 0; \\ 0, & \text{otherwise.} \end{cases} \tag{3.63}$$

If we derive the equation for the hydrodynamic contribution to the first normal stress difference from equation (3.33),

$$\frac{N_1^H}{\eta_s\dot{\gamma}\phi^2} = \left(\frac{5}{\pi}\right)^{1/2} \int_2^\infty M(r) \left(B_{4,1}(r;Pe) - \frac{1}{\sqrt{7}} B_{4,3}(r;Pe) \right) g(\mathbf{r}) r^2 dr, \tag{3.64}$$

and expand $f_{BM}(2)$ in terms of surface spherical harmonics, we find that $B_{4,1} = 0$ and $B_{4,3} = 0$, leading to no hydrodynamic contribution to the first normal stress difference. When the angular velocity terms are retained in the analysis, the structure within the

boundary layer will change from f_{BM}. Based on the results of this numerical analysis at $Pe = 1 - 10$, it's expected that $B_{4,1} < 0$ and $B_{4,3} > 0$ near particle contact for $Pe \gg 1$, leading to a non-zero first normal stress at high Peclet number.

Since $B_{4,1} < 0$ and $B_{4,3} > 0$ near particle contact, then the first normal stress difference is negative. Behavior only near particle contact is required to achieve an approximation of the first normal stress difference, as shown in Figure 3.28, where the solid black diamond is the result at $Pe = 10$ when the integral for the first normal stress difference is evaluated for $(r-2)Pe < 6$.

The fact that there is a negative first normal stress difference for dispersions is surprising since only a few systems, such as liquid crystalline polymers [Magda *et al.* (1991)], exhibit such behavior. We can understand why the hydrodynamic contribution to the first normal stress difference is negative in two ways—from a purely mathematical point of view and from a physical viewpoint.

Mathematically, we can study how variations from $f_{BM}(2)$ affect $B_{4,1}$ and $B_{4,3}$ when $f(2)$ is expanded in terms of surface spherical harmonics. The result of Brady & Morris (1997), $f_{BM}(2)$, is cast in more general form,

$$f(2) \sim \begin{cases} -\sin[(\theta - \pi + \delta) + \pi]\cos[\alpha(\theta - \frac{\pi}{2} + \delta + \epsilon) + \frac{\pi}{2}]\cos[\beta\varphi], & \text{if} > 0; \\ 0, & \text{otherwise.} \end{cases} \tag{3.65}$$

where α controls the position of the maximum in the velocity-gradient plane, β contracts/expands the φ coordinate, δ shifts the region downstream (upstream) in the velocity-gradient plane with a positive (negative) value while keeping the range of θ the same, and ϵ increases (decreases) the range of values of θ for which f is non-zero in the velocity-gradient plane for positive (negative) values of ϵ. As long as $\beta = 1$, $B_{4,3} = 0$ because of the orthogonality properties of $\cos[\varphi]$, and we find that $0 < \beta < 1$ yields $B_{4,3} > 0$. We now investigate changes in the behavior of $f(2)$ in the velocity-gradient plane and the effect of these changes on the value of $B_{4,1}$ when $\beta = 1$. The position of the maximum value in the compressional zone can be moved downstream, while keeping the range and position of the endpoints the same as f_{BM}, by using $\alpha > 1$ with $\delta = \epsilon = 0$. Physically, the fact that the maximum is pushed downstream

makes sense, but this set of parameters results in $B_{4,1} > 0$ in disagreement with the numerical results of this study. Note that if $\alpha < 1$, then $B_{4,1} < 0$. A second likely scenario is that the entire region is slightly shifted downstream, but the maximum value remains in the center of the region. This behavior is accomplished by using positive values of δ with $\alpha = 1$ and $\epsilon = 0$. Again, physically this situation can be visualized, but $B_{4,1} > 0$. Another behavior that seems physical is for the leading edge to remain at the same point while the range of the boundary layer extends further downstream than f_{BM} with the maximum value remaining at the midpoint of the range. To achieve this behavior, positive values of ϵ are used with $\alpha = 1$ and $\delta = 0$, but $B_{4,1} > 0$. Based on the density plots in Figure 3.20 and the plot of $f(2)$ in Figure 3.21, we should expect the leading edge to be shifted slightly downstream (positive values of δ) and the width of the range to be extended further downstream (positive values of ϵ), but both of these result in $B_{4,1} > 0$. To compensate for this behavior, the maximum value within the boundary layer must be pushed from the midpoint of the range toward the leading edge of the boundary layer. Even though the maximum value of f in the boundary layer is on the leading edge side of the midpoint of the range, this doesn't mean that the maximum value is upstream of its low Peclet position. In fact, as seen in Figure 3.21, the maximum value is still slightly downstream. Physically, the position of the maximum value of f at particle contact is pushed downstream from the compressional axis—the position of the maximum value at low Peclet number, but the separation point is pushed further into the extensional zone from the gradient axis—the position of separation at low Peclet number—because of lubrication forces.

A second physical explanation can be made for the region outside of the boundary layer, where we visualize how the shear-induced structure differs from its desired state and how an incompressible fluid element in the velocity-gradient plane must relax to attain this desired state. If the fluid element contracts in the velocity direction and expands in the gradient direction, a positive first normal stress difference occurs since the tools of the cone-and-plate geometry would be pushed apart; whereas, if the fluid element contracts in the gradient direction and expands in the velocity

direction, a negative first normal stress difference occurs. This argument is used by Marrucci (1997) to explain the sign change of the first normal stress difference for liquid crystalline polymers. For Brownian motion, the desired state is an isotropic structure while fore-aft symmetry is the desired state for pure hydrodynamics for low Reynolds number flow. We can see from the density plots, Figure 3.20 that a contraction in the velocity direction is required to achieve an isotropic state; thus, the Brownian contribution to the first normal stress difference is positive. To achieve fore-aft symmetry at high Peclet numbers, the structure in the compressional zone remains the same while the region of $f > 0$ in the extensional zone must be pushed toward the velocity axis. This motion results in a contraction in the gradient direction; thus, the hydrodynamic contribution to the first normal stress difference is negative.

Next we use the scaling argument of Brady (1993b) to extend these dilute results for the first normal stress difference to concentrated systems. In Figure 3.31 the numerical results are compared to Stokesian Dynamics simulations [Foss *et al.* (1999)]. The most exciting feature of this figure is the fact that the dilute theory and simulation data agree that a sign change occurs in N_1 near $\overline{Pe} \approx 10$. At low Peclet number the error in the simulation data is large and it's difficult to test the validity of the scaling.

In contrast to the behavior of the first normal stress difference, the second normal stress difference isn't very interesting. The $O(\phi^2)$ contributions to the nondimensional second normal stress difference are shown in Figure 3.32 and all contributions are negative at all Peclet numbers. The low Peclet behavior is better seen in Figure 3.33a, where the Brownian and interparticle contributions are shown to be $O(Pe)$ and result from the $O(Pe^2)$ deformation of the microstructure. The hydrodynamic contribution is also $O(Pe)$, but it arises from the $O(Pe)$ deformation of the microstructure. The next correction at low Peclet number is $O(Pe^{5/2})$ for all contributions. The Brownian and interparticle force contributions are caused by the $O(Pe^{7/2})$ term of the inner expansion, but the $O(Pe^{5/2})$ term of the outer solution results in the hydrodynamic contribution, as shown for the first normal stress difference. Finally, the scaling argument of Brady (1993b) is used to extend these results to concentrated dispersions and compared with Stokesian Dynamics data [Foss *et al* (1999)] in Figure 3.15. The

theory predicts that a maximum value occurs near $\overline{Pe} \approx 4$, in reasonable agreement with simulation data. As for the first normal stress difference, the large error in the low Peclet values makes it difficult to compare the theory with simulation data.

Finally, since both N_1 and N_2 are known as a function of Peclet number, rod climbing behavior [Lodge, Schieber & Bird (1988)] can be calculated, as done for the case when hydrodynamic interactions are neglected. In Figure 3.35, we see that the rod climbing coefficient is negative at all Peclet numbers, predicting that hard-sphere colloidal dispersions only exhibit negative rod climbing. This prediction has been experimentally confirmed in the high Peclet limit by Leighton (1997).

Osmotic pressure

The $O(\phi Pe)$ contributions to the osmotic pressure are shown in Figure 3.36. As discussed in the introduction to this section, the hydrodynamic contribution to the osmotic pressure is not included for $Pe > 1$ since it does not meet the convergence criterion. The low Peclet behavior is shown in Figure 3.37a, where the Brownian, hydrodynamic and interparticle force contributions to $\Pi/nkT - 1 - 4\phi$ are all $O(\phi Pe^2)$. The Brownian and interparticle force contributions are a result of the $O(Pe^2)$ deformation of the equilibrium microstructure, while the $O(Pe)$ term of the inner expansion yields the $O(\phi Pe^2)$ hydrodynamic contribution, as shown by Jeffrey, Morris & Brady (1993). The next correction to the osmotic pressure at low Peclet number is shown in Figure 3.37b, where the hydrodynamic contribution is $O(\phi Pe^3)$ while the Brownian and interparticle force contributions are both $O(Pe^{5/2})$. The Brownian and interparticle force contributions are caused by the isotropic, $O(Pe^{5/2})$ term of the inner expansion, as shown for the case when hydrodynamic interactions are neglected. The $O(\phi Pe^3)$ term of the hydrodynamic contribution remains an open issue. Only one moment, $B_{2,1}$, is involved in the calculation of the hydrodynamic osmotic pressure, and $B_{2,1} \sim O(Pe) + O(Pe^3)$ in the near-field; thus, the near-field microstructure is not responsible for the $O(\phi Pe^3)$ hydrodynamic term since an $O(Pe^2)$ deformation is required. Furthermore, the lowest term of the outer solution is $O(Pe^{5/2})$, yielding an $O(\phi Pe^{7/2})$ hydrodynamic contribution to the osmotic pressure; thus, the outer solu-

tion cannot cause the $O(\phi Pe^3)$ term for the osmotic pressure. Next, the possibility of an error in the form of the calculation is eliminated by showing that the hydrodynamic stress tensor is traceless when the proper pressure moment equals zero, $\mathcal{B}\left(r\frac{b}{a}\right) = 0$. Numerical inaccuracy is the only remaining cause of the apparent $O(\phi Pe^3)$ term of the hydrodynamic contribution to the osmotic pressure. Numerical inaccuracy is quite possible since the hydrodynamic contribution to the osmotic pressure barely meets the convergence criterion at low Peclet number and there is an $O(Pe^{-2})$ ratio in the orders of magnitude between the first contribution, $O(\phi Pe^2)$ and the expected scaling of the second contribution, $O(\phi Pe^4)$.

There are no other theoretical results nor are there experimental or simulation results with which to compare the predictions of this section.

3.4.3 Varying b/a ratios

In this section the Smoluchowski equation, equation (3.16), and its boundary conditions, equations (3.17) and (3.18), are solved with varying ratios of the thermodynamic and hydrodynamic radii for $b/a = 1.01$, 1.10, 1.20, 1.60, 2.50, and 5.00. All two-particle hydrodynamic functions are evaluated at $r\frac{b}{a}$ while the effective hard-sphere interaction occurs at $r = 2$.

Since the b/a ratio is varied, the concept of an effective hard-sphere interaction is introduced [Buscall (1994); Quemada (1994)]. For dilute hard spheres, the equilibrium radial-distribution function is simply

$$g_{eq}(r) = \begin{cases} 0, & \text{if } r < 2; \\ 1, & \text{if } r \geq 2. \end{cases} \tag{3.66}$$

This effective hard-sphere interaction can be caused by the presence of either a steric stabilizing layer on the surface of the particles or a long-range, repulsive interparticle force. For the case of steric stabilizers, b/a is nearly unity since the length of the steric stabilizer, δ, is quite small, $\sim O(1 - 10\text{nm})$ [Genz *et al.* (1994)], and the

thermodynamic radius, b, is approximated by

$$b = a + \delta. \tag{3.67}$$

Typically, $b/a < 1.1$ for steric stabilized colloidal dispersions [Buscall (1994)], and the length of the steric stabilizing layer is approximated by assuming that the molecule is fully extended.

When a long-range, repulsive interparticle interaction is present, the electrical double layers surrounding the particles interact, preventing the particles from making physical contact. The length of the double layer is approximated by the Debye length, κ^{-1} [Nagele *et al.* (1994)]; thus, the thermodynamic radius, b, is approximated by

$$b = a + \kappa^{-1}. \tag{3.68}$$

Typically, charged latices have $b/a > 2$ [Buscall (1994)], and the Debye length can be approximated by [Hoffman (1998)],

$$\kappa^{-1} = \left(\frac{\epsilon kT}{e^2 I}\right)^{1/2}, \tag{3.69}$$

where ϵ is the dielectric constant of the fluid, e is the electronic charge, and I is the ionic strength. The Debye length can reach quite large distances since the minimum ionic strength is $5\text{x}10^{-6}$–$1\text{x}10^{-5}$ M for conventional dialysis and $2\text{x}10^{-7}$ M when using a mixed bed of cation and anion exchange resins [Okubo (1987)].

Experimentally, the effective volume fraction or thermodynamic radius is approximated by one of three measurements—osmotic pressure, first peak of the equilibrium radial-distribution function, or phase behavior [Nagele *et al.* (1994); Reus *et al.* (1995)]. When using osmotic pressure, the effective volume fraction is a fitting parameter so that the volume-fraction dependence of the osmotic pressure fits the expected hard-sphere behavior. For the equilibrium radial-distribution function, the radius of the first peak is indicative of the location of thermodynamic hard-sphere behavior, and the radius of the peak equals $2b$, the interparticle separation when two particles

are in thermodynamic contact. When using phase behavior, the effective volume fraction is determined by finding the hydrodynamic volume fraction, $\phi_a = 4\pi na^3/3$, of the freezing point at equilibrium and using an effective volume fraction of $\phi_b = 0.494$, the freezing volume fraction [Pusey & van Megen (1987)] to determine b/a. Ideally, at least one of these tests is performed whenever measuring the rheological response of charged colloidal dispersions, but rarely is this done.

Despite the fact that the thermodynamic radius can be measured or approximated and has a physical origin, there are some disadvantages of using the effective hard-sphere model. Both the steric stabilizing layer and the long-range repulsive interactions are soft interactions since the steric stabilizing layer can be compressed or interpenetrate and double layers can overlap. Additionally, the effective hard-sphere model remains a central potential despite changes in shear rate which may cause a deformation of the double layer from its spherically symmetric shape when there is no flow. The steric stabilizing layer should nearly maintain its equilibrium shape with an increase in shear rate, and the double layer should also nearly maintain its equilibrium shape since the Peclet number of the macroions in the double layer is small.

The theory of Ogawa *et al.* (1997) is the most complete theory to predict the shear-rate dependence of the viscosity of charged colloidal dispersions, although the theory is semi-empirical and valid only for concentrated dispersions with a long-range, repulsive potential. The model does not include the prediction of normal stress differences. Ogawa *et al.* (1997) bases the theory on the Eyring activated process model, where a test particle is in a mean-field energy minimum formed by adjacent particles and the test particle exchanges places with its neighbors.

There are no simulations for charged colloidal dispersions with $b/a > 1$ and for which hydrodynamic interactions are exactly included. Rastogi, Wagner & Lustig (1996) study charged systems for $b/a = 1.25$ but do not include hydrodynamic interactions in the dynamics and include the hydrodynamic contribution to the viscosity only through the experimentally-determined, high Peclet constant viscosity, η_∞. Later, Rastogi & Wagner (1997) continue their study on charged systems, but only

include preaveraged hydrodynamic interactions. Such an approximate way of including hydrodynamic interactions is also used by Heyes & Mitchell (1997) in their study of Brownian dynamics using mean-field hydrodynamic calculations.

Not only are there no simulations, but there are few sets of experiments for which the shear-rate dependent viscosity is measured with a systematic variation of b/a ratios by changing particle size and/or Debye length [Mallamace, Micali & Vasi (1990); Ogawa *et al.* (1997)]. There are no experiments for which there is a systematic variation of b/a and an accompanying measurement to approximate the thermodynamic radius. Mallamace, Micali & Vasi (1990) show how the shear viscosity decreases with a decrease in the thermodynamic radius for a given hydrodynamic radius by increasing the salt concentration. Ogawa *et al.* (1997) show that the viscosity increases and the shear rate for the start of the high Peclet plateau also increases with (i) a decrease in particle size, a, while keeping κ^{-1} and ϕ_a constant and (ii) an increase in the thermodynamic radius by increasing κ^{-1} while keeping ϕ_a and particle size, a, constant. Ogawa's semi-empirical model predicts these trends, and it is shown that the model presented here also predicts these trends. Unfortunately, Ogawa *et al.* (1997) is not able to measure the low-shear Newtonian viscosity for any of the dispersions.

In this section the Smoluchowski equation is solved using the same set of parameters as in the previous section when $b/a \to 1$. The expansion for the deformation of the equilibrium microstructure is truncated at $\ell_{max} = 10$ and $\ell_{max} = 16$ while using 400 and 160 intervals for each ordinary differential equation when $Pe \leq 1$ and $Pe > 1$, respectively. All macroscopic properties are reported since all properties, including the hydrodynamic contribution to the osmotic pressure when $Pe_b > 1$, meet the convergence criterion.

Microstructure

The descriptions of the meaning of all microstructure plots in the previous sections apply to this set of microstructure plots as well.

Qualitatively, the density plots in Figures 3.38–3.43 are remarkably similar. Note that the legend is the same for all b/a-ratios, showing that the structure at a given

Peclet number, Pe_b, is fairly insensitive to the strength of hydrodynamic interactions included in the calculations. Despite the similarities, there are a few subtle differences between the figures. One feature is most noticeable for $Pe_b = 1$ near particle contact in the compressional zone. For $b/a = 1.01$ there is no yellow in the compressional zone—yellow is the color associated with the highest probability of finding a second particle in the density plots. But there is a significant region of yellow for $b/a = 1.20$, and this region disappears when $b/a = 5.00$. Physically, the appearance of the yellow region with increasing b/a ratio is not surprising since lubrication interactions are eliminated as b/a increases and the two particles can more easily make contact. Secondly, the angle of the extension of the boundary layer into the extensional zone increases as b/a increases. For $b/a = 1.01$, the boundary layer separates from particle contact and the region of high probability advects into the extensional zone nearly parallel with the velocity direction; whereas, for $b/a = 5.00$, the same region has a significant angle with respect to the velocity direction. This angle appears to monotonically increase as b/a increases.

In Figure 3.44 the contact value of f/Pe_b in the compressional zone in the velocity-gradient plane is shown for $Pe_b = 1$ and $Pe_b = 10$. At $Pe_b = 1$ the region of θ for which $f > 0$ and the value of θ of the maximum value of $f(2)/Pe_b$ do not change as b/a changes. But, as seen by the yellow region in the density plots, the maximum value of $f(2)/Pe_b$ changes with b/a. In fact $f(2)/Pe_b$ has its largest value when $b/a = 1.6$ while the θ-dependence of $f(2)/Pe_b$ is remarkably similar for $b/a = 5.00$ and $b/a = 1.01$.

At $Pe_b = 10$, Figure 3.44b shows the effects of lubrication on the boundary layer in the compressional zone. For $b/a \geq 1.10$, the separation point of the boundary layer and the point of the maximum value of $f(2)/Pe_b$ are relatively independent of b/a. The maximum value of $f(2)/Pe_b$ still changes with b/a and still has its largest value near $b/a = 1.60$. When $b/a = 1.01$ lubrication forces play a significant role and this is exhibited in three features of $f(2)/Pe_b$. The maximum value of $f(2)/Pe_b$ is much smaller for $b/a = 1.01$ than for $b/a = 5.00$, in contrast to $Pe_b = 1$, since lubrication forces in the compressional zone tend to keep two particles apart. The maximum of

$f(2)/Pe_b$ is shifted more downstream from its $Pe_b = 1$ value for $b/a = 1.01$ than for larger values of b/a. Finally, the separation point also occurs further downstream for $b/a = 1.01$ than for larger values of b/a since lubrication forces in the extensional zone tend to keep two particles together.

Even though lubrication has an effect on $f(2)/Pe_b$, the decay of $f(r)/Pe_b$ along the compressional axis doesn't change that much for $Pe_b = 1$ nor in the boundary layer at $Pe_b = 10$, as shown in Figure 3.45. The most significant difference occurs near particle contact for $Pe_b = 10$, where the value of $f(r)/Pe_b$ is much lower for $b/a = 1.01$ than for other values of b/a because of lubrication forces.

Finally, Figure 3.46 provides more concrete evidence for the change in the angle of the region of $f > 0$ in the extensional zone. In Figure 3.46a, there is only a small effect of b/a on the decay of the structure along the extensional axis, especially for larger separations. Near particle contact, the value of $f(2)/Pe_b$ for $b/a = 1.01$ is nearly identical to the value for $b/a = 5.00$ and $f(2)/Pe_b$ has its minimum value for $b/a = 1.60$, the same b/a ratio of the largest value of $f(2)/Pe_b$ in the compressional zone. Figure 3.46b shows the value of separation for which $f = 0$. For $b/a = 1.01$, the value of r is small because the value of θ at which the boundary layer separates is further downstream than the other b/a ratios and the region of $f > 0$ in the extensional zone is nearly parallel with the velocity axis. For $b/a \geq 1.10$, the separation point of the boundary layer is nearly identical, as shown earlier, and the only remaining effect is the angle that the $f > 0$ region makes with respect to the velocity axis. As b/a increases, the value of r at which $f = 0$ also increases, leading to the conclusion that the angle of the region of $f > 0$ in the extensional zone increases as b/a increases.

Shear viscosity

The $O(\phi_b^2)$ contributions to the relative shear viscosity are shown in Figures 3.47–3.49 for a range of b/a ratios. Since b/a increases while ϕ_b is constant, the value of the hydrodynamic radius decreases and tends to a point particle while the thermodynamic radius remains constant. Physically, the particle size decreases while the Debye length increases to maintain a constant thermodynamic radius in a charge-stabilized system.

Since the particle size decreases, the particle diffusivity also decreases, leading to a decrease in the Brownian contribution to the shear viscosity as b/a increases. In addition, since the particle size decreases, the effect of hydrodynamic interactions also decreases, resulting in a decrease in the hydrodynamic contribution to the shear viscosity. As the hydrodynamic radius decreases, the stress is transferred to the interparticle force contribution and at $b/a = 2.50$ the interparticle force is nearly the only remaining contribution to the viscosity.

Even though the hydrodynamic contribution decreases as b/a increases, shear thickening of the hydrodynamic component still occurs and can be seen for b/a up to 1.60 in the results presented here. It's expected that hydrodynamic shear thickening will always occur as the boundary layer near particle contact forms, but the magnitude of the shear thickening decreases with increasing b/a since the value of the hydrodynamic function at thermodynamic contact decreases as b/a increases. Additionally, the value of Pe_b at which hydrodynamic shear thickening occurs increases as b/a increases and cannot be calculated for $b/a > 2.00$ since hydrodynamic shear thickening occurs at $Pe_b > 10$. Since the hydrodynamic contribution shear thickens, the total viscosity will also shear thicken as long as the hydrodynamic viscosity increases faster than the other contributions shear thin. Based on the results of the previous section and Figure 3.47, shear thickening of the total viscosity occurs at higher Peclet numbers as b/a increases.

At some value of b/a, the hydrodynamic viscosity appears as a small, nearly constant value and the interparticle force contribution dominates, as seen in Figure 3.49a. Even though the hydrodynamic viscosity appears nearly constant on the $O(\phi_b^2)$ scale, there is a small degree of shear thickening on the $O(\phi_a^2)$ scale which is evident when the numerical data is analyzed.

The effect of b/a ratios on the hydrodynamic, Brownian and interparticle force contributions to the low shear, Newtonian viscosity are best seen in Figure 3.50. Figure 3.50a shows that the interparticle force contribution grows as $\sim O(b/a - 1)$ for $b/a - 1 \ll 1$, as expected based on the $\left(1 - A\left(2\frac{b}{a}\right)\right)$ in the interparticle force stress, equation (3.33), and the fact that $A(r\frac{b}{a}) \sim 1 - O(r\frac{b}{a} - 2)$ for $r - 2 \ll 1$. For large val-

ues of b/a, Figure 3.50b shows that the hydrodynamic viscosity decays as $\sim O((a/b)^6)$ and the Brownian viscosity decays as $\sim O((a/b)^7)$. The $O(\phi_b^2)$ hydrodynamic contribution decays as $\sim O((a/b)^6)$ simply because the hydrodynamic contribution scales as $O(\phi_a^2)$. The Brownian contribution has an additional factor of a/b because of the decrease in the particle diffusivity as the hydrodynamic radius decreases. Finally, the interparticle force contribution is approximated, with excellent agreement, by the results for the case of no hydrodynamic interactions, 12/5, with a factor of a/b to account for the decrease in the particle diffusivity.

The total viscosity can be plotted in such a way that the coefficients are always $O(1)$, independent of the value of b/a. In Figure 3.51a, the $O(\phi_b^2(a/b))$ term of the relative shear viscosity is plotted versus Pe_b. The extra factor of b/a for the relative viscosity is convenient since the (ϕ_b^2) term is $\sim O(1)$ when $b/a \sim O(1)$ and when $b/a - 1 \ll 1$, but the (ϕ_b^2) term is $\sim O(a/b)$ when $b/a \gg 1$. The results of the two previous sections provide bounds on this figure with the case of no hydrodynamic interactions providing a lower bound and the case of $b/a \to 1$ providing an upper bound.

A more realistic situation is studied by Mallamace, Micali & Vasi (1990) in which the particle radius and hydrodynamic volume fraction are constant while the thermodynamic radius and thermodynamic volume fraction are changed by varying the salt concentration of the suspending fluid. As the salt concentration increases, the Debye length decreases and the thermodynamic radius decreases while the hydrodynamic radius is held constant; thus, b/a decreases as salt is added to the system. The viscosity results of this section are rescaled in Figure 3.51b, where the $O(\phi_a^2)$ contribution of the shear viscosity is plotted versus the particle Peclet number, $Pe_a = 6\pi\eta_s\dot{\gamma}a^3/kT$. Note that these results are only valid for $\phi_b \ll 1$, imposing a severe restriction on the hydrodynamic volume fraction for which these results are valid, $\phi_a \ll (a/b)^3$. As b/a decreases, the low Peclet, Newtonian shear viscosity monotonically decreases and approaches its value for the case of $b/a \to 1$ presented in the previous section. The decrease in shear viscosity with a decrease in b/a qualitatively agrees with the viscosity results of Mallamace, Micali & Vasi (1990), where the viscosity is measured for

a single particle radius as a function of salt concentration at a given particle volume fraction. Furthermore, the shear viscosity begins to shear thin at some critical value of the particle Peclet number and this critical value increases as b/a decreases.

Another physical system is studied by Ogawa *et al.* (1997) in which the particle size is varied while the Debye length and the *hydrodynamic* volume fraction are kept approximately constant. Ogawa *et al.* (1997) find that the viscosity increases as the particle size decreases. They also find that there is a critical shear rate for the onset of the high-shear, constant viscosity regime and that this critical shear rate increases with a decrease in particle size. Since the Debye length is constant, the b/a ratio increases as the particle size decreases. Since ϕ_a is constant, Figure 3.51b is used to analyze the behavior of the viscosity. As b/a increases, the viscosity increases, in agreement with the results of Ogawa *et al.* (1997). Unfortunately, Ogawa *et al.* (1997) do not report measurements of the low Peclet viscosity and comparison cannot be made with the onset of shear thinning, but based on their model, the critical shear rate for the onset of shear thinning decreases with a decrease in particle size. In Figure 3.51a, the onset of shear thinning occurs at the same value of the Peclet number, Pe_b, and this fact is used to show that the results presented here predict that the critical shear rate for the onset of shear thinning should increase as the particle size decreases,

$$
\begin{aligned}
&Pe_{b,1} = Pe_{b,2}, \\
&\dot{\gamma}_1 a_1 b_1^2 = \dot{\gamma}_2 a_2 b_2^2, \\
&\dot{\gamma}_1 a_1 \left(a_1 + \kappa^{-1}\right)^2 = \dot{\gamma}_2 a_2 \left(a_2 + \kappa^{-1}\right)^2, \\
&\frac{\dot{\gamma}_2}{\dot{\gamma}_1} = \frac{a_1}{a_2}\left(\frac{a_1 + \kappa^{-1}}{a_2 + \kappa^{-1}}\right)^2 .
\end{aligned}
$$

If the particle size decreases, $a_2 < a_1$, then the shear rate increases, $\dot{\gamma}_2 > \dot{\gamma}_1$, and the two models do not agree. The model here predicts that the critical shear rate for the onset of shear thinning increases with decreasing particle size while the model of Ogawa *et al.* (1997) predicts that the critical shear rate decreases. There is no experimental data to determine which of the two models predicts the correct behavior.

Both models do predict, in agreement with experimental data, that there is a critical shear rate for the beginning of the high-shear, constant viscosity regime and that this critical shear rate increases as the particle size decreases. The model of Ogawa *et al.* (1997) has an advantage since predictions can be easily made for infinite shear rate, but no such predictions can be made by the model presented here.

Normal stress differences

The $O(\phi_b^2)$ contributions to the nondimensional first normal stress difference are shown in Figures 3.52–3.54 for a range of b/a ratios. As for shear viscosity, these results are valid for $\phi_b \ll 1$. Physically, the hydrodynamic radius changes as b/a changes while the thermodynamic radius and thermodynamic volume fraction both remain constant. By $b/a = 2.50$, the Brownian and hydrodynamic contributions are nearly zero. As seen in the previous section for $b/a \to 1$, the first normal stress difference changes sign at some critical Peclet number. The value of this critical Peclet number increases as b/a increases, and at some value of b/a, there is no longer a sign change. The value of b/a for which the first normal stress difference is positive definite cannot be calculated because of the upper limit of $Pe_b = 10$ for the calculations.

The contributions to the low Peclet, nondimensional first normal stress difference coefficient, $N_1/\eta_s\dot{\gamma}Pe_b\phi_b^2$, are shown in Figure 3.55. Only the Brownian and interparticle force contributions are shown since the hydrodynamic contribution is $O(Pe^{5/2})$, as shown in the section with $b/a \to 1$. In Figure 3.55a, the interparticle force contribution is $\sim O(b/a - 1)$ for $b/a - 1 \ll 1$, just as for the shear viscosity. For high values of b/a, Figure 3.55b, the Brownian contribution is $\sim O((a/b)^7)$ for $b/a \gg 1$, and the interparticle force contribution is well-approximated by the result when hydrodynamic interactions are neglected, $N_1/\eta_s\dot{\gamma}Pe_b\phi_b^2 = (16/15)(a/b)$.

The second normal stress difference is not as interesting since all components have the same sign for all values of Pe_b and b/a, as shown in Figures 3.56–3.59. By $b/a = 2.50$, the Brownian and hydrodynamic contributions are nearly zero, just as for the first normal stress difference.

For the low Peclet, nondimensional second normal stress difference coefficient,

$N_2/\eta_s\dot{\gamma}Pe_b\phi_b^2$, the interparticle force and Brownian contributions scale exactly as for the first normal stress difference, as shown in Figures 3.58a and 3.58b. The interparticle force contribution at large values of b/a is well-approximated by the result when hydrodynamic interactions are neglected, $-N_2/\eta_s\dot{\gamma}Pe_b\phi_b^2 = (21/15)(a/b)$. The hydrodynamic contribution scales as $O((a/b)^6)$, in agreement with the hydrodynamic contribution to the shear stress.

There are no experiments nor other theories with which to compare.

Osmotic pressure

The $O(\phi_b Pe_b)$ contributions to the nondimensional osmotic pressure, Π/nkT, are shown in Figures 3.60–3.62 for a range of value of b/a. By $b/a = 5.00$, the Brownian and hydrodynamic contributions nearly equal zero. The hydrodynamic contribution is positive for all Peclet numbers for $b/a < 1.01$, but at $b/a = 1.10$, the hydrodynamic contribution becomes negative. A positive contribution to this term of the virial expansion is typically due to the existence of a repulsive interparticle force, and, in this case, lubrication forces in the compressional zone act as the repulsive force. A negative contribution is indicative of an attractive interparticle force, and, as b/a increases, the effect of the far-field hydrodynamic interactions in the extensional zone dominate the effect of the far-field hydrodynamic interactions in the compressional zone. In the extensional zone hydrodynamic interactions tend to keep two particles from moving apart while in the compressional zone, hydrodynamic interactions tend to keep two particles from moving together. Also note that the hydrodynamic contribution also decays with respect to changes in b/a much faster than either of the normal stress differences and is nearly equal to zero at $b/a = 1.60$.

3.5 Conclusions

In this work the Smoluchowski equation is solved for two particles interacting with an effective hard-sphere force over a range of Peclet numbers, $Pe_b = 6\pi\eta_s\dot{\gamma}ab^2/kT$, and a range of b/a, where b/a is the ratio of the thermodynamic radius, b, to the

hydrodynamic radius, a. The resulting nonequilibrium microstructure is used to calculate the hydrodynamic, Brownian and interparticle force stresses and resulting rheological properties. These dilute results for the rheological properties are extended to higher concentrations by using the scaling theory of Brady (1993b).

First, dispersions are studied for which $b/a = 1$ and hydrodynamic interactions are neglected. At high Peclet number a boundary layer forms at particle contact in the compressional zone and the contact value of the nonequilibrium microstructure is $\sim O(Pe)$, resulting in a viscous scaling for the stress as $Pe \to \infty$. The dilute macroscopic properties are scaled [Brady (1993b)], compared with Brownian Dynamics simulations [Foss & Brady (1999)] and found to be in reasonable agreement for smaller volume fractions. At higher volume fractions there is a volume-fraction dependent relaxation time [Bergenholtz (1999)] in contrast to the single relaxation time predicted by Brady (1993b). The $O(Pe^{5/2})$ isotropic term of the inner expansion at low Peclet number is calculated, and the resulting contribution to the osmotic pressure is in excellent agreement with the numerical results.

Next, the case of $b/a \to 1$ with two-particle hydrodynamic interactions is analyzed. Shear thinning is caused by the decreased importance of Brownian motion as the shear rate increases, resulting in a shear thinning Brownian viscosity. Shear thickening at high Peclet number is caused by the formation of a boundary layer at particle contact and the existence of hydrodynamic interactions, resulting in a shear thickening hydrodynamic viscosity. Scaling theory [Brady (1993b)] produces a master curve of simulation and experimental data, but the dilute theory is only in qualitative agreement. The first normal stress difference changes sign since the Brownian and hydrodynamic contributions have different signs. At low Peclet number the Brownian contribution dominates, and at high Peclet number the hydrodynamic contribution dominates. Scaling theory [Brady (1993b)] collapses simulation data, and the dilute theory correctly predicts that the sign change occurs near $Pe\eta'_\infty \approx 10$. Additionally, the dilute theory also correctly predicts a maximum value of $N_2/\eta_s\dot{\gamma}$ near $Pe\eta'_\infty \approx 4$ in agreement with Stokesian Dynamics simulations [Foss *et al.* (1999)]. Lastly, the dilute theory predicts negative rod climbing in agreement with the experimental results of

Leighton (1997) at $Pe \to \infty$.

Finally, the b/a ratio is varied and two-particle hydrodynamic interactions are used. As b/a increases, lubrication forces are eliminated and then the effects of far-field hydrodynamic interactions decrease. This decrease in the effect of hydrodynamic interactions and the decrease of the hydrodynamic stress cause both shear thickening and the sign change of the first normal stress difference to occur at higher Peclet numbers as b/a increases. Eventually, at some value of b/a, shear thickening of the total viscosity no longer occurs and the first normal stress difference no longer changes sign. When salt is added to a colloidal dispersion to reduce the thermodynamic radius, the theory predicts that the shear viscosity decreases in agreement with experiments [Mallamace, Micali & Vasi (1990)]. When the particle size decreases while the Debye length and hydrodynamic volume fraction remain constant, the shear viscosity increases, also in agreement with experiments [Ogawa *et al.* (1997)].

Since the Smoluchowski equation and the bulk stress in sections 3.2 and 3.3 are written using two-particle hydrodynamic functions, the method presented here can be extended to any case for which the suspended bodies are spherical and the two-particle hydrodynamic functions are known. Two non-coalescing, spherical droplets and two spherical bodies of different sizes are examples of such cases. The current program can be easily modified to include these cases since each hydrodynamic function is evaluated by calling a separate function. The function call currently only includes the particle separation based on the hydrodynamic radius, $r\frac{b}{a}$, but the particle size ratio, $\beta = a_2/a_1$, and the viscosity ratio, $\lambda = \eta_d/\eta_s$, can be included, where a_2 and a_1 are the radii of the different sized spheres and η_d is the viscosity of the dispersed phase of an emulsion.

Additionally, the Smoluchowski equation is presented in a form that can be used for any linear flow. In fact, preliminary calculations have been completed and density plots for planar and uniaxial extensional flows are shown in Figure 3.63.

Finally, the equilibrium pair-distribution function is chosen to be $g_{eq}(r \geq 2) = 1$ in

this work, but the Smoluchowski equation can be for other cases by using

$$g(\mathbf{r}) = g_{eq}(\mathbf{r})(1+f); \tag{3.70}$$

thus, allowing different interparticle potentials to be investigated. The most interesting of these potentials is any potential that is not purely repulsive — attractive hard spheres, the dumbbell model of polymer solutions and others. For the attractive force, it would be interesting to see if there is shear thinning in the hydrodynamic viscosity at small Peclet numbers for a dispersion of attractive hard spheres as the shear flow increases and tends to pull the two particles apart along the extensional axis. While for the dumbbell model, one will obtain a better understanding of why $|N_2/N_1| \approx 1$ for dispersions but $|N_2/N_1| \ll 1$ for polymer solutions. An hypothesis for the difference in behavior is that the spring between the two beads is the major contribution to N_1 for polymer solutions since the spring wants to return to its equilibrium length and the dumbbell tends to align with the flow in the velocity-gradient plane. It is not necessary to study purely repulsive interactions to understand how the parameters in the interparticle force affect rheology since a purely repulsive interaction can be recast in the form of an effective hard-sphere interaction. By simply understanding how the parameters affect the thermodynamic radius and using the results of this study, one can understand how the parameters qualitatively affect dispersion rheology.

References

Acrivos, A. & T.D. Taylor, "Heat and mass transfer from single spheres in Stokes flow." Phys. Fluids **5**, 387–394 (1962).

Acrivos, A., R. Mauri & X. Fan, "Shear-induced resuspension in a Couette device." Int. J. Multiphase Flow **19**, 797–802 (1993).

Aral, B.K. & D.M. Kalyon, "Viscoelastic material functions of noncolloidal suspensions with spherical particles." J. Rheol. **41**, 599–620 (1997).

Batchelor, G.K. & J.T. Green, "The hydrodynamic interaction of two small freely-

moving spheres in a linear flow field." J. Fluid Mech. **56**, 375–400 (1972a).

Batchelor, G.K. & J.T. Green, "The determination of the bulk stress in a suspension of spherical particles to order c^2." J. Fluid Mech. **56**, 401–427 (1972b).

Batchelor, G.K., "Brownian diffusion of particles with hydrodynamic interaction." J. Fluid Mech. **74**, 1–29 (1976).

Batchelor, G.K., "The effect of Brownian motion on the bulk stress in a suspension of spherical particles." J. Fluid Mech. **83**, 97–117 (1977).

Beenakker, C.W.J., "The effective viscosity of a concentrated suspension of spheres and its relation to diffusion." Physica A **128**, 48–81 (1984).

Bender, J.W. & N.J. Wagner, "Optical measurement of the contributions of colloidal forces to the rheology of concentrated suspensions." J. Coll. & Int. Sci. **172**, 171–184 (1995).

Bender, J.W. & N.J. Wagner, "Reversible shear thickening in monodisperse and bidisperse colloidal dispersions." J. Rheol. **40**, 899–916 (1996).

Bergenholtz, J., personal communication (1999).

Bergenholtz, J., F.M. Horn, W. Richtering, N. Willenbacher & N.J. Wagner, "Relationship between short-time self-diffusion and high-frequency viscosity in charge-stabilized dispersions." Phys. Rev. E **58**, R4088–R4091 (1998).

Blawzdziewicz, J. & G. Szamel, "Structure and rheology of semidilute suspension under shear." Phys. Rev. E **48**, 4632–4636 (1993).

Boek, E.S., P.V. Coveney, H.N.W. Lekkerkerker & P. van der Schoot, "Simulating the rheology of dense colloidal suspensions using dissipative particle dynamics." Phys. Rev. E **55**, 3124–3133 (1997).

Boersma, W.H., J. Laven & H.N. Stein, "Shear thickening (dilatancy) in concentrated dispersions." AIChE J. **36**, 321–332 (1990).

Bossis, G. & J.F. Brady, "Dynamic simulation of sheared suspensions. 1. General method." J. Chem. Phys. **80**, 5141–5154 (1984).

Brady, J.F. & G. Bossis, "Stokesian Dynamics." Ann. Rev. Fluid Mech. **20**, 111-157 (1988).

Brady, J.F., "Brownian motion, hydrodynamics, and the osmotic pressure." J. Chem. Phys. **98**, 3335–3341 (1993a).

Brady, J.F., "The rheological behavior of concentrated colloidal dispersions." J. Chem. Phys. **99**, 567–581 (1993b).

Brady, J.F., "The long-time self-diffusivity in concentrated colloidal dispersions." J. Fluid Mech. **272**, 109–133 (1994).

Brady, J.F. & M. Vicic, "Normal stresses in colloidal dispersions." J. Rheol. **39**, 545–566 (1995).

Brady, J.F. "Model hard-sphere dispersions: Statistical mechanical theory, simulations, and experiments." Curr. Op. Coll. & Int. Sci. **1**, 472–480 (1996).

Brady, J.F. & J.F. Morris, "Microstructure of strongly-sheared suspensions and its impact on rheology and diffusion." J. Fluid Mech. **348**, 103–139 (1997).

Buscall, R., "An effective hard-sphere model of the non-Newtonian viscosity of stable colloidal dispersions: Comparison with further data for sterically stabilised latices and with data for microgel particles." Coll. & Surf. A: Physic. & Eng. Aspects **83**, 33–42 (1994).

Carnahan, N.F. & K.E. Starling, "Equation of state for nonattracting rigid spheres." J. Chem. Phys. **51**, 635–636 (1969).

Chan, D. & R.L. Powell, "Rheology of suspensions of spherical particles in a Newtonian and a non-Newtonian fluid." J. Non-Newt. Fluid Mech. **15**, 165–179 (1984).

Chow, A.W., S.W. Sinton, J.H. Iwamiya & T.S. Stephens, "Shear-induced particle migration in couette and parallel-plate viscometers — NMR imaging and stress measurements." Phys. Fluids **6**, 2561–2576 (1994).

de Kruif, C.G., E.M.F. van Iersel, A. Vrij & W.B. Russel, "Hard sphere colloidal dispersions: Viscosity as a function of shear rate and volume fraction." J. Chem. Phys. **83**, 4717–4725 (1985).

D'Haene, P., "Rheology of polymerically stabilized suspensions." Ph.D. Thesis, Katholieke Universiteit Leuven (1992).

D'Haene, P., J. Mewis & G.G. Fuller, "Scattering dichroism measurements of flow-induced structure of a shear thickening suspension." J. Coll. & Int. Sci. **156**, 350–358 (1993).

Dhont, J.K.G., "On the distortion of the static structure factor of colloidal fluids in shear flow." J. Fluid Mech. **204**, 421–431 (1989).

Elrick, D.E., "Source functions for diffusion in uniform shear flow." Aust. J. Phys. **15**, 283–288 (1962).

Foss, D.R., T.N. Phung, J.F. Brady & G. Bossis, "Stokesian Dynamics simulation of Brownian suspensions." in preparation (1999).

Foss, D.R. & J.F. Brady, "Brownian Dynamics simulation of hard-sphere colloidal dispersions." in preparation (1999).

Foss, D.R., Ph.D. Thesis, California Institute of Technology (1999).

Gadala-Maria, F., "The rheology of concentrated suspensions." Ph.D. Thesis, Stanford University (1979).

Genz, U., B. D'Aguanno, J. Mewis & R. Klein, "Structure of sterically stabilized colloids." Langmuir **10**, 2206–2212 (1994).

Heyes, D.M. & J.R. Melrose, "Brownian dynamics simulations of model hard-sphere suspensions." J. Non-Newt. Fluid Mech. **46**, 1–28 (1993).

Heyes, D.M., P.J. Mitchell, P.B. Visscher & J.R. Melrose, "Brownian Dynamics simulation of concentrated dispersions: Viscoelasticity and near-Newtonian behaviour." J. Chem. Soc. Faraday Trans. **90**, 1133–1141 (1994).

Heyes, D.M. & P.J. Mitchell, "Mean-field hydrodynamic Brownian dynamics simulations of stabilized colloidal liquids under shear." J. Non-Newt. Fluid Mechn. **68**, 101–124 (1997).

Hoffman, R.L., "Explanations for the cause of shear thickening in concentrated colloidal dispersions." J. Rheol. **42**, 111–123 (1998).

Jeffrey, D.J., J.F. Morris & J.F. Brady, "The pressure moments for two rigid spheres in low-Reynolds-number flow." Phys. Fluids A **5**, 2317–2325 (1993).

Jomha, A.I. & P.A. Reynolds, "An experimental study of the first normal stress difference — shear stress relationship in simple shear flow for concentrated shear thickening suspensions." Rheol. Acta **32**, 457–464 (1993).

Jones, D.A.R., B. Leary & D.V. Boger, "The rheology of concentrated colloidal suspensions of hard spheres." J. Coll. & Int. Sci. **147**, 479–495 (1991).

Kaffashi, B., V.T. O'Brien, M.E. Mackay & S.M. Underwood, "Elastic-like and viscous-like components of the shear viscosity for nearly hard-sphere, Brownian suspensions." J. Coll. & Int. Sci. **187**, 22–28 (1997).

Kalogrianitis, S.G. & J.W. van Egmond, "Full tensor optical rheometry of polymer fluids." J. Rheol. **41**, 343–364 (1997).

Kim, S. & R.T. Mifflin, "The resistance and mobility functions of two equal spheres in low-Reynolds-number flow." Phys. Fluids **28**, 2033–2045 (1985).

Kim, S. & S.J. Karrila, *Microhydrodynamics: Principles and selected applications* (Butterworth-Heinemann, Boston, 1991).

Krieger, I.M., "Rheology of monodisperse latices." Adv. Coll. & Int. Sci. **3**, 111–136 (1972).

Ladd, A.J.C., "Fluctuating lattice-Boltzmann equation." Phys. Rev. Lett. **70**, 1339–1342 (1993).

Ladd, A.J.C., "Numerical simulations of particulate suspensions via a discretized Boltzmann-equation. 1. Theoretical foundations." J. Fluid Mech. **271**, 285–309 (1994a).

Ladd, A.J.C., "Numerical simulations of particulate suspensions via a discretized Boltzmann-equation. 2. Numerical results." J. Fluid Mech. **271**, 311–339 (1994b).

Laun, H.M., "Normal stresses in extremely shear thickening polymer dispersions." J. Non-Newt. Fluid Mech. **54**, 87–108 (1994).

Leal, L.G., *Laminar flow and convective transport processes: Scaling principles and asymptotic analysis* (Butterworth-Heinemann, Boston, 1992).

Leighton, D.T., personal communication (1997).

Lionberger, R.A., "Shear thinning in colloidal dispersions." J. Rheol. **42**, 843–863 (1998).

Lodge, A.S., J.D. Schieber & R.B. Bird, "The Weissenberg effect at finite rod-rotation speeds." J. Chem. Phys. **88**, 4001–4007 (1988).

Mackay, M.E., C.H. Liang & P.J. Halley, "Instrument effects on stress jump measurements." Rheol. Acta **31**, 481–489 (1992).

Magda, J.J., S.G. Baek, K.L. DeVries & R.G. Larson, "Unusual pressure profiles and fluctuations during shear flows of liquid crystal polymers." Polymer **32**, 1794–1797 (1991).

Mallamace, F., N. Micali & C. Vasi, "Viscoelastic properties of charged colloids, polystyrene, and silica-water suspensions." Phys. Rev. A **42**, 7304–7311 (1990).

Marrucci, G., "Rheology of liquid crystalline polymers; linear and nonlinear behavior of the nematic phase." in *Theoretical challenges in the dynamics of complex fluids* (Kluwer Academic, Dordrecht, 1997).

McQuarrie, D.A., *Quantum chemistry* (University Science Books, Mill Valley, CA, 1983).

Mitchell, P.J., D.M. Heyes & J.R. Melrose, "Brownian-dynamics simulations of model stabilised colloidal dispersions under shear." J. Chem. Soc. Faraday Trans. **91**, 1975–1989 (1995).

Nagele, G., B. Steininger, U. Genz & R. Klein, "Short-time dynamics of charge-stabilized colloidal suspensions." Physica Scripta **T55**, 119–126 (1994).

Nolan, G.T. & P.E. Kavanagh, "Computer simulation of random packing of hard spheres." Powder Tech. **72**, 149–155 (1992).

O'Brien, V.T. & M.E. Mackay, "Stress components and shear thickening of hard sphere suspensions," personal communication (1996).

Ogawa, A., H. Yamada, S. Matsuda, K. Okajima & M. Doi, "Viscosity equation for concentrated suspensions of charged colloidal particles." J. Rheol. **41**, 769–785 (1997).

Ohl, N. & W. Gleissle, "The characterization of the steady-state shear and normal stress functions of highly concentrated suspensions formulated with viscoelastic liquids." J. Rheol. **37**, 381–406 (1993).

Okubo, T., "The viscosity of colloidal spheres in deionized suspensions." J. Chem. Phys. **87**, 6733–6739 (1987).

Phung, T.N., J.F. Brady & G. Bossis, "Stokesian Dynamics simulation of Brownian suspensions." J. Fluid Mech. **313**, 181–207 (1996).

Poslinski, A.J., M.E. Ryan, R.K. Gupta, S.G. Seshadri & F.J. Frechette, "Rheological behavior of filled polymeric systems. I. Yield stress and shear-thinning effects." J. Rheol. **32**, 703–735 (1988).

Press, W.H., S.A. Teukolsky, W.T. Vetterling & B.P. Flannery, *Numerical recipes in Fortran: The art of scientific computing* (Cambridge University Press, 2nd edition, 1992).

Pusey, P.N. & W. van Megen, in *An Exxon monograph: Physics of complex fluids and supermolecular fluids* (Wiley-Interscience, New York, 1987).

Quemada, D., "Concentrated colloidal suspensions at low ionic strength: a hard-sphere model of zero shear viscosity, involving the hard-sphere phase transitions." Europhys. Lett. **25**, 149–155 (1994).

Rastogi, S.R., N.J. Wagner & S.R. Lustig, "Rheology, self-diffusion, and microstructure of charged colloids under simple shear by massively parallel nonequilibrium Brownian Dynamics." J. Chem. Phys. **104**, 9234–9248 (1996).

Rastogi, S.R. & N.J. Wagner, "Quantitative predictions of suspension rheology by nonequilibrium Brownian dynamics and hydrodynamic preaveraging." J. Rheol. **41**, 893–899 (1997).

Reus, V., L. Belloni, T. Zemb, N. Lutterbach & H. Versmold, "Spectres de diffusion et pression osmotique de suspensions colloïdales de particules de latex chargées." J. Chim. Phys. **92**, 1233–1256 (1995).

Ronis, D., "Theory of fluctuations in colloidal suspensions undergoing steady shear flow." Phys. Rev. A **29**, 1453–1460 (1984).

Ronis, D., "Configurational viscosity of dilute colloidal suspensions." Phys. Rev. A **34**, 1472–1480 (1986).

Smart, J.R. & D.T. Leighton, "Measurement of the hydrodynamic surface-roughness of noncolloidal spheres." Phys. Fluids A **1**, 52–60 (1989).

van der Werff, J.C., C.G. de Kruif & J.K.G. Dhont, "The shear-thinning behaviour of colloidal dispersions. II. Experiments." Physica A **160**, 205–212 (1989).

Wagner, N.J., personal communication (1998).

Willey, S.J. & C.W. Macosko, "Steady shear rheological behavior of PVC plasticols." J. Rheol. **22**, 525–545 (1978).

Woodcock, L.V., "Glass transition in the hard sphere model and Kauzman's paradox." Ann. N.Y. Acad. Sci. **37**, 274–298 (1981).

Appendix A:

Definite integral of the product of two Associated Legendre Polynomials and most powers of sine and cosine

The result of this section is used to evaluate the integrals in the Smoluchowski equation for a general linear flow after the nonequilibrium microstructure has been expanded in terms of surface spherical harmonics and integration is performed using the orthogonality property of the harmonics. There are angularly-dependent terms remaining in the Smoluchowski equation that cannot be immediately integrated and must be numerically integrated in a general way since the integrand is dependent on the type of flow as well as the rank and order of the harmonic. The method presented here has been successfully used for all four rheologically significant flows—simple shear flow, planar extensional flow, biaxial extensional flow and uniaxial extensional flow. Since the numerical scheme is new, a proof of the validity of the scheme is presented here. The main advantage of this method is that many of the integrals which are zero are immediately recognized, thus eliminating time-intensive, numerical integration.

If ℓ is an integer such that $\ell \geq 0$,

m is an integer such that $|m| \leq \ell$,

p is an integer such that $p \geq 0$,

q is an integer such that $|q| \leq q$,

α is an integer,

β is an integer such that $\beta > |q| - |m| - 2$ and $\beta + |m| + |q|$ is even,

then $$\int_{-1}^{1} \mu^{\alpha} \left(1-\mu^2\right)^{\beta/2} P_{\ell}^{|m|}(\mu) P_{p}^{|q|}(\mu) d\mu =$$

$$\sum_{k=0}^{\lfloor \ell/2 - |m|/2 \rfloor} \sum_{j=0}^{\min[\gamma, \lfloor \eta/2 - k \rfloor]} \sum_{i=0}^{\eta-2k-2j} \frac{(-1)^{k+|q|+\gamma-j} (2\ell-2k)!}{2^{\ell} k! (\ell-k)! (\ell-2k-|m|)!} \times \binom{\gamma}{j} \frac{(\eta+|q|-2k-2j)!}{(\eta-2k-2j)!} \frac{2}{2p+1} a_i \delta_{ip},$$

where $\mu = \cos[\theta]$,

$P_{\ell}^{|m|}(\mu)$ is the Associated Legendre Polynomial of rank ℓ, order m,

$\lfloor x \rfloor$ is the integer floor of x,

$\min[x, y]$ is the minimum of x and y,

$\eta = \alpha + \beta + \ell$,

$\gamma = \frac{1}{2}(\beta + |m| + |q|)$,

$$\binom{\gamma}{j} = \frac{\gamma!}{j!(\gamma-j)!},$$

$$\delta_{ip} = \begin{cases} 1, & \text{if } i = p; \\ 0, & \text{otherwise.} \end{cases}$$

$$a_i = \begin{cases} \frac{(2i+1)2^i(\eta-2k-2j)!}{(\eta-2k-2j+i+1)!} \frac{\left(\frac{1}{2}(\eta-2k-2j+i)\right)!}{\left(\frac{1}{2}(\eta-2k-2j-i)\right)!}, & \text{if } \eta-2k-2j-i \geq 0 \text{ and even;} \\ 0, & \text{otherwise.} \end{cases}$$

Proof

We start by defining the following function

$$I = I(\alpha, \beta, \ell, m, p, q) = \int_{-1}^{1} \mu^{\alpha} \left(1 - \mu^2\right)^{\beta/2} P_{\ell}^{|m|}(\mu) P_{p}^{|q|}(\mu) d\mu. \tag{A.1}$$

Recall the definition of the Associated Legendre Polynomial [McQuarrie (1983)],

$$P_{\ell}^{|m|}(\mu) = \left(1 - \mu^2\right)^{|m|/2} \frac{d^{|m|} P_{\ell}(\mu)}{d\mu^{|m|}}. \tag{A.2}$$

Substituting this definition into equation [A.1],

$$\begin{aligned} I = & \int_{-1}^{1} \mu^{\alpha} \left(1 - \mu^2\right)^{\beta/2} \left(1 - \mu^2\right)^{|m|/2} \\ & \times \frac{d^{|m|} P_{\ell}(\mu)}{d\mu^{|m|}} \left(1 - \mu^2\right)^{|q|/2} \frac{d^{|q|} P_{p}(\mu)}{d\mu^{|q|}} d\mu. \end{aligned} \tag{A.3}$$

At this point we define a new variable,

$$\gamma = \frac{1}{2}\left(\beta + |m| + |q|\right). \tag{A.4}$$

It should be noted that γ is *always* an integer since $\beta + |m| + |q|$ is even, as stated in the hypothesis. We shall require the fact that γ is an integer later in this proof.

Before we continue, we need to make a few comments about the restrictions on $|q|$ and $|m|$. If $|q| > p$ or $|m| > \ell$, then the Associated Legendre Polynomial is identically zero; so $I = 0$. For the remainder of this proof, we shall only consider $|q| \leq p$ and $|m| \leq \ell$, as per the hypothesis.

If $|q| > 0$, then we define the following two variables for integration by parts:

$$u = \mu^{\alpha} \left(1 - \mu^2\right)^{\gamma} \frac{d^{|m|} P_{\ell}(\mu)}{d\mu^{|m|}}, \tag{A.5}$$

$$dv = \frac{d}{d\mu}\left(\frac{d^{|q|-1} P_{p}(\mu)}{d\mu^{|q|-1}}\right) d\mu. \tag{A.6}$$

Using these definitions, we integrate by parts if $|q| > 0$. We do nothing if $|q| = 0$.

Equation [A.3] yields:

$$I = \left(\mu^{\alpha}\left(1-\mu^{2}\right)^{\gamma}\frac{d^{|m|}P_{\ell}(\mu)}{d\mu^{|m|}}\right)\frac{d^{|q|-1}P_{p}(\mu)}{d\mu^{|q|-1}}\Bigg|_{-1}^{1}$$
$$-\int_{-1}^{1}\frac{d}{d\mu}\left(\mu^{\alpha}\left(1-\mu^{2}\right)^{\gamma}\frac{d^{|m|}P_{\ell}(\mu)}{d\mu^{|m|}}\right)$$
$$\times\frac{d^{|q|-1}P_{p}(\mu)}{d\mu^{|q|-1}}d\mu, \text{ if } 0<|q|\leq p; \tag{A.7a}$$

$$I = \int_{-1}^{1}\mu^{\alpha}\left(1-\mu^{2}\right)^{\gamma}\frac{d^{|m|}P_{\ell}(\mu)}{d\mu^{|m|}}P_{p}(\mu)d\mu, \text{ if } |q|=0. \tag{A.7b}$$

If $0<|q|\leq p$, we continue to integrate by parts for a total of $|q|$ times for equation [A.7]. In addition, we rewrite equation [A.7].

$$I = \sum_{k=0}^{|q|-1}(-1)^{k}\frac{d^{k}}{d\mu^{k}}\left(\mu^{\alpha}\left(1-\mu^{2}\right)^{\gamma}\frac{d^{|m|}P_{\ell}(\mu)}{d\mu^{|m|}}\right)\frac{d^{|q|-k-1}P_{p}(\mu)}{d\mu^{|q|-k-1}}\Bigg|_{-1}^{1}$$
$$+(-1)^{|q|}\int_{-1}^{1}\frac{d^{|q|}}{d\mu^{|q|}}\left(\mu^{\alpha}\left(1-\mu^{2}\right)^{\gamma}\frac{d^{|m|}P_{\ell}(\mu)}{d\mu^{|m|}}\right)$$
$$\times P_{p}(\mu)d\mu, \text{ if } 0<|q|\leq p; \tag{A.8a}$$

$$I = (-1)^{|q|}\int_{-1}^{1}\frac{d^{|q|}}{d\mu^{|q|}}\left(\mu^{\alpha}\left(1-\mu^{2}\right)^{\gamma}\frac{d^{|m|}P_{\ell}(\mu)}{d\mu^{|m|}}\right)$$
$$\times P_{p}(\mu)d\mu, \text{ if } |q|=0. \tag{A.8b}$$

If $\beta > |q|-|m|-2$, then all of the terms in the summation in equation [A.8] vanish. (This statement is proved in Lemma 1 immediately following this proof.) Since the summation in equation [A.8] vanishes, equations [A.8] and [A.8] can be combined into a single equation,

$$I = (-1)^{|q|}\int_{-1}^{1}\frac{d^{|q|}}{d\mu^{|q|}}\left(\mu^{\alpha}\left(1-\mu^{2}\right)^{\gamma}\frac{d^{|m|}P_{\ell}(\mu)}{d\mu^{|m|}}\right)P_{p}(\mu)d\mu, \text{ if } |q|\leq p. \tag{A.9}$$

In Lemma 2 it is shown that

$$\frac{d^{|m|}P_\ell(\mu)}{d\mu^{|m|}} = \sum_{k=0}^{\lfloor \ell/2-|m|/2 \rfloor} \frac{(-1)^k (2\ell-2k)!}{2^\ell k!\,(\ell-k)!\,(\ell-2k-|m|)!}\mu^{\ell-2k-|m|}. \tag{A.10}$$

Substituting equation [A.10] into equation [A.9],

$$I = (-1)^{|q|}\int_{-1}^{1} \frac{d^{|q|}}{d\mu^{|q|}}\left(\mu^\alpha\left(1-\mu^2\right)^\gamma \cdot \times \sum_{k=0}^{\lfloor \ell/2-|m|/2 \rfloor} \frac{(-1)^k (2\ell-2k)!}{2^\ell k!\,(\ell-k)!\,(\ell-2k-|m|)!}\mu^{\ell-2k-|m|}\right) P_p(\mu)d\mu. \tag{A.11}$$

We perform the following operations to equation [A.11]: (1) distribute the factors of μ and $(1-\mu^2)$ into the summation, (2) exchange differentiation and summation since the sum is uniformly convergent and the sum of the derivatives of the terms is also uniformly convergent, and (3) exchange summation and integration since the sum is uniformly convergent and the sum of the integrals is also uniformly convergent,

$$I = \sum_{k=0}^{\lfloor \ell/2-|m|/2 \rfloor} \frac{(-1)^{k+|q|} (2\ell-2k)!}{2^\ell k!\,(\ell-k)!\,(\ell-2k-|m|)!} \times \int_{-1}^{1} \frac{d^{|q|}}{d\mu^{|q|}}\left(\mu^{\alpha+\ell-2k-|m|}\left(1-\mu^2\right)^\gamma\right) P_p(\mu)d\mu. \tag{A.12}$$

In Lemma 3 it is shown that

$$\frac{d^{|q|}}{d\mu^{|q|}}\left(\mu^{\alpha+\ell-2k-|m|}\left(1-\mu^2\right)^\gamma\right) = \sum_{j=0}^{\min[\gamma,\lfloor \eta/2-k \rfloor]} (-1)^{\gamma-j}\binom{\gamma}{j}\frac{(\eta+|q|-2k-2j)!}{(\eta-2k-2j)!}\mu^{\eta-2k-2j}. \tag{A.13}$$

We substitute equation [A.13] into equation [A.12] and then perform the following operations: (1) distribute $P_p(\mu)$ through the summation, (2) interchange summation and integration because of uniform convergence and (3) distribute terms through the

summation,

$$I = \sum_{k=0}^{\lfloor \ell/2-|m|/2 \rfloor} \sum_{j=0}^{\min[\gamma,\lfloor \eta/2-k \rfloor]} \frac{(-1)^{k+|q|+\gamma-j}\,(2\ell-2k)!}{2^{\ell} k!\,(\ell-k)!\,(\ell-2k-|m|)!} \times \binom{\gamma}{j} \frac{(\eta+|q|-2k-2j)!}{(\eta-2k-2j)!} \int_{-1}^{1} \mu^{\eta-2k-2j} P_p(\mu) d\mu. \tag{A.14}$$

Any nth degree polynomial can be expressed as a linear combination of the first n Legendre Polynomials since the first n Legendre Polynomials form a basis for n-dimensional polynomial space. We have the following result from [Whittaker & Watson (1992)],

$$\mu^n = \sum_{i=0}^{n} a_i P_i(\mu), \tag{A.15a}$$

$$a_i = \begin{cases} \frac{(2i+1)2^i(n)!}{(n+i+1)!} \frac{\left(\frac{1}{2}(n+i)\right)!}{\left(\frac{1}{2}(n-i)\right)!}, & \text{if } n-i \text{ is even and non-negative;} \\ 0, & \text{otherwise.} \end{cases} \tag{A.15b}$$

We let $n = \eta - 2k - 2j$ in equation [A.15] and substitute the result into equation [A.14],

$$I = \sum_{k=0}^{\lfloor \ell/2-|m|/2 \rfloor} \sum_{j=0}^{\min[\gamma,\lfloor \eta/2-k \rfloor]} \frac{(-1)^{k+|q|+\gamma-j}\,(2\ell-2k)!}{2^{\ell} k!\,(\ell-k)!\,(\ell-2k-|m|)!} \binom{\gamma}{j} \times \frac{(\eta+|q|-2k-2j)!}{(\eta-2k-2j)!} \int_{-1}^{1} \left(\sum_{i=0}^{\eta-2k-2j} a_i P_i(\mu) \right) P_p(\mu)\, d\mu. \tag{A.16}$$

We now perform the following operations on equation [A.16]: (1) distribute $P_p(\mu)$ into the summation, (2) interchange summation and integration since the terms are uniformly convergent, and (3) remove a_i from the integral,

$$I = \sum_{k=0}^{\lfloor \ell/2-|m|/2 \rfloor} \sum_{j=0}^{\min[\gamma,\lfloor \eta/2-k \rfloor]} \sum_{i=0}^{\eta-2k-2j} \frac{(-1)^{k+|q|+\gamma-j}\,(2\ell-2k)!}{2^{\ell} k!\,(\ell-k)!\,(\ell-2k-|m|)!} \times \binom{\gamma}{j} \frac{(\eta+|q|-2k-2j)!}{(\eta-2k-2j)!} a_i \int_{-1}^{1} P_i(\mu)\, P_p(\mu)\, d\mu. \tag{A.17}$$

Finally, we use the orthogonality property of Legendre Polynomials [Tuma (1987)],

$$\int_{-1}^{1} P_i(\mu)\, P_p(\mu)\, d\mu = \frac{2}{2p+1}\delta_{ip}, \tag{A.18}$$

where δ_{ip} is the Kronecker delta, in equation [A.17],

$$I = \sum_{k=0}^{\lfloor \ell/2-|m|/2 \rfloor} \sum_{j=0}^{\min[\gamma,\lfloor \eta/2-k \rfloor]} \sum_{i=0}^{\eta-2k-2j} \frac{(-1)^{k+|q|+\gamma-j}\,(2\ell-2k)!}{2^{\ell} k!\,(\ell-k)!\,(\ell-2k-|m|)!} \times \binom{\gamma}{j} \frac{(\eta+|q|-2k-2j)!}{(\eta-2k-2j)!} \frac{2}{2p+1} a_i \delta_{ip}. \tag{A.19}$$

Lemma 1

Hypothesis

If ℓ is an integer such that $\ell \geq 0$,

m is an integer such that $|m| \leq \ell$,

p is an integer such that $p \geq 0$,

q is an integer such that $|q| \leq q$,

k is an integer such that $k0 \leq k \leq |q| - 1$,

β is an integer such that $\beta > |q| - |m| - 2$ and $\beta + |m| + |q|$ is even,

then $\dfrac{d^k}{d\mu^k}\left(\mu^{\alpha}\left(1-\mu^2\right)^{\gamma} \dfrac{d^{|m|}P_{\ell}(\mu)}{d\mu^{|m|}}\right) = 0$ at $\mu = \pm 1\ \forall k$.

Proof

We start with the following,

$$\frac{d^k}{d\mu^k}\left(\mu^{\alpha}\left(1-\mu^2\right)^{\gamma} \frac{d^{|m|}P_{\ell}(\mu)}{d\mu^{|m|}}\right). \tag{A.20}$$

We twice use Liebnitz' Rule of Differentiation [Tuma (1987)],

$$D^n(uv) = \sum_{r=0}^{n} \binom{n}{r} \left(D^{n-r}u\right)\left(D^r v\right), \tag{A.21}$$

on equation [A.20],

$$\frac{d^k}{d\mu^k}\left(\mu^\alpha\left(1-\mu^2\right)^\gamma\frac{d^{|m|}P_\ell(\mu)}{d\mu^{|m|}}\right)=$$
$$\sum_{r=0}^{k}\binom{k}{r}\frac{d^{k-r}}{d\mu^{k-r}}\left(\mu^\alpha\left(1-\mu^2\right)^\gamma\right)\frac{d^{|m|+r}P_\ell(\mu)}{d\mu^{|m|+r}}, \tag{A.22}$$
$$\frac{d^{k-r}}{d\mu^{k-r}}\left(\mu^\alpha\left(1-\mu^2\right)^\gamma\right)=$$
$$\sum_{t=0}^{k-r}\binom{k-r}{t}\frac{d^{k-r-t}\mu^\alpha}{d\mu^{k-r-t}}\frac{d^t\left(1-\mu^2\right)^\gamma}{d\mu^t}. \tag{A.23}$$

Combining these last two results, equations [A.22] and [A.23],

$$\frac{d^k}{d\mu^k}\left(\mu^\alpha\left(1-\mu^2\right)^\gamma\frac{d^{|m|}P_\ell(\mu)}{d\mu^{|m|}}\right)=$$
$$\sum_{r=0}^{k}\sum_{t=0}^{k-r}\binom{k}{r}\binom{k-r}{t}\frac{d^{k-r-t}\mu^\alpha}{d\mu^{k-r-t}}\frac{d^t\left(1-\mu^2\right)^\gamma}{d\mu^t}\frac{d^{|m|+r}P_\ell(\mu)}{d\mu^{|m|+r}}. \tag{A.24}$$

We notice that the middle derivative in the double summation equals zero when evaluated at $\mu=\pm1$ for some values of t and γ. If we can show that the middle term equals zero when evaluated at $\mu=\pm1$ for all possible values of t and γ, as specified in the hypothesis, then we have shown that the conclusion is true.

From the second summation, we see that $\max[t]=k-r$. But from the first summation, we see that $0\le r\le k$ and $\min[r]=0$; therefore, $\max[t]=k$ since $k>0$. But from the hypothesis we see that $\max[k]=|q|-1$; thus, $\max[t]=|q|-1$.

By the hypothesis and the definition for γ, we conclude that

$$\beta>|q|-|m|-2\mapsto\gamma>|q|-1. \tag{A.25}$$

But we have shown that $\max[t]=|q|-1$; therefore,

$$\gamma>\max[t]. \tag{A.26}$$

Since γ is an integer and $\gamma > \max[t]$, the following is true,

$$\frac{d^t\left(1-\mu^2\right)^\gamma}{d\mu^t} = (-2\mu)^t \frac{\gamma!}{(\gamma-t)!}\left(1-\mu^2\right)^{\gamma-t} + \sum_{w=1}^{t} f_w(\mu)\left(1-\mu^2\right)^{\gamma-t+w}, \tag{A.27}$$

where $f_w(\mu)$ is some function of μ. (The exact form of the function is not important for this lemma.) Since $\gamma > \max[t]$, we see that the following is true,

$$\left(1-\mu^2\right)^{\gamma-t} = 0 \text{ at } \mu = \pm 1 \ \forall t. \tag{A.28}$$

Since $w > 0$, we can also say that the following is true,

$$\left(1-\mu^2\right)^{\gamma-t+w} = 0 \text{ at } \mu = \pm 1 \ \forall t, w. \tag{A.29}$$

Using the last two results, equations [A.28] and [A.29], we conclude that the middle derivative in equation [A.24] is equal to zero when evaluated at $\mu = \pm 1$ for all values of t and γ; thus,

$$\frac{d^k}{d\mu^k}\left(\mu^\alpha\left(1-\mu^2\right)^\gamma \frac{d^{|m|}P_\ell(\mu)}{d\mu^{|m|}}\right) = 0 \text{ at } \mu = \pm 1 \ \forall k. \tag{A.30}$$

Lemma 2

Hypothesis

If ℓ is an integer such that $\ell \geq 0$,

m is an integer such that $|m| \leq \ell$,

k is an integer such that $0 \leq k \leq |q| - 1$,

then $$\frac{d^{|m|}P_\ell(\mu)}{d\mu^{|m|}} = \sum_{k=0}^{\lfloor \ell/2 - |m|/2 \rfloor} \frac{(-1)^k (2\ell-2k)!}{2^\ell k!\,(\ell-k)!\,(\ell-2k-|m|)!}\mu^{\ell-2k-|m|}.$$

Proof

We start with the series representation for the ℓth Legendre Polynomial [Zill (1986)],

$$P_\ell(\mu) = \sum_{k=0}^{\lfloor \ell/2 \rfloor} \frac{(-1)^k (2\ell - 2k)!}{2^\ell k! (\ell - k)! (\ell - 2k)!} \mu^{\ell - 2k}, \tag{A.31}$$

where $\lfloor x \rfloor$ is the integer floor of x (i.e., the greatest integer not greater than x).

We now take the $|m|$th derivative of both sides of equation [A.31]. Furthermore, we interchange summation and differentiation because the series is uniformly convergent,

$$\frac{d^{|m|} P_\ell(\mu)}{d\mu^{|m|}} = \sum_{k=0}^{\lfloor \ell/2 \rfloor} \frac{(-1)^k (2\ell - 2k)!}{2^\ell k! (\ell - k)! (\ell - 2k)!} \frac{d^{|m|} \mu^{\ell - 2k}}{d\mu^{|m|}}. \tag{A.32}$$

Since m, ℓ, k are all integers, $|m| \leq 1$ (by the hypothesis), and $k \leq \lfloor \ell/2 \rfloor$ (based on the upper limit of the summation), then $\ell - 2k - |m| \geq 0$; thus, the $|m|$th derivative will have one of two values,

$$\frac{d^{|m|} \mu^{\ell - 2k}}{d\mu^{|m|}} = \begin{cases} \frac{(\ell - 2k)!}{(\ell - 2k - |m|)!} \mu^{\ell - 2k - |m|}, & \text{if } \ell - 2k - |m| \geq 0 \ ; \\ 0, & \text{otherwise.} \end{cases} \tag{A.33}$$

Since k must be an integer and the sum $\ell + |m|$ is not necessarily an even integer, then we can be more specific about the range of the non-zero values of the $|m|$th derivative. Rewriting equation [A.33],

$$\frac{d^{|m|} \mu^{\ell - 2k}}{d\mu^{|m|}} = \begin{cases} \frac{(\ell - 2k)!}{(\ell - 2k - |m|)!} \mu^{\ell - 2k - |m|}, & \text{if } k \leq \lfloor \ell/2 - |m|/2 \rfloor \ ; \\ 0, & \text{otherwise.} \end{cases} \tag{A.34}$$

Finally, we split the summation in equation [A.32] into two ranges, $0 \leq k \leq \lfloor \ell/2 - |m|/2 \rfloor$ and $\lfloor \ell/2 - |m|/2 \rfloor + 1 \leq k \leq \lfloor \ell/2 \rfloor$, and use the results from equation [A.34],

$$\frac{d^{|m|} P_\ell(\mu)}{d\mu^{|m|}} = \sum_{k=0}^{\lfloor \ell/2 - |m|/2 \rfloor} \frac{(-1)^k (2\ell - 2k)!}{2^\ell k! (\ell - k)! (\ell - 2k - |m|)!} \mu^{\ell - 2k - |m|}. \tag{A.35}$$

Lemma 3

Hypothesis

If ℓ is an integer such that $\ell \geq 0$,

m is an integer such that $|m| \leq \ell$,

p is an integer such that $p \geq 0$,

q is an integer such that $|q| \leq q$,

k is an integer such that $k \geq 0$,

α is an integer such that $\alpha \geq 0$,

β is an integer such that $\beta > |q| - |m| - 2$ and $\beta + |m| + |q|$ is even,

$\gamma = (\beta + |m| + |q|)/2$,

then $$\frac{d^{|q|}}{d\mu^{|q|}}\left(\mu^{\alpha+\ell-2k-|m|}\left(1-\mu^2\right)^{\gamma}\right) = \sum_{j=0}^{\min[\gamma,\lfloor \eta/2-k \rfloor]} (-1)^{\gamma-j}\binom{\gamma}{j}\frac{(\alpha+\beta+\ell+|q|-2k-2j)!}{(\alpha+\beta+\ell-2k-2j)!}\mu^{\alpha+\beta+\ell-2k-2j}.$$

Proof

We begin by using the binomial theorem to expand $(1-\mu^2)^{\gamma}$ in a series of polynomials of μ. Note that the series truncates at $j = \gamma$ since γ is an integer.

$$\left(1-\mu^2\right)^{\gamma} = \sum_{j=0}^{\gamma}(-1)^{\gamma-j}\binom{\gamma}{j}\mu^{2\gamma-2j}. \tag{A.36}$$

We multiply both sides of equation [A.36] by $\mu^{\alpha+\ell-2k-|m|}$ and multiply through the summation on the left-hand side,

$$\mu^{\alpha+\ell-2k-|m|}\left(1-\mu^2\right)^{\gamma} = \sum_{j=0}^{\gamma}(-1)^{\gamma-j}\binom{\gamma}{j}\mu^{2\gamma-2j+\alpha+\ell-2k-|m|}. \tag{A.37}$$

Recall that $2\gamma = \beta + |m| + |q|$ from the hypothesis and substitute into equation

[A.37],

$$\mu^{\alpha+\ell-2k-|m|}\left(1-\mu^2\right)^{\gamma}=\sum_{j=0}^{\gamma}(-1)^{\gamma-j}\binom{\gamma}{j}\mu^{\alpha+\beta+\ell+|q|-2k-2j}. \tag{A.38}$$

At this point we need to make sure that the exponent of μ is non-negative on the right-hand side of equation [A.38]. We show that the exponent is non-negative if $\alpha \geq 0$.

$$\begin{aligned}
&\alpha+\beta+\ell+|q|-2k-2j\geq 0,\\
&j_{\max}=\gamma \text{ from the summation},\\
&\alpha+\beta+\ell+|q|-2k-2\gamma\geq 0,\\
&2\gamma=\beta+|m|+|q| \text{ from the hypothesis},\\
&\alpha+\ell-|m|-2k\geq 0,\\
&k_{\max}=(\ell-|m|)/2 \text{ from equation [A.35]},\\
&\alpha\geq 0.
\end{aligned}$$

Since $\alpha \geq 0$ is part of the hypothesis, the exponent of μ on the right-hand side of equation [A.38] is non-negative.

Since the exponent of μ is non-negative in equation [A.38], we can take the qth derivative of both sides. We also interchange differentiation and summation because of uniform convergence,

$$\frac{d^{|q|}}{d\mu^{|q|}}\left(\mu^{\alpha+\ell-2k-|m|}\left(1-\mu^2\right)^{\gamma}\right)=\sum_{j=0}^{\gamma}(-1)^{\gamma-j}\binom{\gamma}{j}\frac{d^{|q|}}{d\mu^{|q|}}\mu^{\alpha+\beta+\ell+|q|-2k-2j}. \tag{A.39}$$

Since the integer of μ in the summation is an integer, we know that the $|q|$th derivative has one of two values,

$$\begin{aligned}
&\frac{d^{|q|}\mu^{\alpha+\beta+\ell+|q|-2k-2j}}{d\mu^{|q|}}=\\
&\begin{cases}
\frac{(\alpha+\beta+\ell+|q|-2k-2j)!}{(\alpha+\beta+\ell-2k-2j)!}\mu^{\alpha+\beta+\ell-2k-2j}, & \text{if } |q|\leq \alpha+\beta+\ell+|q|-2k-2j\\
0, & \text{if } |q|>\alpha+\beta+\ell+|q|-2k-2j.
\end{cases}
\end{aligned} \tag{A.40}$$

We subtract $|q|$ from both sides of the inequalities in equation [A.40] and solve explicitly for j. Furthermore, since j only has integer values, we can take the integer floor of each term on the right-hand side of the inequalities without affecting the result,

$$\frac{d^{|q|}\mu^{\alpha+\beta+\ell+|q|-2k-2j}}{d\mu^{|q|}} = \begin{cases} \frac{(\alpha+\beta+\ell+|q|-2k-2j)!}{(\alpha+\beta+\ell-2k-2j)!}\mu^{\alpha+\beta+\ell-2k-2j}, & \text{if } j \leq \lfloor(\alpha+\beta+\ell)/2-k\rfloor\ ; \\ 0, & \text{if } j > \lfloor(\alpha+\beta+\ell)/2-k\rfloor. \end{cases} \tag{A.41}$$

We shall substitute equation [A.41] into the summation in equation [A.38], but first we must analyze the upper limit of the summation. From the above equation it appears that we should just set the upper limit of j equal to $\lfloor\alpha/2+\beta/2+\ell/2-k\rfloor$, but we must analyze two different cases.

(1) If $\lfloor\alpha/2+\beta/2+\ell/2-k\rfloor > \gamma$, the upper limit should be γ since γ was the original limit of the summation.

(2) If $\lfloor\alpha/2+\beta/2+\ell/2-k\rfloor < \gamma$, then the upper limit is $\lfloor\alpha/2+\beta/2+\ell/2-k\rfloor$.

From these two cases we see that the upper limit of j should be set equal to the minimum value of γ and $\lfloor\alpha/2+\beta/2+\ell/2-k\rfloor$,

$$\frac{d^{|q|}}{d\mu^{|q|}}\left(\mu^{\alpha+\ell-2k-|m|}\left(1-\mu^2\right)^{\gamma}\right) = \tag{A.42}$$
$$\sum_{j=0}^{\min[\gamma,\lfloor\eta/2-k\rfloor]}(-1)^{\gamma-j}\binom{\gamma}{j}\frac{(\alpha+\beta+\ell+|q|-2k-2j)!}{(\alpha+\beta+\ell-2k-2j)!}\mu^{\alpha+\beta+\ell-2k-2j}.$$

References

McQuarrie, D.A., *Quantum chemistry* (University Science Books, Mill Valley, CA, 1983).

Tuma, J.T., *Engineering mathematics handbook* (3rd edition, McGraw-Hill, New York, 1987).

Whittaker, E.T. & G.N. Watson, *A course of modern analysis* (4th edition, Cambridge Univ. Press, Cambridge, 1992).

Zill, D.G., *A first course in differential equations with applications* (3rd edition, Prindle, Weber & Schmidt, Boston, 1986).

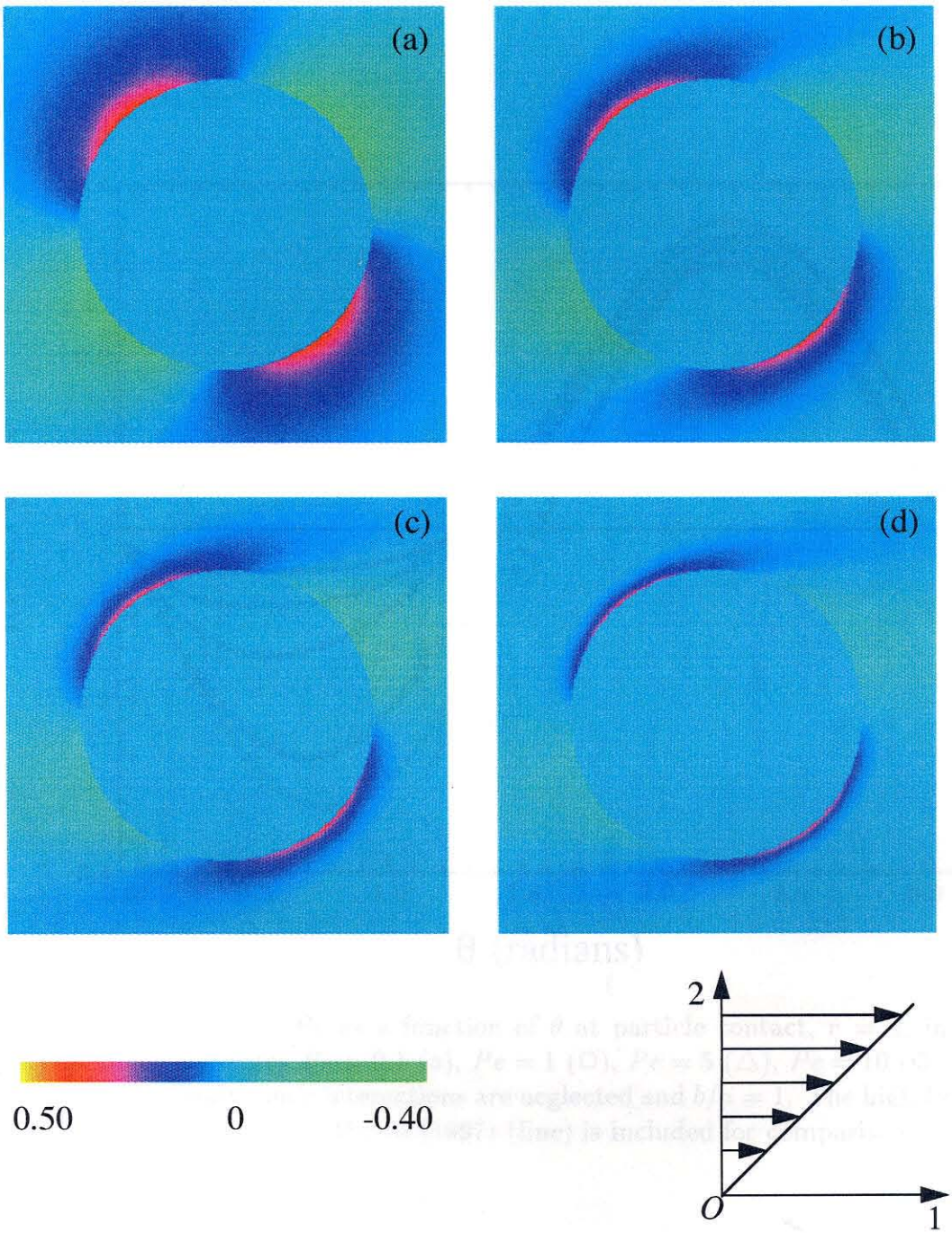

Figure 3.1: Results for f/Pe in the velocity–gradient plane at steady-state for (a) $Pe = 1$, (b) $Pe = 5$, (c) $Pe = 10$, and (d) $Pe = 20$, where f is the difference from the equilibrium microstructure and $Pe = 6\pi\eta_s\dot{\gamma}a^3/kT$. Hydrodynamic interactions are neglected and $b/a = 1$.

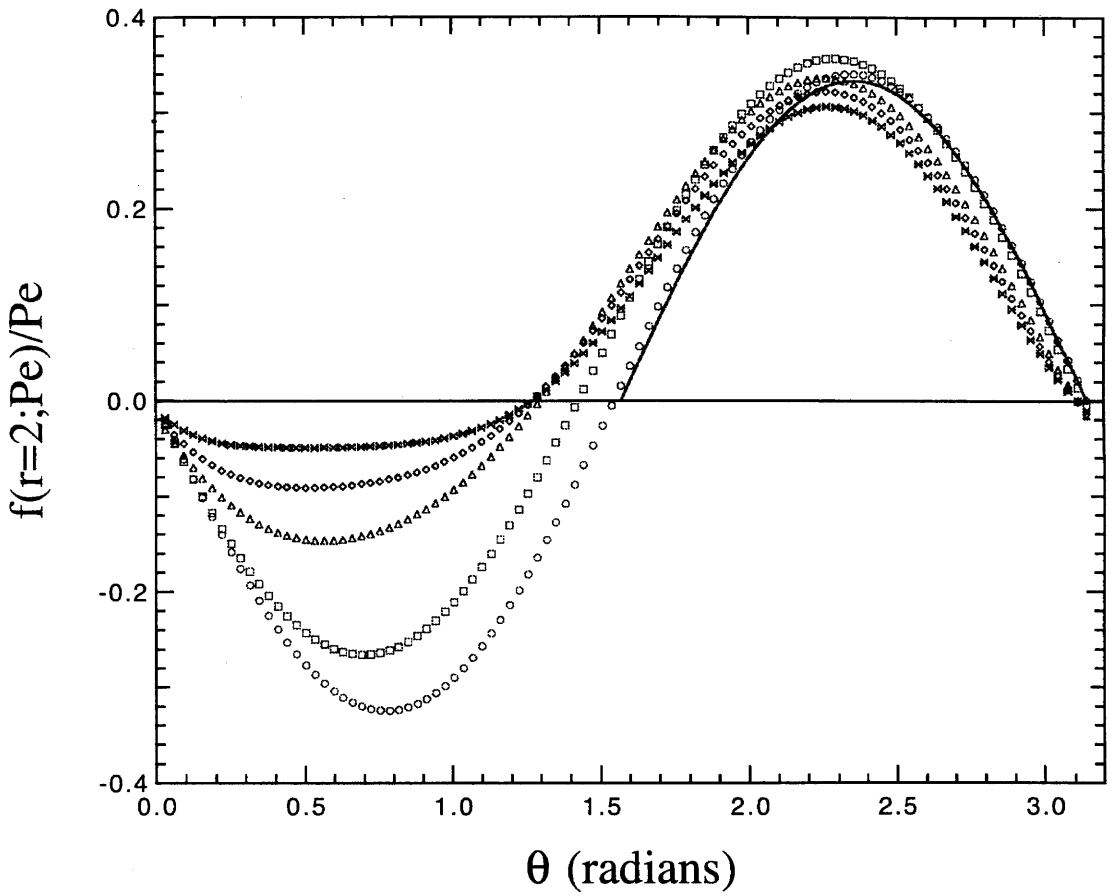

Figure 3.2: Results for f/Pe as a function of θ at particle contact, $r = 2$, in the velocity-gradient plane, for $Pe = 0.1$ (○), $Pe = 1$ (□), $Pe = 5$ (△), $Pe = 10$ (◇) and $Pe = 20$ (⋈). Hydrodynamic interactions are neglected and $b/a = 1$. The high Peclet asymptotic result of Brady & Morris (1997) (line) is included for comparison.

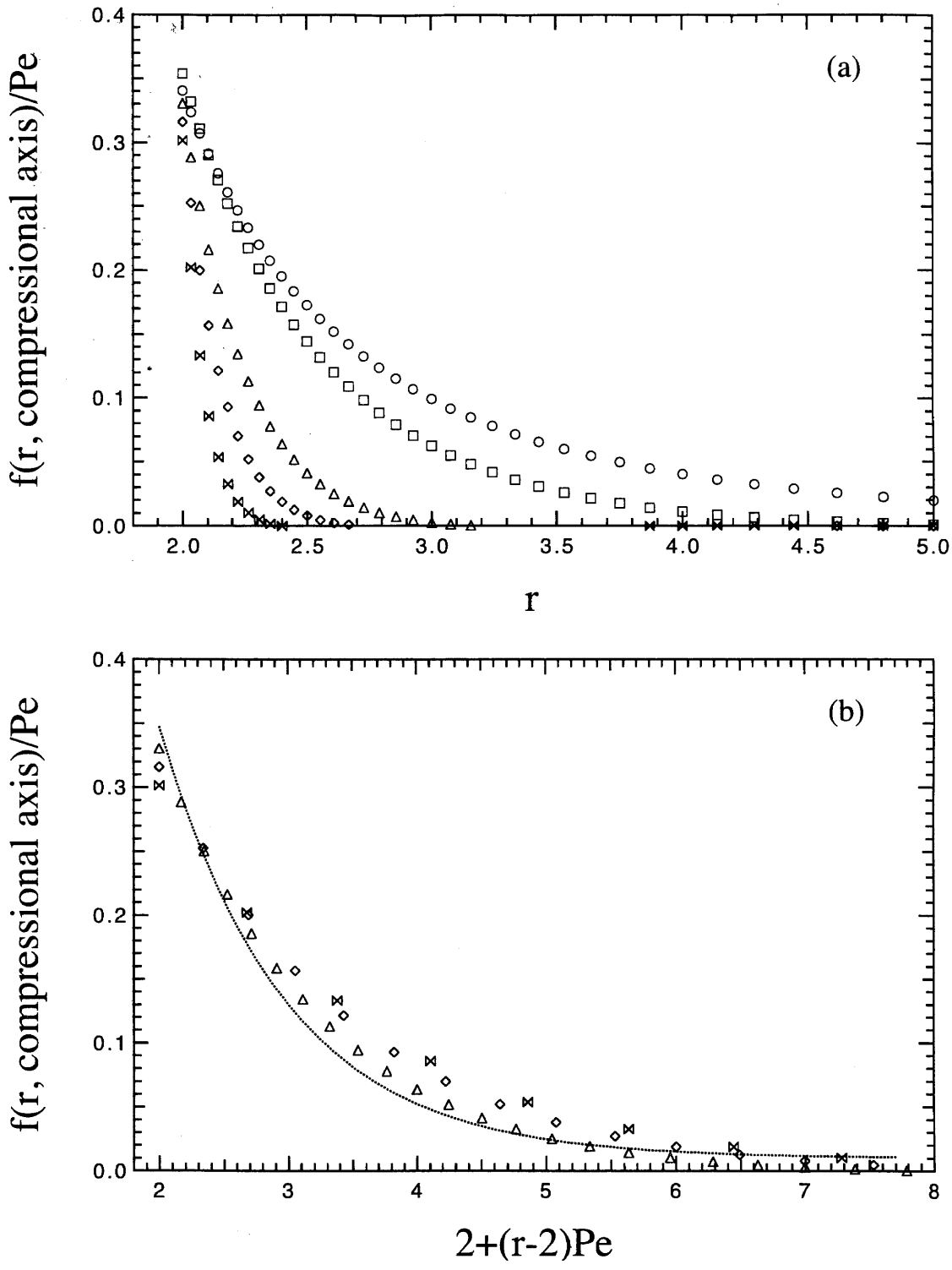

Figure 3.3: Results for f/Pe along the compressional axis as a function of (a) separation, r, and (b) boundary layer length, $2+(r-2)Pe$, for $Pe = 0.1$ ($\circ$), $Pe = 1$ ($\square$), $Pe = 5$ ($\triangle$), $Pe = 10$ ($\diamond$) and $Pe = 20$ ($\bowtie$). Hydrodynamic interactions are neglected and $b/a = 1$. The high Peclet asymptotic result of Brady & Morris (1997) (dotted line) is included for comparison for $Pe = 100$.

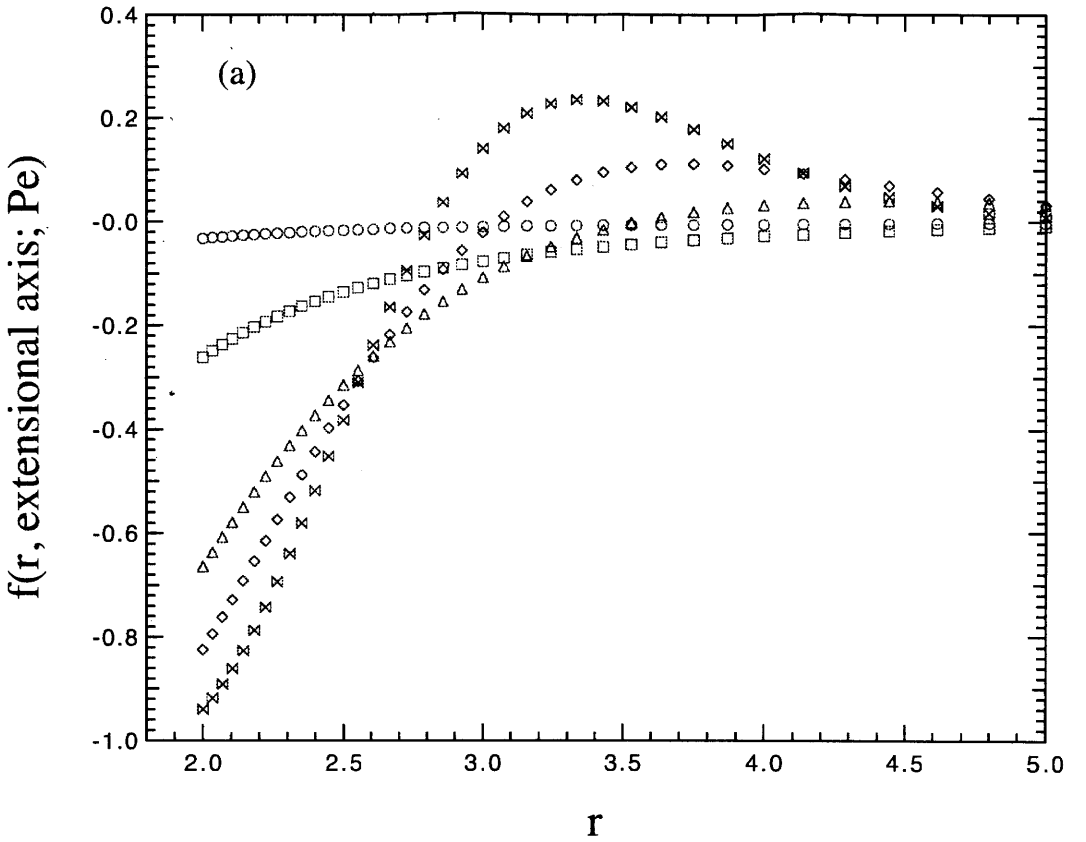

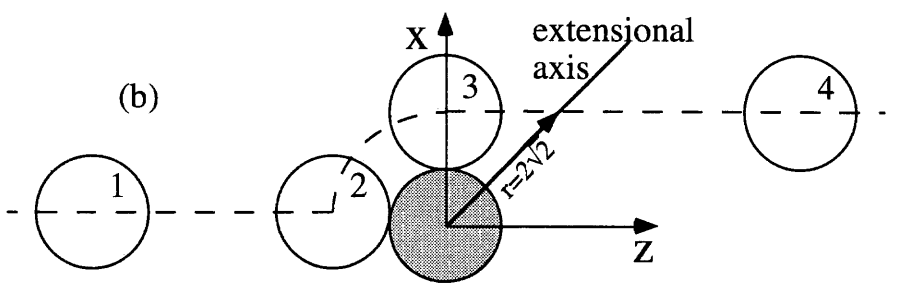

Figure 3.4: Results for f along the extensional axis as a function of separation, r, for $Pe=0.1$ (○), $Pe=1$ (□), $Pe=5$ (△), $Pe=10$ (◇) and $Pe=20$ (⋈) are shown in (a). Hydrodynamic interactions are neglected and $b/a = 1$. The value of r on the extensional axis at which $f \approx 0$ when $Pe \gg 1$ is predicted in (b). A test particle (grey) is placed at the origin. An upstream particle (1) is advected by the external flow, makes contact with the test particle (2), is swept over the test particle (3) and is advected downstream (4). The particle crosses the extensional axis at $r = 2\sqrt{2} \approx 2.83$.

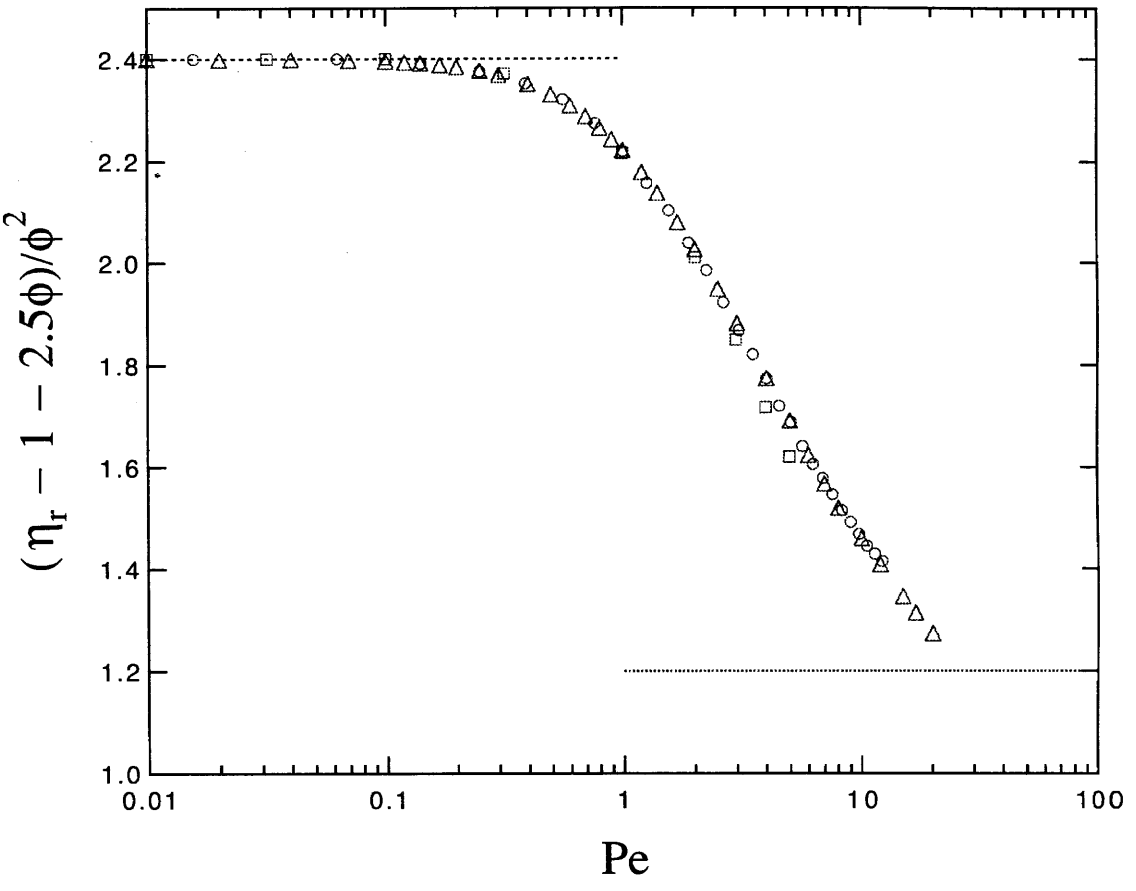

Figure 3.5: The $O(\phi^2)$ contribution to the relative shear viscosity, η_r, as a function of Peclet number, $Pe = 6\pi\eta_s\dot{\gamma}a^3/kT$. Hydrodynamic interactions are neglected and $b/a = 1$. Numerical results ($\triangle$) are compared to the low Peclet asymptotic result, $(\eta_r - 1 - 2.5\phi) = (12/5)\phi^2$, [Brady & Vicic (1995)] (dashed line), the high Peclet approximate asymptotic result, $(\eta_r - 1 - 2.5\phi) = (6/5)\phi^2$, [Brady & Morris (1997)] (dotted line) and the numerical results of Blawzdziewicz & Szamel (1993) ($\circ$) and Lionberger (1998) ($\square$).

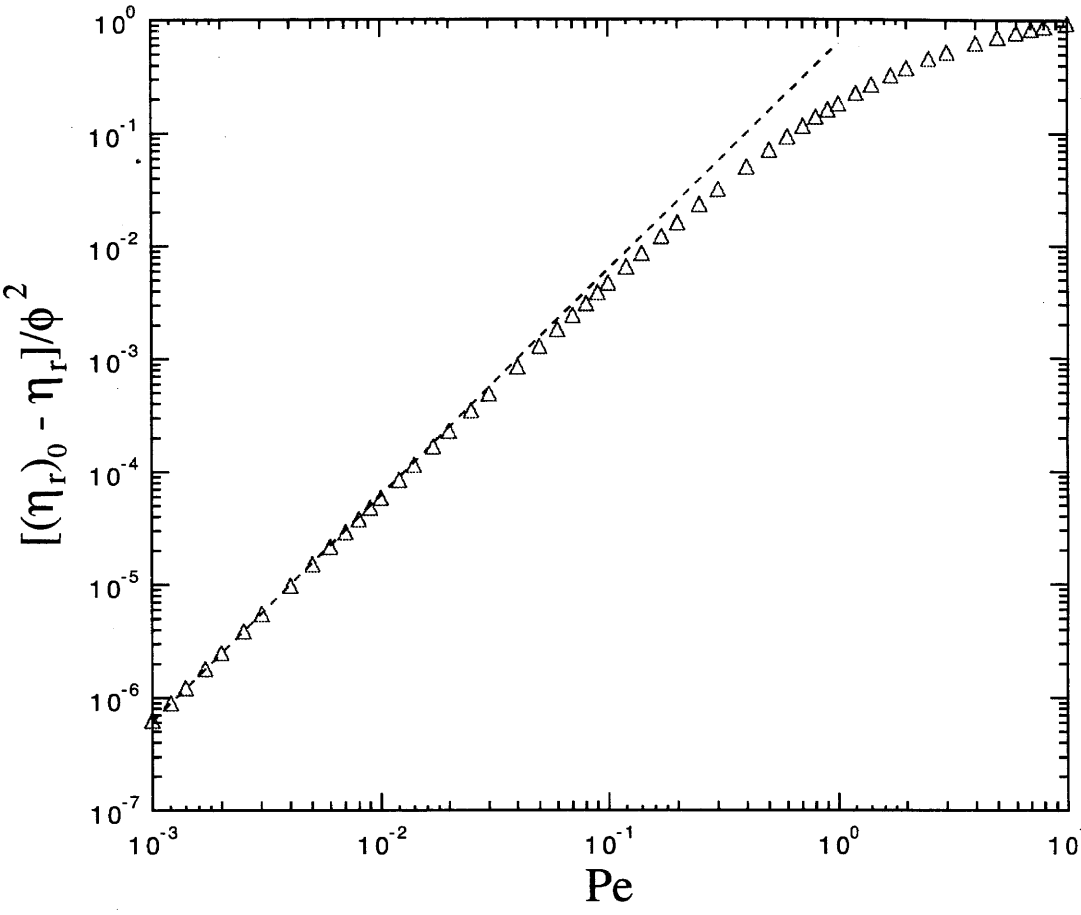

Figure 3.6: Results for the relative shear viscosity, η_r, as a function of Peclet number, $Pe = 6\pi\eta_s\dot{\gamma}a^3/kT$, are used to numerically find the $O(\phi^2 Pe^2)$ contribution when $Pe \ll 1$, $b/a = 1$, and hydrodynamic interactions are neglected. The relative shear viscosity at the given Peclet number is subtracted from the low shear limit of the relative viscosity, $(\eta_r)_0$. The dashed line, $0.62Pe^2$, is a curve fit to the numerical data for $Pe \ll 1$.

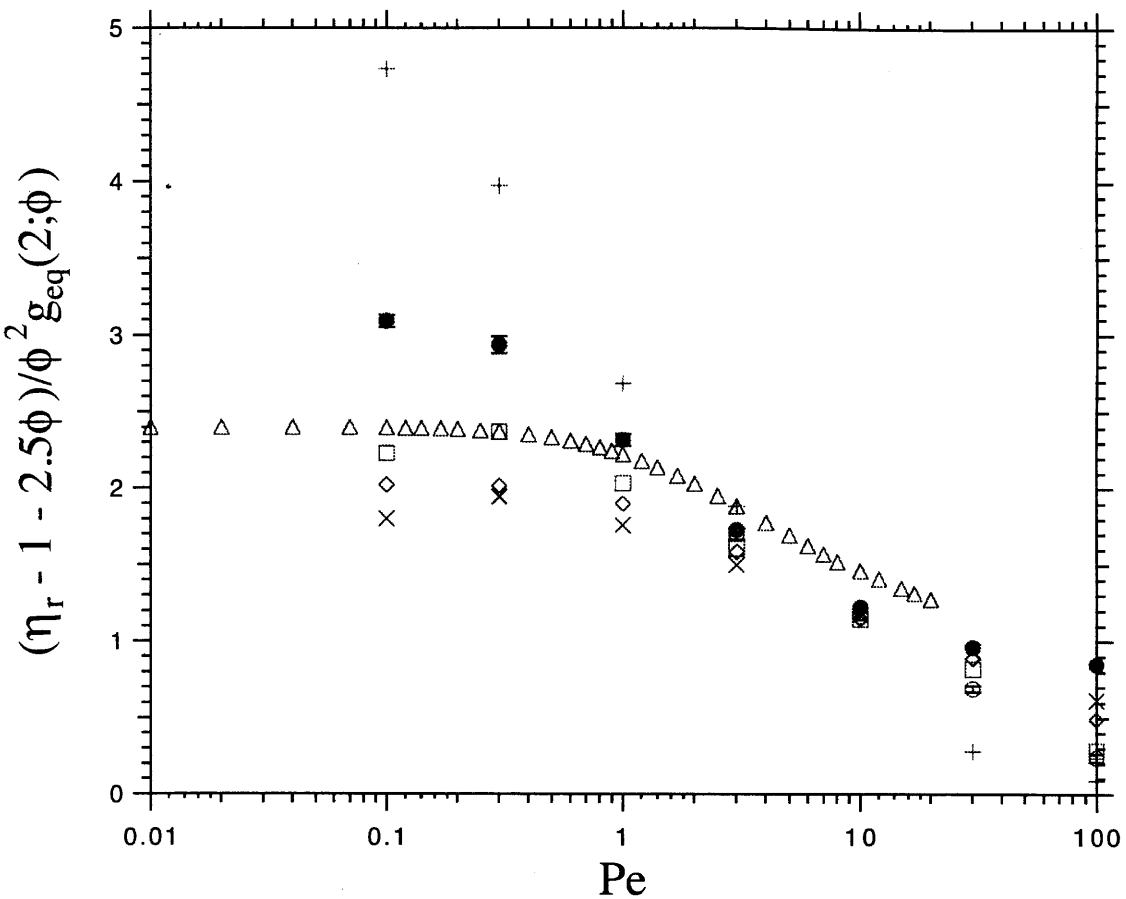

Figure 3.7: Results for the scaled shear viscosity as a function of Peclet number, $Pe = 6\pi\eta_s\dot{\gamma}a^3/kT$, using the scaling theory of Brady (1993b) when hydrodynamic interactions are neglected. Numerical results of this work ($\triangle$) are compared with the Brownian Dynamics simulations of Foss & Brady (1999) for $\phi = 0.30$ ($\times$), $\phi = 0.35$ ($\diamond$), $\phi = 0.40$ ($\square$), $\phi = 0.45$ ($\circ$), and $\phi = 0.50$ ($+$). Shear viscosity for $\phi = 0.45$ is also measured after startup but prior to the time at which the dispersion begins structural changes as part of the shear-induced phase transition ($\bullet$).

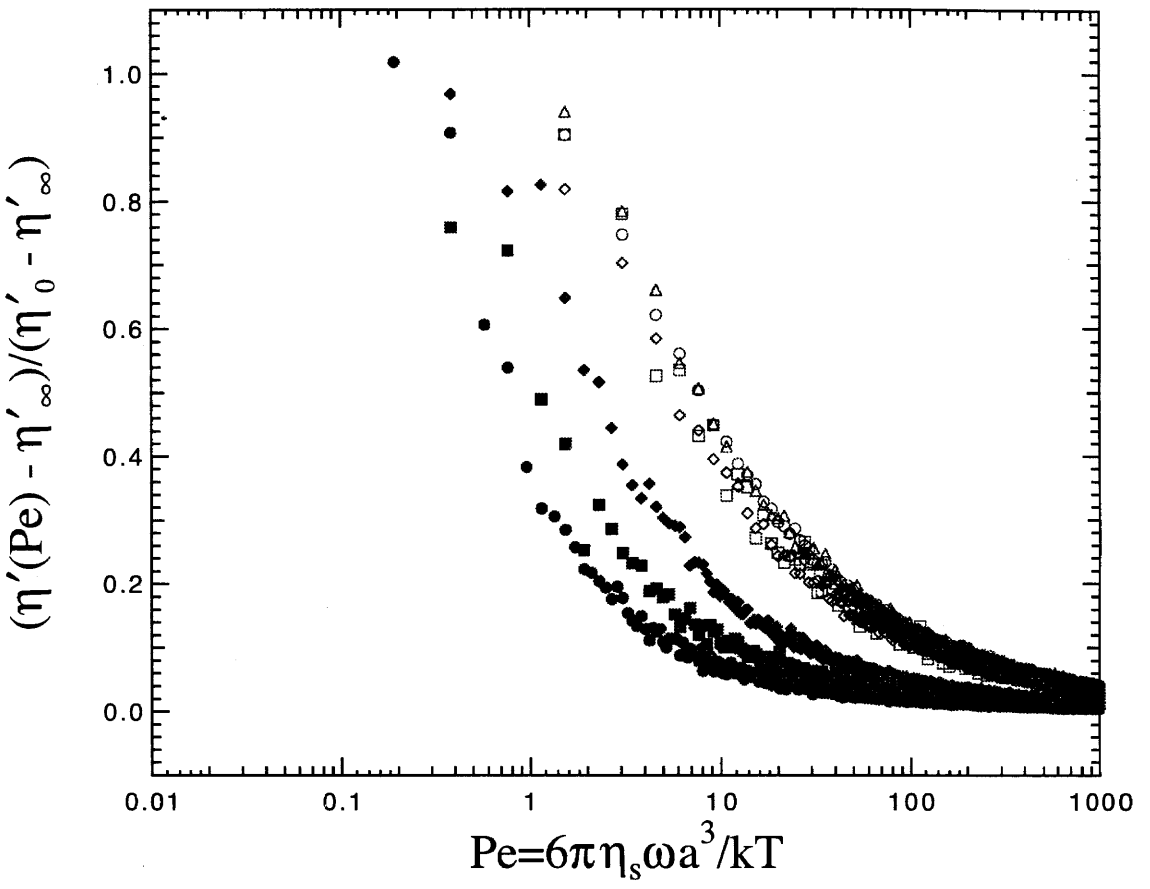

Figure 3.8: Results of Bergenholtz (1999) using the Green-Kubo algorithm and the Brownian Dynamics simulation method of Foss (1999) for $\phi = 0.20$ ($\circ$), $\phi = 0.30$ ($\triangle$), $\phi = 0.35$ ($\diamond$), $\phi = 0.40$ ($\square$), $\phi = 0.50$ (solid diamond), $\phi = 0.52$ (solid box) and $\phi = 0.55$ ($\bullet$).

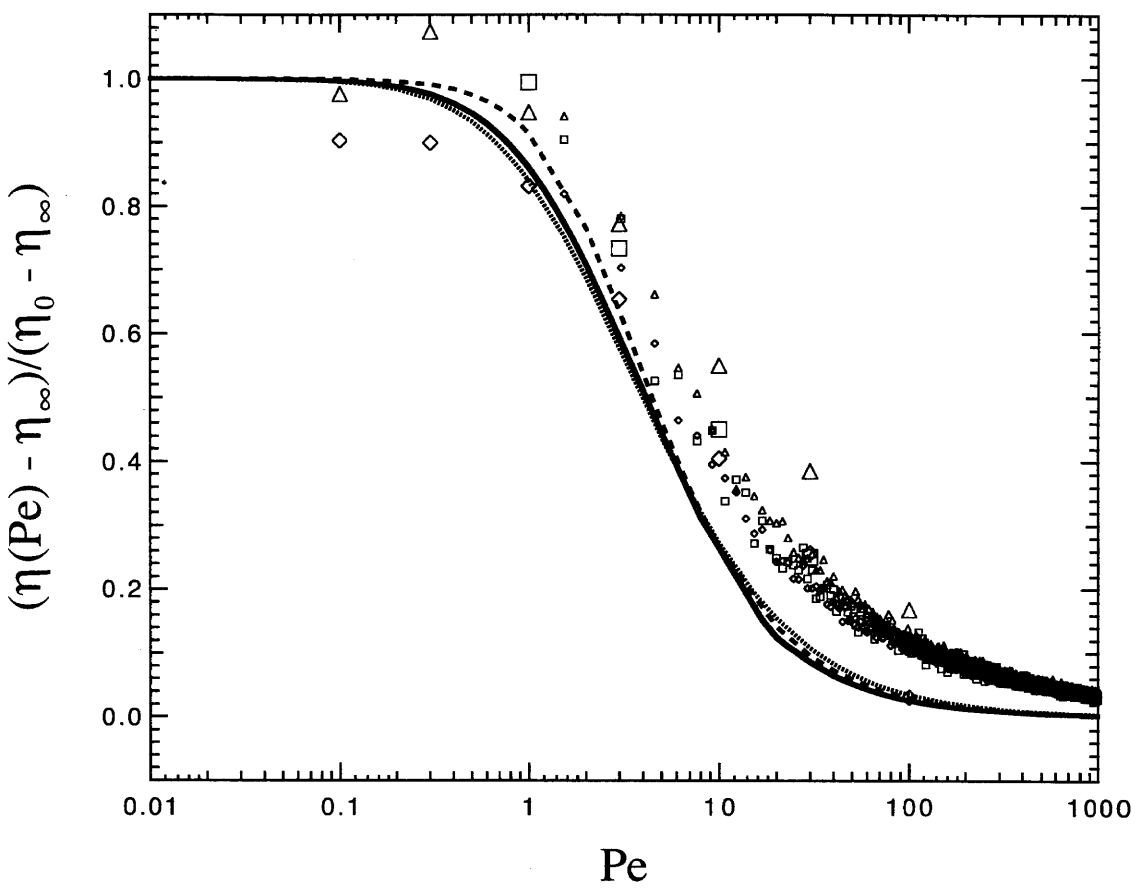

Figure 3.9: Results for the reduced viscosity as a function of Peclet number, $Pe = 6\pi\eta_s\dot{\gamma}a^3/kT$ for steady flow and $Pe = 6\pi\eta_s\omega a^3/kT$ for oscillatory flow, for numerical results of this work (solid line), the linear viscoelastic prediction of Brady (1993b) (dashed line), a Padé approximate for the results of this work (dotted line), steady [Foss & Brady (1999)] (large symbols) and oscillatory [Bergenholtz (1999)] (small symbols) results from Brownian Dynamics simulations for $\phi = 0.30$ ($\triangle$), $\phi = 0.35$ ($\diamond$), $\phi = 0.40$ ($\square$).

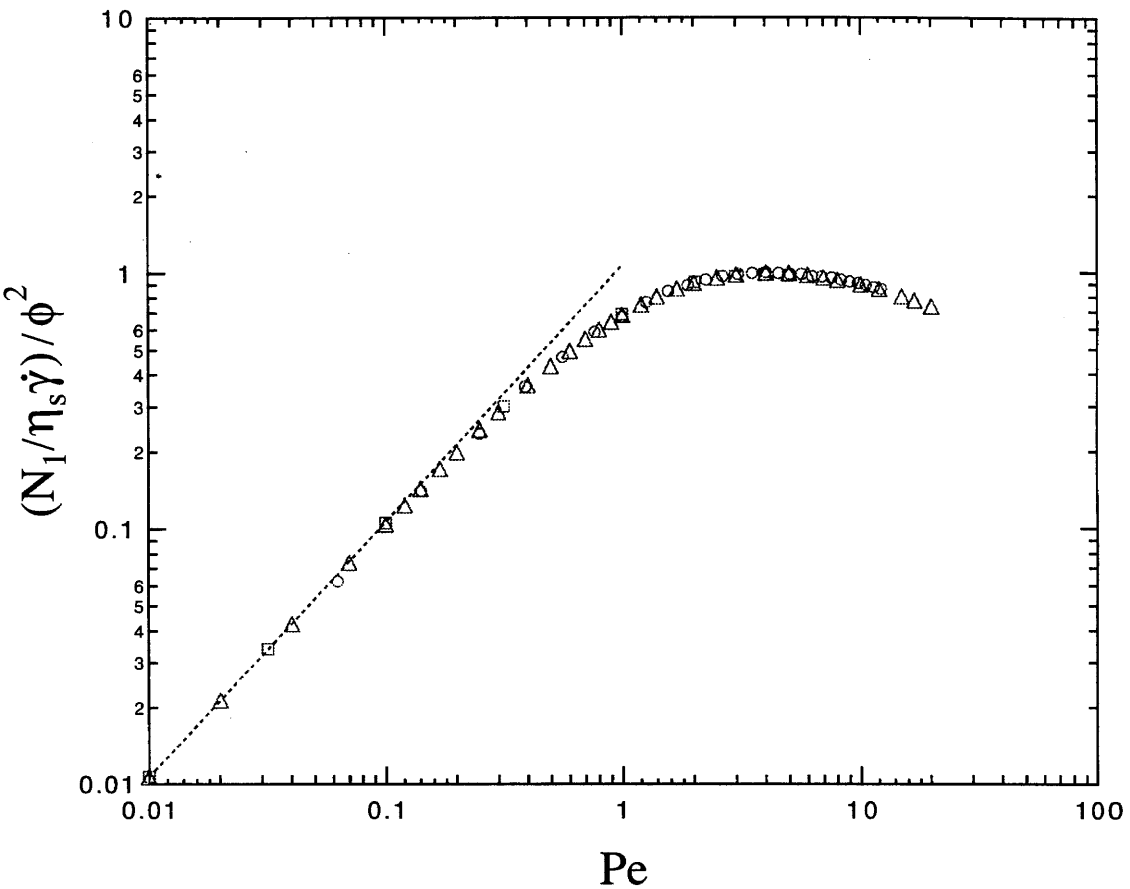

Figure 3.10: The $O(\phi^2)$ contribution to the nondimensional first normal stress difference, $N_1/\eta_s\dot{\gamma}$, as a function of Peclet number, $Pe = 6\pi\eta_s\dot{\gamma}a^3/kT$. Hydrodynamic interactions are neglected and $b/a = 1$. Numerical results ($\triangle$) are compared to the low Peclet asymptotic result, $N_1/\eta_s\dot{\gamma} = (16/15)\phi^2 Pe$ [Brady & Vicic (1995)] (dashed line) and the numerical results of Blawzdziewicz & Szamel (1993) ($\circ$) and Lionberger (1998) ($\square$). The high Peclet approximate asymptotic result [Brady & Morris (1997)] predicts $N_1 = 0$.

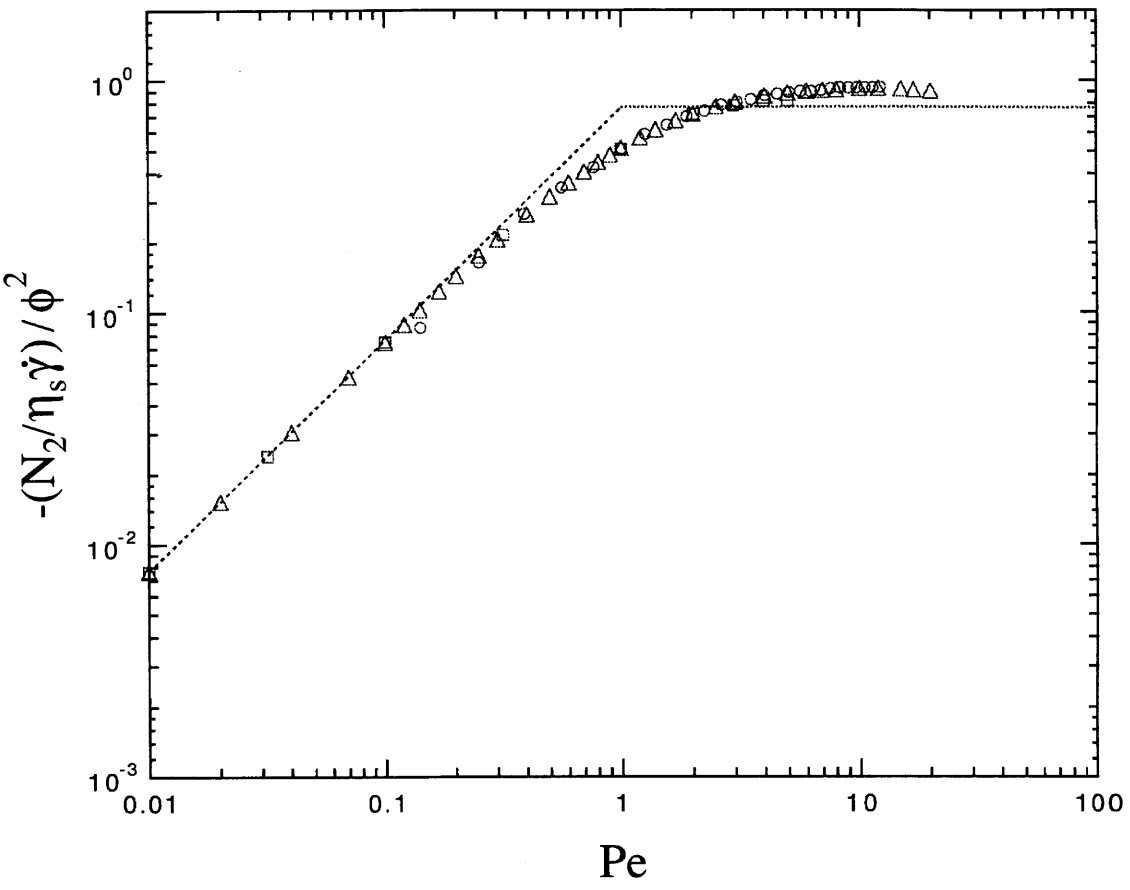

Figure 3.11: The $O(\phi^2)$ contribution to the nondimensional second normal stress difference, $N_2/\eta_s\dot{\gamma}$, as a function of Peclet number, $Pe = 6\pi\eta_s\dot{\gamma}a^3/kT$. Hydrodynamic interactions are neglected and $b/a = 1$. Numerical results ($\triangle$) are compared to the low Peclet asymptotic result, $N_2/\eta_s\dot{\gamma} = -(16/21)\phi^2 Pe$ [Brady & Vicic (1995)] (dashed line), the high Peclet approximate asymptotic result, $N_2/\eta_s\dot{\gamma} = -(12/5\pi)\phi^2$, [Brady & Morris (1997)] (dotted line) and the numerical results of Blawzdziewicz & Szamel (1993) (o) and Lionberger (1998) ($\square$).

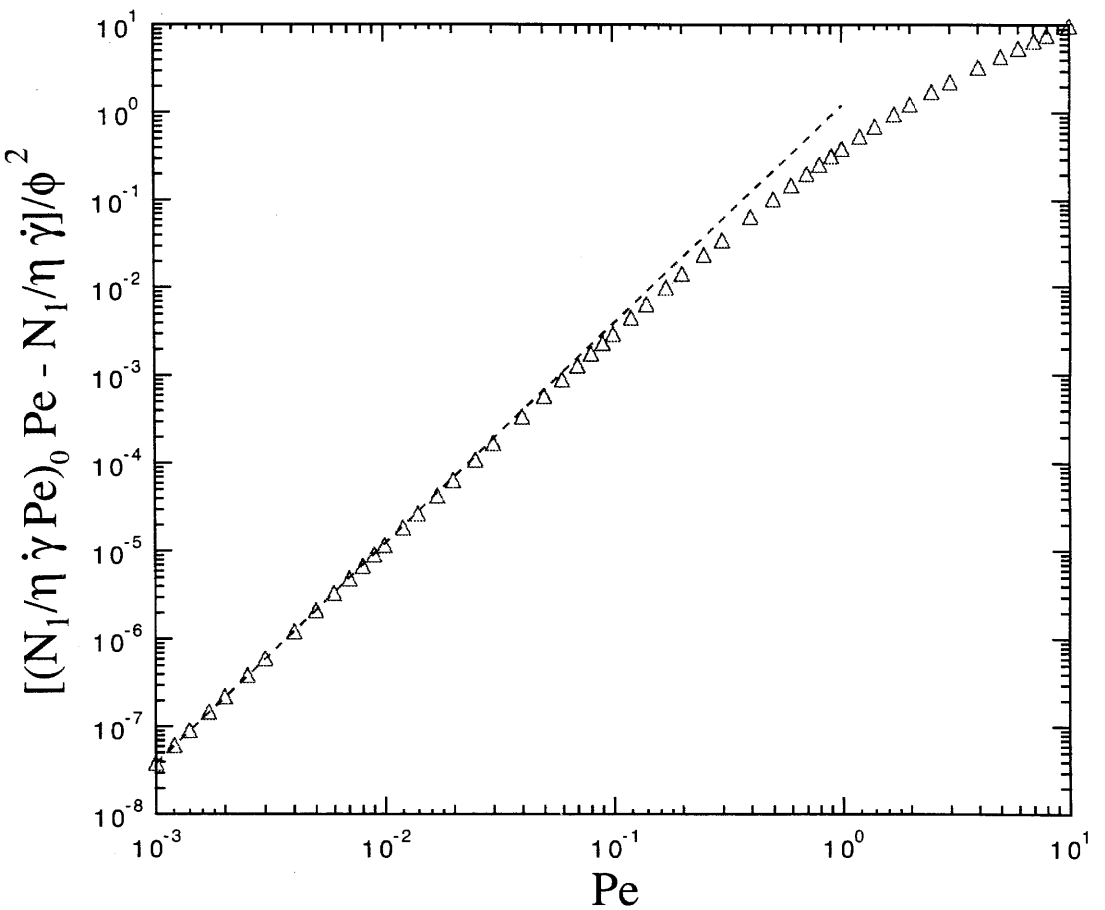

Figure 3.12: Results for the nondimensional first normal stress difference, $N_1/\eta_s\dot{\gamma}$, as a function of Peclet number, $Pe = 6\pi\eta_s\dot{\gamma}a^3/kT$, are used to numerically find the $O(\phi^2 Pe^{5/2})$ contribution when $Pe \ll 1$, $b/a = 1$, and hydrodynamic interactions are neglected. The value of $N_1/\eta_s\dot{\gamma}$ at the given Peclet number is subtracted from the low shear limit, $(N_1/\eta_s\dot{\gamma}Pe)_0 Pe$. The dashed line, $1.2Pe^{5/2}$, is a curve fit to the numerical data for $Pe \ll 1$.

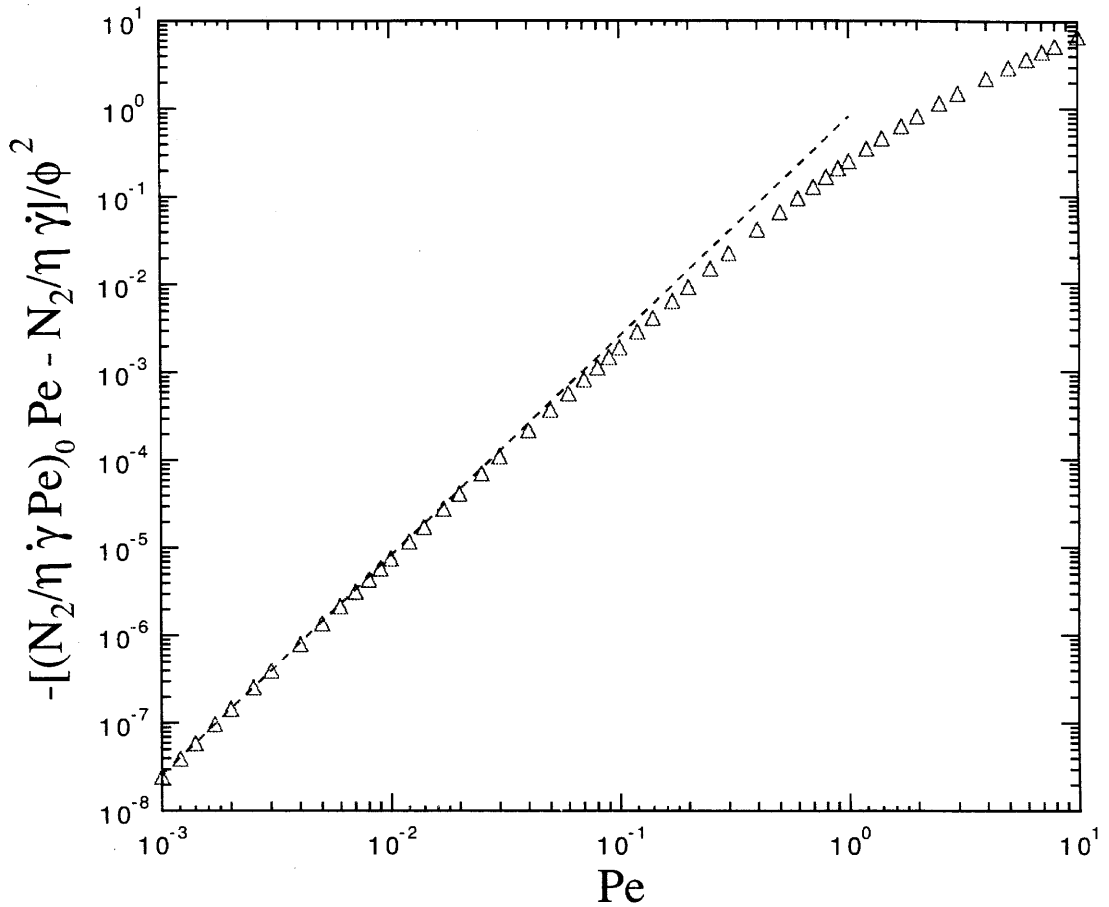

Figure 3.13: Results for the nondimensional second normal stress difference, $N_2/\eta_s\dot{\gamma}$, as a function of Peclet number, $Pe = 6\pi\eta_s\dot{\gamma}a^3/kT$, are used to numerically find the $O(\phi^2 Pe^{5/2})$ contribution when $Pe \ll 1$, $b/a = 1$, and hydrodynamic interactions are neglected. The value of $N_2/\eta_s\dot{\gamma}$ at the given Peclet number is subtracted from the low shear limit, $(N_2/\eta_s\dot{\gamma}Pe)_0 Pe$. The dashed line, $0.81Pe^{5/2}$, is a curve fit to the numerical data for $Pe \ll 1$.

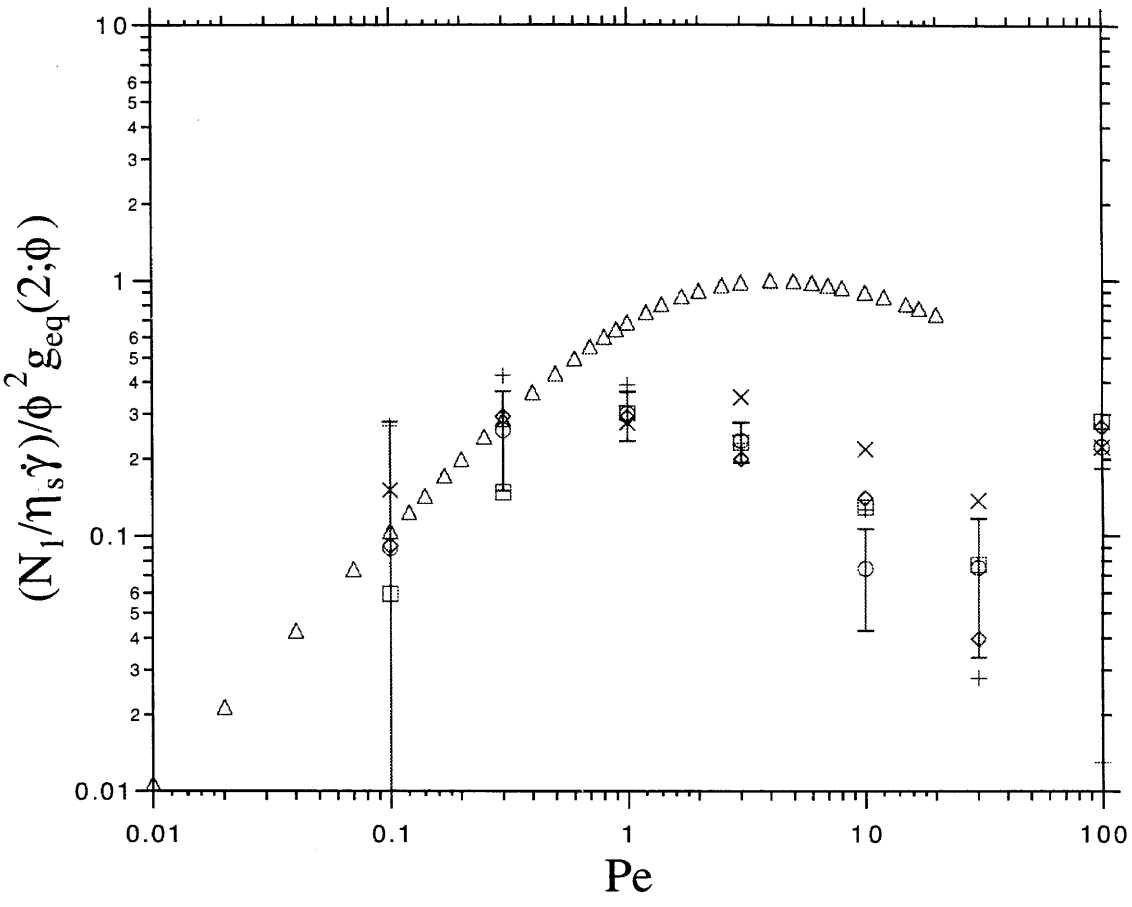

Figure 3.14: Results for the scaled first normal stress difference as a function of Peclet number, $Pe = 6\pi\eta_s\dot{\gamma}a^3/kT$, using the scaling theory of Brady (1993b) when hydrodynamic interactions are neglected. Numerical results of this work ($\triangle$) are compared with the Brownian Dynamics simulations of Foss & Brady (1999) for $\phi = 0.30$ ($\times$), $\phi = 0.35$ ($\diamond$), $\phi = 0.40$ ($\square$), $\phi = 0.45$ ($\circ$), and $\phi = 0.50$ ($+$).

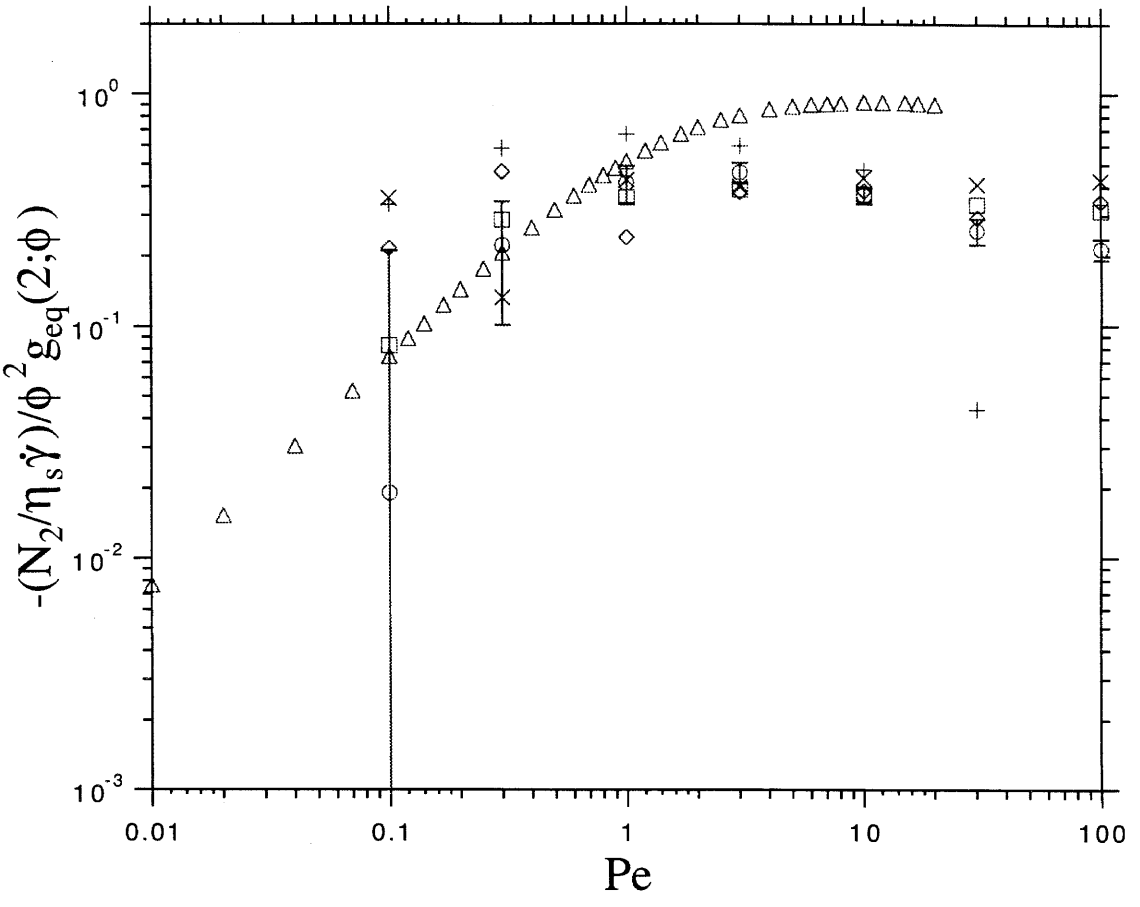

Figure 3.15: Results for the scaled second normal stress difference as a function of Peclet number, $Pe = 6\pi\eta_s\dot{\gamma}a^3/kT$, using the scaling theory of Brady (1993b) when hydrodynamic interactions are neglected. Numerical results of this work ($\triangle$) are compared with the Brownian Dynamics simulations of Foss & Brady (1999) for $\phi = 0.30$ ($\times$), $\phi = 0.35$ ($\diamond$), $\phi = 0.40$ ($\square$), $\phi = 0.45$ ($\circ$), and $\phi = 0.50$ ($+$).

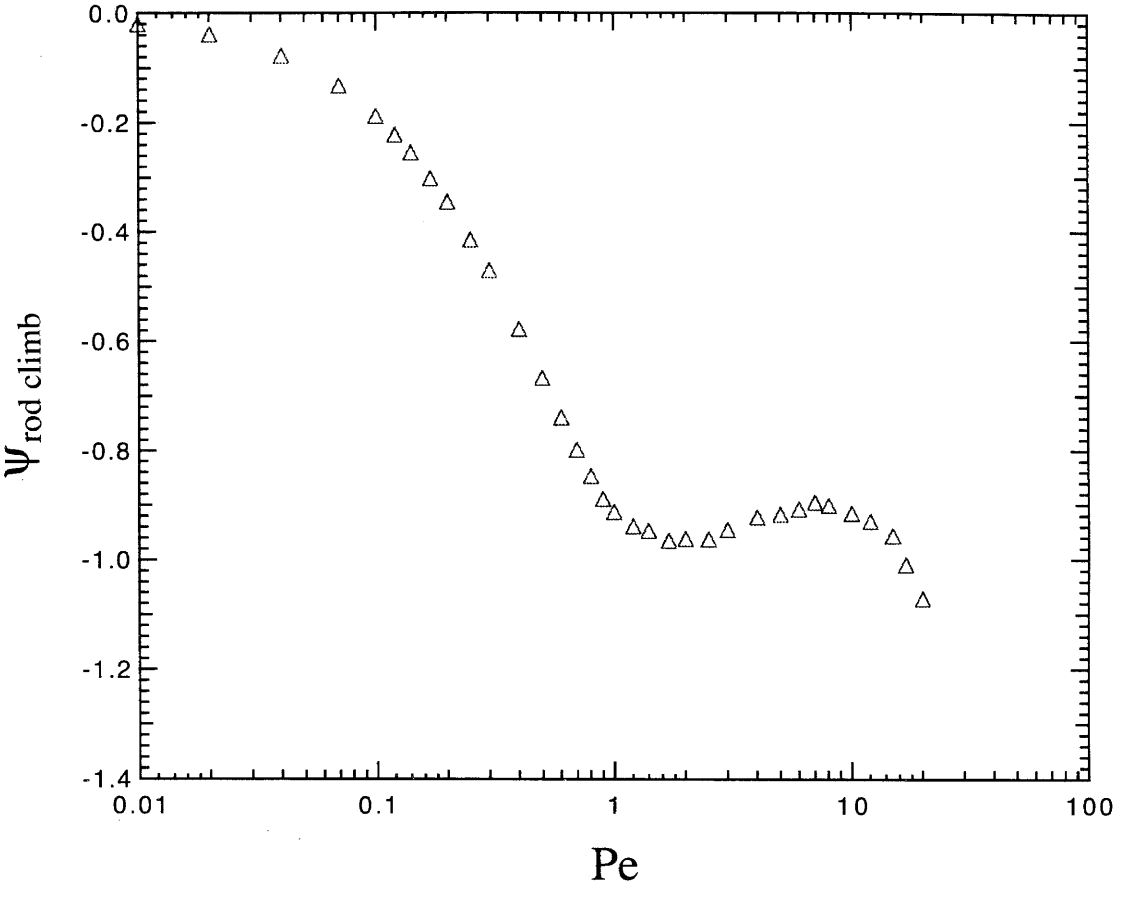

Figure 3.16: Results for the rod climbing variable, $\psi_{rod\ climb} = r\left(\partial p_{zz}/\partial r\right)/\eta_s\dot{\gamma}\phi^2$, as a function of Peclet number, $Pe = 6\pi\eta_s\dot{\gamma}a^3/kT$, using the numerical results of this work (solid line). Hydrodynamic interactions are neglected and $b/a = 1$. Since the rod climbing variable is negative for all values of Peclet number, only negative rod climbing should occur.

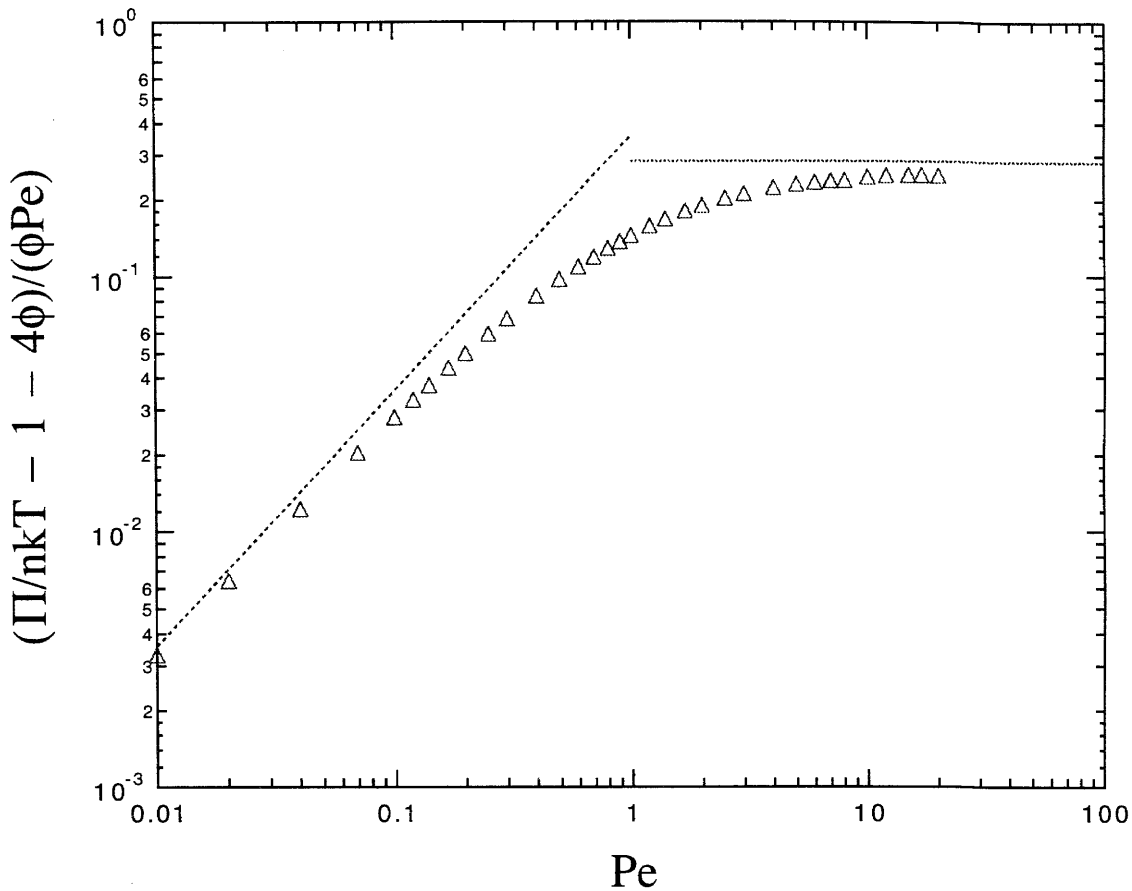

Figure 3.17: The $O(\phi Pe)$ contribution to the nondimensional osmotic pressure, Π/nkT, as a function of Peclet number, $Pe = 6\pi\eta_s\dot{\gamma}a^3/kT$. Hydrodynamic interactions are neglected and $b/a = 1$. Numerical results ($\triangle$) are compared to the low Peclet asymptotic result, $(\Pi/nkT - 1 - 4\phi) = (16/45)\phi Pe^2$, [Brady & Vicic (1995)] (dashed line) and the high Peclet approximate asymptotic result, $(\Pi/nkT - 1 - 4\phi) = (8/9\pi)\phi Pe$, [Brady & Morris (1997)] (dotted line). No numerical results are reported by Blawzdziewicz & Szamel (1993) nor Lionberger (1998) for osmotic pressure.

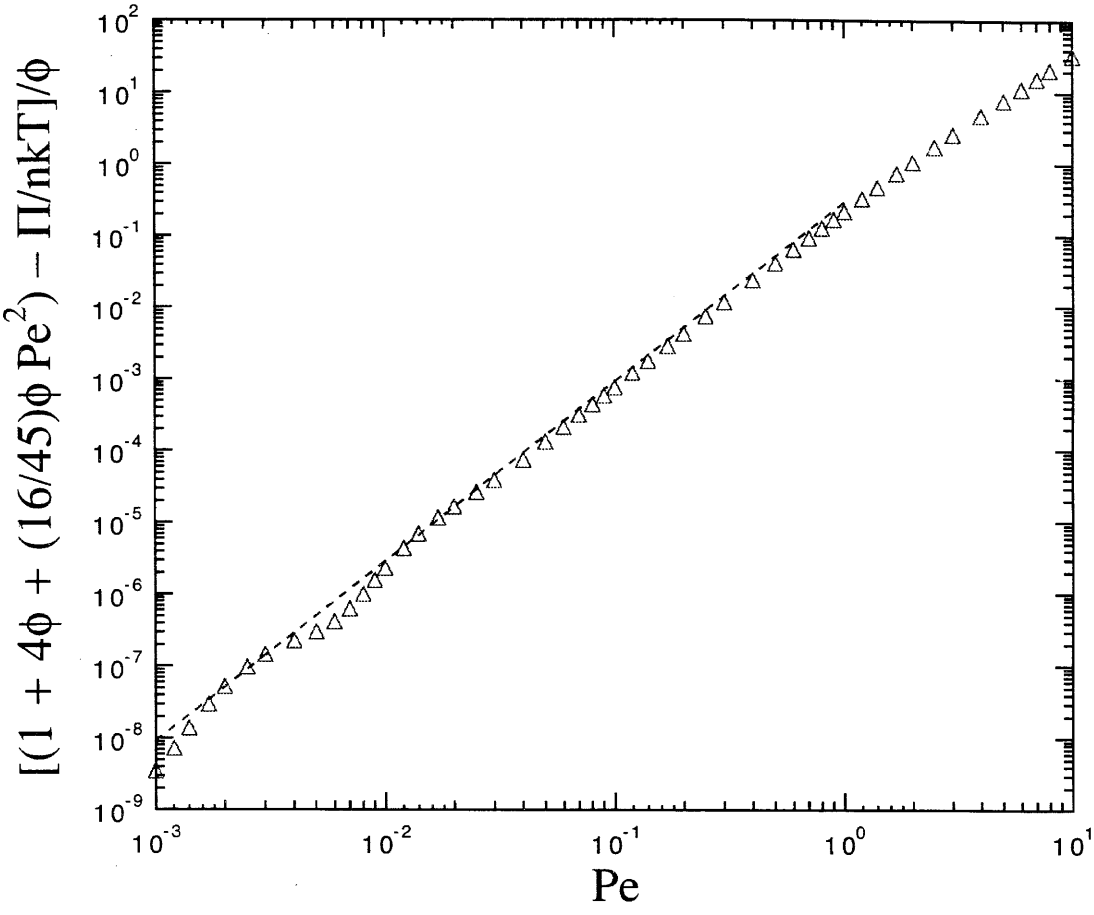

Figure 3.18: Results for the nondimensional osmotic pressure, Π/nkT, as a function of Peclet number, $Pe = 6\pi\eta_s\dot{\gamma}a^3/kT$, are used to numerically confirm the $O(\phi^2 Pe^{5/2})$ contribution when $Pe \ll 1$, $b/a = 1$, and hydrodynamic interactions are neglected. The value of Π/nkT at the given Peclet number is subtracted from its low shear limit, $1 + 4\phi + (16/45)\phi Pe^2$. The dashed line, $0.286 Pe^{5/2}$, is the result of matching the inner solution at $O(Pe^{5/2})$ with the first mismatched term of the outer solution for $Pe \ll 1$.

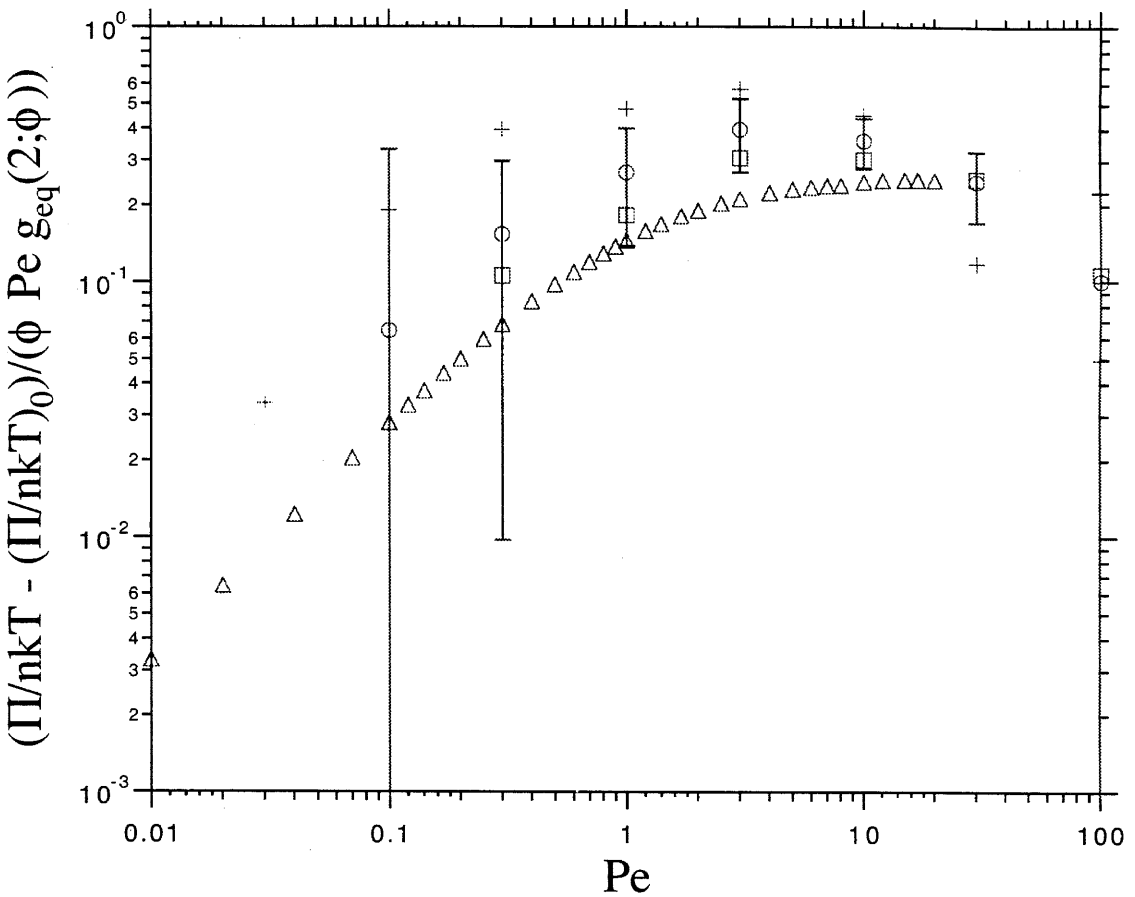

Figure 3.19: Results for the scaled osmotic pressure as a function of Peclet number, $Pe = 6\pi\eta_s\dot{\gamma}a^3/kT$, using the scaling theory of Brady (1993b) when hydrodynamic interactions are neglected and $b/a = 1$. Numerical results of this work ($\triangle$) are compared with the Brownian Dynamics simulations of Foss & Brady (1999) for $\phi = 0.30$ ($\times$), $\phi = 0.35$ ($\diamond$), $\phi = 0.40$ ($\square$), $\phi = 0.45$ ($\circ$), and $\phi = 0.50$ ($+$).

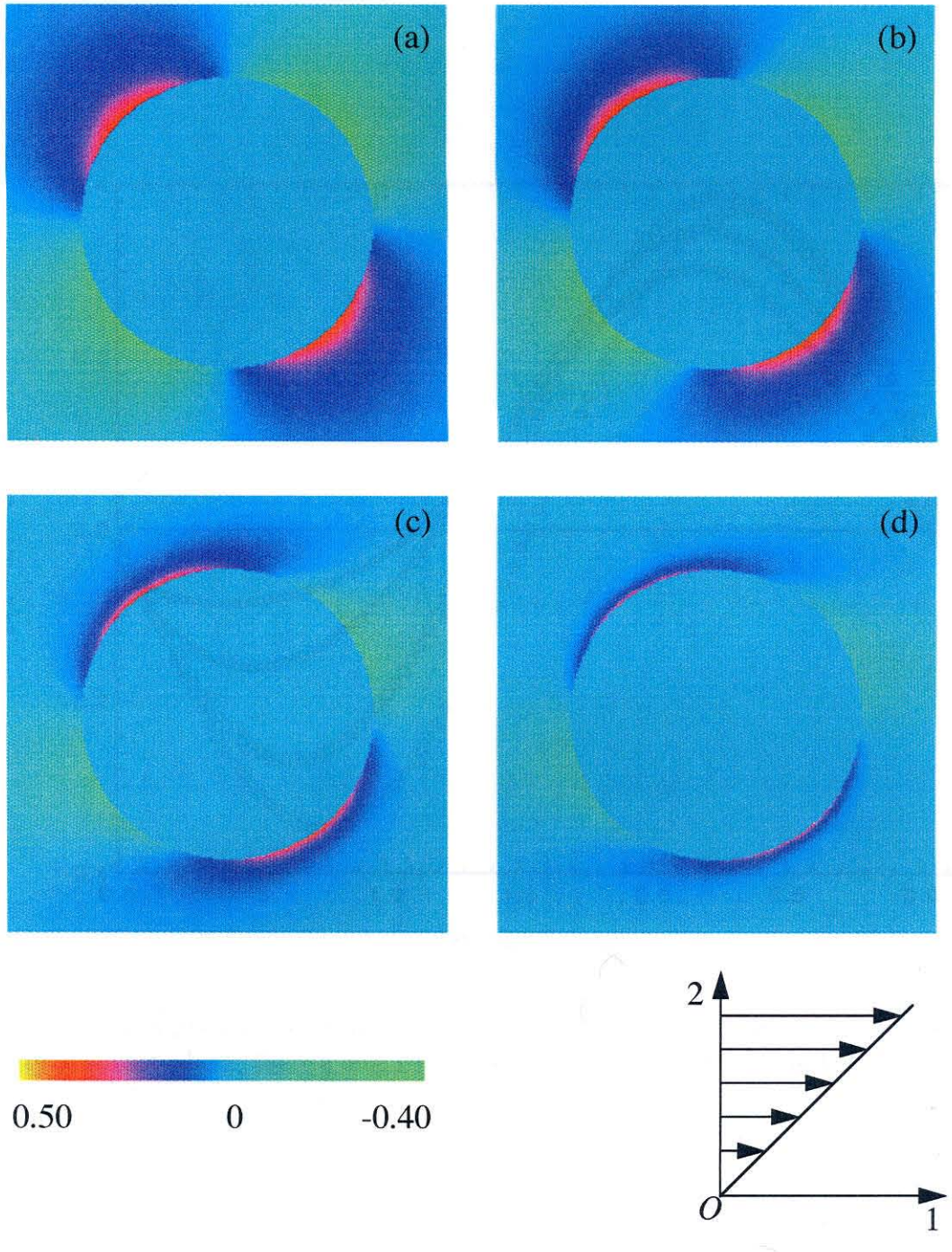

Figure 3.20: Results for f/Pe in the velocity–gradient plane at steady-state for (a) $Pe = 0.1$, (b) $Pe = 1$, (c) $Pe = 4$, and (d) $Pe = 10$, where f is the difference from the equilibrium microstructure and $Pe = 6\pi\eta_s\dot{\gamma}a^3/kT$ for $b/a = 1.001$.

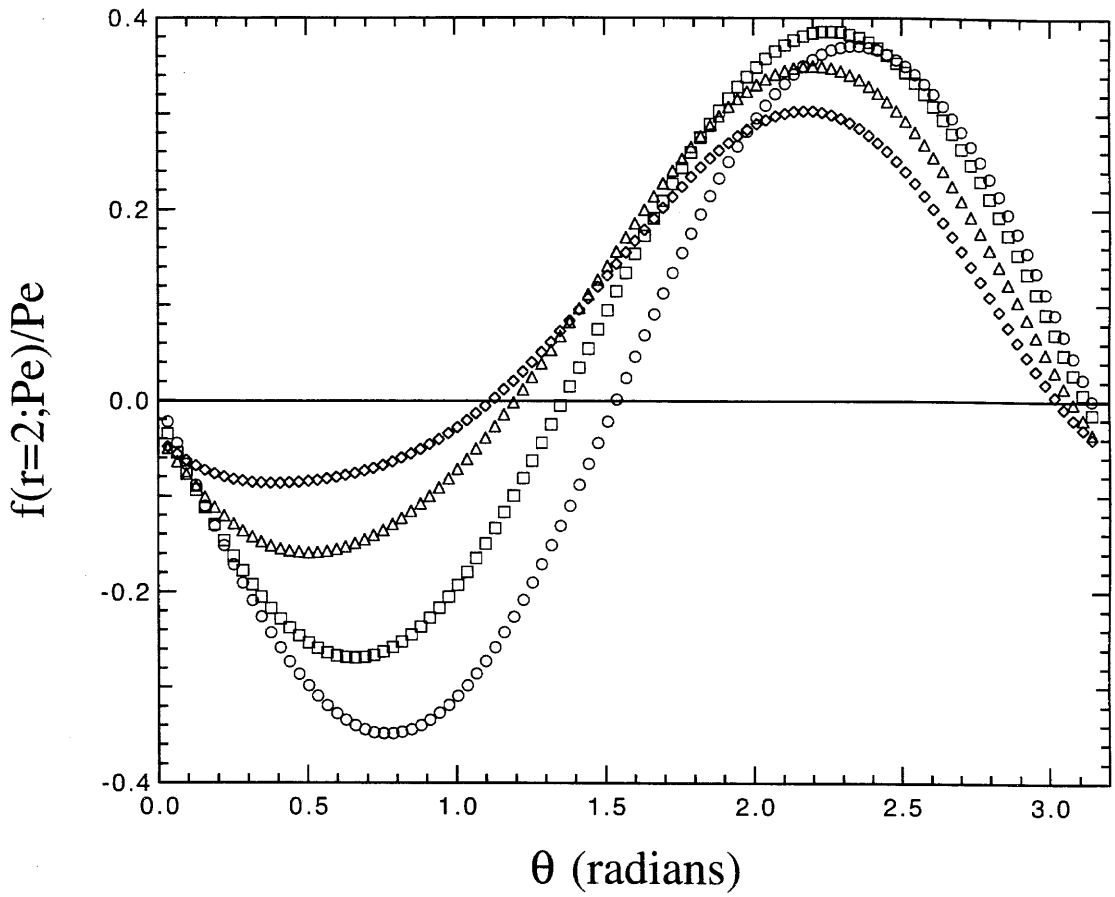

Figure 3.21: Results for f/Pe as a function of θ at particle contact, $r = 2$, in the velocity-gradient plane, for $Pe = 0.1$ (○), $Pe = 1$ (□), $Pe = 4$ (△) and $Pe = 10$ (◇) for $b/a = 1.001$.

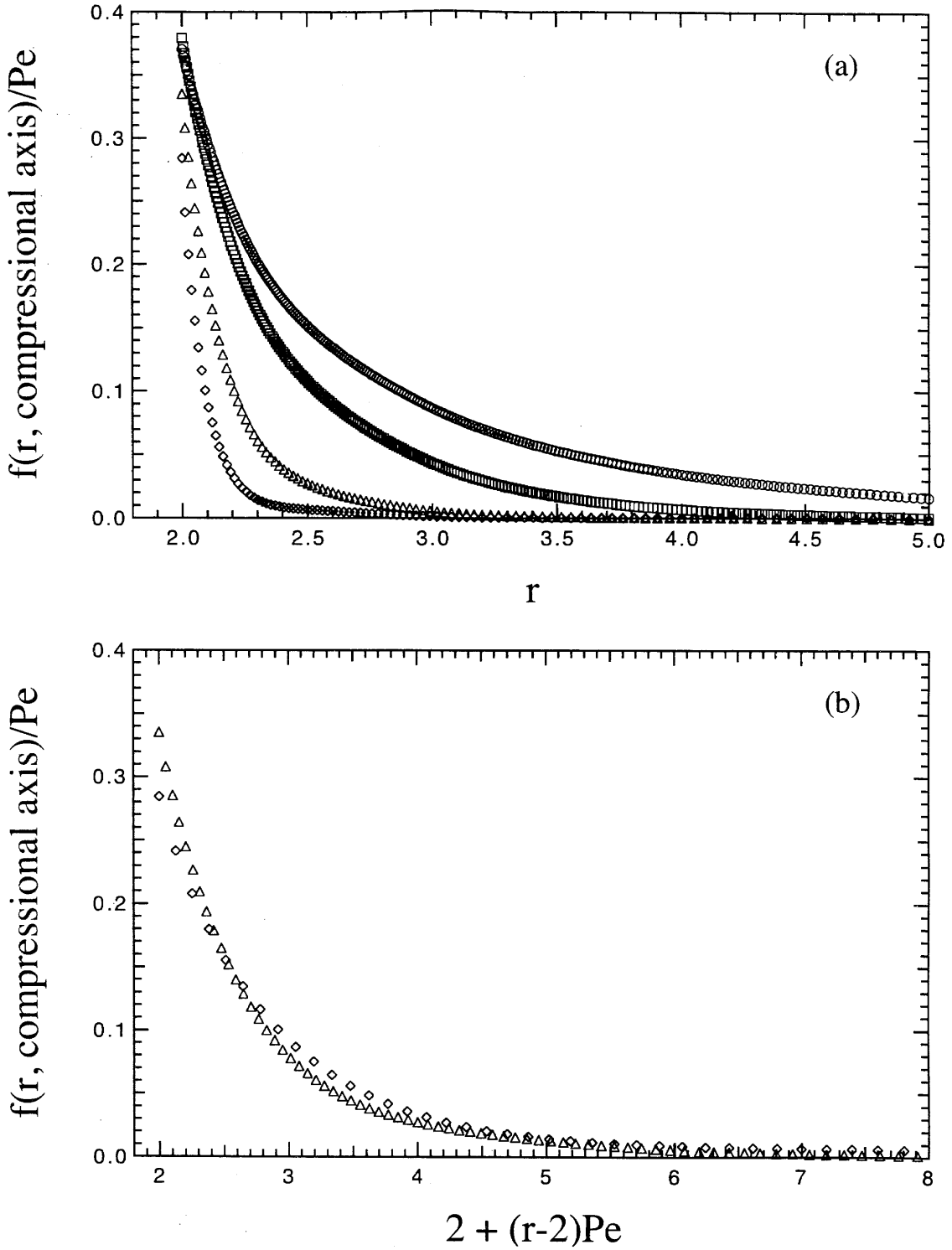

Figure 3.22: Results for f/Pe along the compressional axis as a function of (a) separation, r, and (b) boundary layer length, $2+(r-2)Pe$, for $Pe = 0.1$ (o), $Pe = 1$ ($\square$), $Pe = 4$ ($\triangle$) and $Pe = 10$ ($\diamond$) for $b/a = 1.001$.

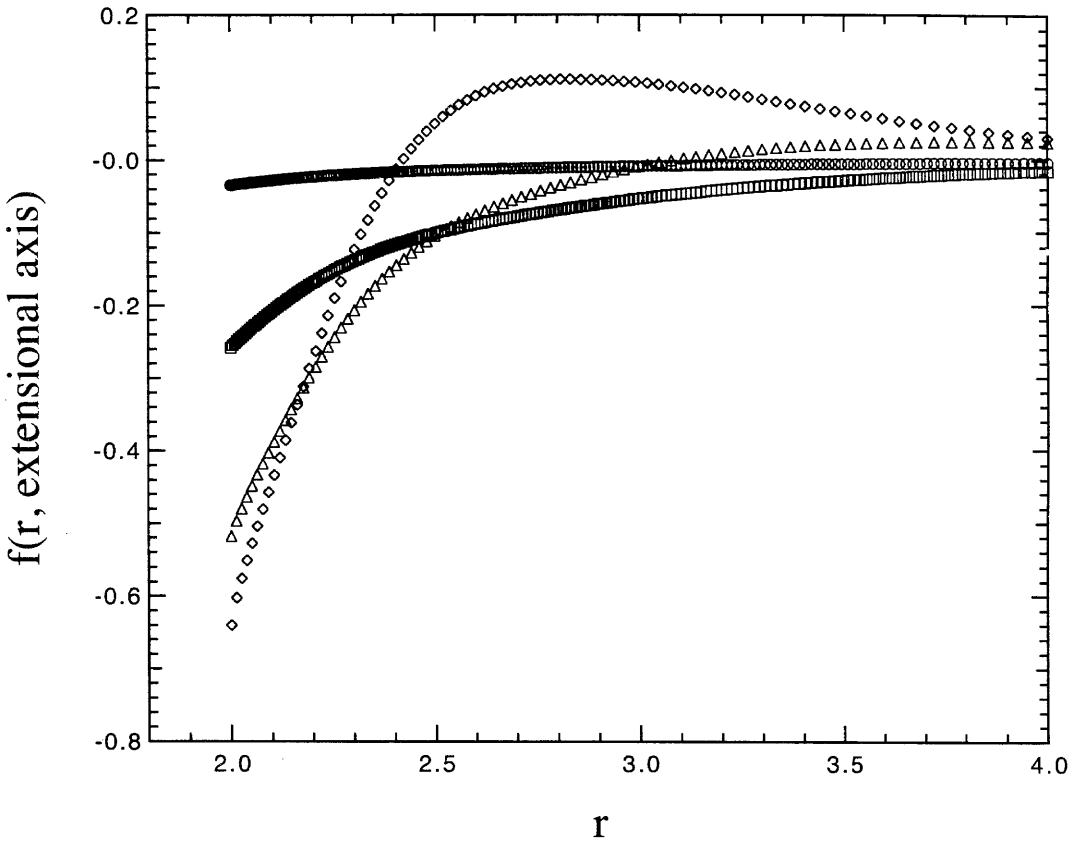

Figure 3.23: Results for f along the extensional axis as a function of separation, r, for $Pe=0.1$ ($\circ$), $Pe=1$ ($\square$), $Pe=4$ ($\triangle$) and $Pe=10$ ($\diamond$) for $b/a = 1.001$.

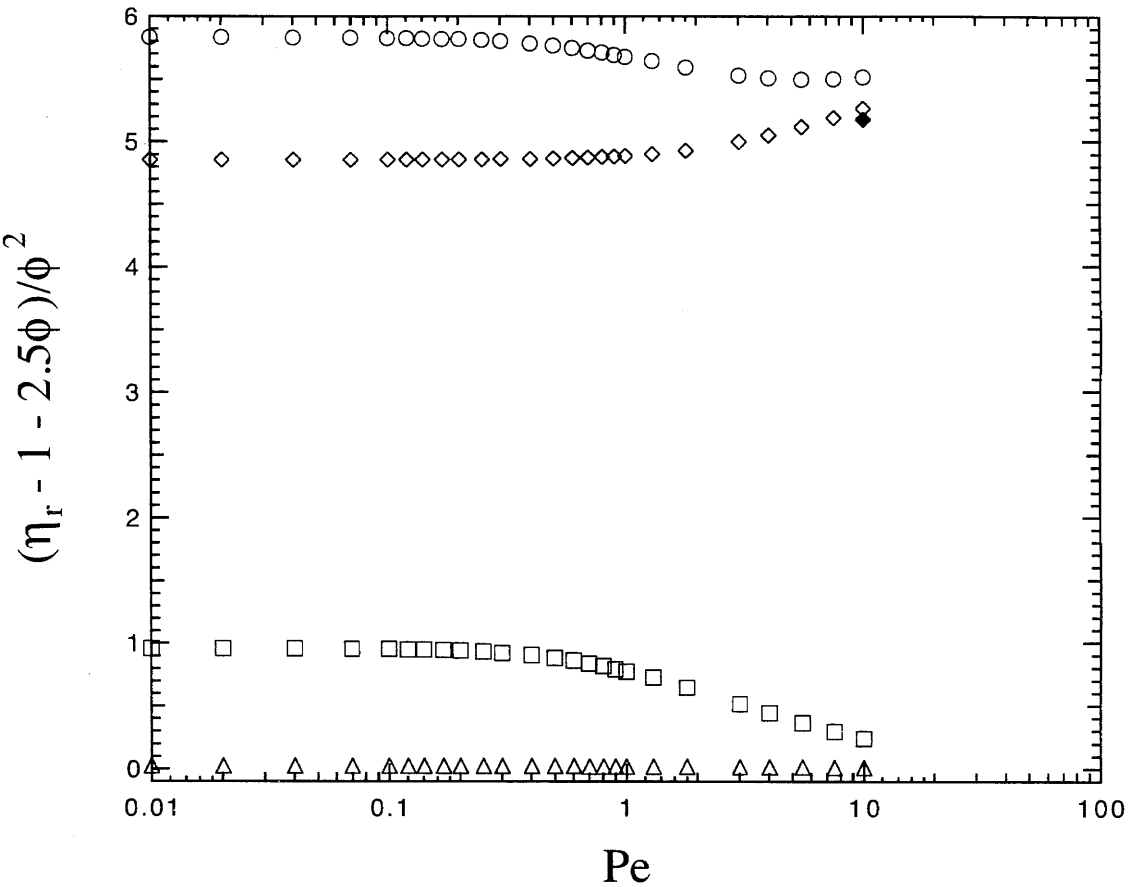

Figure 3.24: The $O(\phi^2)$ contributions to the relative shear viscosity, η_r, as a function of Peclet number, $Pe = 6\pi\eta_s\dot{\gamma}a^3/kT$, for $b/a = 1.001$. Hydrodynamic ($\diamond$), Brownian ($\square$) and interparticle force ($\triangle$) contributions to the total ($\circ$) viscosity are reported. At $Pe = 10$ a second calculation (solid diamond) is performed in which the hydrodynamic stress consists of two parts — the equilibrium contribution and the contribution from the deformation of the equilibrium microstructure for $(r-2)Pe \leq 6$. The two calculations at $Pe = 10$ yield slightly different values since $O(1)$ variations of the nonequilibrium microstructure outside of the boundary layer are important.

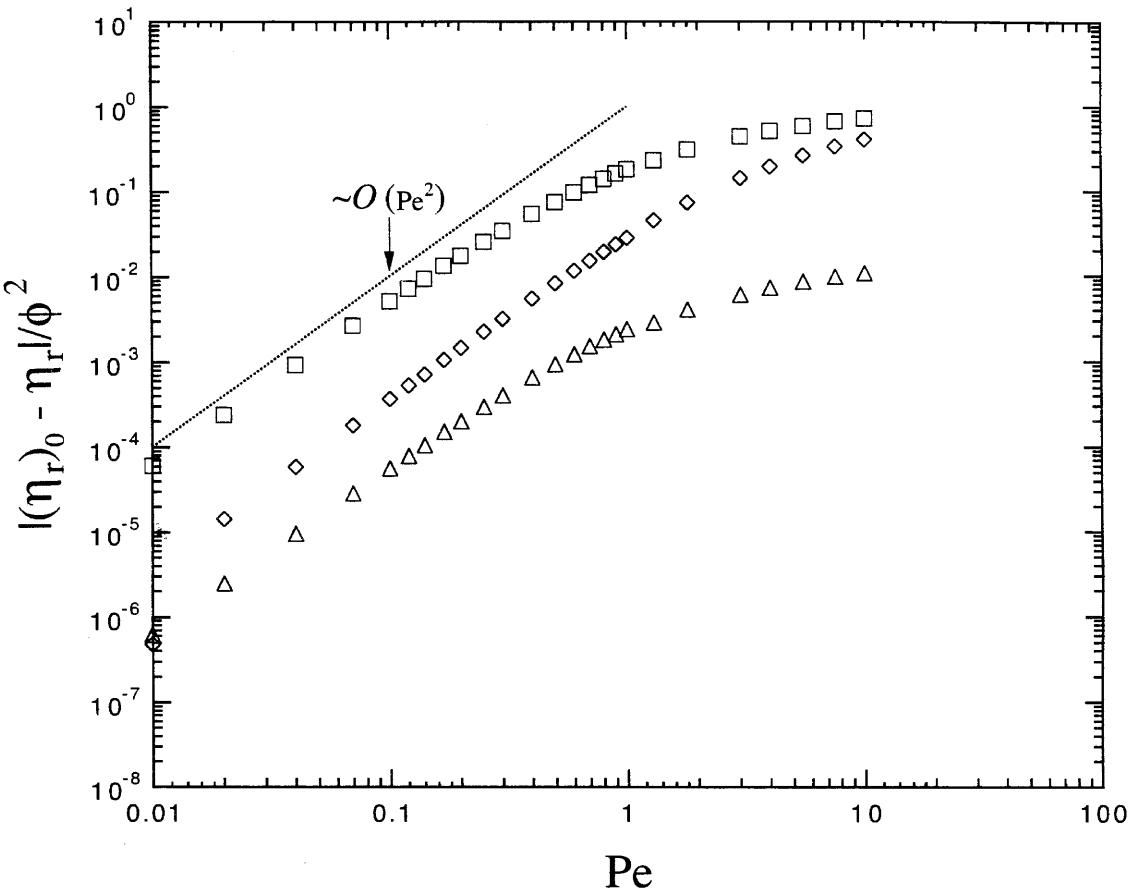

Figure 3.25: Results for the relative shear viscosity, η_r, as a function of Peclet number, $Pe = 6\pi\eta_s\dot{\gamma}a^3/kT$, are used to show the $O(\phi^2 Pe^2)$ contributions when $Pe \ll 1$ and $b/a = 1.001$. The relative shear viscosity at the given Peclet number is subtracted from the low shear limit of the relative viscosity, $(\eta_r)_0$, for the hydrodynamic ($\diamond$), Brownian ($\square$) and interparticle force ($\triangle$) contributions. The dashed line is drawn to guide the eye.

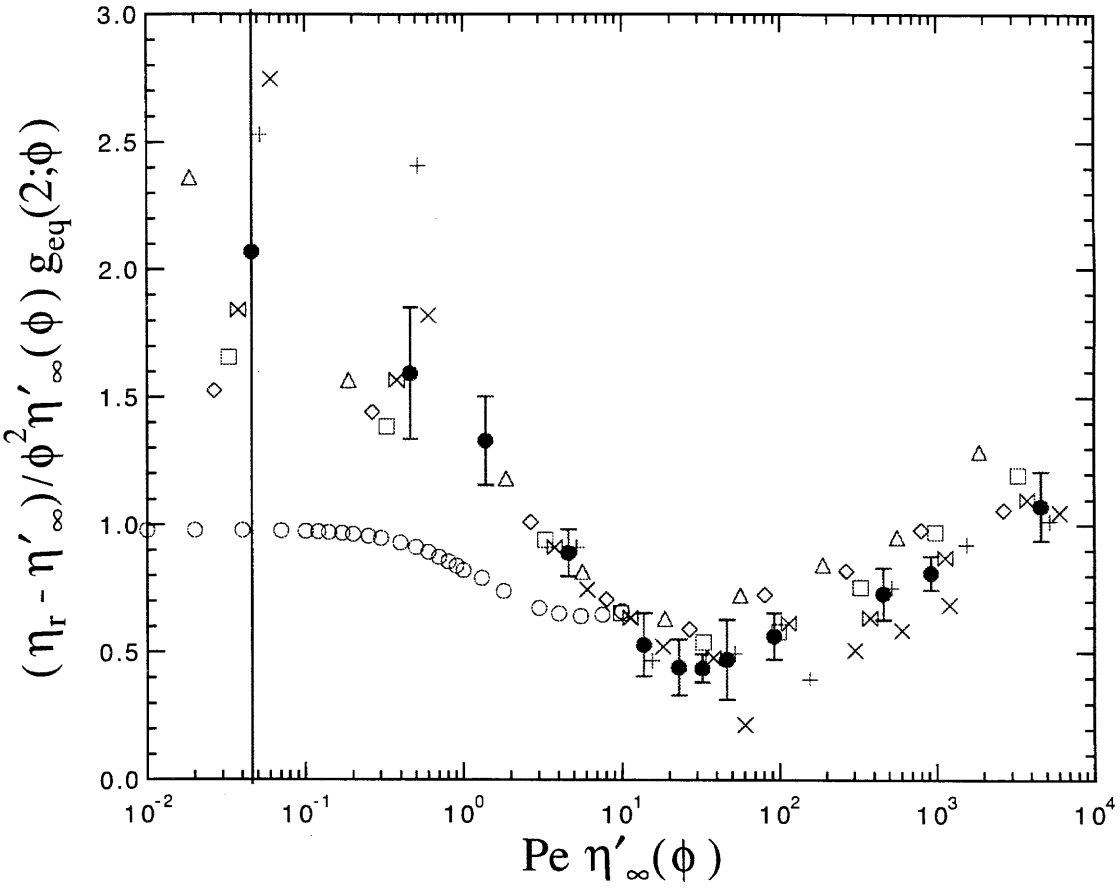

Figure 3.26: Results for the scaled shear viscosity as a function of Peclet number, $Pe = 6\pi\eta_s\dot{\gamma}a^3/kT$, using the scaling theory of Brady (1993b). Numerical results of this work (○) are compared with the Stokesian Dynamics simulations of Foss *et al.* (1999) for $\phi = 0.316$ (△), $\phi = 0.37$ (◇), $\phi = 0.40$ (□), $\phi = 0.419$ (⋈), $\phi = 0.45$ (•), $\phi = 0.47$ (+), and $\phi = 0.49$ (×).

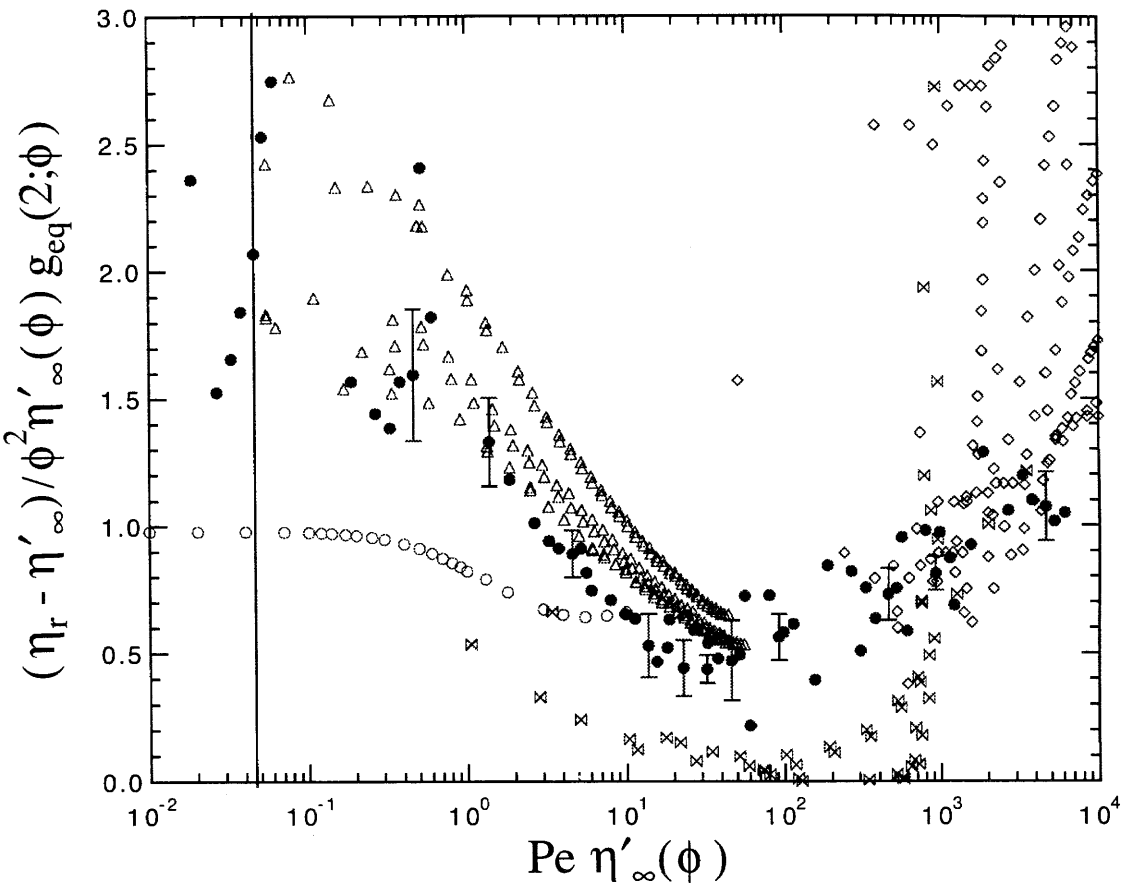

Figure 3.27: Results for the scaled shear viscosity as a function of Peclet number, $Pe = 6\pi\eta_s\dot{\gamma}a^3/kT$, using the scaling theory of Brady (1993b). Numerical results of this work (○) are compared with the Stokesian Dynamics simulations of Foss *et al.* (1999) (●) and the experimental results of van der Werff, de Kruif & Dhont (1989) (△), D'Haene, Mewis & Fuller (1993) (◇), and Bender & Wagner (1995) (⋈).

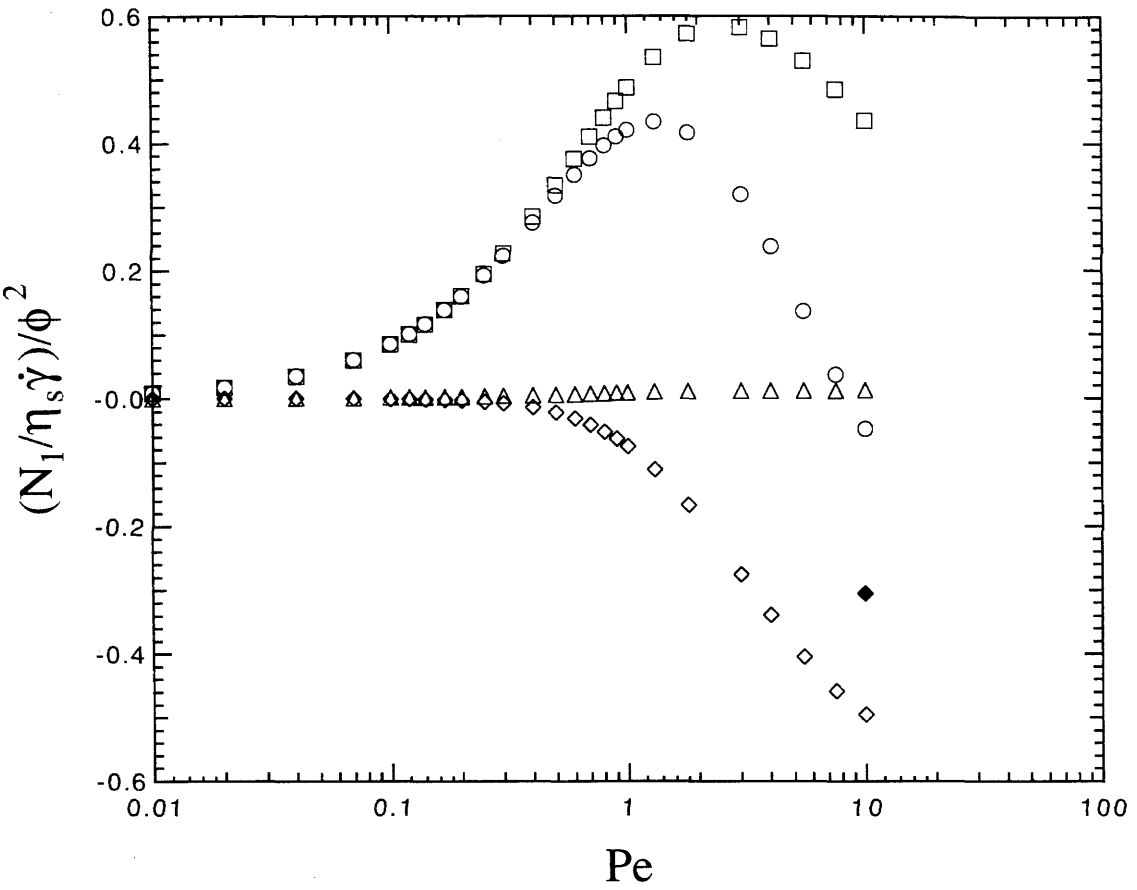

Figure 3.28: The $O(\phi^2)$ contributions to the nondimensional first normal stress difference, $N_1/\eta_s\dot{\gamma}$, as a function of Peclet number, $Pe = 6\pi\eta_s\dot{\gamma}a^3/kT$, for $b/a = 1.001$. Hydrodynamic ($\diamond$), Brownian ($\square$) and interparticle force ($\triangle$) contributions to the total ($\circ$) first normal stress difference are reported. At $Pe = 10$ a second calculation (solid diamond) is performed in which the hydrodynamic stress consists of two parts — the equilibrium contribution and the contribution from the deformation of the equilibrium microstructure for $(r-2)Pe \leq 6$.

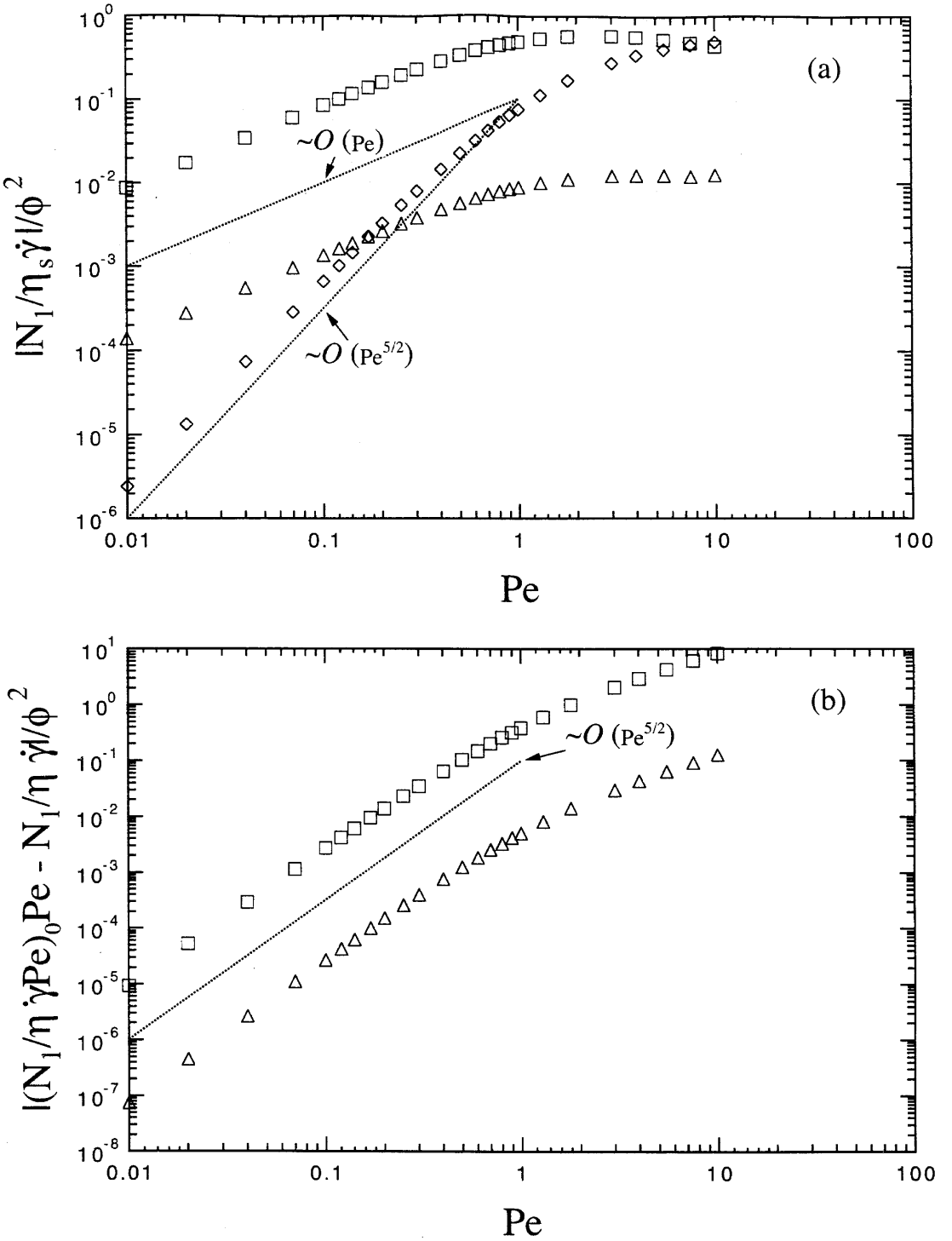

Figure 3.29: Results for the nondimensional first normal stress difference, $N_1/\eta_s\dot{\gamma}$, as a function of Peclet number, $Pe = 6\pi\eta_s\dot{\gamma}a^3/kT$, for $b/a = 1.001$ are used to show the (a) low Peclet behavior and (b) the next correction for $Pe \ll 1$. In (b), the value of $N_1/\eta_s\dot{\gamma}$ at the given Peclet number is subtracted from the low shear limit, $(N_1/\eta_s\dot{\gamma}Pe)_0Pe$, for the hydrodynamic ($\diamond$), Brownian ($\square$) and interparticle force ($\triangle$) contributions. The dashed lines are drawn to guide the eye.

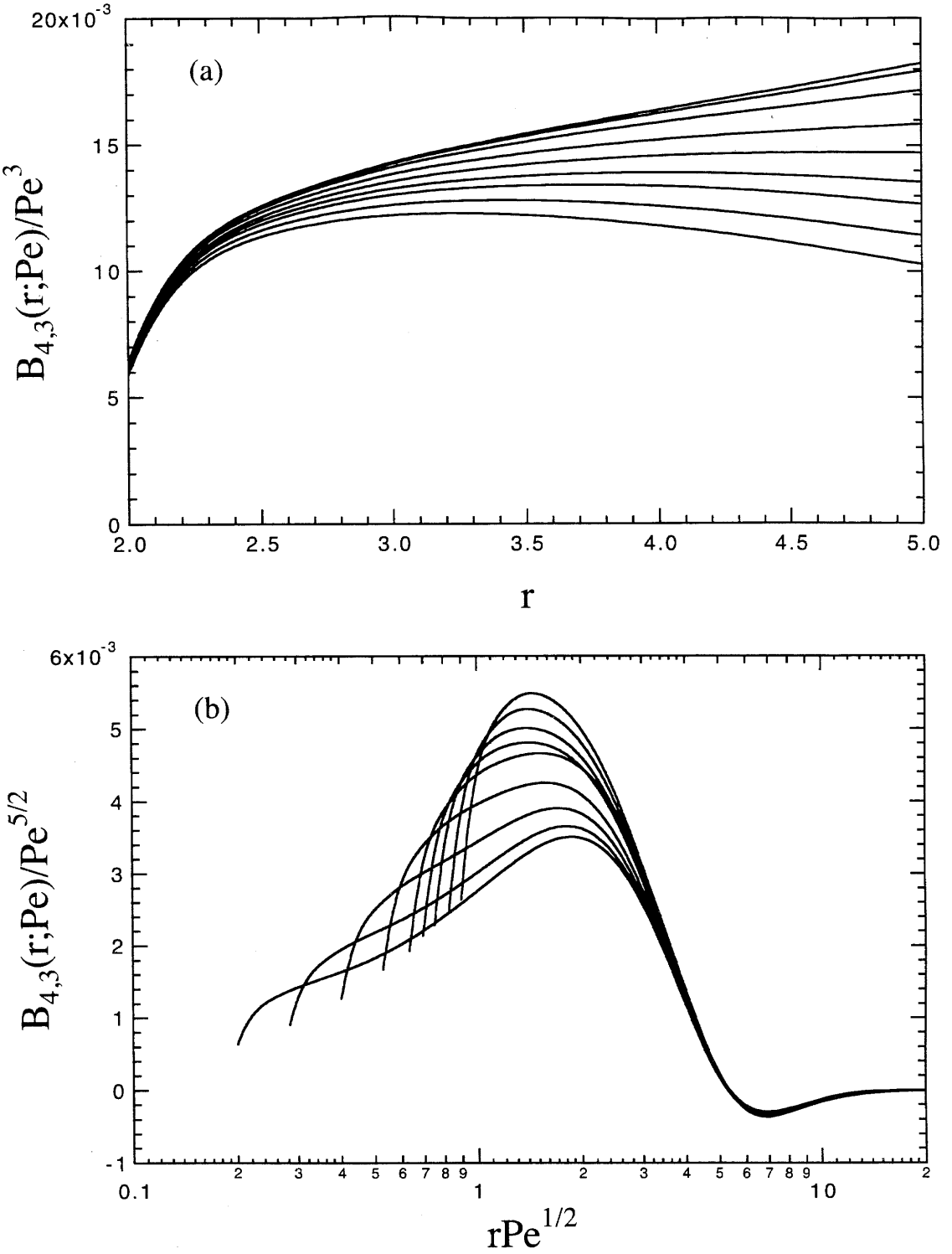

Figure 3.30: Results for the (a) near-field and (b) far-field behavior of $B_{4,3}$, one of the moments in the calculation of the first normal stress difference, for $Pe = 0.01$, 0.02, 0.04, 0.07, 0.1, 0.12, 0.14, 0.17, and 0.20. Near particle contact, $B_{4,3} \sim O(Pe^3)$ and the inner expansion yields an $O(Pe^3)$ contribution to N_1. In the far-field, $B_{4,3} \sim O(Pe^{5/2})$ and the outer expansion yields an $O(Pe^{5/2})$ contribution to N_1 for $Pe \ll 1$.

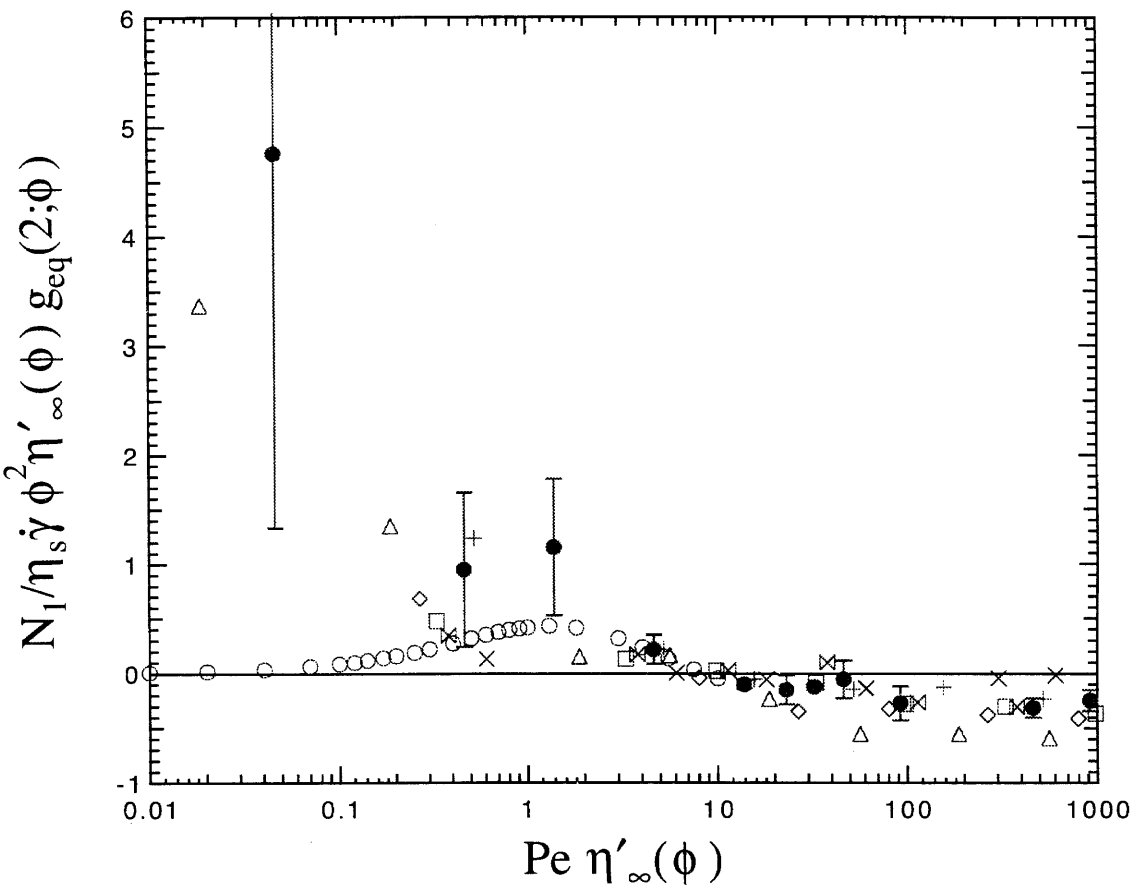

Figure 3.31: Results for the scaled first normal stress difference as a function of Peclet number, $Pe = 6\pi\eta_s\dot{\gamma}a^3/kT$, using the scaling theory of Brady (1993b). Numerical results of this work ($\circ$) are compared with the Stokesian Dynamics simulations of Foss *et al.* (1999) for $\phi = 0.316$ ($\triangle$), $\phi = 0.37$ ($\diamond$), $\phi = 0.40$ ($\square$), $\phi = 0.419$ ($\bowtie$), $\phi = 0.45$ ($\bullet$), $\phi = 0.47$ ($+$), and $\phi = 0.49$ ($\times$).

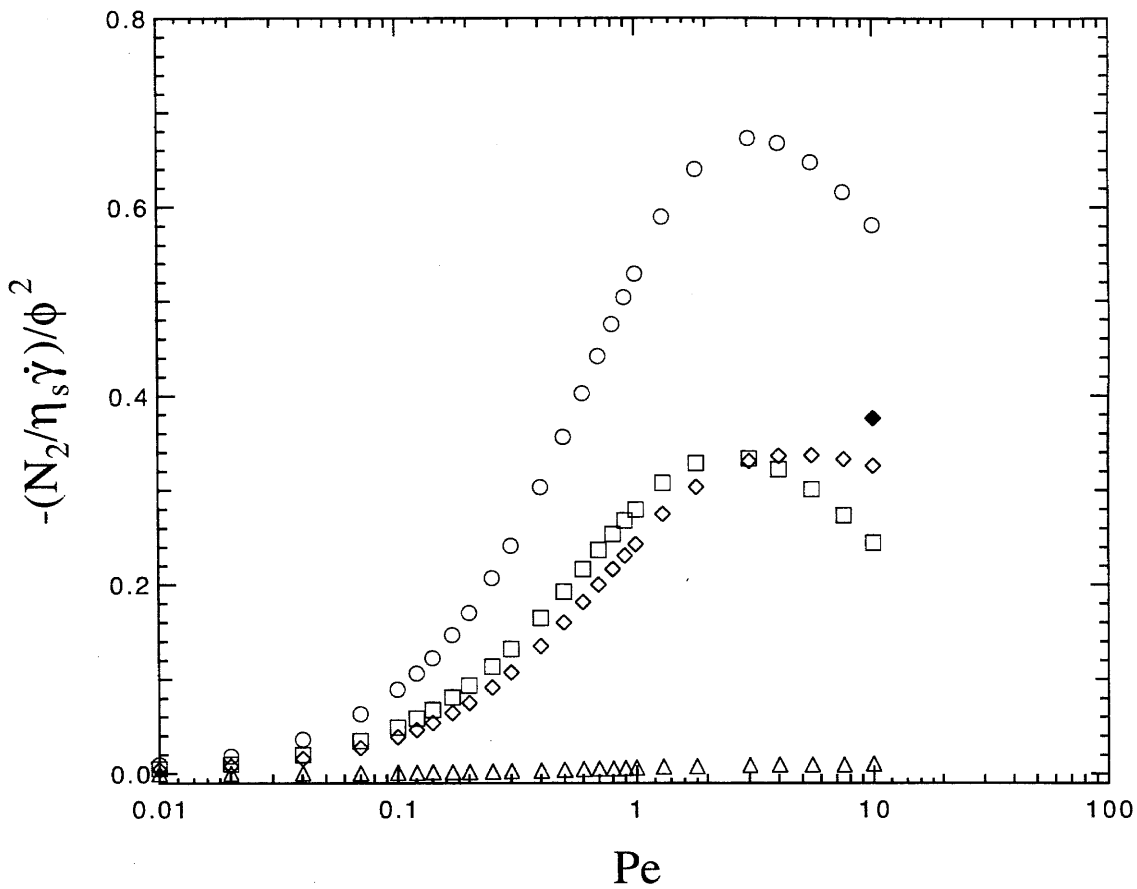

Figure 3.32: The $O(\phi^2)$ contributions to the nondimensional second normal stress difference, $N_2/\eta_s\dot{\gamma}$, as a function of Peclet number, $Pe = 6\pi\eta_s\dot{\gamma}a^3/kT$, for $b/a = 1.001$. Hydrodynamic ($\diamond$), Brownian ($\square$) and interparticle force ($\triangle$) contributions to the total ($\circ$) second normal stress difference are reported. At $Pe = 10$ a second calculation (solid diamond) is performed in which the hydrodynamic stress consists of two parts — the equilibrium contribution and the contribution from the deformation of the equilibrium microstructure for $(r-2)Pe \leq 6$.

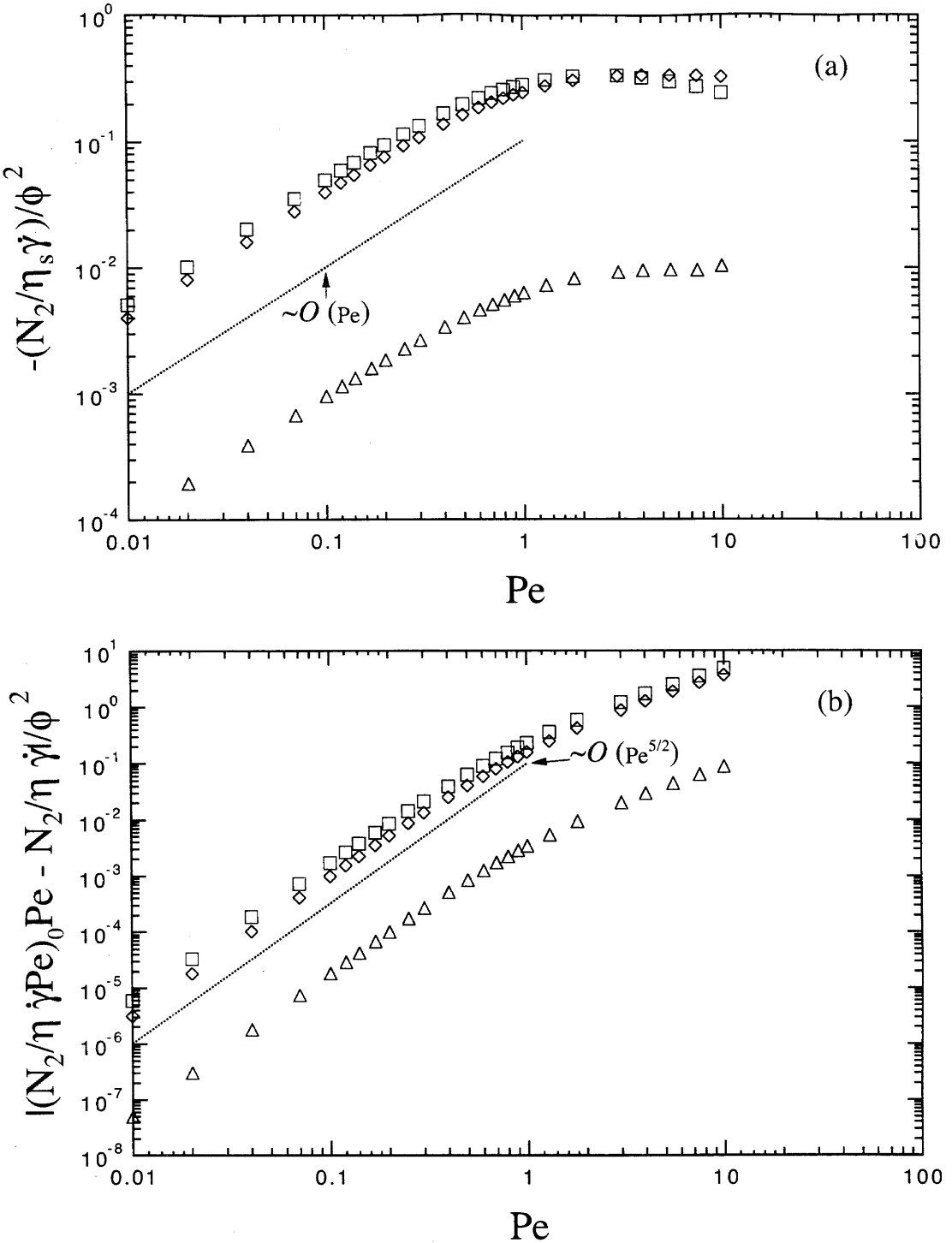

Figure 3.33: Results for the nondimensional second normal stress difference, $N_2/\eta_s\dot{\gamma}$, as a function of Peclet number, $Pe = 6\pi\eta_s\dot{\gamma}a^3/kT$, for $b/a = 1.001$ are used to show the (a) low Peclet behavior and (b) the next correction for $Pe \ll 1$. In (b), the value of $N_2/\eta_s\dot{\gamma}$ at the given Peclet number is subtracted from the low shear limit, $(N_2/\eta_s\dot{\gamma}Pe)_0 Pe$, for the hydrodynamic ($\diamond$), Brownian ($\square$) and interparticle force ($\triangle$) contributions. The dashed lines are drawn to guide the eye.

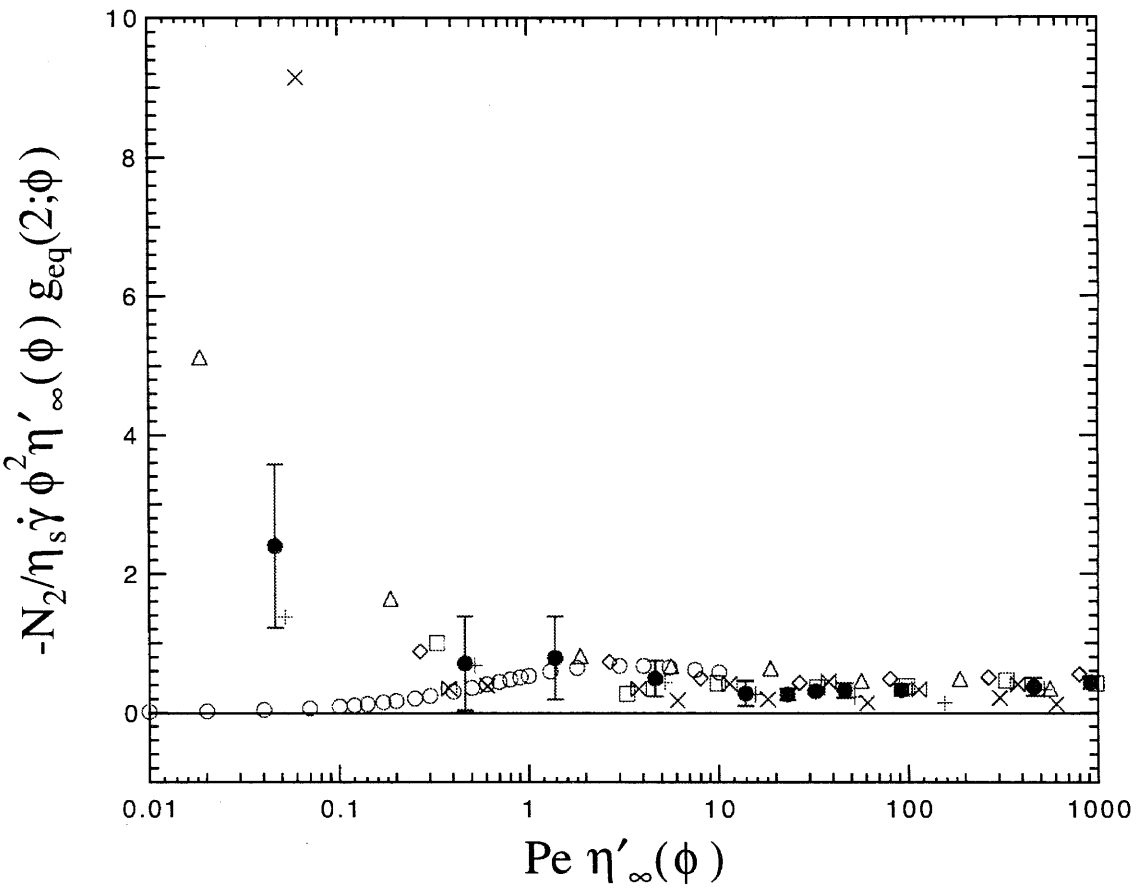

Figure 3.34: Results for the scaled second normal stress difference as a function of Peclet number, $Pe = 6\pi\eta_s\dot{\gamma}a^3/kT$, using the scaling theory of Brady (1993b). Numerical results of this work ($\circ$) are compared with the Stokesian Dynamics simulations of Foss *et al.* (1999) for $\phi = 0.316$ ($\triangle$), $\phi = 0.37$ ($\diamond$), $\phi = 0.40$ ($\square$), $\phi = 0.419$ ($\bowtie$), $\phi = 0.45$ ($\bullet$), $\phi = 0.47$ ($+$), and $\phi = 0.49$ ($\times$).

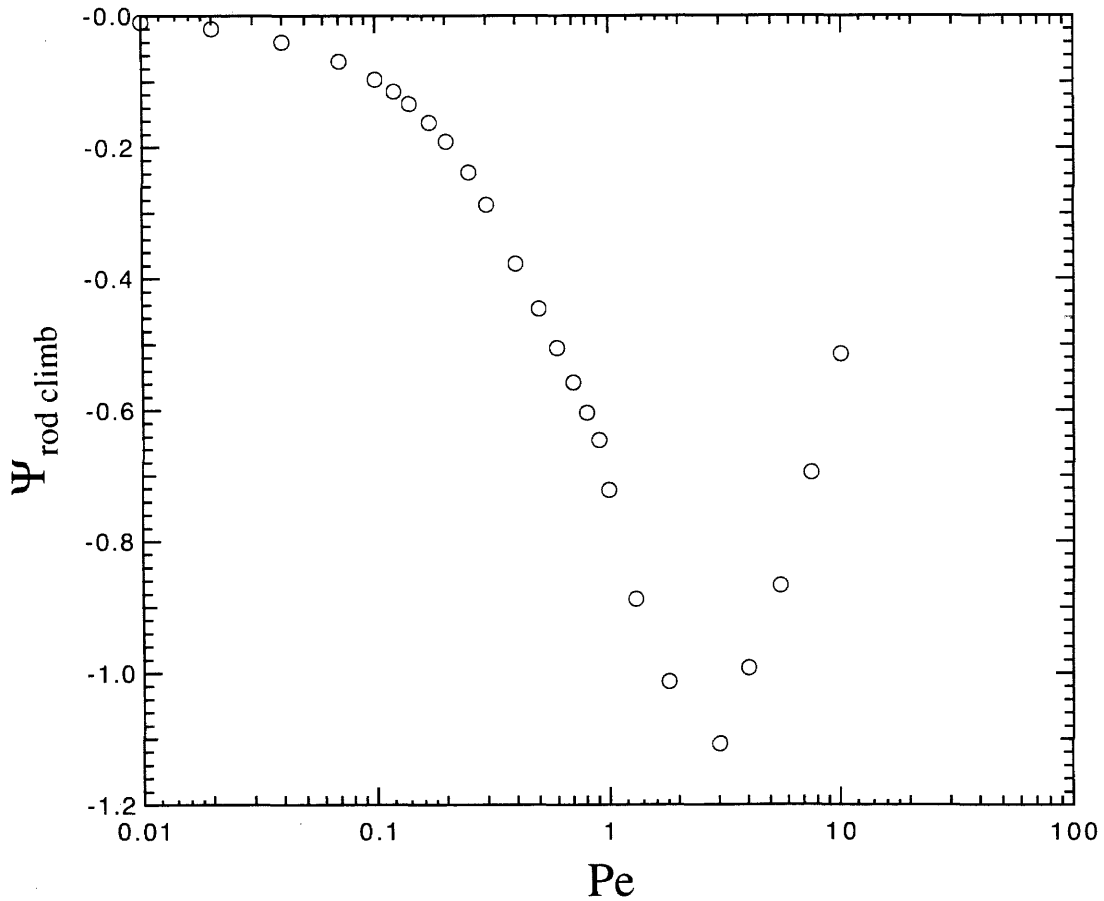

Figure 3.35: Results for the rod climbing variable, $\psi_{rod\ climb} = r\left(\partial p_{zz}/\partial r\right)/\eta_s\dot{\gamma}\phi^2$, as a function of Peclet number, $Pe = 6\pi\eta_s\dot{\gamma}a^3/kT$, using the numerical results for $b/a = 1.001$ (o). Since the rod climbing variable is negative for all values of Peclet number, only negative rod climbing should occur.

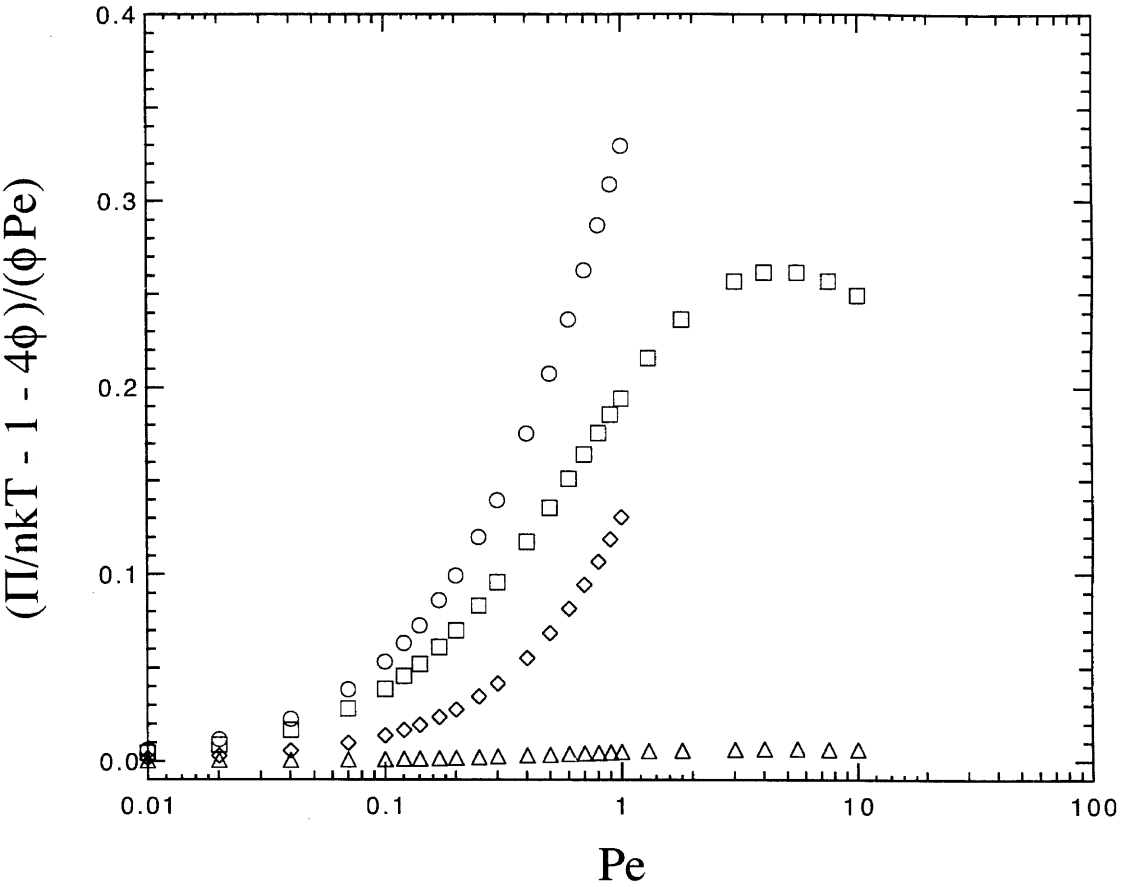

Figure 3.36: The $O(\phi^2)$ contribution to the nondimensional osmotic pressure, Π/nkT, as a function of Peclet number, $Pe = 6\pi\eta_s\dot{\gamma}a^3/kT$, for $b/a = 1.001$. Hydrodynamic ($\diamond$), Brownian ($\square$) and interparticle force ($\triangle$) contributions to the total ($\circ$) osmotic pressure are reported..

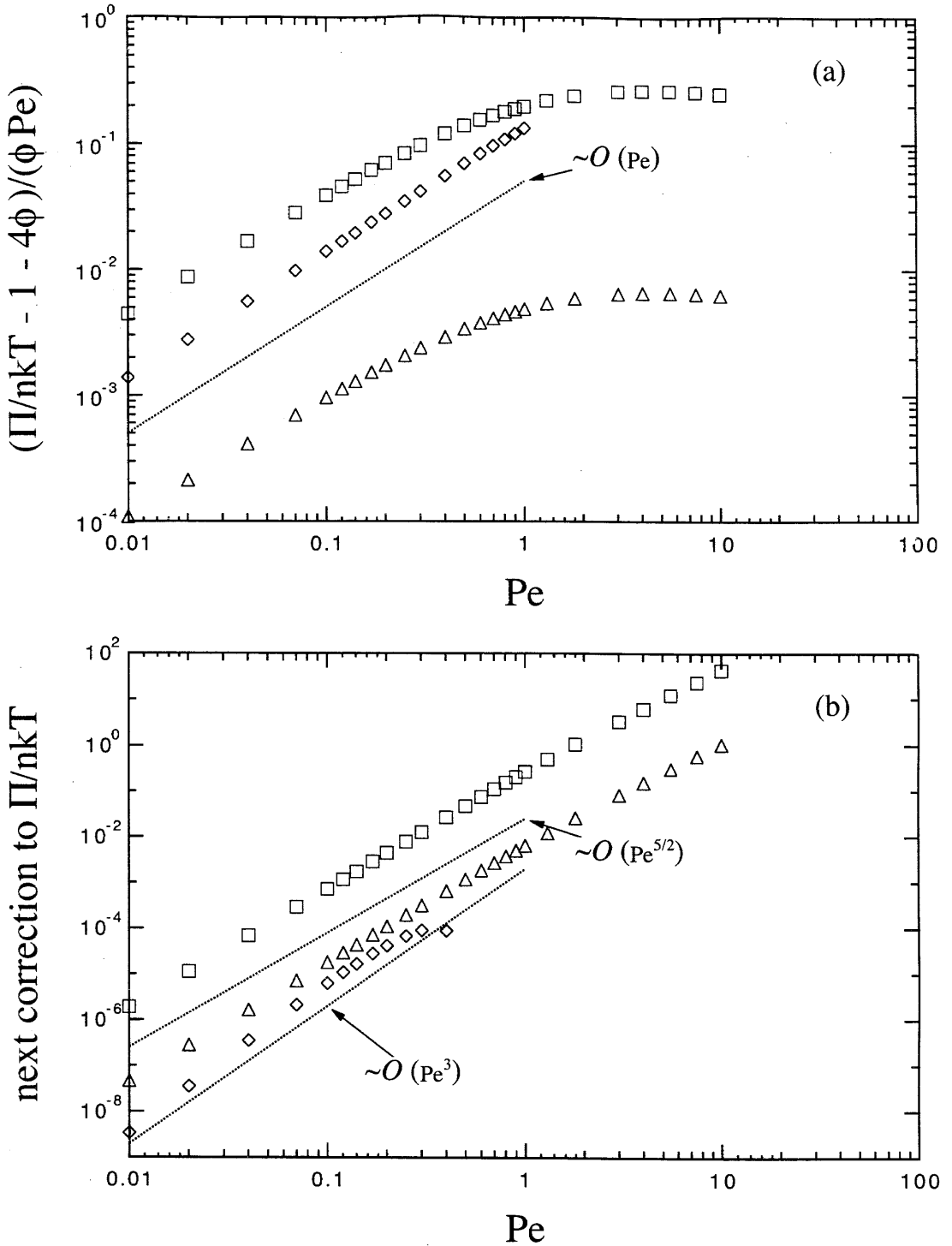

Figure 3.37: Results for the nondimensional osmotic pressure, Π/nkT, as a function of Peclet number, $Pe = 6\pi\eta_s\dot{\gamma}a^3/kT$, for $b/a = 1.001$ are used to show the (a) low Peclet behavior and (b) the next correction for $Pe \ll 1$. In (b), the value of Π/nkT at the given Peclet number is subtracted from its low shear limit for the hydrodynamic ($\diamond$), Brownian ($\square$) and interparticle force ($\triangle$) contributions. The dashed lines are drawn to guide the eye.

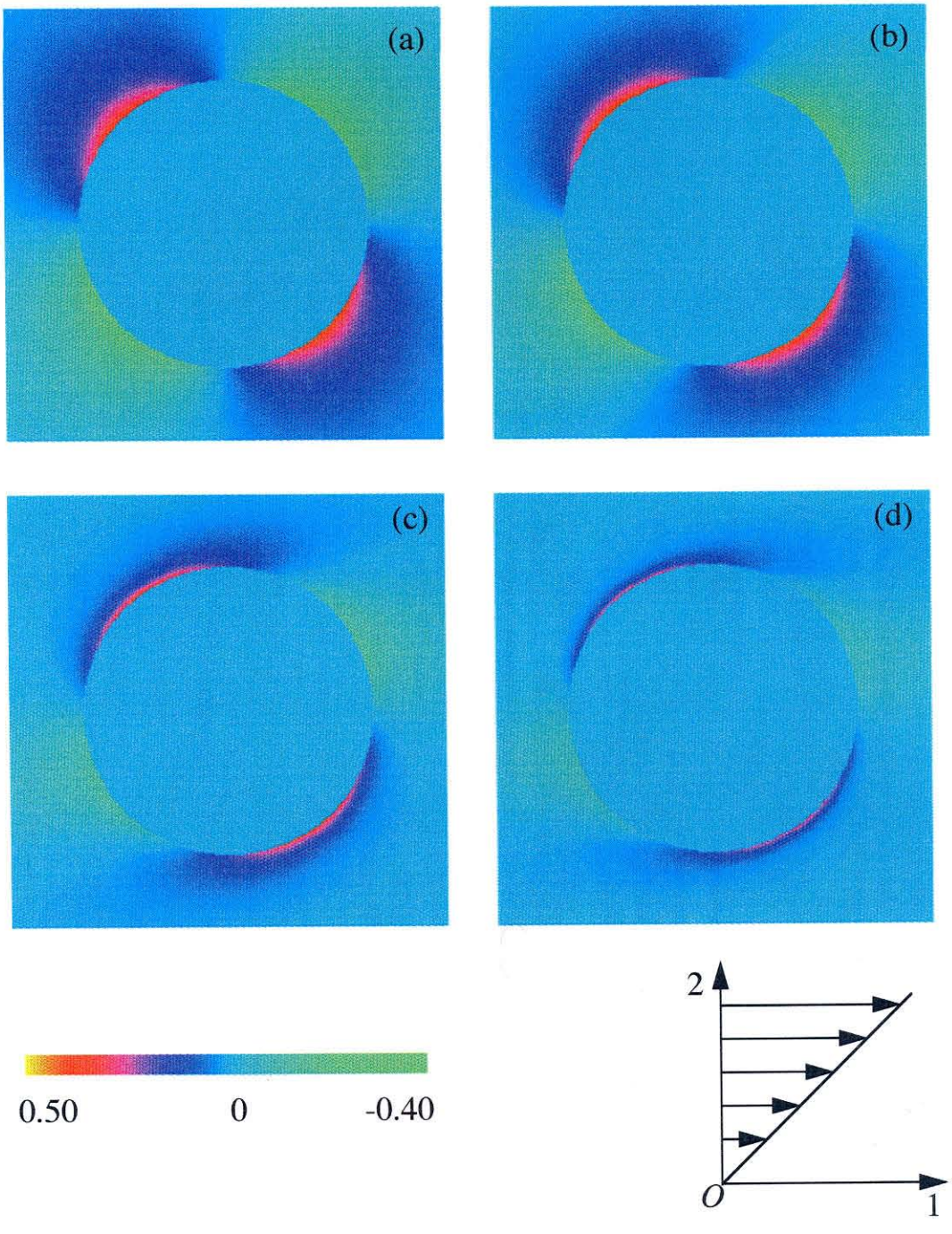

Figure 3.38: Results for f/Pe_b in the velocity–gradient plane at steady-state for (a) $Pe_b = 0.1$, (b) $Pe_b = 1$, (c) $Pe_b = 4$, and (d) $Pe_b = 10$, where f is the difference from the equilibrium microstructure and $Pe_b = 6\pi\eta_s\dot{\gamma}ab^2/kT$ for $b/a = 1.01$.

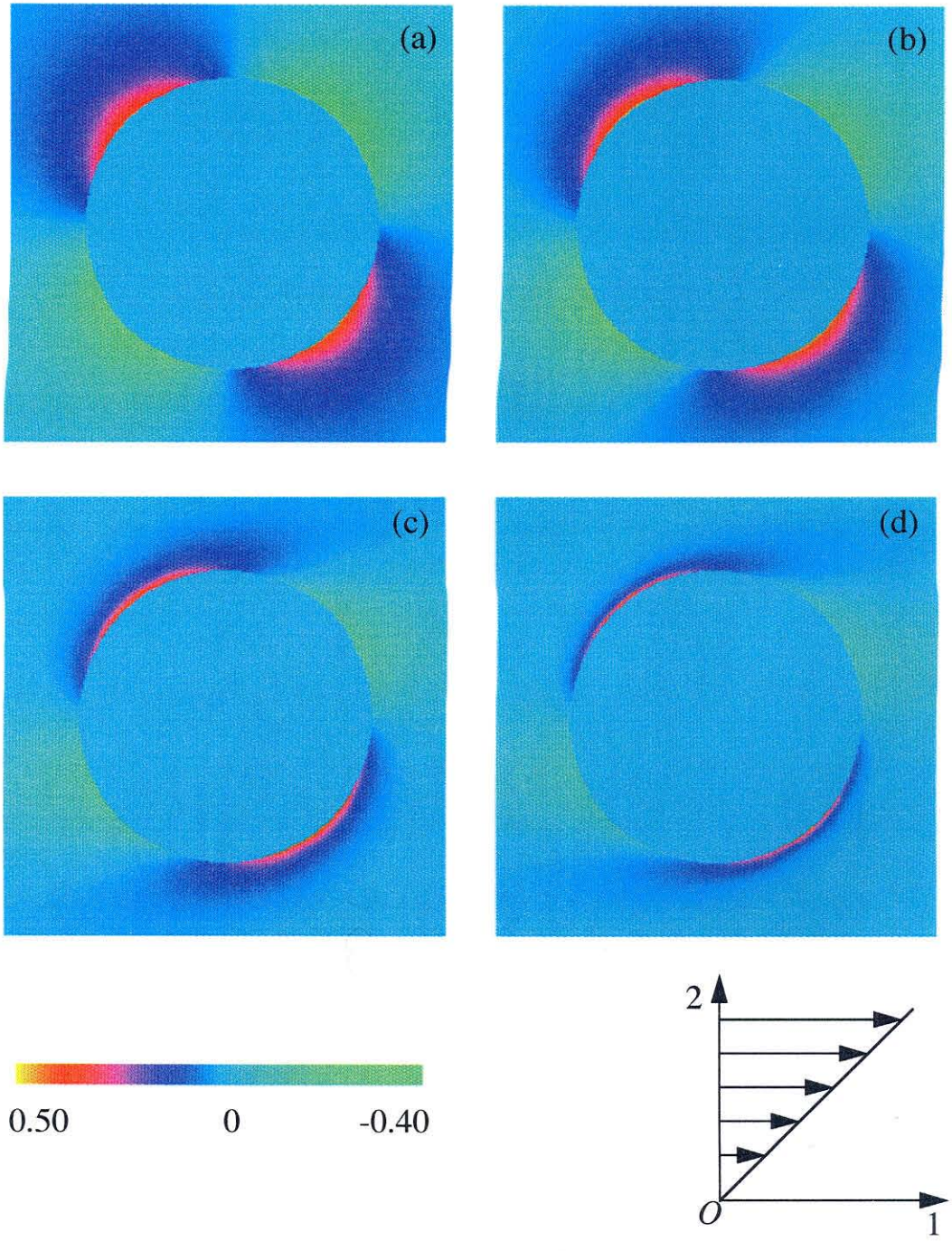

Figure 3.39: Results for f/Pe_b in the velocity–gradient plane at steady-state for (a) $Pe_b = 0.1$, (b) $Pe_b = 1$, (c) $Pe_b = 4$, and (d) $Pe_b = 10$, where f is the difference from the equilibrium microstructure and $Pe_b = 6\pi\eta_s\dot{\gamma}ab^2/kT$ for $b/a = 1.10$.

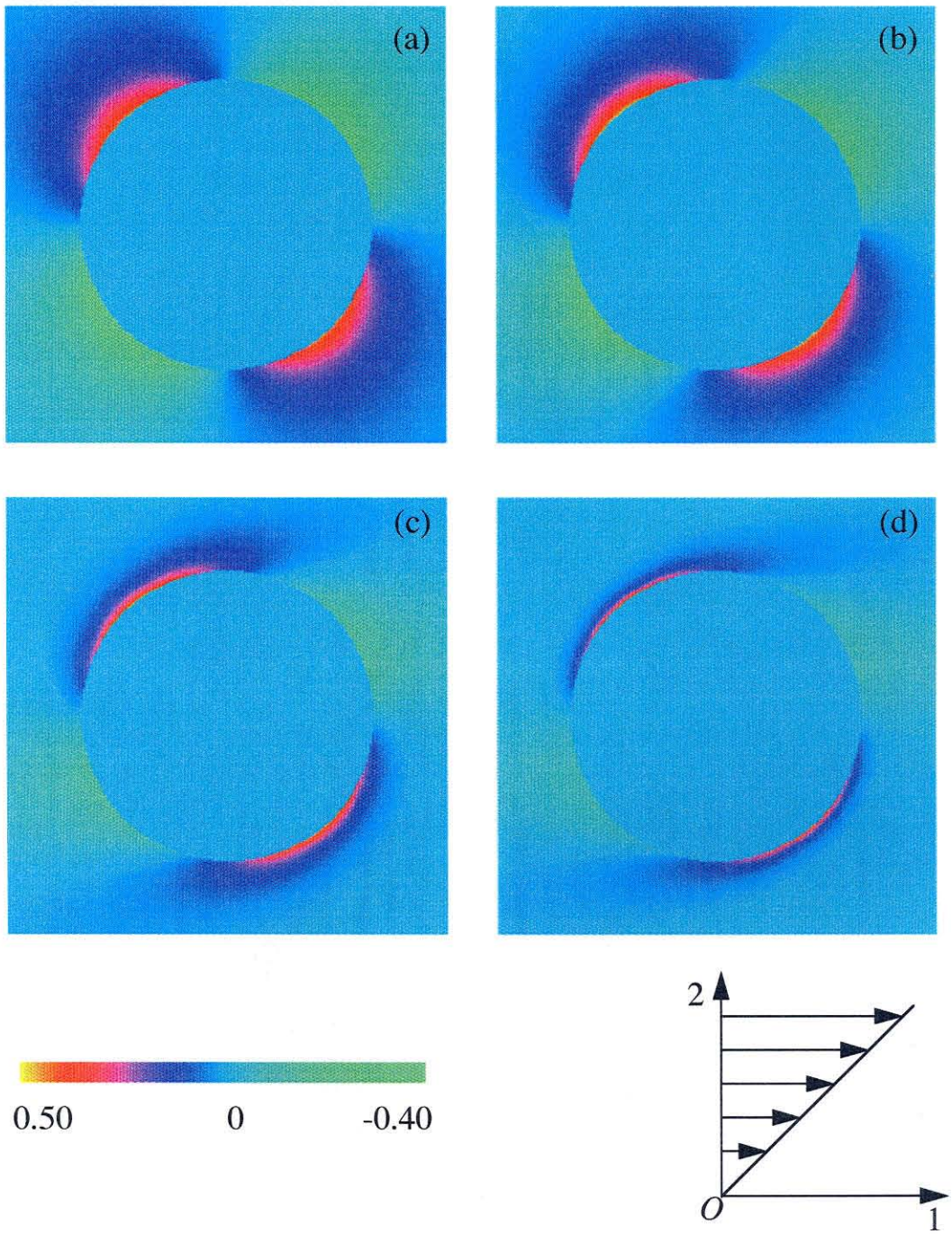

Figure 3.40: Results for f/Pe_b in the velocity–gradient plane at steady-state for (a) $Pe_b = 0.1$, (b) $Pe_b = 1$, (c) $Pe_b = 4$, and (d) $Pe_b = 10$, where f is the difference from the equilibrium microstructure and $Pe_b = 6\pi\eta_s\dot{\gamma}ab^2/kT$ for $b/a = 1.20$.

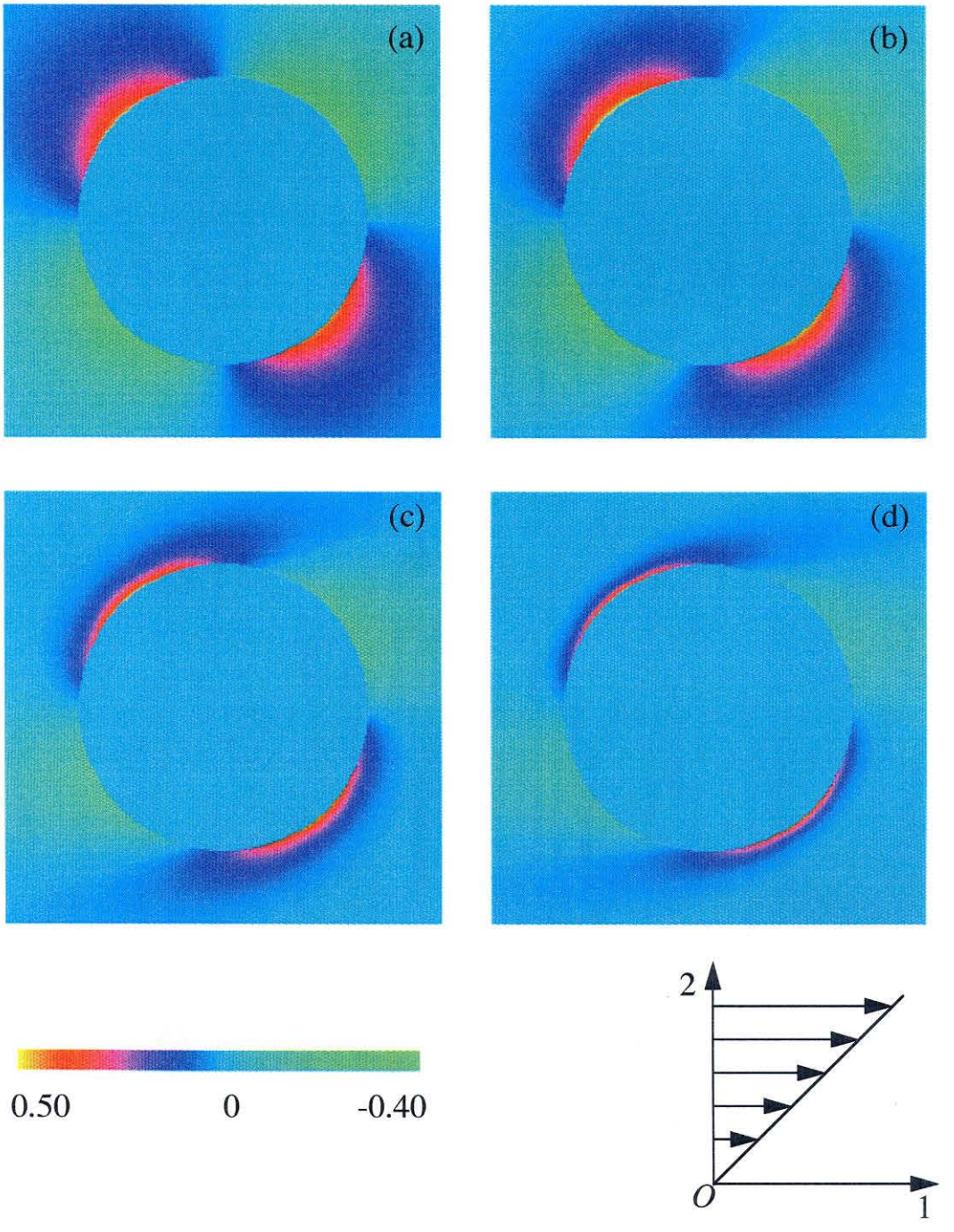

Figure 3.41: Results for f/Pe_b in the velocity–gradient plane at steady-state for (a) $Pe_b = 0.1$, (b) $Pe_b = 1$, (c) $Pe_b = 4$, and (d) $Pe_b = 10$, where f is the difference from the equilibrium microstructure and $Pe_b = 6\pi\eta_s\dot{\gamma}ab^2/kT$ for $b/a = 1.60$.

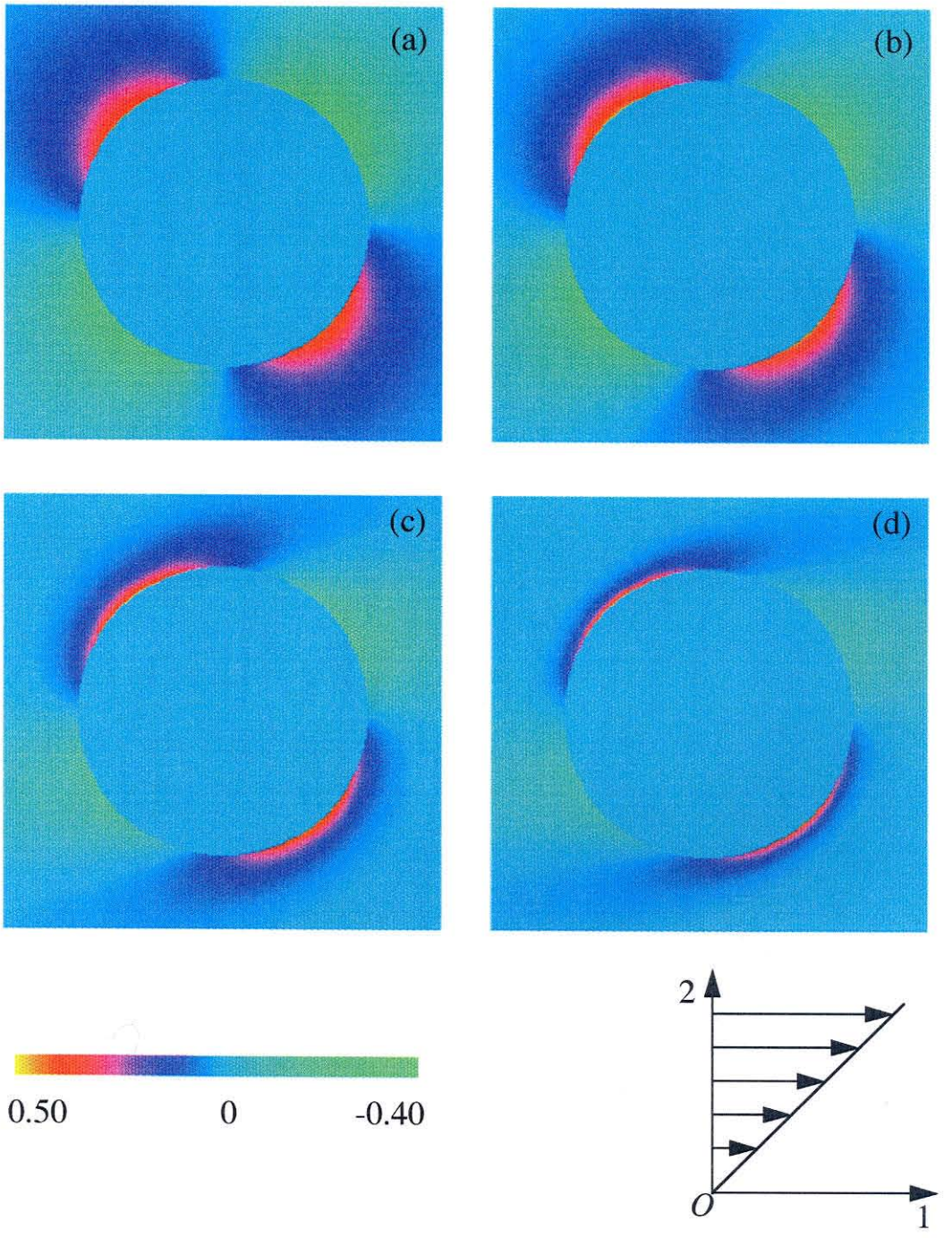

Figure 3.42: Results for f/Pe_b in the velocity–gradient plane at steady-state for (a) $Pe_b = 0.1$, (b) $Pe_b = 1$, (c) $Pe_b = 4$, and (d) $Pe_b = 10$, where f is the difference from the equilibrium microstructure and $Pe_b = 6\pi\eta_s\dot{\gamma}ab^2/kT$ for $b/a = 2.50$.

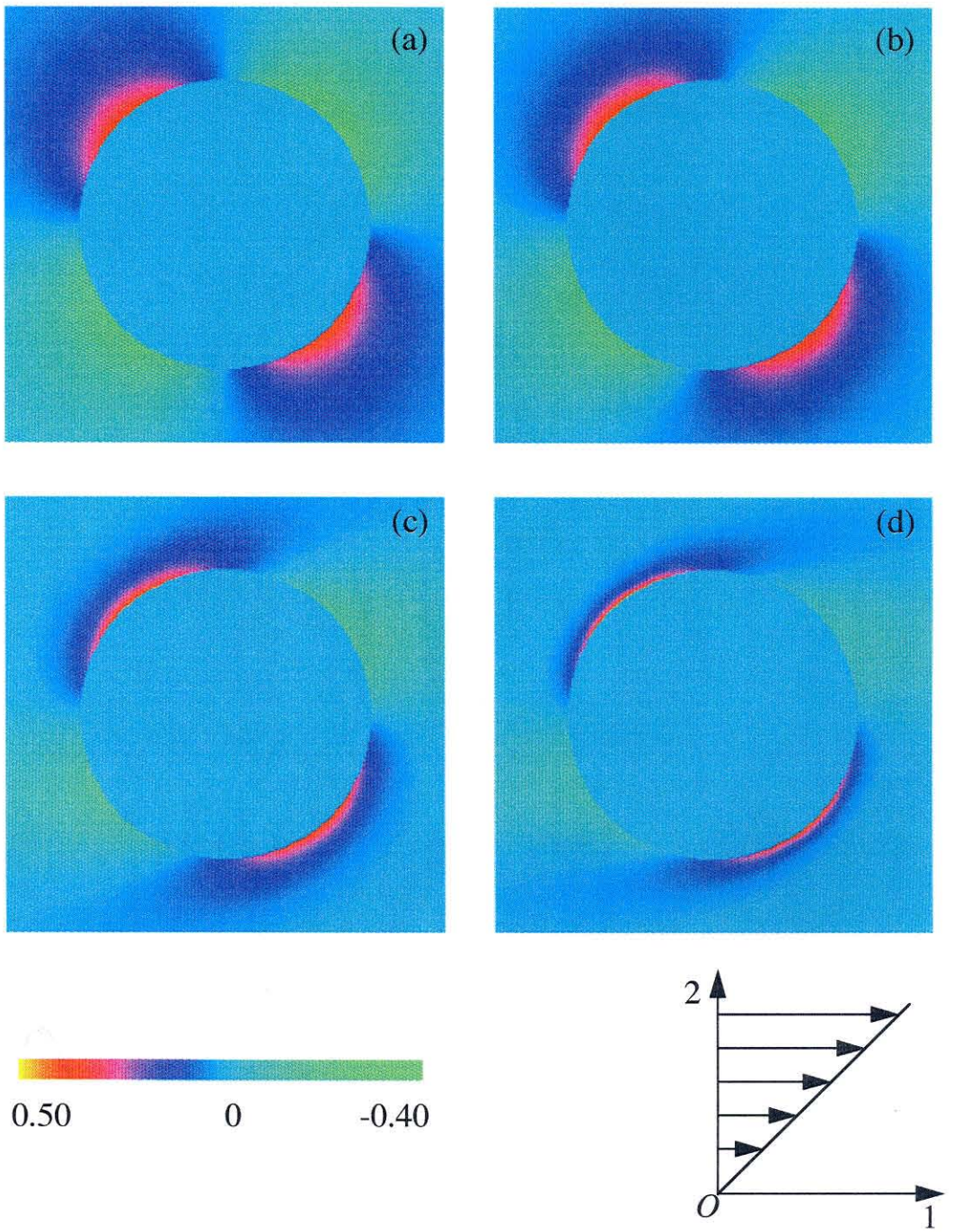

Figure 3.43: Results for f/Pe_b in the velocity–gradient plane at steady-state for (a) $Pe_b = 0.1$, (b) $Pe_b = 1$, (c) $Pe_b = 4$, and (d) $Pe_b = 10$, where f is the difference from the equilibrium microstructure and $Pe_b = 6\pi\eta_s\dot{\gamma}ab^2/kT$ for $b/a = 5.00$.

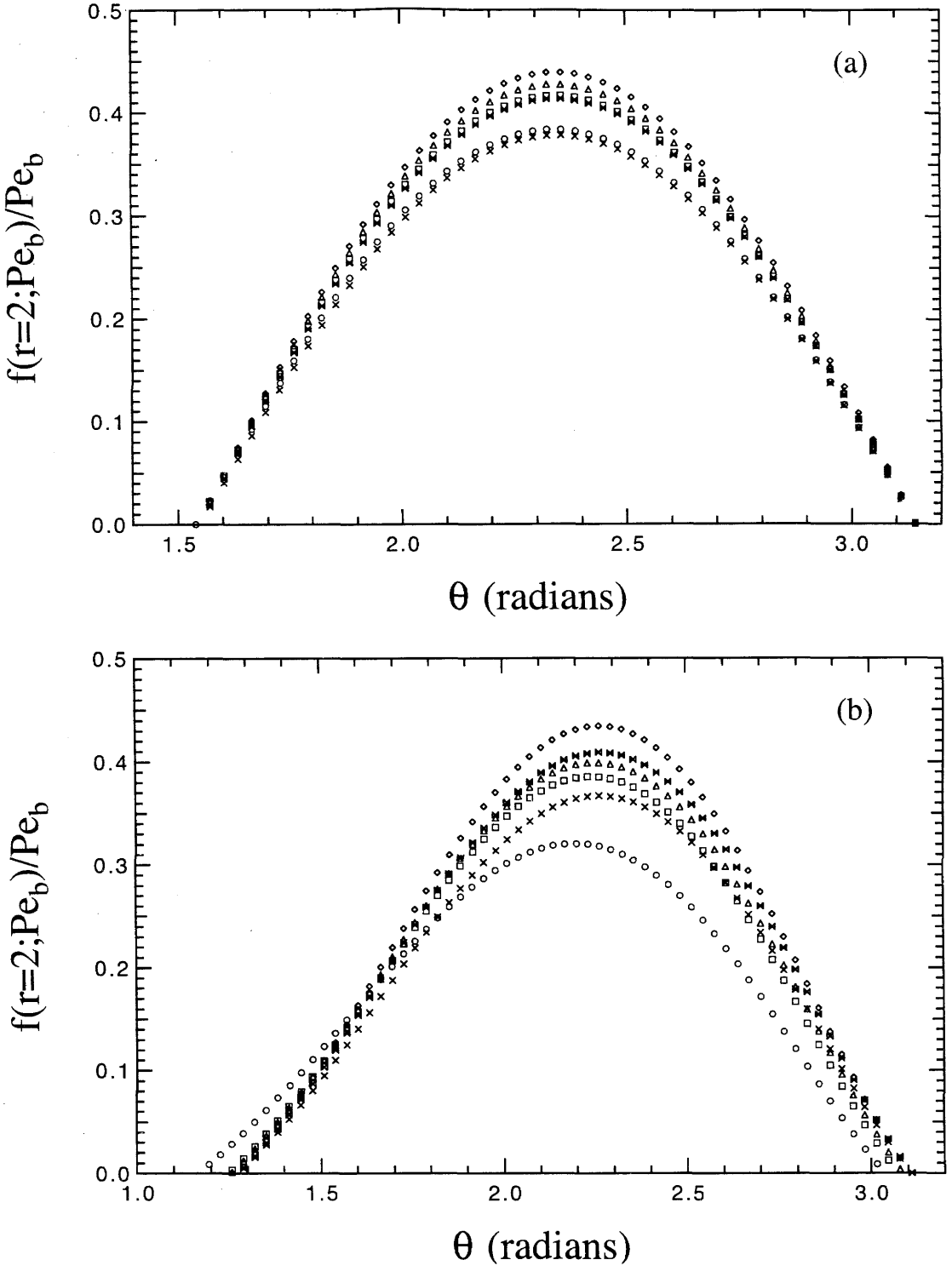

Figure 3.44: Results for f/Pe_b as a function of θ at particle contact, $r = 2$, in the velocity-gradient plane, for $b/a = 1.01$ ($\circ$), $b/a = 1.1$ ($\square$), $b/a = 1.2$ ($\triangle$), $b/a = 1.6$ ($\diamond$), $b/a = 2.5$ ($\bowtie$), and $b/a = 5.0$ ($\times$) when (a) $Pe_b = 1$ and (b) $Pe_b = 10$.

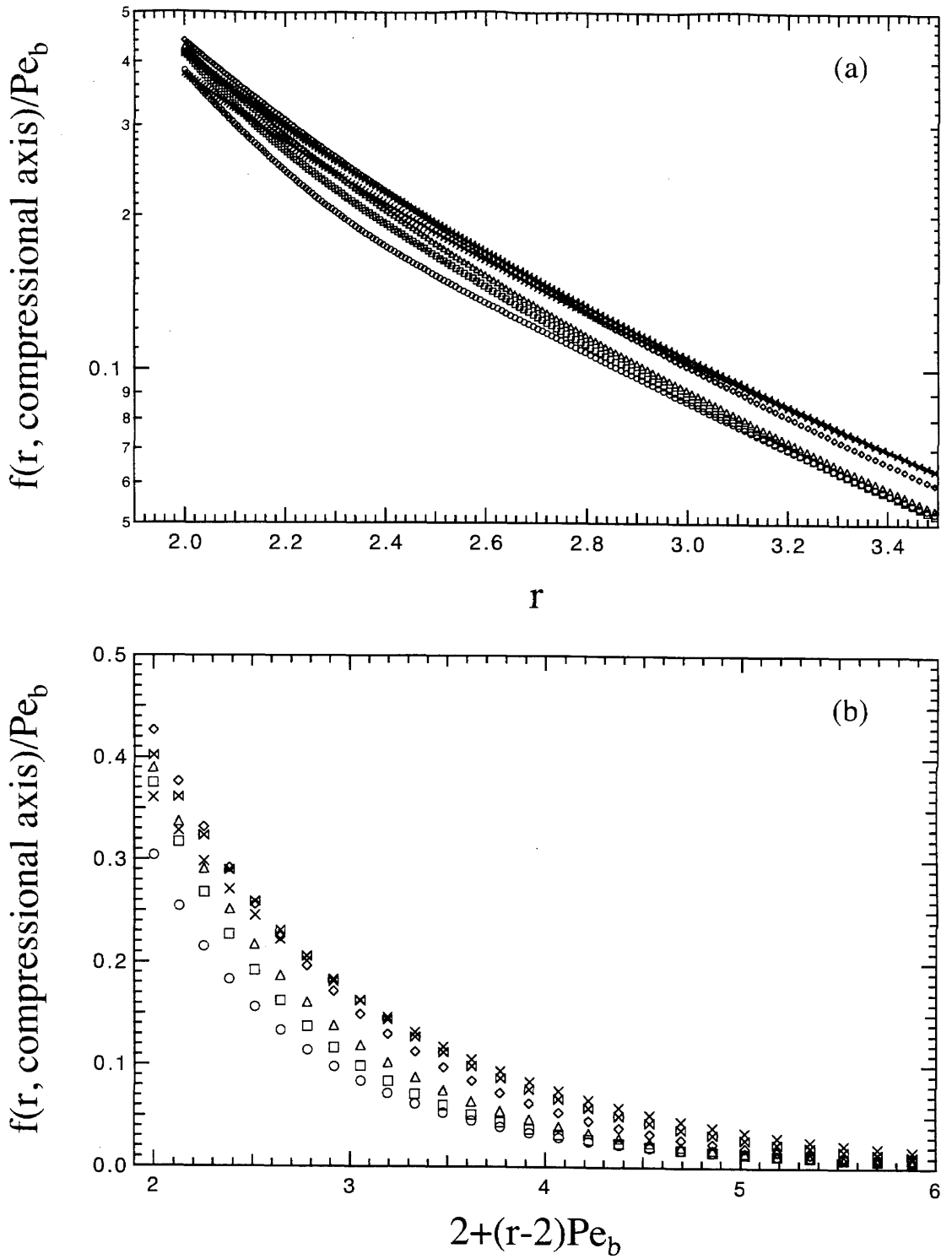

Figure 3.45: Results for f/Pe_b along the compressional axis as a function of (a) radius, r, at $Pe_b = 1$ and (b) boundary layer length, $2 + (r-2)Pe_b$, and $Pe_b = 10$ when $b/a = 1.01$ ($\circ$), $b/a = 1.1$ ($\square$), $b/a = 1.2$ ($\triangle$), $b/a = 1.6$ ($\diamond$), $b/a = 2.5$ ($\bowtie$), and $b/a = 5.0$ ($\times$).

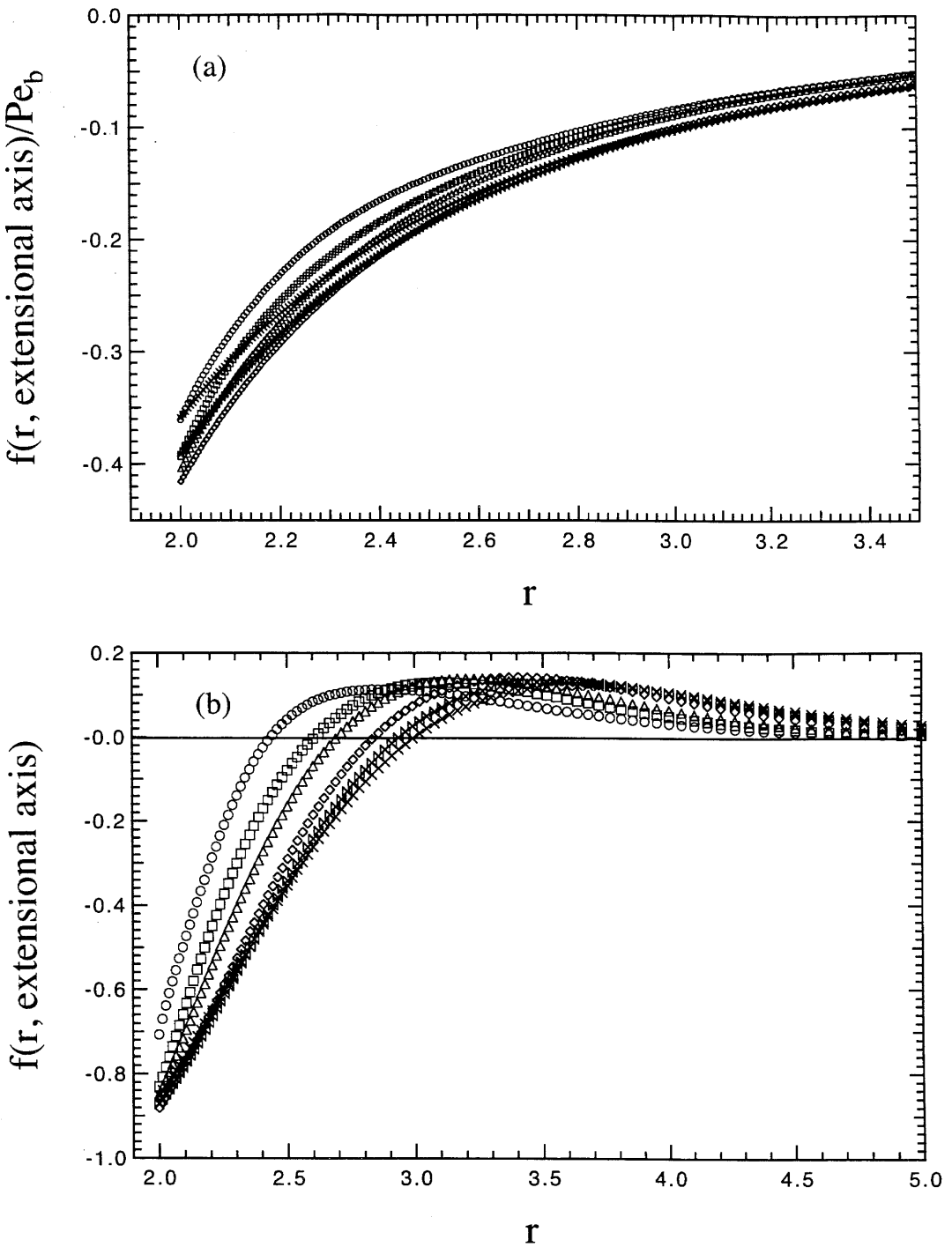

Figure 3.46: Results for f along the extensional axis as a function of radius, r, for (a) $Pe_b = 1$ and (b) $Pe = 10$ when $b/a = 1.01$ ($\circ$), $b/a = 1.1$ ($\square$), $b/a = 1.2$ ($\triangle$), $b/a = 1.6$ ($\diamond$), $b/a = 2.5$ ($\bowtie$), and $b/a = 5.0$ ($\times$).

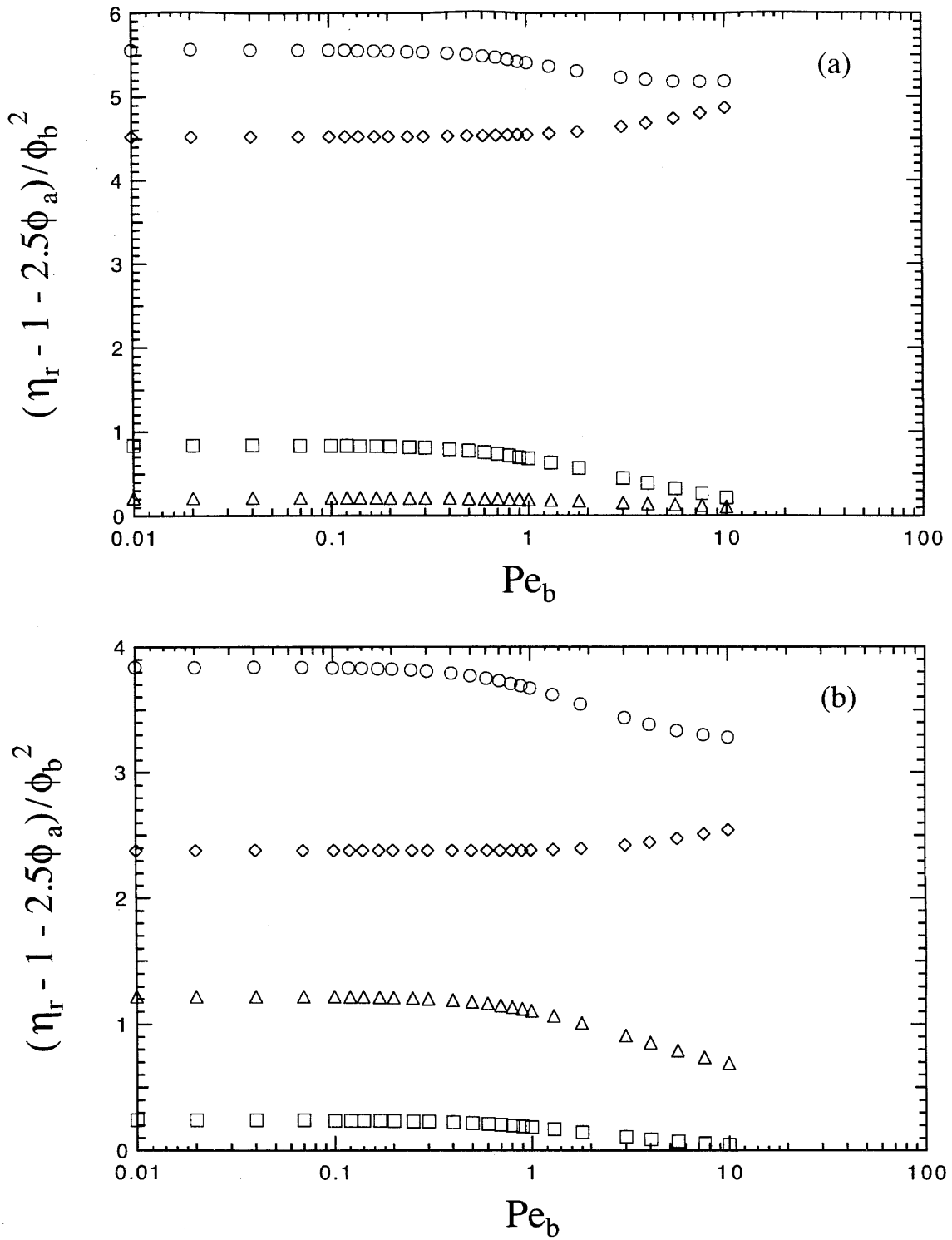

Figure 3.47: The $O(\phi_b^2)$ contributions to the relative shear, η_r, as a function of Peclet number, $Pe_b = 6\pi\eta_s\dot{\gamma}ab^2/kT$, for (a) $b/a = 1.01$ and (b) $b/a = 1.1$. Hydrodynamic ($\diamond$), Brownian ($\square$) and interparticle force ($\triangle$) contributions to the total ($\circ$) viscosity are reported.

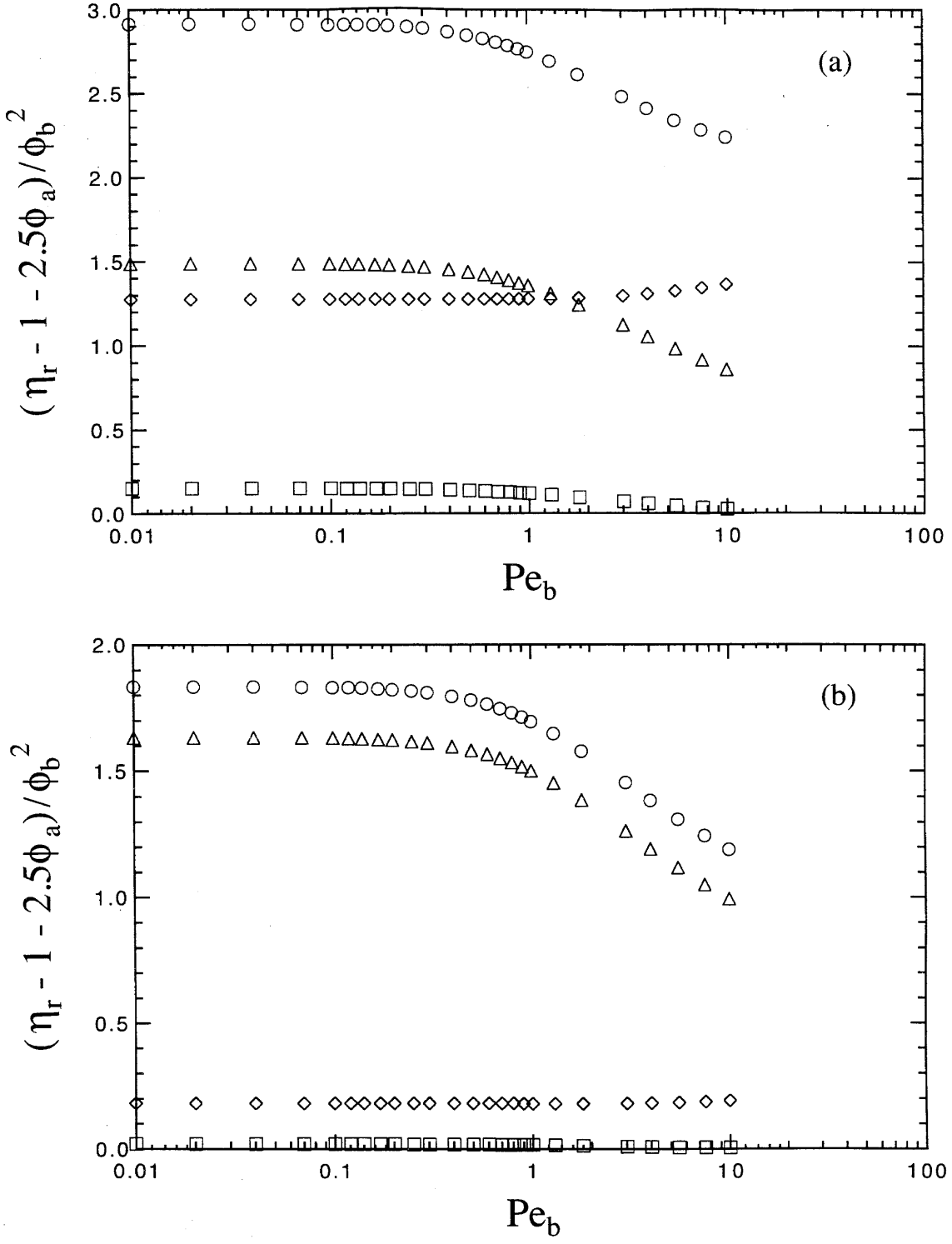

Figure 3.48: The $O(\phi_b^2)$ contributions to the relative shear viscosity, η_r, as a function of Peclet number, $Pe_b = 6\pi\eta_s\dot{\gamma}ab^2/kT$, for (a) $b/a = 1.2$ and (b) $b/a = 1.6$. Hydrodynamic ($\diamond$), Brownian ($\square$) and interparticle force ($\triangle$) contributions to the total ($\circ$) viscosity are reported.

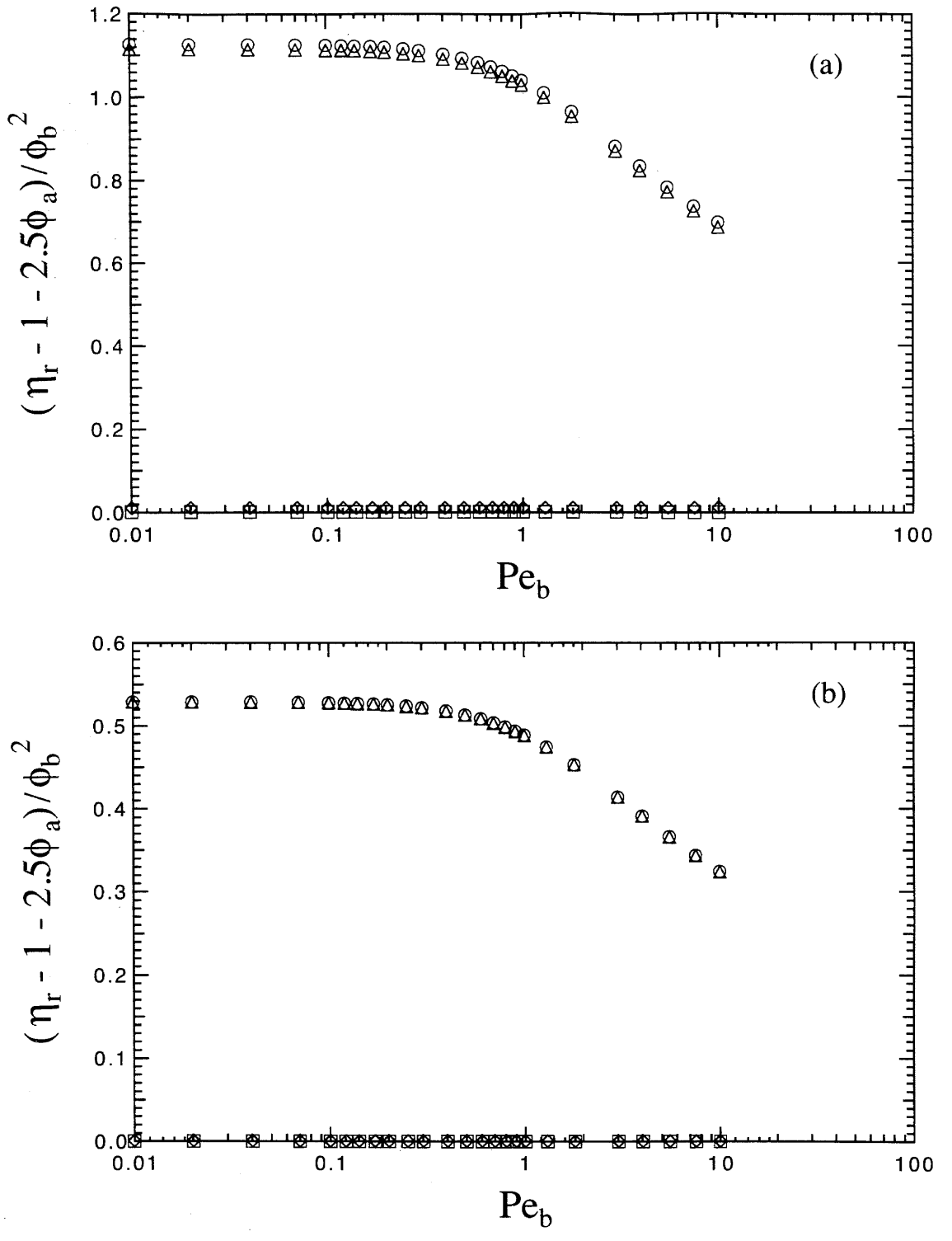

Figure 3.49: The $O(\phi_b^2)$ contributions to the relative shear viscosity, η_r, as a function of Peclet number, $Pe_b = 6\pi\eta_s\dot{\gamma}ab^2/kT$, for (a) $b/a = 2.5$ and (b) $b/a = 5.0$. Hydrodynamic ($\diamond$), Brownian ($\square$) and interparticle force ($\triangle$) contributions to the total ($\circ$) viscosity are reported.

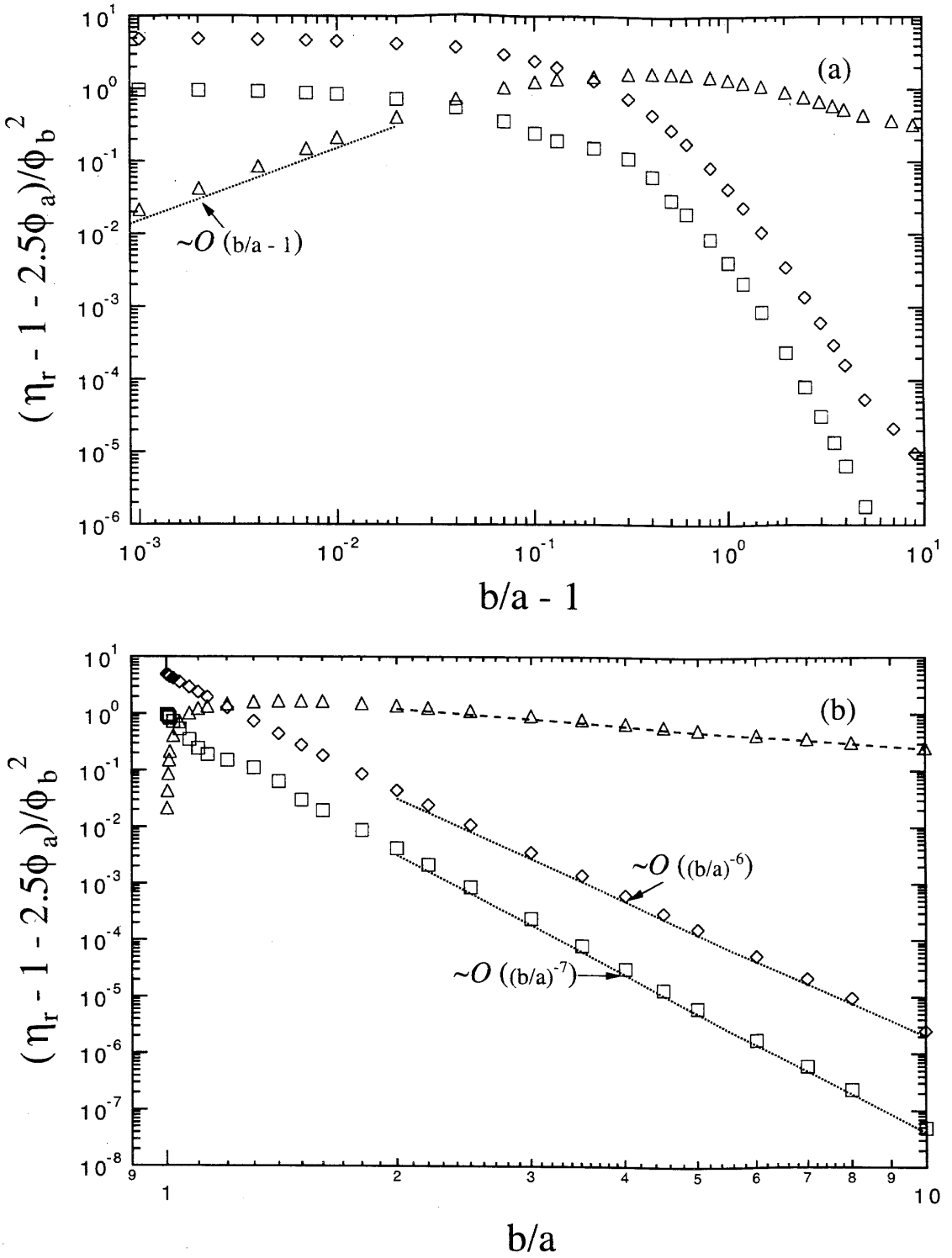

Figure 3.50: Effect of b/a on the $O(\phi_b^2)$ Brownian ($\square$), hydrodynamic ($\diamond$), and interparticle force ($\triangle$) contributions to the low shear relative viscosity. The results for the case of no hydrodynamic interactions with $b/a = 1$ (dotted line) are included to compare with data for $b/a \to \infty$.

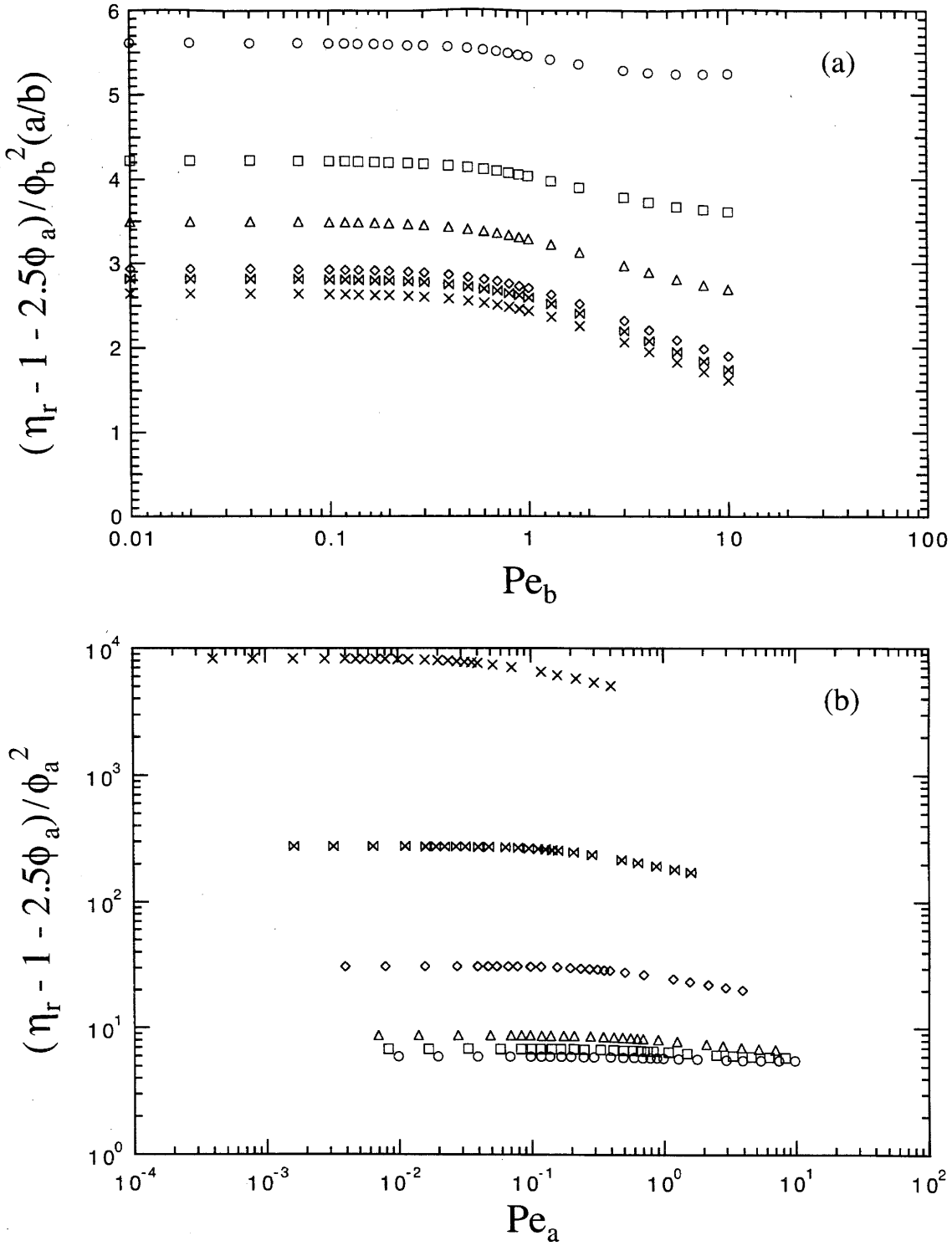

Figure 3.51: Effect of the proper scaling on the relative shear viscosity, η_r. Results for (a) the $O(\phi_b^2(a/b))$ contribution to the relative shear viscosity as a function of the properly scaled Peclet number, $Pe_b = 6\pi\eta_s\dot{\gamma}ab^2/kT$, and (b) the $O(\phi_a^2)$ contribution to the relative shear viscosity as a function of the particle Peclet number, $Pe_a = 6\pi\eta_s\dot{\gamma}a^3/kT$ for $b/a = 1.01$ ($\circ$), $b/a = 1.1$ ($\square$), $b/a = 1.2$ ($\triangle$), $b/a = 1.6$ ($\diamond$), $b/a = 2.5$ ($\bowtie$), and $b/a = 5.0$ ($\times$).

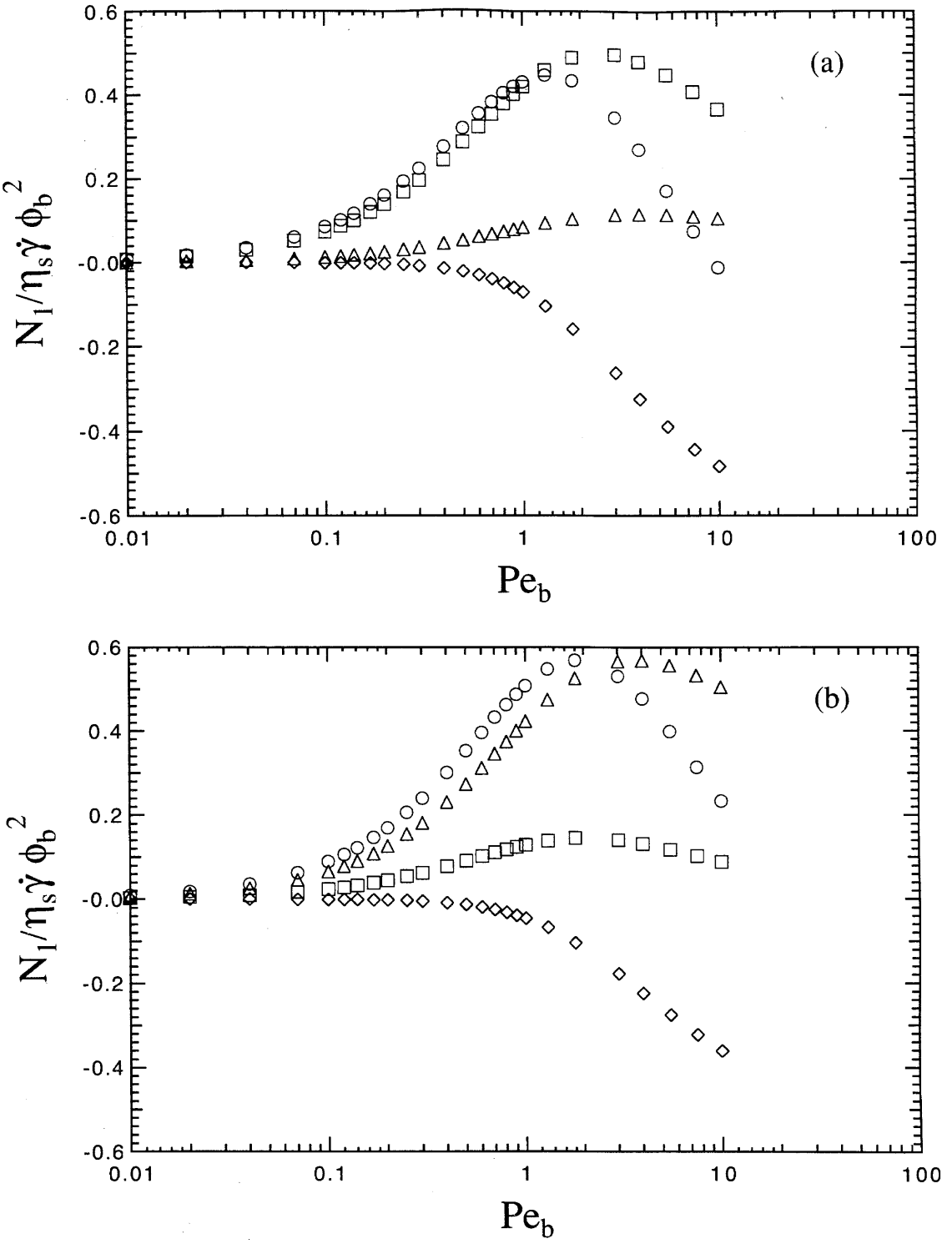

Figure 3.52: The $O(\phi_b^2)$ contribution to the nondimensional first normal stress difference, $N_1/\eta_s\dot{\gamma}$, as a function of Peclet number, $Pe_b = 6\pi\eta_s\dot{\gamma}ab^2/kT$, for (a) $b/a = 1.01$ and (b) $b/a = 1.1$. Hydrodynamic ($\diamond$), Brownian ($\square$) and interparticle force ($\triangle$) contributions to the total ($\circ$) first normal stress difference are reported.

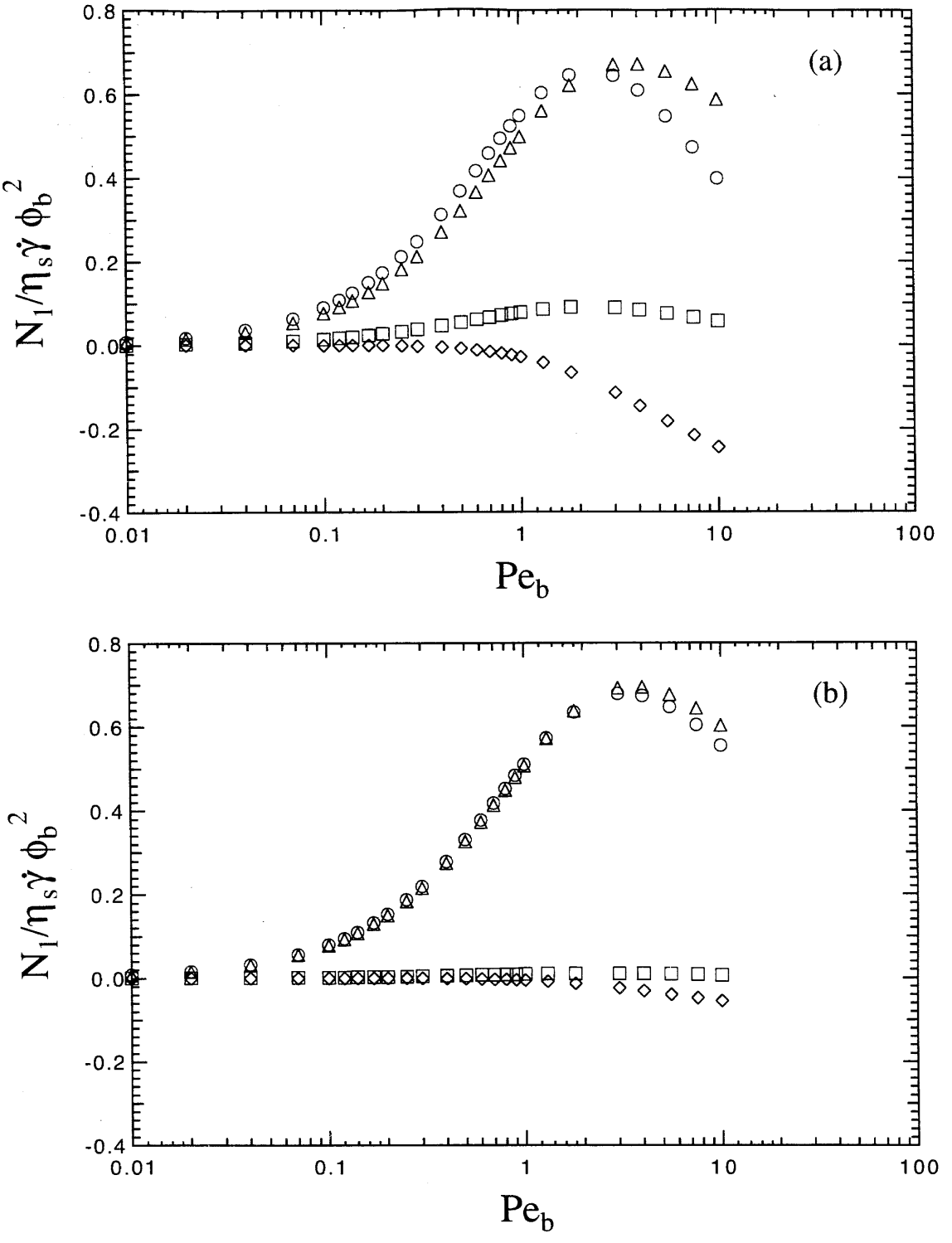

Figure 3.53: The $O(\phi_b^2)$ contribution to the nondimensional first normal stress difference, $N_1/\eta_s\dot{\gamma}$, as a function of Peclet number, $Pe_b = 6\pi\eta_s\dot{\gamma}ab^2/kT$, for (a) $b/a = 1.2$ and (b) $b/a = 1.6$. Hydrodynamic ($\diamond$), Brownian ($\square$) and interparticle force ($\triangle$) contributions to the total ($\circ$) first normal stress difference are reported.

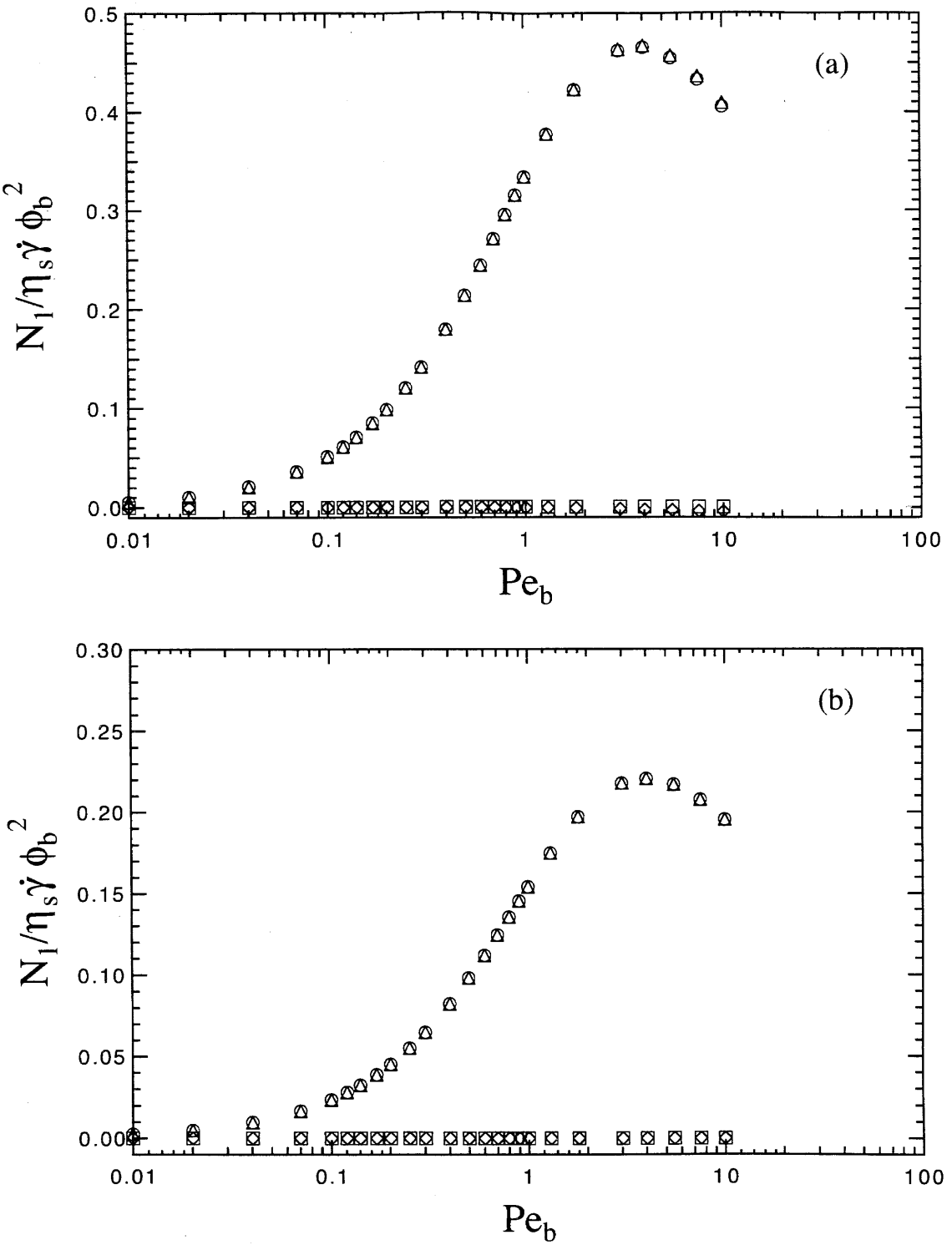

Figure 3.54: The $O(\phi_b^2)$ contribution to the nondimensional first normal stress difference, $N_1/\eta_s\dot{\gamma}$, as a function of Peclet number, $Pe_b = 6\pi\eta_s\dot{\gamma}ab^2/kT$, for (a) $b/a = 2.5$ and (b) $b/a = 5.0$. Hydrodynamic ($\diamond$), Brownian ($\square$) and interparticle force ($\triangle$) contributions to the total ($\circ$) first normal stress difference are reported.

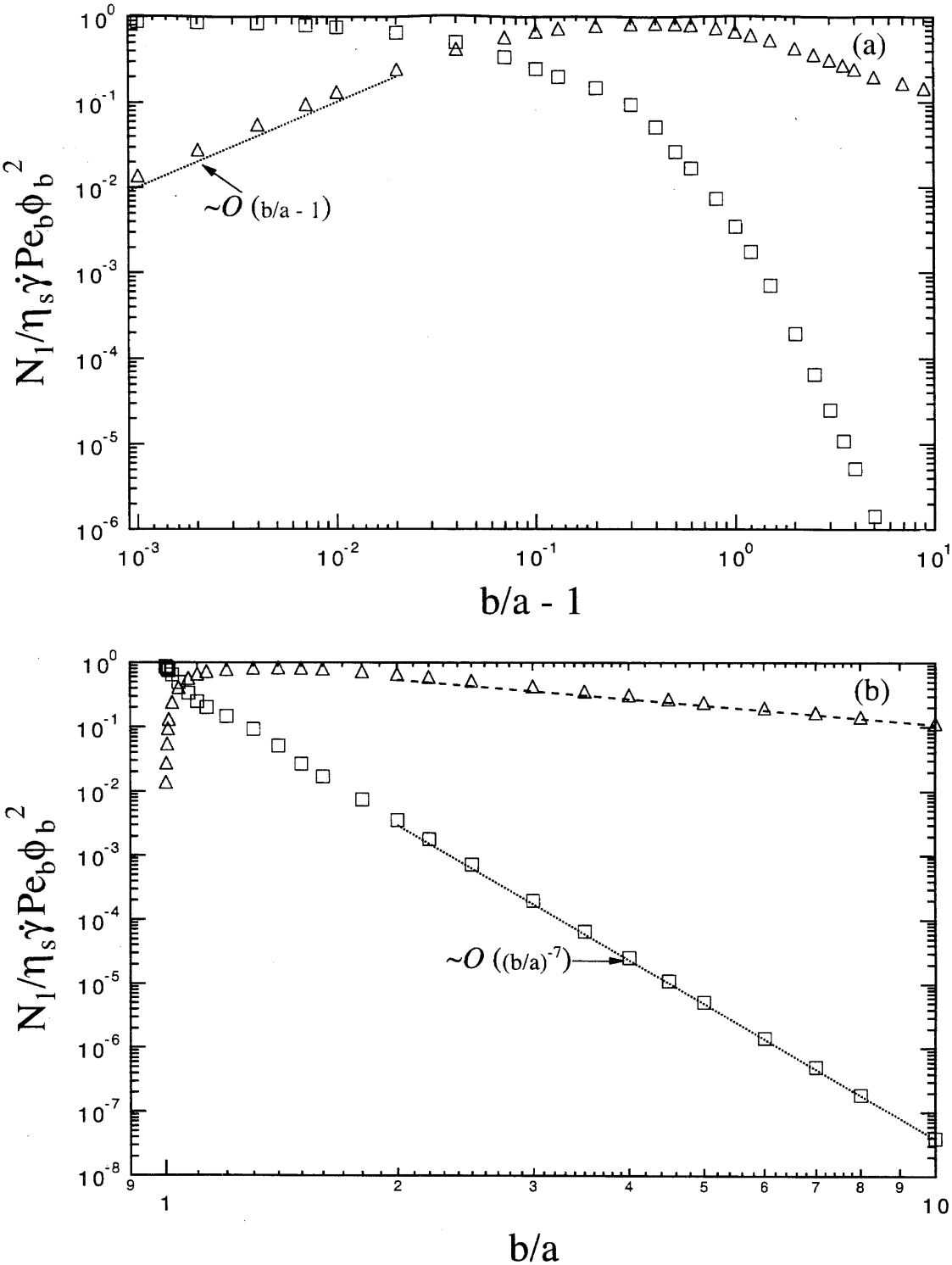

Figure 3.55: Effect of b/a on the $O(\phi_b^2 Pe_b)$ Brownian (□) and interparticle force (△) contributions to the low shear, nondimensional, first normal stress difference, $N_1/\eta_s\dot{\gamma}$. The hydrodynamic contribution is not included since $N_1^H/\eta_s\dot{\gamma}\phi_b^2 \sim o(Pe_b)$. The results for the case of no hydrodynamic interactions with $b/a = 1$ (dotted line) are included to compare with data for $b/a \to \infty$.

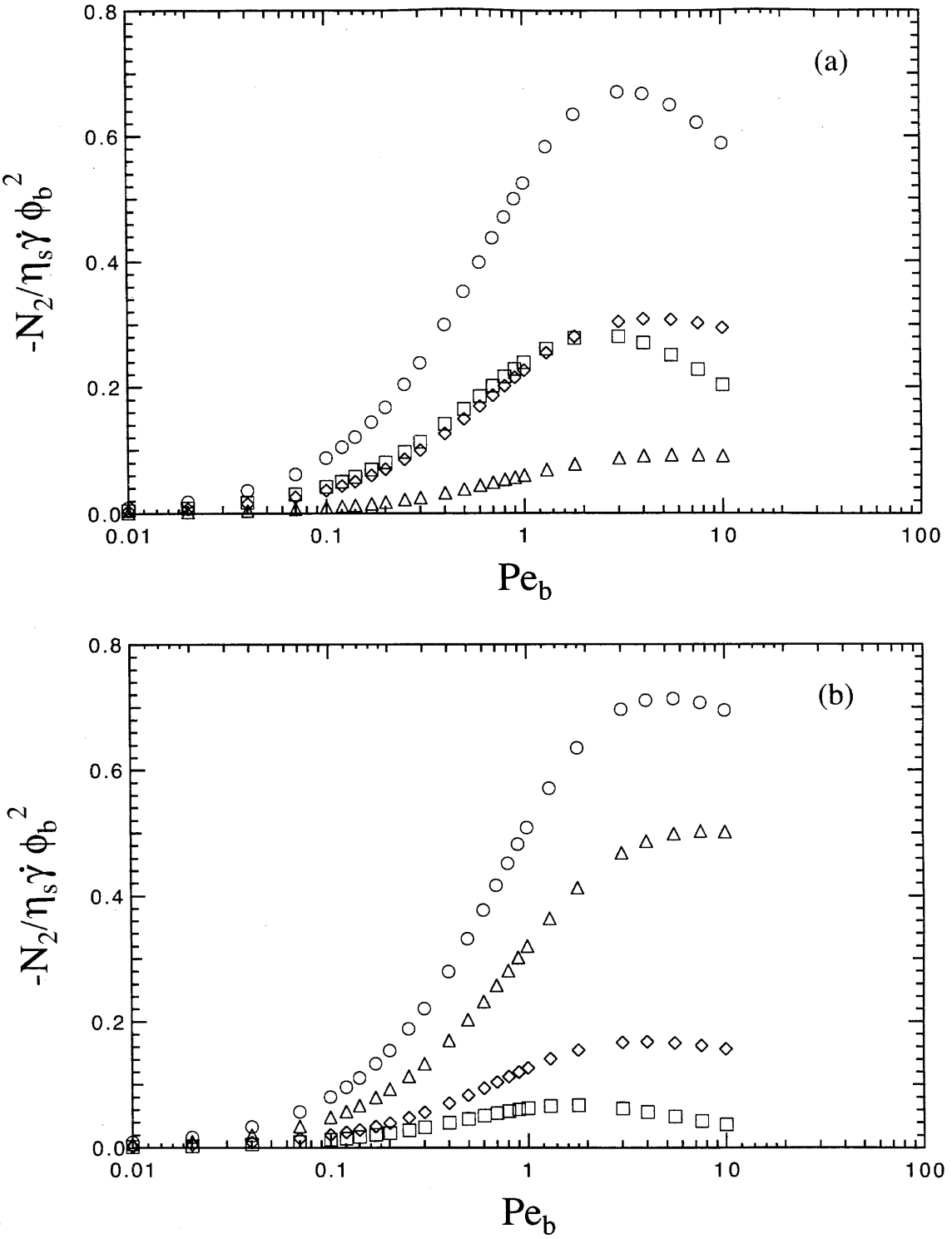

Figure 3.56: The $O(\phi_b^2)$ contribution to the nondimensional second normal stress difference, $N_2/\eta_s\dot{\gamma}$, as a function of Peclet number, $Pe_b = 6\pi\eta_s\dot{\gamma}ab^2/kT$, for (a) $b/a = 1.01$ and (b) $b/a = 1.1$. Hydrodynamic ($\diamond$), Brownian ($\square$) and interparticle force ($\triangle$) contributions to the total ($\circ$) second normal stress difference are reported.

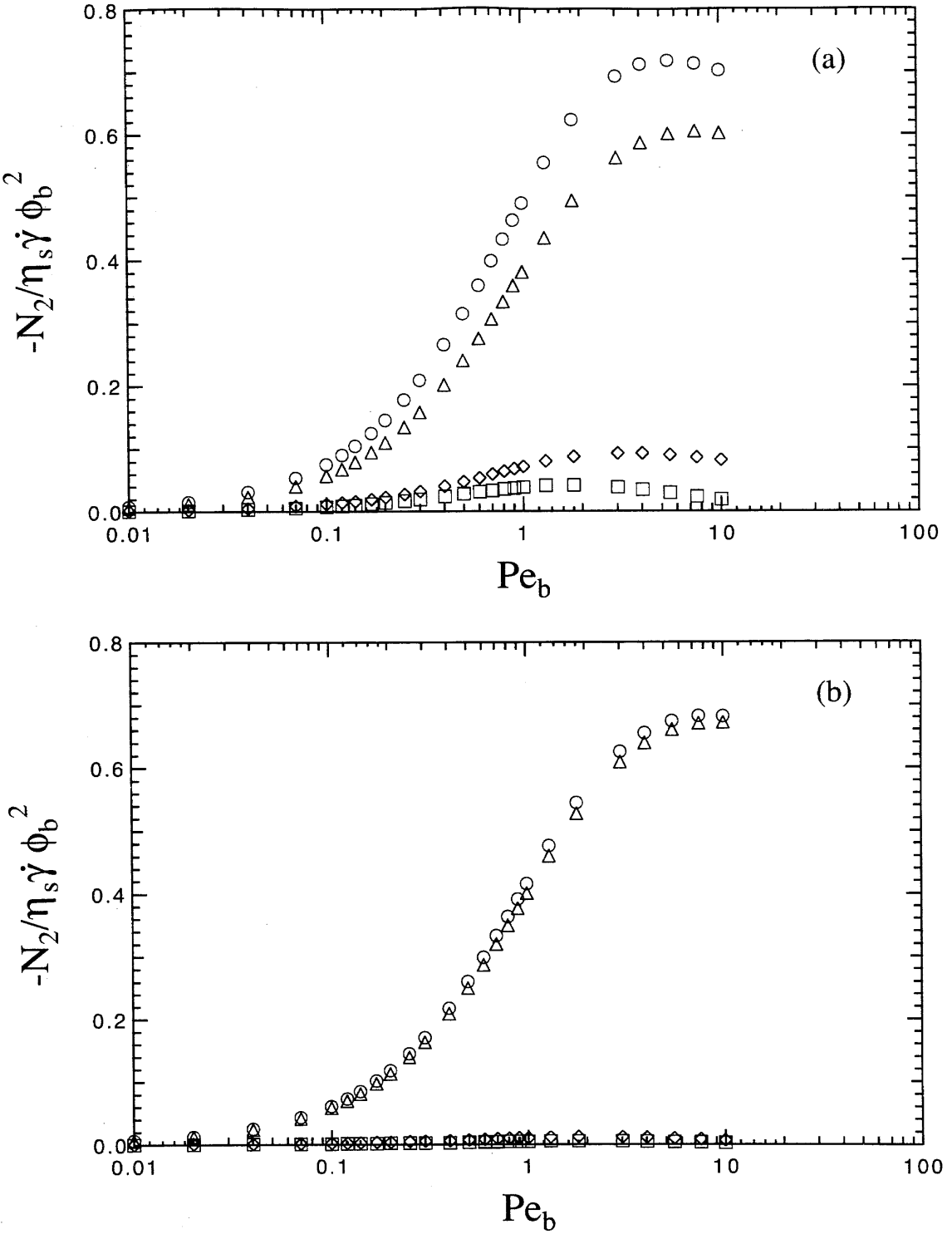

Figure 3.57: The $O(\phi_b^2)$ contribution to the nondimensional second normal stress difference, $N_2/\eta_s\dot{\gamma}$, as a function of Peclet number, $Pe_b = 6\pi\eta_s\dot{\gamma}ab^2/kT$, for (a) $b/a = 1.2$ and (b) $b/a = 1.6$. Hydrodynamic ($\diamond$), Brownian ($\square$) and interparticle force ($\triangle$) contributions to the total ($\circ$) second normal stress difference are reported.

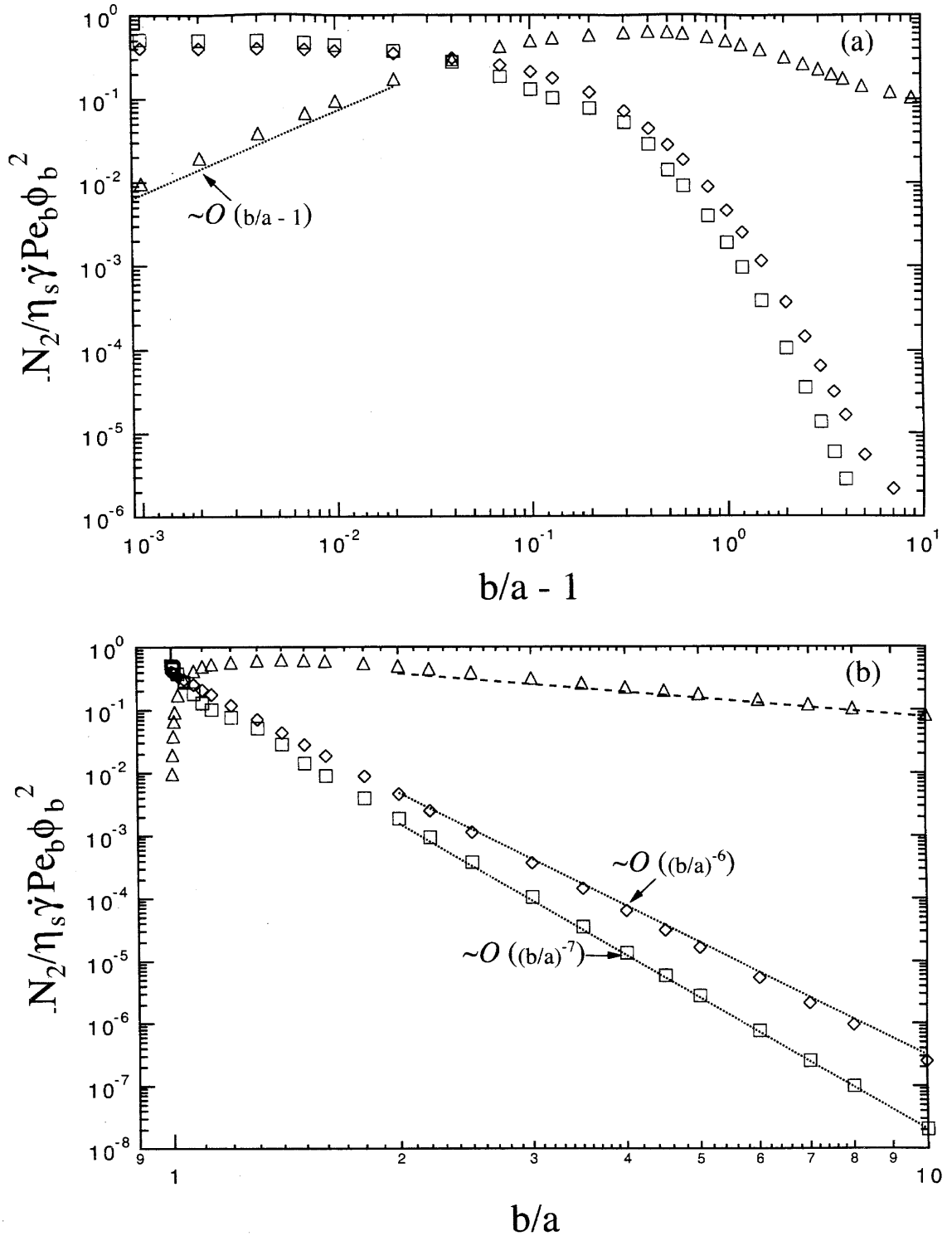

Figure 3.58: Effect of b/a on the $O(\phi_b^2 Pe_b)$ Brownian ($\square$), hydrodynamic ($\diamond$), and interparticle force ($\triangle$) contributions to the low shear, nondimensional, second normal stress difference, $N_2/\eta_s\dot{\gamma}$. The results for the case of no hydrodynamic interactions with $b/a = 1$ (dotted line) are included to compare with data for $b/a \to \infty$.

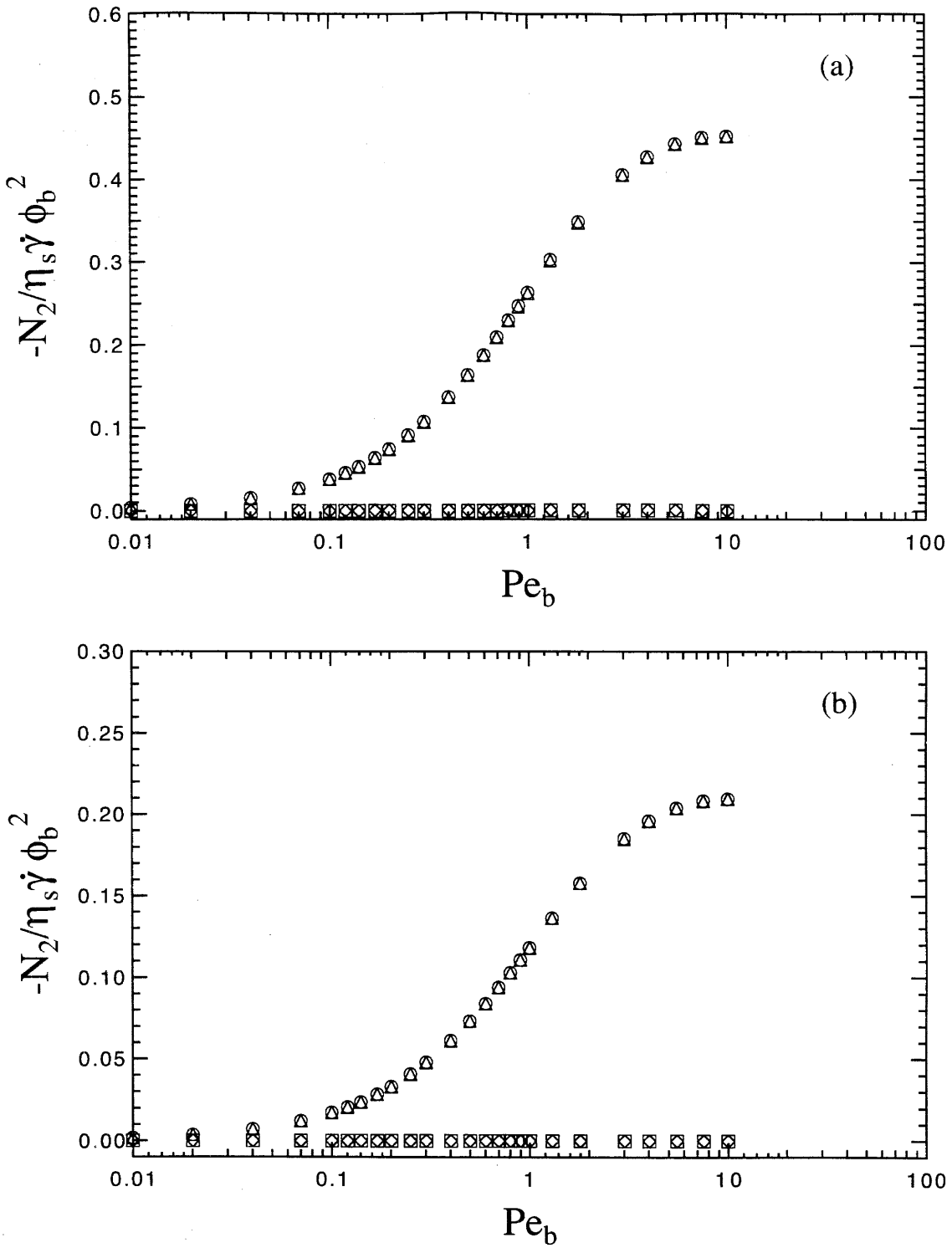

Figure 3.59: The $O(\phi_b^2)$ contribution to the nondimensional second normal stress difference, $N_2/\eta_s\dot{\gamma}$, as a function of Peclet number, $Pe_b = 6\pi\eta_s\dot{\gamma}ab^2/kT$, for (a) $b/a = 2.5$ and (b) $b/a = 5.0$. Hydrodynamic ($\diamond$), Brownian ($\square$) and interparticle force ($\triangle$) contributions to the total ($\circ$) second normal stress difference are reported.

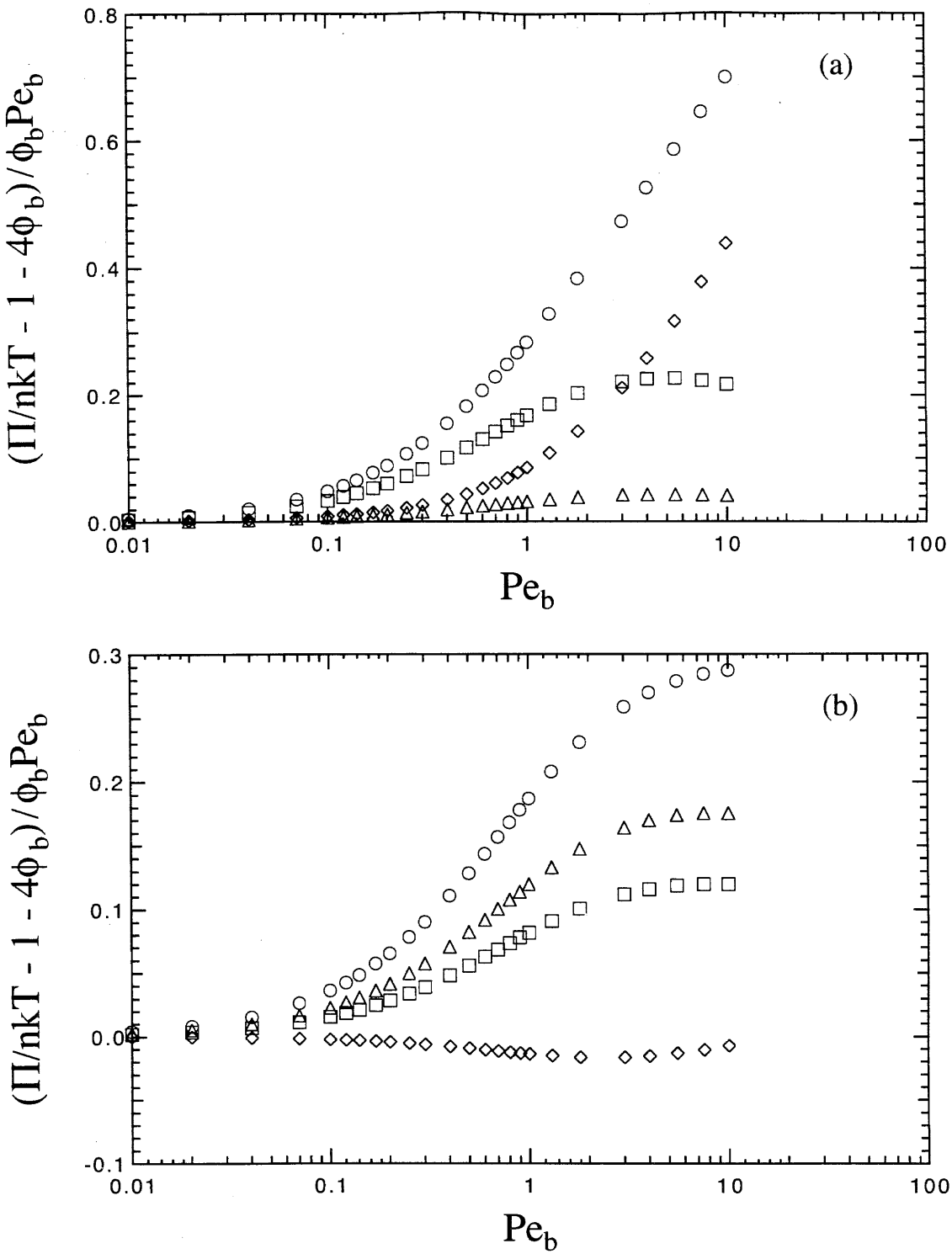

Figure 3.60: The $O(\phi_b^2)$ contribution to the nondimensional osmotic pressure, Π/nkT, as a function of Peclet number, $Pe_b = 6\pi\eta_s\dot{\gamma}ab^2/kT$, for (a) $b/a = 1.01$ and (b) $b/a = 1.1$. Hydrodynamic ($\diamond$), Brownian ($\square$) and interparticle force ($\triangle$) contributions to the total ($\circ$) osmotic pressure are reported.

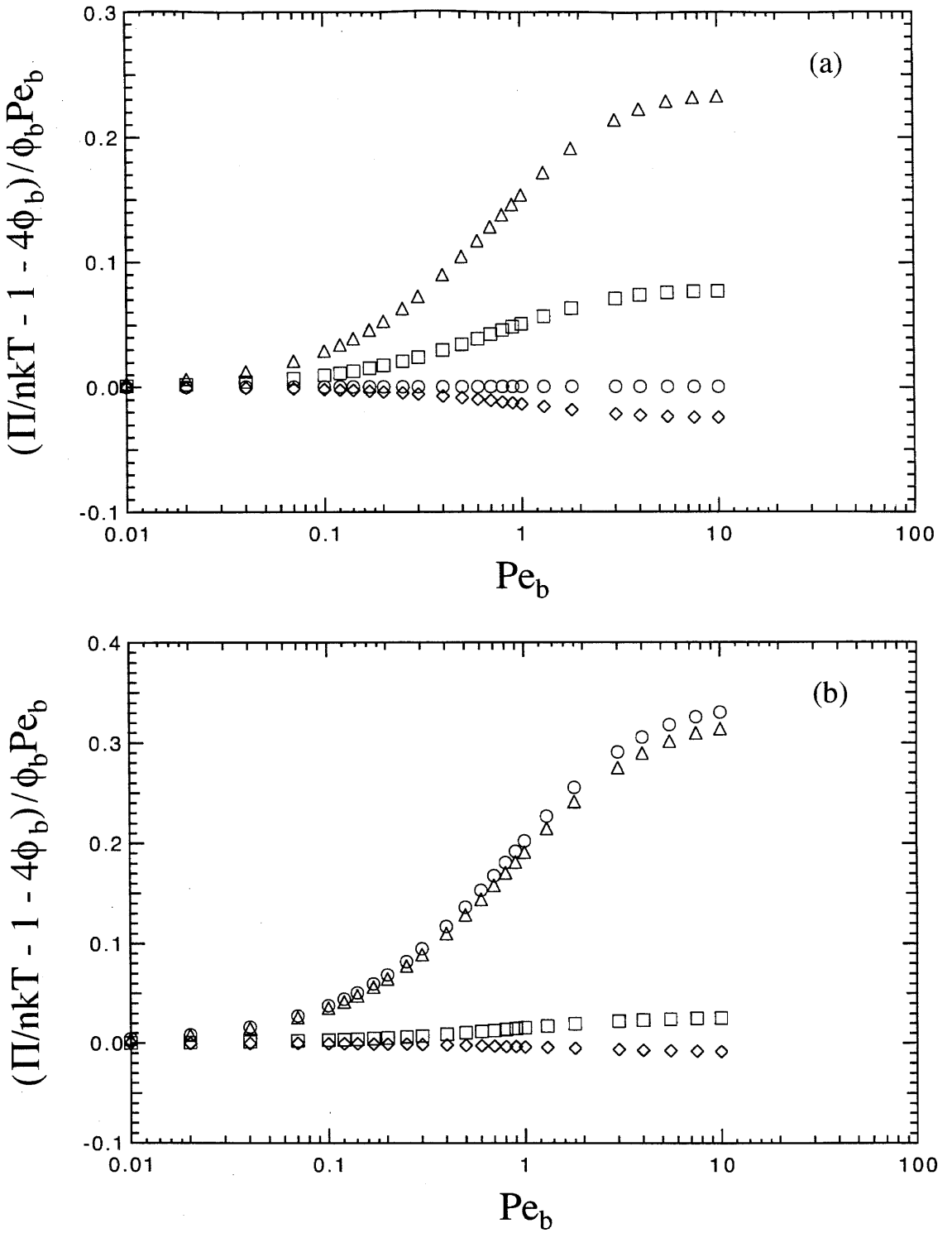

Figure 3.61: The $O(\phi_b^2)$ contribution to the nondimensional osmotic pressure, Π/nkT, as a function of Peclet number, $Pe_b = 6\pi\eta_s\dot{\gamma}ab^2/kT$, for (a) $b/a = 1.2$ and (b) $b/a = 1.6$. Hydrodynamic ($\diamond$), Brownian ($\square$) and interparticle force ($\triangle$) contributions to the total ($\circ$) osmotic pressure are reported.

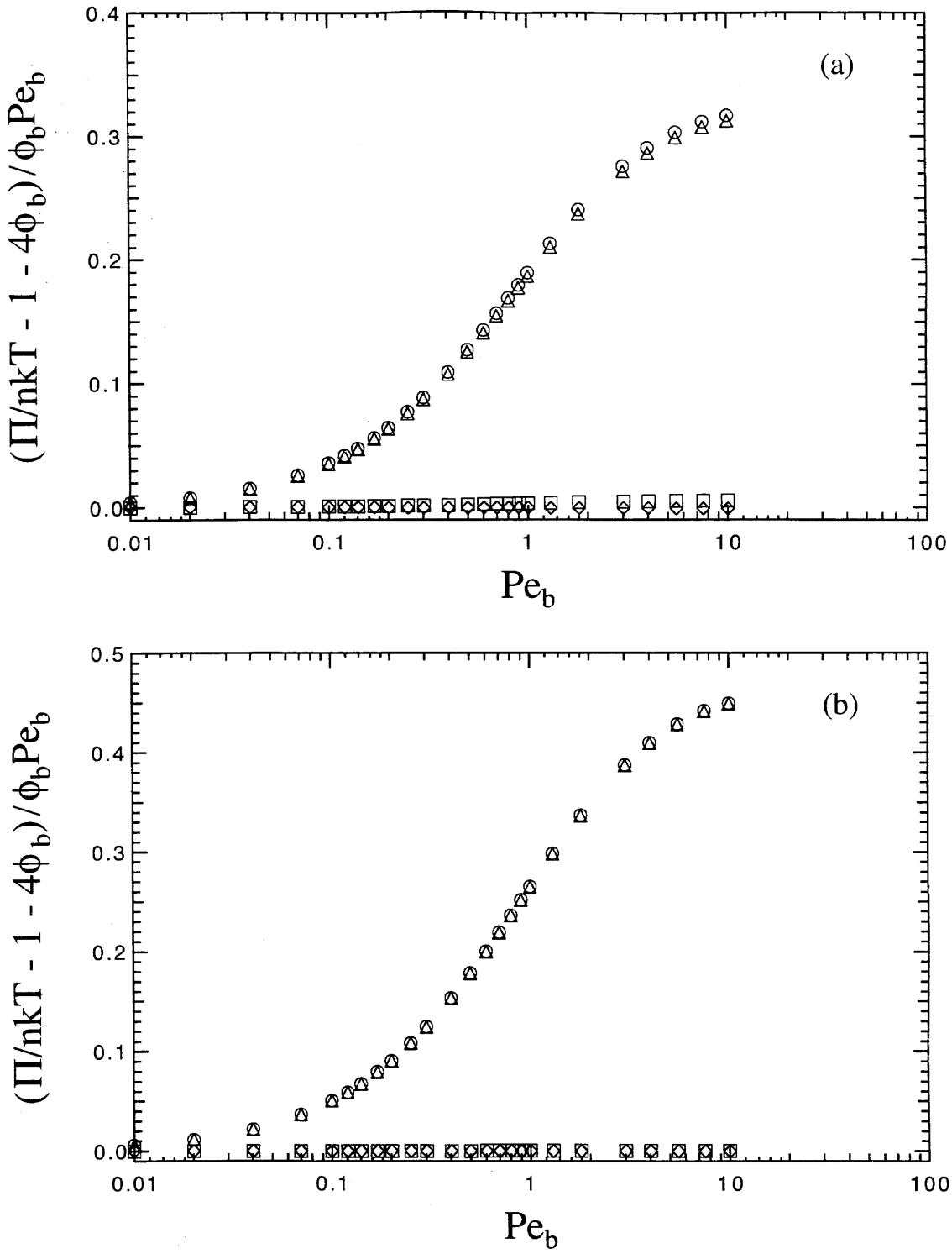

Figure 3.62: The $O(\phi_b^2)$ contribution to the nondimensional osmotic pressure, Π/nkT, as a function of Peclet number, $Pe_b = 6\pi\eta_s\dot{\gamma}ab^2/kT$, for (a) $b/a = 2.5$ and (b) $b/a = 5.0$. Hydrodynamic ($\diamond$), Brownian ($\square$) and interparticle force ($\triangle$) contributions to the total ($\circ$) osmotic pressure are reported.

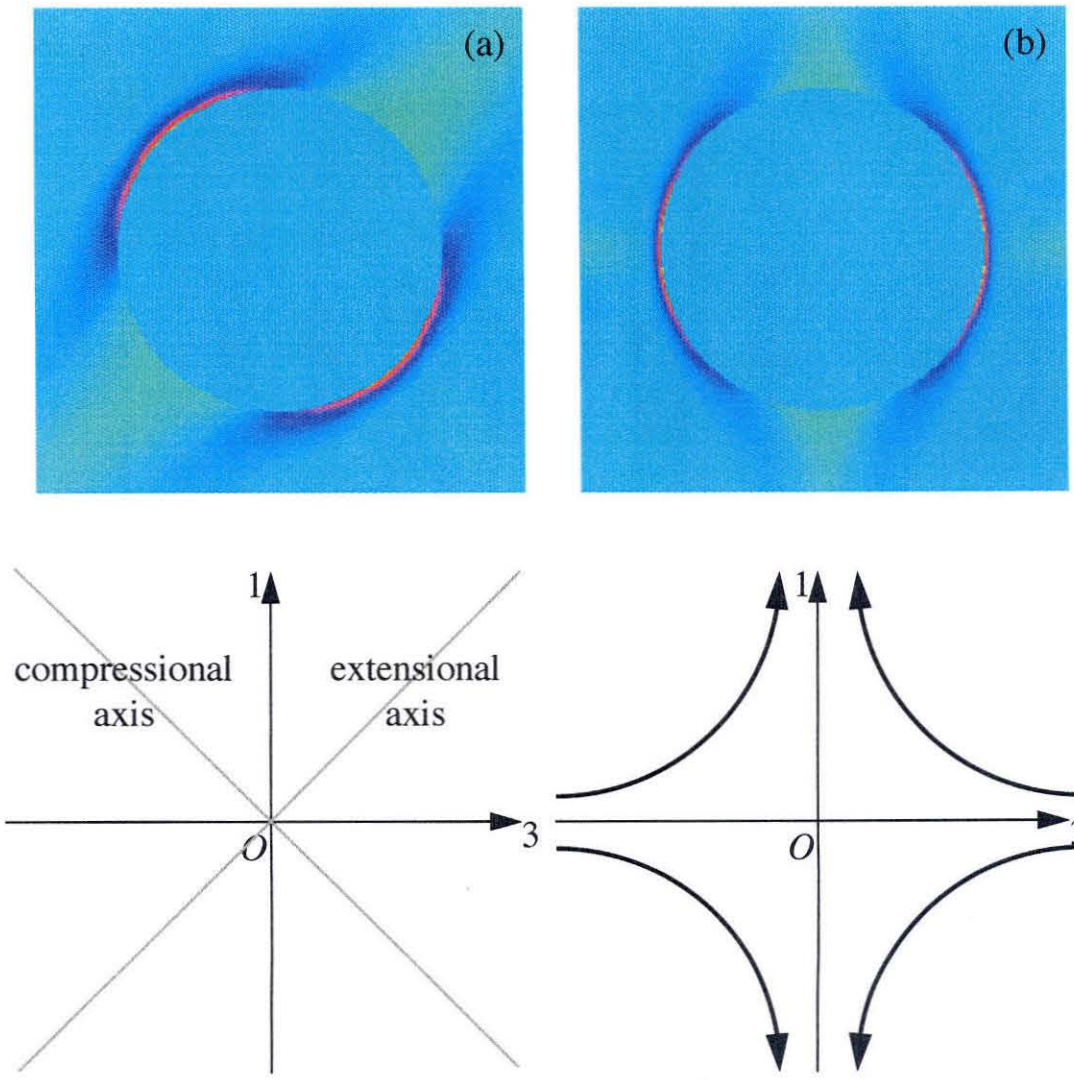

Figure 3.63: Results for f/Pe at steady-state and $Pe = 10$ for (a) planar extensional flow ($\langle \mathbf{E} \rangle = \delta_1\delta_3 + \delta_3\delta_1$) in the 1-3 plane and (b) biaxial extensional flow ($\langle \mathbf{E} \rangle = \delta_1\delta_1 + \delta_2\delta_2 - 2\delta_3\delta_3$) in the 1-3 plane. f is the difference from the equilibrium microstructure, $Pe = 6\pi\eta_s\dot{\epsilon}a^3/kT$, hydrodynamic interactions are neglected and $b/a = 1$.

Chapter 4
Emulsions at the critical capillary number in steady simple shear flow

4.1 Introduction

Emulsions and polymer blends are processed as systems that contain droplets of one fluid dispersed in a second fluid. Emulsions are commonly used in the food (e.g., ice cream, margarine, mayonnaise), pharmaceutical (e.g., chemotherapy, blood substitutes), and cosmetic (e.g., creams, sunscreen) industries, while polymer blends are often used as external structures for automobiles and appliances [Chappat (1994); Stone (1994)]. During processing, an emulsion is subjected to different flow fields which determine the size, shape and orientation of the droplets; thus, it is important to predict how an imposed flow field affects the emulsion microstructure and the resulting bulk rheological properties.

For a single droplet there is a balance between the viscous force, which tends to deform the droplet, and the interfacial tension force, which tends to restore a droplet to a spherical shape. This balance of forces is described by the capillary number, $Ca = \eta_s \dot{\gamma} a/\sigma$, where η_s is the suspending fluid viscosity, $\dot{\gamma}$ is a characteristic shear rate, a is the radius of the undeformed droplet, and σ is the interfacial tension. When $Ca \ll 1$, the droplet remains nearly spherical, but as the capillary number increases, the droplet deforms until it bursts at the critical capillary number, Ca_c. The value of the critical capillary number is dependent on the type of flow and the viscosity ratio, $\lambda = \eta_d/\eta_s$, where η_d is the viscosity of the droplet fluid [Rallison (1984); Stone (1994), Janssen, Boon & Agteroff (1994)].

The theory of small deformations of the surface of a single droplet is well-developed [Taylor (1932); Chaffey & Brenner (1967); Schowalter, Chaffey & Brenner (1968); Cox (1969); Frankel & Acrivos (1970); Barthes-Biesel & Acrivos (1973a, 1973b); Rallison (1980)]. A small deformation parameter, ϵ, is used in all theories, where $\epsilon \ll 1$ is used in a regular perturbation expansion for the deformation of the surface from a sphere when (i) $Ca \ll 1$ and $\lambda \sim O(1)$ or (ii) $\lambda \gg 1$ and $Ca \sim O(1)$. The theory of Barthes-Biesel & Acrivos (1973a, 1973b) predicts the $O(\epsilon^2)$ deformation of the surface and the $O(\epsilon^2 \eta_s \dot{\gamma} \phi)$ contribution to the bulk stress for a transient, general linear flow. In addition to deformation, the theory also predicts droplet breakup in simple shear flow,

but only for emulsions with a viscosity ratio in the range $0.1 < \lambda < 3.6$. The theory fails for small values of the viscosity ratio since large deformations are required to induce droplet burst, and large deformation theory [Hinch & Acrivos (1980)] must be used. Droplet breakup does not occur when $\lambda \gg 1$ in simple shear flow since vorticity dominates, and the deformed droplet rotates instead of extending and bursting. This theory of small deformations has been extended to calculate the shear viscosity of two, interacting, nearly spherical droplets [Zinchenko (1984)] and the bulk rheology of mildly deformed droplets in a non-dilute emulsion by using a cell method [Choi & Schowalter (1975)].

A number of experiments have been performed to study the effect of flow type, capillary number and viscosity ratio on the deformation and burst of a single droplet [Taylor (1934); Rumscheidt & Mason (1961); Torza, Cox & Mason (1972); Grace (1982); de Bruijn (1989); Varanasi, Ryan & Stroeve (1994); Janssen, Boon & Agterof (1994)]. These experiments are found to be in excellent agreement with the small deformation theory over its range of validity. In addition to droplet shape, these experiments showed the effect of the viscosity ratio on the critical capillary number and the existence of a critical value of the viscosity ratio for simple shear flow, $\lambda_c = 4$, above which droplet breakup no longer occurs.

In addition to experiments, numerical simulations have been performed to test the small deformation theory as well as study emulsions for which the theory is not applicable (e.g., multiple droplets; bounded flows; Ca, $\lambda \sim O(1)$) [Rallison (1981); Pozrikidis (1993); Zhou & Pozrikidis (1993); Kennedy, Pozrikidis & Skalak (1994); Li, Zhou & Pozrikidis (1995); Li, Charles & Pozrikidis (1996); Loewenberg & Hinch (1996); Zinchenko, Rother & Davis (1997)]. The deformation of a single droplet was studied as a function of viscosity ratio and capillary number and found to be in excellent agreement with the small deformation theory. Even though droplet breakup did not occur in these simulations, the point of droplet breakup could be detected. One criterion is that droplet breakup occurs at the point when the steady shear stress curve reaches a maximum with increasing imposed shear [Loewenberg & Hinch (1996)]. This criterion is used to analyze results of numerical simulations at the

critical capillary number.

Despite the progress in theory and numerical simulations, the rheology and microstructure of a concentrated emulsion that includes droplet breakup remains a difficult problem, but important results can still be obtained. When an emulsion is at the critical capillary number, the stress from the interface is linear in shear rate for $\lambda = 1$ and $\phi = 0.50$, as shown by Doi & Ohta (1991) in their scaling argument. This result for emulsions is important since an unstabilized emulsion in flow is always at the critical capillary number. When subjected to an external flow, an unstabilized emulsion exhibits both droplet breakup and coalescence. The size, shape and orientation of the dispersed droplets reach steady state only when there is a balance between breakup and coalescence, resulting in a droplet size that is inversely proportional to the imposed rate, $a \sim O(1/\dot{\gamma})$. Since $a \sim O(1/\dot{\gamma})$, the capillary number of the emulsion, $Ca = \eta_s \dot{\gamma} a/\sigma$, does not change and is always at the critical capillary number, Ca_c.

Based simply on dimensional analysis, the Doi-Ohta scaling should be valid for arbitrary values of volume fraction and viscosity ratio when an emulsion is at the critical capillary number. As a test of this result, a number of experiments have been performed at different values of λ and ϕ. Takahashi *et al.* (1994a, 1994b) experimentally showed the validity of the Doi-Ohta scaling for the case of $\lambda = 1$ for a range of volume fractions, including $\phi = 0.50$. Vinckier *et al.* (1996a, 1996b) studied a range of viscosity ratios ($\lambda = 0.15, 0.44, 0.80, 1.2, 2.3$) over all volume fractions, while Kitade *et al.* (1997) studied a few viscosity ratios ($\lambda = 0.155, 0.826$) at 10wt% dispersed fluid.

The purpose of this work is to present a scaling argument for the volume-fraction dependence of the stress of an emulsion at the critical capillary number and provide experimental evidence to confirm the scaling argument for the viscosity and first normal stress difference of an emulsion of two Newtonian fluids in simple shear flow. Data from this and other works are combined to construct master curves for the scaled viscosity and first normal stress difference which are only functions of the viscosity ratio, λ, at the critical capillary number. Quantitative agreement with the master

viscosity curve and qualitative agreement with the master curve for first normal stress difference are obtained simply by using small deformation theory in simple shear flow.

4.2 Theory

The bulk stress, $\mathbf{\Sigma}$, of a suspension of force-free droplets in an incompressible, Newtonian fluid can be written as [Batchelor (1970)],

$$\mathbf{\Sigma} = -p\mathbf{I} + 2\eta_s\mathbf{E} + \mathbf{\Sigma}^P, \tag{4.1}$$

where $\mathbf{E}$ is the bulk rate-of-strain tensor and $\mathbf{\Sigma}^P$ is the particle contribution to the stress.

For a dilute emulsion containing non-Brownian droplets at low particle Reynolds number with incompressible, Newtonian dispersed and suspending fluids having constant surface tension, the particle stress takes the form,

$$\frac{\mathbf{\Sigma}^P}{\eta_s\dot{\gamma}} = -\frac{3}{4\pi}\frac{\phi}{Ca}\int\left(\mathbf{nn} - \frac{1}{3}\mathbf{I}\right)dA + \phi(\lambda - 1)\frac{3}{4\pi}\int(\mathbf{un} + \mathbf{nu})\,dA, \tag{4.2}$$

where the integrals are taken over the surface of the droplet, $\mathbf{n}$ is the outward normal to the surface and $\mathbf{u}$ is the velocity of a point on the surface, nondimensionalized by $a\dot{\gamma}$. Equation (4.2) can be re-written in more compact notation,

$$\frac{\mathbf{\Sigma}^P}{\eta_s\dot{\gamma}} = -\frac{\phi}{Ca}\mathbf{Q}(\phi, \lambda, Ca) + \phi(\lambda - 1)\,\mathbf{P}(\phi, \lambda, Ca), \tag{4.3}$$

where $\mathbf{Q}$ is the anisotropy tensor,

$$\mathbf{Q} = \frac{3}{4\pi}\int\left(\mathbf{nn} - \frac{1}{3}\mathbf{I}\right)dA, \tag{4.4}$$

and $\mathbf{P}$ is

$$\mathbf{P} = \frac{3}{4\pi}\int(\mathbf{un} + \mathbf{nu})\,dA. \tag{4.5}$$

The anisotropy tensor is only a function of the droplet shape and orientation and is

a measure of droplet deformation relative to a sphere with $\mathbf{Q} = \mathbf{0}$ for a sphere. $\mathbf{P}$ is proportional to the average rate-of-strain tensor within the droplet since

$$\int_{V_0} 2\mathbf{E} dV = \int_{A_0} (\mathbf{un} + \mathbf{nu})\, dA \tag{4.6}$$

is a step in the derivation of equation (4.2), where V_0 is the volume of the droplet and A_0 is the surface of the droplet. To obtain this result, the definition of $\mathbf{E}$,

$$\mathbf{E} = \frac{1}{2}\left(\nabla\mathbf{u} + (\nabla\mathbf{u})^t\right), \tag{4.7}$$

is used with the divergence theorem, where ^{t} denotes the transpose. Volume-fraction dependence is included for both $\mathbf{Q}$ and $\mathbf{P}$ in equation (4.3) since the bulk stress of a concentrated emulsion can be calculated using the average shape and orientation of only a single droplet [Loewenberg & Hinch (1996)]. Since the average shape and orientation of a droplet can be affected by the presence of other droplets, $\mathbf{Q}$ and $\mathbf{P}$ can be affected by changes in volume fraction.

In this work we are interested only in the case when the droplets are at the critical capillary number, Ca_c,

$$\frac{\mathbf{\Sigma}^P}{\eta_s \dot{\gamma}} = -\frac{\phi}{Ca_c(\phi,\lambda)}\mathbf{Q}\left(\phi,\lambda;Ca_c(\phi,\lambda)\right) + \phi(\lambda-1)\,\mathbf{P}\left(\phi,\lambda;Ca_c(\phi,\lambda)\right), \tag{4.8}$$

and the particle stress is linear in shear rate for any value of ϕ and λ since the right-hand side of equation (4.8) is independent of rate, as predicted by the scaling of Doi & Ohta (1991). Since the anisotropy tensor is independent of shear rate, the shape and orientation of the droplets are self-similar with respect to changes in the external flow as long as the emulsion is at the critical capillary number.

There are two key requirements for the scaling behavior of the volume-fraction dependence of the particle stress. The first assumption is that the critical capillary number is only a weak function of volume fraction for a given flow,

$$Ca_c(\phi,\lambda) \approx Ca_c(\lambda). \tag{4.9}$$

This assumption is validated by the data of Mason & Bibette (1997) who show that the droplet radius is a weak function of volume fraction up to $\phi \approx 0.50$ when emulsions of different volume fractions are sheared at the same rate for a given value of λ.

To complete the volume-fraction scaling of the particle stress, it is further assumed that the droplet shape and orientation are weak functions of volume fraction at the critical capillary number. If this assumption is true,

$$\mathbf{Q}\left(\phi, \lambda; Ca_c(\lambda)\right) \approx \mathbf{Q}\left(\lambda; Ca_c(\lambda)\right), \tag{4.10}$$

since the anisotropy tensor is only a function of shape and orientation. Furthermore,

$$\mathbf{P}\left(\phi, \lambda; Ca_c(\lambda)\right) \approx \mathbf{P}\left(\lambda; Ca_c(\lambda)\right), \tag{4.11}$$

since the flow field inside the droplet is unchanged if the droplet shape and orientation as well as the external flow field are unchanged. Obviously, the assumption about droplet shape and orientation is valid for dilute emulsions since the droplets don't interact. For concentrations near maximum packing, the scaling will fail, but it is expected that the scaling should be valid over a wide range of volume fractions since the lubrication force between two droplets is quite weak [Davis, Schonberg & Rallison (1989)].

Both of these assumptions are validated by the numerical results of Loewenberg & Hinch (1996). In their simulations, the shear stress shows a maximum with increasing capillary number, and the capillary number at which the maximum stress occurs is taken as the critical capillary number, as suggested by Loewenberg & Hinch (1996). For the case of $\lambda = 1$, for which data is reported at volume fractions of ϕ=0.00, 0.10, 0.20, and 0.30, the critical capillary number is a weak function of volume fraction. In addition, the Taylor deformation parameter, a measure of the droplet shape, and the orientation angle are also weak functions of volume fraction; thus, $\mathbf{Q}$ and $\mathbf{P}$ are weak functions of volume fraction.

The main point of this scaling argument is that droplet shape and orientation

are self-similar with respect to changes in external flow [Doi & Ohta (1991)] *and* changes in volume fraction when a dilute to moderately-concentrated emulsion is at the critical capillary number. Using the assumptions that $\mathbf{Q}$, $\mathbf{P}$, and Ca_c are all weak functions of volume fraction, the scaled particle stress, $\mathbf{\Sigma}^*$, is determined by simply eliminating volume fraction from the right-hand side of equation (4.8),

$$\mathbf{\Sigma}^* = \frac{\mathbf{\Sigma}^P}{\eta_s \dot{\gamma} \phi} = -\frac{\mathbf{Q}\left(\lambda; Ca_c(\lambda)\right)}{Ca_c(\lambda)} + (\lambda - 1)\,\mathbf{P}\left(\lambda; Ca_c(\lambda)\right), \tag{4.12}$$

where the scaled particle stress is only a function of the viscosity ratio, λ. Note that equation (4.12) is independent of the flow type since there has been no assumption regarding the type of flow, such as shear, planar extension, uniaxial extension. It is only assumed that the flow is linear and that the emulsion is at the critical capillary number for the given flow. The values for $\mathbf{Q}$, $\mathbf{P}$ and Ca_c will certainly not be the same for both shear and planar extensional flows, but the values of $\mathbf{Q}$, $\mathbf{P}$ and Ca_c should be weak functions of volume fraction for a given type of flow.

Using the equations for the bulk stress and the scaled particle stress, equations (4.1) and (4.12), scaled rheological properties can be found that are only functions of the viscosity ratio, λ, at the critical capillary number in simple shear flow,

$$\eta^*(\lambda) = \frac{\eta_r - 1}{\phi}, \tag{4.13a}$$

$$N_1^*(\lambda) = \frac{N_1}{\eta_s \dot{\gamma} \phi}, \tag{4.13b}$$

$$N_2^*(\lambda) = \frac{N_2}{\eta_s \dot{\gamma} \phi}, \tag{4.13c}$$

where $\eta_r = \eta/\eta_s$ is the relative shear viscosity, η is the shear viscosity, N_1 is the first normal stress difference, and N_2 is the second normal stress difference. Master curves for only $\eta^*(\lambda)$ and $N_1^*(\lambda)$ are constructed in this work.

4.3 Experiment

4.3.1 Materials

Only two fluids were used: a polymerized castor oil (Pale 1000) from Caschem, Inc., and a 10,000 cSt polydimethylsiloxane (PDMS) from Nye Lubricants. These two fluids were chosen because they (i) are immiscible (σ = 6.0 dyn/cm at 22°C [Koh & Leal (1990)]), (ii) have similar densities (ρ =0.974 and 1.018 g/cm^3 for PDMS and Pale 1000, respectively), (iii) have vastly different viscosity-temperature coefficients, (iv) have nearly equal coefficients of expansion and (v) are quite viscous.

Since the two fluids have all of these properties, one sample can be made to study a single volume fraction and a wide range of values of λ. The value of λ is varied by simply changing the temperature of the emulsion, but the volume fraction remains constant since the coefficients of expansion of the two fluids are nearly the same. A total of seven weight fractions were studied: 10, 15, 20, 25, 30, 35, and 40 *weight* percent Pale 1000 in PDMS.

4.3.2 Experimental techniques

All measurements were completed using a constant stress rheometer (SR-5000; Rheometrics, Inc.) equipped with the normal force option and Peltier environmental system. A water circulator (F3; Haake) was connected to the Peltier to remove heat from the system. A 25-mm diameter cone (cone angle=0.1 rad) was used. There are isolated cases where different geometries or different options are used on the SR-5000, but these cases are clearly identified.

The normal force option uses a piezoelectric transducer capable of measuring force to the nearest milligram, but the transducer exhibits signal drift during measurements. This signal drift was no more than 0.2-g during an experiment of 150-sec, independent of the applied force between 0.0-g and 250-g. Since the normal force was automatically reset to zero by the rheometer software and the emulsion droplets relaxed to an equilibrium structure between successive stresses, signal drift is an iso-

lated effect for a single stress. Based on the magnitude of signal drift during a single experiment, 2.0-g is used as the minimum measurable normal force for this work.

Steady tests were completed on the pure fluids as a function of stress and temperature using a 25-mm cone. (See Figure 4.1 for typical data.) There was less than 1.5% change in the steady viscosity of either fluid over a stress range of 50-500 Pa at a given temperature for all temperatures between 20.0-50.0°C; hence, the viscosities of the fluids are essentially independent of applied stress at a given temperature throughout the experiments. The measured normal force in these experiments was always smaller than the lower limit of the rheometer.

In an attempt to approximate the first normal stress difference coefficient, $\psi_1 = N_1/\dot{\gamma}^2$, for the two pure fluids, a 40-mm diameter cone (cone angle=0.04-rad) was used with a higher range of stresses, 500-2900 Pa, at 20.0°C. Note that the stresses used here are out of the range of stresses used for tests on emulsions in this work, but to obtain a measurable normal force, high stresses were required. Results show that $\psi_1 \approx 0.008 \pm 0.001$ and 0.03 ± 0.02 Pa sec^2 for PDMS and Pale 1000, respectively; thus, the two fluids are considered to be Newtonian fluids throughout the experiments.

The steady viscosities of the pure fluids were measured at a stress of 100 Pa as a function of temperature in increments of 5.0°C from 20.0-50.0°C and are listed in Table 4.1. Ten different experiments were completed by a single person for each fluid. The ratio of the standard deviation to the average was less than 4% for viscosity during multiple experiments on a single fluid for both fluids at all temperatures. The ratio of the standard deviation to the average for viscosity during a single experiment at one stress was less than 0.1%.

For all tests on emulsions, Pale 1000 was the droplet phase and PDMS was the suspending fluid; therefore, the viscosity ratio is uniquely defined and shown in Figure 4.2 as a function of temperature. To insure that Pale 1000 remained the droplet phase, all experiments were completed below the phase inversion volume fraction. Paul & Barlow (1980) empirically found that $(\eta_1/\eta_2)(\phi_2/\phi_1) = 1$ approximates the point of phase inversion of two immiscible polymers. In addition to the phase inversion point, there is a region around the phase inversion point in which the phases are

co-continuous [Utracki (1991)]. This co-continuous region is also avoided.

The (λ, ϕ)-parameter space available for study is shown in Figure 4.3. There are four separate curves that describe the boundaries of this region. An upper bound of $\lambda = 4$ is used since emulsions in simple shear flow do not exhibit droplet breakup if $\lambda > 4$ [Grace (1982); de Bruijn (1989); Janssen, Boon & Agterof (1994); Varanasi, Ryan & Stroeve (1994)]. The phase inversion curve of Paul & Barlow (1980) is written in a different form, $\phi_{PI} = \lambda/(1+\lambda)$, where ϕ_{PI} is the phase inversion volume fraction. Instead of using ϕ_{PI}, an upper bound of $\phi_{PI} - 0.1$ is used to avoid the coexistence regime. A lower bound of $\phi = 0.09$ is used so that the number density of droplets is large enough to provide a measurable particle stress. Finally, an upper bound of $\phi = 0.39$ is used so that the emulsion is well within the volume fraction range for which the critical capillary number is a weak function of volume fraction [Mason & Bibette (1997)]. All experiments in this study are denoted by a solid circle on Figure 4.3.

The following test protocol was used for every experiment. The emulsion was mixed by hand with a spatula until a uniform, milky color was obtained. Improper mixing was easily detected since Pale 1000 is amber in color while PDMS is clear. The sample was then placed in a vacuum oven at room temperature and the vent was toggled on/off until the sample stopped frothing. The sample was kept in the oven at 30-mm Hg vacuum for an additional ten minutes to eliminate any remaining air bubbles.

A series of 13 stresses between 50 and 435 Pa, inclusive, were applied in order of increasing stress for 150 seconds each using a 25-mm cone and Peltier. The ratio of τ_{i+1}/τ_i was kept at a constant 1.2 for consecutive values of stress so that the system was only slightly above the critical capillary number at the beginning of a new stress, prior to droplet breakup. A value of 1.2 was chosen so that a single isolated droplet would burst into two large and three satellite droplets [Rallison (1981); Rallison (1984); Stone (1994)]. A time of 150 seconds was chosen based on (i) the results of Takahashi *et al.* (1994a) that 200 strains was sufficient to reach steady state for a similar system when $\dot{\gamma}_f/\dot{\gamma}_i = 2.0$ and (ii) the smallest shear rate of the study at

20.0°C and 50 Pa for the 40.0wt% sample. Both the rotation rate and normal force were measured as a function of time for each experiment. After the stress sequence was completed, the sample was removed from the rheometer and a new sample was loaded for each experiment. As for the pure fluids, a series of tests was completed to determine sampling effects on rheological properties. The ratio of the standard deviation to the average was 4% and 6% for viscosity and first normal stress difference, respectively, when one investigator runs tests on multiple samples of the same volume fraction.

4.4 Results

Figure 4.4 shows an example of steady viscosity, η, and first normal stress difference, N_1, as a function of applied stress, τ, for an emulsion with 30.0wt% dispersed phase. At low stresses the viscosity decreases with increasing stress, but the viscosity is approximately constant at intermediate stresses. The effect at low stresses is more pronounced for higher values of the viscosity ratio and higher volume fractions. At high stresses, drastic shear thinning is evident and this effect is mostly eliminated from this study by choosing an upper limit for the applied stress of 445 Pa. The onstart of shear thinning is evident in Figure 4.4 for $\lambda = 0.800$ at the highest stresses reported. Shear thinning at high stresses is more pronounced for higher volume fractions and smaller values of the viscosity ratio. The first normal stress difference increases with increasing stress and is approximately linear in stress, as predicted by the Doi-Ohta scaling. Complete results of viscosity and first normal stress difference as a function of stress are listed in Tables 4.2-4.23.

Doi & Ohta (1991) predict that the shear viscosity is independent of the imposed rate (or stress, in this case), yet there are two regions of stress in which the viscosity shows shear thinning behavior. Each of these regions of stress are studied more closely to understand why shear thinning occurs. It is shown that shear thinning at low stresses is caused by a combination of geometry effects and incomplete coalescence at small volume fractions. Shear thinning at high stresses is caused by edge fracture of

the sample. These two regions of stress are eliminated when analyzing the rheological data since the change in macroscopic properties are not due solely to changes in the droplet size, shape and orientation.

4.4.1 Low stress effects

At low stresses, the cone angle affects the value of the apparent viscosity, as shown in Figure 4.5, where the viscosity at low stresses increases with decreasing cone angle. If the geometry has no effect, differences in viscosity should be simply due to sample-to-sample variation. It's obvious that sample-to-sample variation cannot account for the large difference in apparent viscosities at low stresses for the three cone angles used. These experiments were performed with 25-mm diameter, aluminum, snap-in cones of varying cone angles (0.10, 0.07, 0.04-radians). These snap-in cones were attached to the upper disposable tool fixture that is typically used as a standard tool on Rheometrics constant rate rheometers instead of constant stress rheometers. The Peltier was replaced with the electrically heated plate option to accommodate the extra length of the upper tool. All experiments were carried out at room temperature.

To further confirm the geometry effect at low stresses, a simple analysis is completed to determine the stress above which geometry effects are negligible. For flows in which two parallel walls bound the fluid and the walls are separated by a distance H, $H/2a > 10$ is a typical criterion used to place a bound on the maximum value of the particle radius for which wall effects are negligible. For the case of the cone-and-plate geometry, H is a function of the radius from the center of the tool. Note that there is a minimum value of $H = 53$-μm since the cone is truncated; thus, an emulsion with droplets having $a < 2.6$-μm shows no geometry effects. In most cases, the droplet size is much larger than 2.6-μm, and a more detailed analysis is required.

Since it's improbable that the entire measuring surface of the tool encloses a region of fluid for which wall effects are negligible, a compromise must be made. Geometry effects are assumed to be negligible if 90% of the measuring surfaces enclose a volume of fluid for which $H/2a > 10$. Based on this assumption, we find a criterion of

$a_{max} \approx$ 30-μm to neglect wall effects in a cone-and-plate geometry with a 25-mm diameter cone having a cone angle of 0.10-radians. Based on the value of the maximum allowable droplet radius, the minimum stress required to obtain this radius can be calculated using the critical capillary number,

$$\tau_{min} \approx Ca_c \frac{\sigma}{a_{max}} \approx 200 Ca_c, \tag{4.14}$$

where τ_{min} has units of Pascals.

The equation of de Bruijn (1989), a curve fit to experimental data, is used to calculate the value of the critical capillary number, Ca_c, for a given value of the viscosity ratio, λ,

$$\log_{10}(Ca_c) = a + b(\log_{10}(\lambda)) + c(\log_{10}(\lambda))^2 + \frac{d}{\log_{10}(\lambda) - \log_{10}(\lambda_c)}, \tag{4.15}$$

where

$$a = -0.506, \tag{4.16a}$$

$$b = -0.0994, \tag{4.16b}$$

$$c = 0.124, \tag{4.16c}$$

$$d = -0.115, \tag{4.16d}$$

$$\lambda_c = 4.08. \tag{4.16e}$$

Equation (4.15) is a curve fit to experimental data for Newtonian droplets in a Newtonian suspending fluid in simple shear flow. For the calculations of τ_{min}, it is also assumed that surface tension does not vary with temperature, which isn't too poor of an assumption considering that the maximum variation of surface tension with temperature for immiscible homopolymer blends is -0.03 mN/m/K [Koberstein (1990)]. Table 4.24 includes the minimum stress required to eliminate geometry effects as a function of viscosity ratio for an emulsion with 30.0wt% dispersed fluid. The value of τ_{min} increases quickly as $\lambda \rightarrow 4$ but remains relatively constant for $\lambda < 1$, which

agrees with the results in Figure 4.4. The values for τ_{min} are used when analyzing the rheological data to eliminate wall effects.

To confirm the required value of a_{max}, the maximum allowable droplet size, microscopic images of emulsions were taken after various stresses for 0.15wt% dispersed phase at a temperature of 25.0°C, as shown in Figure 4.6. The usual test protocol was used for these experiments with one exception—the test was stopped after reaching steady-state at a certain stress. Once the test was stopped, the upper tool was slowly raised to 2.0-mm and a glass pipette was used to take a sample for microscopy. Samples were viewed using a Zeiss microscope (47 16 40-9901) with a 7:1/NA 0.20 objective lens. The sample was backlit by white light without the use of diffusers or polarizers. Photographic images were taken using a Minolta SRT101 camera with Kodak 400-speed, color film and a Zeiss camera tube (47 30 23-9900). At stresses higher than the minimum stress, τ_{min} = 169-Pa, for $\lambda = 2.27$, the droplets are smaller than a_{max}, while at stresses lower that 169-Pa, the droplet size is quite large, as expected, reaching nearly 150-μm and geometry effects will be measurable.

In addition to large droplets at low stresses, the droplet size is very polydisperse. The droplet size has not reached a steady value because coalescence has not occurred at a fast enough rate during the time scale of the experiment. This slow coalescence also causes an increase in the viscosity compared to the expected value since the smaller droplets do not deform in the flow. By the time the minimum stress is reached in the stress sequence, there is sufficient time for droplets to coalesce and dispersity of droplet sizes decreases above τ_{min}. Slow coalescence is only a problem at small volume fractions since the average distance between droplets is $\sim O\left(a\phi^{-1/3}\right)$. At large volume fractions it is expected that the droplets achieve a steady and uniform size during the time a single stress is applied to the sample and only geometry effects remain at low stresses.

4.4.2 High stress effects

At high stresses the steady viscosity shear thins, contrary to the prediction of Doi & Ohta (1991). To test the region of shear thinning at high stresses, an experiment was performed using a 35.0wt% emulsion over an extended range of stresses, 50 to 770-Pa, while simultaneously acquiring rheology data and visual images of the meniscus at the outer edge. Steady viscosity results and steady meniscus images are reported in Figure 4.7. The cone is the white portion of the image with the black dot in the upper, right corner of each image. The surface of the lower tool, the Peltier, is most evident in image (b) of Figure 4.7. The Peltier surface can be seen as a horizontal line approximately 2/5 from the bottom along the left side of the image.

The images of the meniscus were captured using a Sony VHS camcorder (VL-L50U) with a 12x zoom lens and an additional lens between the sample and the camcorder's objective lens to provide greater magnification. The sample was backlit with white light, bounced off the stainless steel back of the rheometer stage, so that the meniscus appeared as a silhouette. A soft, diffuse white light was directed at the tool from behind the camcorder's objective lens to provide enough light to capture the image. All ambient light was eliminated. Still shots were captured from VHS tape using a Sony stereo videocassette recorder (SVO-2000) and a Macintosh Quadra 660AV.

At low stresses, where shear thinning is caused by wall effects, the meniscus does not change shape from the no-flow surface. At the highest stress used in the standard protocol, 445-Pa, the meniscus slightly changes shape and the cone is no longer fully covered with fluid. Incomplete coverage of the cone surface by the sample is more evident at 770-Pa where the viscosity has decreased to approximately 50% of its value at intermediate stresses. At stresses higher than 770-Pa, the fluid no longer contacts the cone, allowing the cone to spin freely.

Since the Peltier has a larger diameter than the cone, it appears from the images that the Peltier provides a place for fluid to accumulate with little resistance and that edge fracture, and resulting shear thinning, might be caused by the choice of tools.

Experiments at room temperature on a 30.0wt% emulsion using a 40-mm diameter cone (cone angle=0.04-radians) for the upper tool and the 40-mm diameter electrically heated plate for the lower tool show similar behavior. The sample is expelled from the tools quite easily and shear thinning, though not as severe, still occurs. Edge fracture at high stresses, and the resulting shear thinning, is not caused by the use of tools with different diameters.

4.4.3 Analysis of rheology

The results for viscosity at low and high stresses do not contradict the scaling argument of Doi & Ohta (1991) since shear thinning occurs in these regions because of wall effects and edge fracture, respectively. Shear thinning does not occur because of changes in the size, shape or orientation of the droplets; thus, the Doi-Ohta scaling cannot be applied to regions of low or high stresses in this study. There is an intermediate region of stresses, $\tau_{min} < \tau <$ 445-Pa, for which the Doi-Ohta scaling can be applied and is valid. In the intermediate stress regime, the viscosity is approximately constant and the first normal stress difference, when measurable, is approximately linear in applied stress, as predicted by Doi & Ohta (1991). For the case of $\lambda = 3.44$, the value for $\tau_{min} >$ 445-Pa and no intermediate region exists. Data from the four highest stresses are used to approximate the rheological behavior for emulsions with $\lambda = 3.44$.

Since the Doi-Ohta scaling is valid, a single experiment is characterized by a constant steady shear viscosity, η, and a constant nondimensional, first normal stress difference, $N_1/\eta_s\dot{\gamma}$, for a given set of values for the viscosity ratio and volume fraction. Both of these constants are calculated by averaging the data over the intermediate range of stresses, but the standard deviation calculated during this averaging process does not account for sample-to-sample variation. Error bars for η and N_1 must account for sample-to-sample variation since different samples are compared. The proper standard deviations are calculated by

$$s_\eta = (0.04)\, 2^{1/2} \eta, \tag{4.17a}$$

$$s_{N1} = (0.06)\, 2^{1/2} N_1, \tag{4.17b}$$

where s_η and s_{N1} are the standard deviations for the shear viscosity and first normal stress difference, respectively, which account for sample-to-sample variation when only one replication is completed [Bafna (1995)]. In s_η, the factor of 0.04η arises because the sample-to-sample variation of emulsion viscosity is 4% of the average, as measured during a series of tests using a 35.0wt% emulsion. During these same tests, the sample-to-sample variation of the first normal stress difference is 6% of the average, thus accounting for the factor of $0.06N_1$ in the equation for the standard deviation of N_1. The factor of $2^{1/2}$ for both s_η and s_{N1} comes from the fact that only a single experiment is performed and that the standard deviation must be extended to include the 66% confidence interval of the true average and true standard deviation.

Figure 4.8 shows an example of the viscosity and nondimensional, first normal stress difference as a function of volume fraction for $\lambda = 1.55$. Averages and standard deviations are calculated as just described and account for sample-to-sample variation. Visually, a linear curve fit with respect to volume fraction appears reasonable for both curves.

Using data like that presented in Figure 4.8, the scaled viscosity and scaled first normal stress difference can be easily calculated by using a linear curve fit program [Press *et al.* (1992)] for all values of the viscosity ratio. When curve fitting viscosity, both the slope and intercept are left as free parameters. In all cases, the solvent viscosity is included in the 66% confidence interval of the intercept. For the nondimensional, first normal stress difference, the slope is kept as a free parameter, but the intercept is set equal to zero since the fluids are Newtonian over the range of stresses studied. Curve fit results for viscosity and first normal stress difference are presented in Tables 4.25 and 4.26, respectively, including values of the scaled viscosity (η^*), scaled first normal stress difference (N_1^*), the chi-square parameter (χ^2), and the goodness-of-fit parameter, (Q).

Scaled viscosity

In Table 4.25, the curve fitting results for the scaled viscosity are quite remarkable. The goodness-of-fit parameter is greater than 0.85 for all values of viscosity ratio, and a linear fit for viscosity with respect to volume fraction is quite acceptable. The scaled viscosity, η^*, is a valid concept and meaningful property.

The results of the curve fitting procedure are also presented in Figure 4.9, where scaled viscosity, η^*, is plotted as a function of the viscosity ratio, λ. Results of this work are compared to other experimental results [Takahashi *et al.* (1994a, 1994b); Vinckier, Mewis & Moldenaers (1996a); Kitade *et al.* (1997)] and simulation results [Loewenberg & Hinch (1996)]. Agreement between the different systems is quite spectacular considering that the data includes some emulsions for which the pure fluids exhibit non-Newtonian behavior such as shear thinning and/or first normal stress differences [Takahashi *et al.* (1994b); Vinckier, Mewis & Moldenaers (1996a); Kitade *et al.* (1997)].

Finally, a curve to approximately predict the scaled viscosity as a function of λ is a desirable feature. Based on the results of Loewenberg & Hinch (1996) for $\lambda = 1$, the Taylor deformation parameter is less than 0.50 at the critical capillary number for all volume fractions studied; thus, the small deformation theory may be applicable. We start with the results of Taylor (1932) for nearly spherical droplets in simple shear flow,

$$\eta^* = \frac{(5\lambda + 2)}{2(\lambda + 1)}. \tag{4.18}$$

The results of Taylor (1932) are added to Figure 4.9 and found to be in reasonable agreement with the experimental and simulation data over the whole range of the viscosity ratio for which data is available.

Scaled first normal stress difference

Curve fitting results for the scaled first normal stress difference are presented in Table 4.26, and the results are adequate. The goodness-of-fit parameter is quite small, $Q \sim O(0.1 - 0.001)$, for larger values of the viscosity ratio, $\lambda > 1.2$, but the

goodness-of-fit parameter is greater than 0.82 for smaller viscosity ratios, $\lambda < 1.2$. Despite the low value of the goodness-of-fit parameter, the data for scaled first normal stress difference is not as poor as it first appears.

First of all, Press *et al.* (1992) state that investigators may find models acceptable when the goodness-of-fit parameter is as small as 0.001, the smallest value in this study. Secondly, we can reject the linear model for the whole range of volume fraction and, instead, apply the model to a truncated range of volume fraction. If a linear curve fit is performed for $\lambda = 1.55$, eliminating 40.0 and 35.0wt% from the original analysis, the scaled first normal stress difference is 2.76 ± 0.126 instead of 2.89 ± 0.112. In addition, the curve fit over the smaller range of volume fraction yields a goodness-of-fit parameter equal to 0.70 instead of 0.031. By eliminating the two highest volume fractions, the goodness-of-fit parameter reaches a level for which the linear model is now perfectly acceptable, but the scaled first normal stress difference barely changes and is nearly within the 66% confidence interval of its original value. Based on these two facts, the linear model is accepted as an adequate fit for all values of the viscosity ratio.

Figure 4.10 shows the results of the curve fitting procedure for the scaled first normal stress difference, N_1^*, as a function of the viscosity ratio, λ. As for viscosity, results of this work are compared to other experimental results [Takahashi *et al.* (1994a, 1994b); Vinckier, Mewis & Moldenaers (1996a); Kitade *et al.* (1997)] and simulation results [Loewenberg & Hinch (1996)]. Considering the fact that normal stress differences are difficult to measure and the wide-range of systems presented, the agreement between the different systems is excellent.

When including data for the scaled first normal stress difference, N_1^*, in Figure 4.10, only the contribution from the interface is included. When an emulsion is composed of Newtonian fluids, this is not a problem since the measured first normal stress difference occurs solely due to the existence of the interface. But when emulsions are composed of fluids that exhibit measurable first normal stress differences [Takahashi *et al.* (1994b); Vinckier, Mewis & Moldenaers (1996a); Kitade *et al.* (1997)], the contribution to the measured first normal stress difference from the dispersed and

suspending fluids must be subtracted to give the extra stress, ΔN_1. The extra stress is the stress solely due to the existence of the interface and the quantity becomes important at high rates since $N_1 \sim (\dot{\gamma}^2)$ for the pure fluids and dominates the contribution from the interface, $\Delta N_1 \sim (\dot{\gamma})$. The extra first normal stress difference is typically defined [Takahashi *et al.* (1994b)],

$$\Delta N_1(\dot{\gamma}) = N_1(\dot{\gamma}) - \phi N_{1,d}(\dot{\gamma}) - (1-\phi) N_{1,s}(\dot{\gamma}), \tag{4.19}$$

where $N_{1,d}$ and $N_{1,s}$ are the first normal stress differences of the dispersed and suspending fluids, respectively, at the shear rate of interest.

Finally, just as for viscosity, it is desirable to find a curve to approximately predict the scaled first normal stress difference as a function of λ. Since small deformation theory works so well for viscosity, it is used here as well. We start with the first results predicting normal stress differences caused by a single droplet at small deformations [Schowalter, Chaffey & Brenner (1968)], evaluated at the critical capillary number,

$$N_1^* = \frac{Ca_c}{40}\left(\frac{19\lambda+16}{\lambda+1}\right)^2. \tag{4.20}$$

The result of Schowalter, Chaffey & Brenner (1968) is added to Figure 4.10 and found to be in reasonable agreement with the experimental and simulation data only for $\lambda \approx 1$. By visually inspecting equation (4.20), we see that it predicts aphysical behavior as $\lambda \to 4$. Equation (4.20) predicts that the first normal stress difference increases with increasing viscosity ratio since the critical capillary number diverges as $\lambda \to 4$, as seen in equation (4.15). But as the viscosity ratio increases, the droplet is less deformed and should result in a smaller value for the first normal stress difference. This idea is in agreement with experiments since the first normal stress difference of an emulsion at $\lambda \approx 1$ is much easier to measure than the first normal stress difference of hard spheres.

In hopes of correcting the aphysical nature of the predictions of Schowalter, Chaffey & Brenner (1968), the results of Barthes-Biesel & Acrivos (1973a, 1973b) are

analyzed. Barthes-Biesel & Acrivos (1973a, 1973b) predict the $O(Ca^2\eta_s\dot{\gamma}\phi)$ contribution to the bulk stress for $Ca \ll 1$. The new terms in the bulk stress predict a shear thinning viscosity in simple shear flow, but the new terms do not contribute to normal stresses.

There is only one remaining study that predicts a different dependence of the first normal stress difference on the capillary number for small deformations [Choi & Schowalter (1975)]. Choi & Schowalter use a deformable droplet in a cell model in simple shear flow and find

$$N_1^* = \frac{2}{5}\left(\frac{Ca}{1+Z^2}\right)\left(\frac{19\lambda+16}{4(\lambda+1)}\left(1+\phi\frac{5(5\lambda+2)}{4(\lambda+1)}+O\left(\phi^{5/3}\right)\right)\right)^2 \tag{4.21a}$$

$$Z = \frac{(19\lambda+16)(2\lambda+3)}{40(\lambda+1)}Ca\left(1+\phi\frac{5(19\lambda+16)}{4(\lambda+1)(2\lambda+3)}+O\left(\phi^{5/3}\right)\right). \tag{4.21b}$$

Since we are only interested in the dilute behavior of the emulsion at the critical capillary number, take the $\phi \ll 1$ limit of both equations, set $Ca = Ca_c$ and rearrange to find

$$N_1^* = \frac{Ca_c}{40}\left(\frac{19\lambda+16}{\lambda+1}\right)^2\frac{1}{1+Z^2}, \tag{4.22a}$$

$$Z = \frac{(19\lambda+16)(2\lambda+3)}{40(\lambda+1)}Ca_c. \tag{4.22b}$$

If $Ca_c \ll 1$, then $Z \ll 1$ and equation (4.20) is recovered. If $\lambda \to 4$, then $Ca_c \gg 1$, $Z \sim O(Ca_c)$, $Z \gg 1$, and $N_1^* \sim O(1/Ca_c)$ resulting in a scaled first normal stress difference that approaches zero as $\lambda \to 4$. The result of Choi & Schowalter (1975) for $\phi \ll 1$ is added to Figure 4.10 and found to be in reasonable qualitative agreement with the data.

4.5 Conclusions

A scaling argument for the particle stress of an emulsion of two Newtonian fluids in steady flow at the critical capillary number is presented. It is shown that the scaled

particle stress can be written as a function that is dependent only on the ratio of the viscosities of the dispersed and suspending fluids, $\lambda = \eta_d/\eta_s$.

The steady viscosity and first normal stress difference of an emulsion—polymerized castor oil dispersed in polydimethylsiloxane—are measured in simple shear flow at the critical capillary number as a function of the volume fraction of dispersed phase, $\phi = 0.09 - 0.39$, and viscosity ratio, $\lambda = 0.20 - 3.6$. These results confirm the scaling argument for the particle stress for simple shear flow. Master curves are produced for the scaled viscosity and first normal stress difference. Small deformation theory of a single droplet in simple shear flow is used to approximate the master curves.

Acknowledgements

Special thanks to Denis Shcherbakov who completed the experiments for steady rheological properties as a Summer Undergraduate Research Fellowship (SURF) student. Financial support for Denis was made possible through the SURF endowment fund and specifically by Dr. and Mrs. Warren G. Schlinger. I would also like to thank Wayne Wright (Caschem, Inc.) for providing a sample of Pale 1000.

References

Bafna, S.S., "Rheological measurements: Some basic yet vital considerations." J. Appl. Polym. Sci. **58**, 1385–1392 (1995).

Barthes-Biesel, D. & A. Acrivos, "Deformation and burst of a liquid droplet freely suspended in a linear shear field." J. Fluid Mech. **61**, 1–21 (1973a).

Barthes-Biesel, D. & A. Acrivos, "The rheology of suspensions and its relation to phenomenological theories for non-Newtonian fluids." Int. J. Mult. Flow **1**, 1–24 (1973b).

Batchelor, G.K., "The stress system in a suspension of force-free particles." J. Fluid Mech. **41**, 545–570 (1970).

Chaffey, C.E. & H. Brenner, "A second-order theory for shear deformation of drops." J. Coll. Sci. **24**, 258–269 (1967).

Chappat, M., "Some applications of emulsions." Coll. & Surf. A **91**, 57–77 (1994).

Choi, S.J. & W.R. Schowalter, "Rheological properties of nondilute suspensions of deformable particles." Phys. Fluids **18**, 420–427 (1975).

Cox, R.G., "The deformation of a drop in a general time-dependent fluid flow." J. Fluid Mech. **37**, 601–623 (1969).

Davis, R.H., J.A. Schonberg & J.M. Rallison, "The lubrication force between two viscous drops." Phys. Fluids A **1**, 77–81 (1989).

de Bruijn, R.A., "Deformation and breakup of drops in simple shear flows." Ph.D. Thesis, Eindhoven (1989).

Doi, M. & T. Ohta, "Dynamics and rheology of complex interfaces. I." J. Chem. Phys. **95**, 1242–1248 (1991).

Frankel, N.A. & A. Acrivos, "The constitutive equation for a dilute emulsion." J. Fluid Mech. **44**, 65–78 (1970).

Grace, H.P., "Dispersion phenomena in high viscosity immiscible fluid systems and application of static mixers as dispersion devices in such systems." Chem. Eng. Comm. **14**, 225–277 (1982).

Hinch, E.J. & A. Acrivos, "Long slender drops in a simple shear flow." J. Fluid Mech. **98**, 305–328 (1980).

Janssen, J.J.M., A. Boon & W.G.M. Agterof, "Influence of dynamic interfacial properties on droplet breakup in simple shear flow." AIChE J. **40**, 1929–1939 (1994).

Kennedy, M.R., C. Pozrikidis & R. Skalak, "Motion and deformation of liquid drops, and the rheology of dilute emulsions in simple shear flow." Computers Fluids **23**, 251–278 (1994).

Kitade, S., A. Ichikawa, N. Imura, Y. Takahashi & I. Noda, "Rheological properties and domain structures of immiscible polymer blends under steady and oscillatory

shear flows." J. Rheol. **41**, 1039–1060 (1997).

Koberstein, J.T., "Interfacial properties." in *Concise Encyclopedia of Polymer Science and Engineering* edited by I.J. Kroschwtiz (Wiley, New York), 486–489 (1990).

Koh, C.J. & L.G. Leal, "An experimental investigation on the stability of viscous drops translating through a quiescent fluid." Phys. Fluids A **2**, 2103–2109 (1990).

Li, X., H. Zhou & C. Pozrikidis, "A numerical study of the shearing motion of emulsions and foams." J. Fluid Mech. **286**, 379–404 (1995).

Li, X., R. Charles & C. Pozrikidis, "Simple shear flow of suspensions of liquid drops." J. Fluid Mech. **320**, 395–416 (1996).

Loewenberg, M. & E.J. Hinch, "Numerical simulation of a concentrated emulsion in shear flow." J. Fluid Mech. **321**, 395–419 (1996).

Mason, T.G. & J. Bibette, "Shear rupturing of droplets in complex fluids." Langmuir **13**, 4600–4613 (1997).

Paul, D.R. & J.W. Barlow, "Polymer blends (or alloys)." J. Macromol. Sci.-Rev. Macromol. Chem. **C18**, 109–168 (1980).

Pozrikidis, C., "On the transient motion of ordered suspensions of liquid drops." J. Fluid Mech. **246**, 304–320 (1993).

Press, W.H., S.A. Teukolsky, W.T. Vetterling & B.P. Flannery, *Numerical recipes in Fortran: The art of scientific computing.* (Cambridge University Press, 2nd edition, 1992).

Rallison, J.M., "Note on the time-dependent deformation of a viscous drop which is almost spherical." J. Fluid Mech. **98**, 625–633 (1980).

Rallison, J.M., "A numerical study of the deformation and burst of a viscous drop in general shear flows." J. Fluid Mech. **109**, 465–482 (1981).

Rallison, J.M., "The deformation of small viscous drops and bubbles in shear flows." Ann. Rev. Fluid Mech. **16**, 45–66 (1984).

Rumscheidt, F.D. & S.G. Mason, "Particle motions in sheared suspensions. XII. Deformation and burst of fluid drops in shear and hyperbolic flows." J. Coll. Sci. **16**, 238–261 (1961).

Schowalter, W.R., C.E. Chaffey & H. Brenner, "Rheological behavior of a dilute emulsion." J. Coll. & Int. Sci. **26**, 152–160 (1968).

Stone, H.A., "Dynamics of drop deformation and breakup in viscous fluids." Ann. Rev. Fluid Mech. **26**, 65–102 (1994).

Takahashi, Y., N. Kurashima, I. Noda & M. Doi, "Experimental tests of the scaling relation for textured materials in mixtures of two immiscible fluids." J. Rheol. **38**, 699–712 (1994a).

Takahashi, Y., S. Kitade, N. Kurashima & I. Noda, "Viscoelastic properties of immiscible polymer blends under steady and transient shear flows." Polym. J. **26**, 1206–1212 (1994b).

Taylor, G.I., "The viscosity of a fluid containing small drops of another fluid." Proc. R. Soc. London Ser. A **138**, 41–48 (1932).

Taylor, G.I., "The formation of emulsions in definable fields of flow." Proc. R. Soc. London Ser. A **146**, 501–523 (1934).

Torza, S., R.G. Cox & S.G. Mason, "Particle motions in sheared suspensions. XXVII. Transient and steady deformation and burst of liquid drops." J. Coll. Int. Sci. **38**, 395–411 (1972).

Utracki, L.A., "On the viscosity-concentration dependence of immiscible polymer blends." J. Rheol. **35**, 1615–1637 (1991).

Varanasi, P.P., M.E. Ryan & P. Stroeve, "Experimental study on the breakup of model viscoelastic drops in uniform shear flow." Ind. Eng. Chem. Res. **33**, 1858-1866 (1994).

Vinckier, I., J. Mewis & P. Moldenaers, "Immiscible polymer blends: processing and blend structure." Bull. Soc. Chim. Belg. **105**, 799–804 (1996a).

Vinckier, I., P. Moldenaers & J. Mewis, "Relationship between rheology and morphology of model blends in steady shear flow." J. Rheol. **40**, 613–631 (1996b).

Zhou, H. & C. Pozrikidis, "The flow of ordered and random suspensions of two-dimensional drops in a channel." J. Fluid Mech. **255**, 103–127 (1993).

Zinchenko, A.Z., "Effect of hydrodynamic interactions between the particles on the rheological properties of dilute emulsions." Prikl. Mat. Mech. **48**, 198-206 (1984).

Zinchenko, A.Z., M.A. Rother & R.H. Davis, "A novel boundary-integral algorithm for viscous interaction of deformable drops." Phys. Fluids **9**, 1493–1511 (1997).

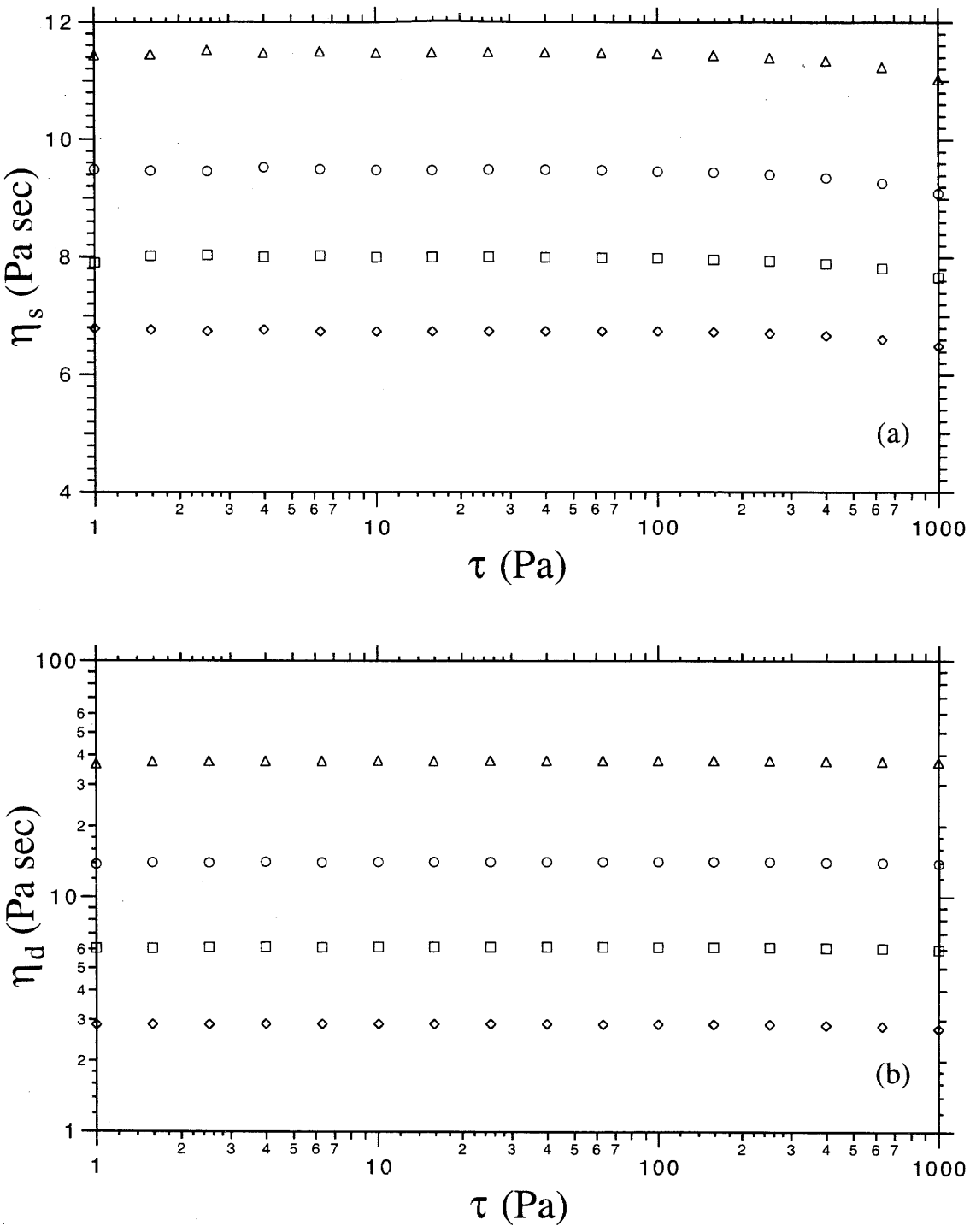

Figure 4.1: Steady-state shear viscosity, η, as a function of applied shear stress, τ, for (a) PDMS and (b) Pale 1000 at T=20.0°C ($\triangle$), T=30.0°C ($\circ$), T=40.0°C ($\square$), and T=50.0°C ($\diamond$).

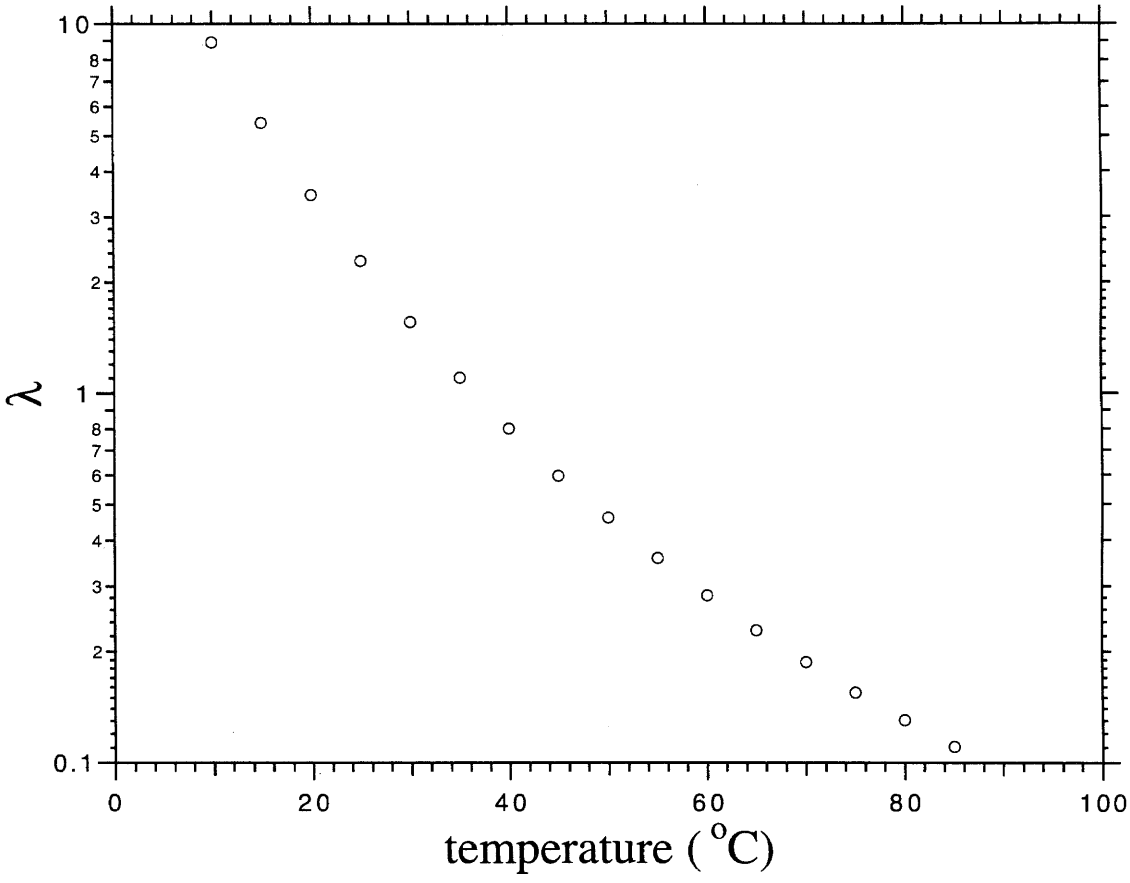

Figure 4.2: Viscosity ratio, $\lambda = \eta_d/\eta_s$, as a function of temperature. Sample-to-sample error bars are not shown since they are small enough to fit inside the circles.

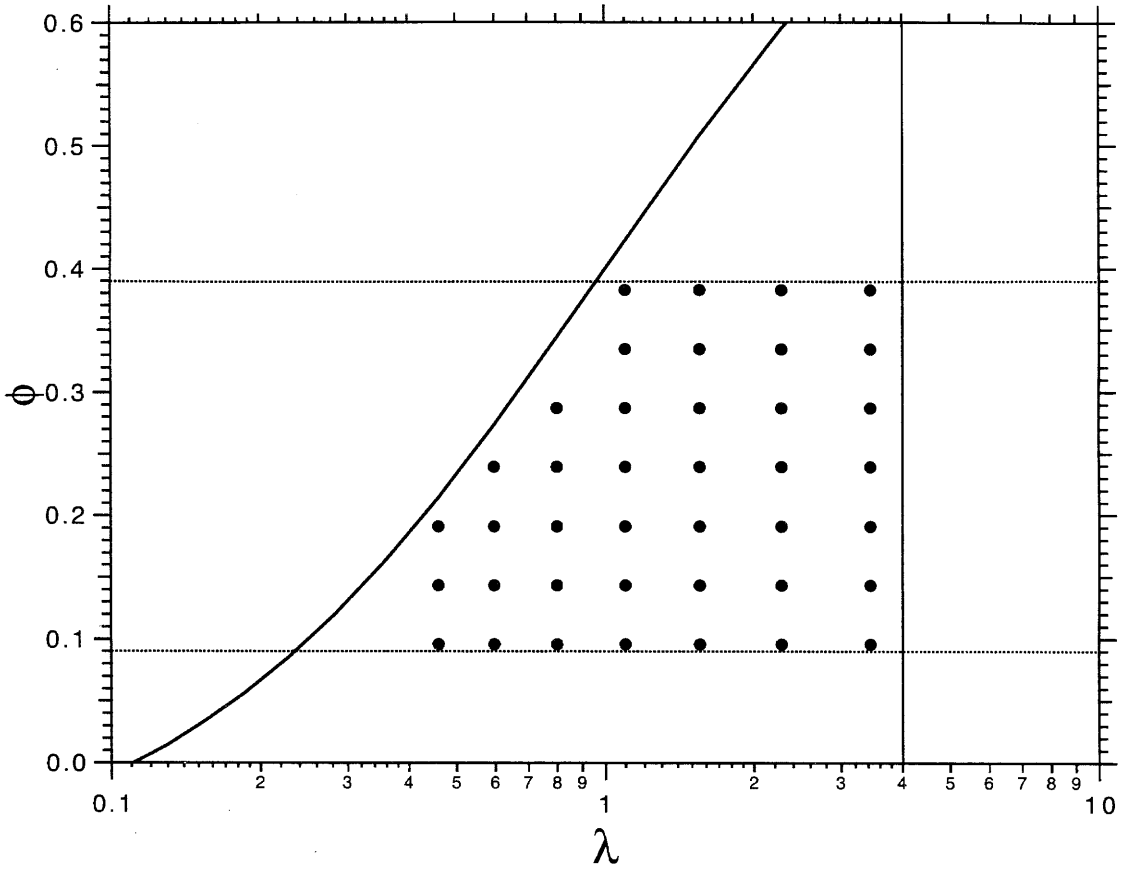

Figure 4.3: Parameter space for (λ, ϕ). Four curves mark the boundary: (1) the viscosity ratio above which droplet breakup no longer occurs in simple shear flow, $\lambda_c = 4$, (solid line), (2) the curve to eliminate phase inversion and the coexistence regime, $\phi_{PI} - 0.1$, (solid line), (3) $\phi = 0.09$ (dashed line), and (4) $\phi = 0.39$ (dashed line). Solid circles (•) are used to mark the points in (λ, ϕ)-space for which experiments were performed.

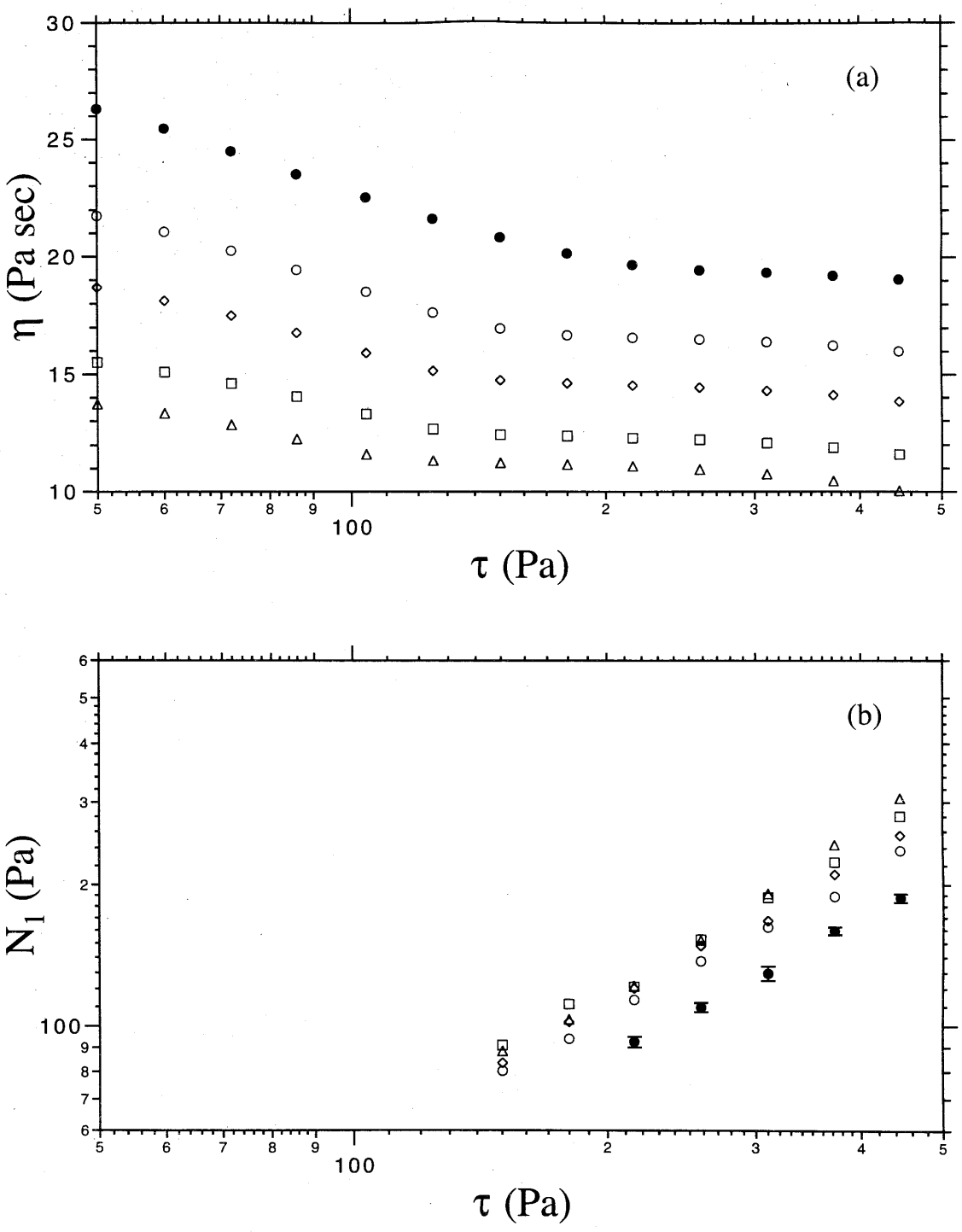

Figure 4.4: Steady-state results for (a) shear viscosity, η, and (b) first normal stress difference, N_1, as a function of applied stress, τ, for 30.0wt% with $\lambda = 3.44$ (•), $\lambda = 2.27$ (○), $\lambda = 1.55$ (◇), $\lambda = 1.10$ (□), and $\lambda = 0.800$ (△). Error bars are shown only for $\lambda = 3.44$.

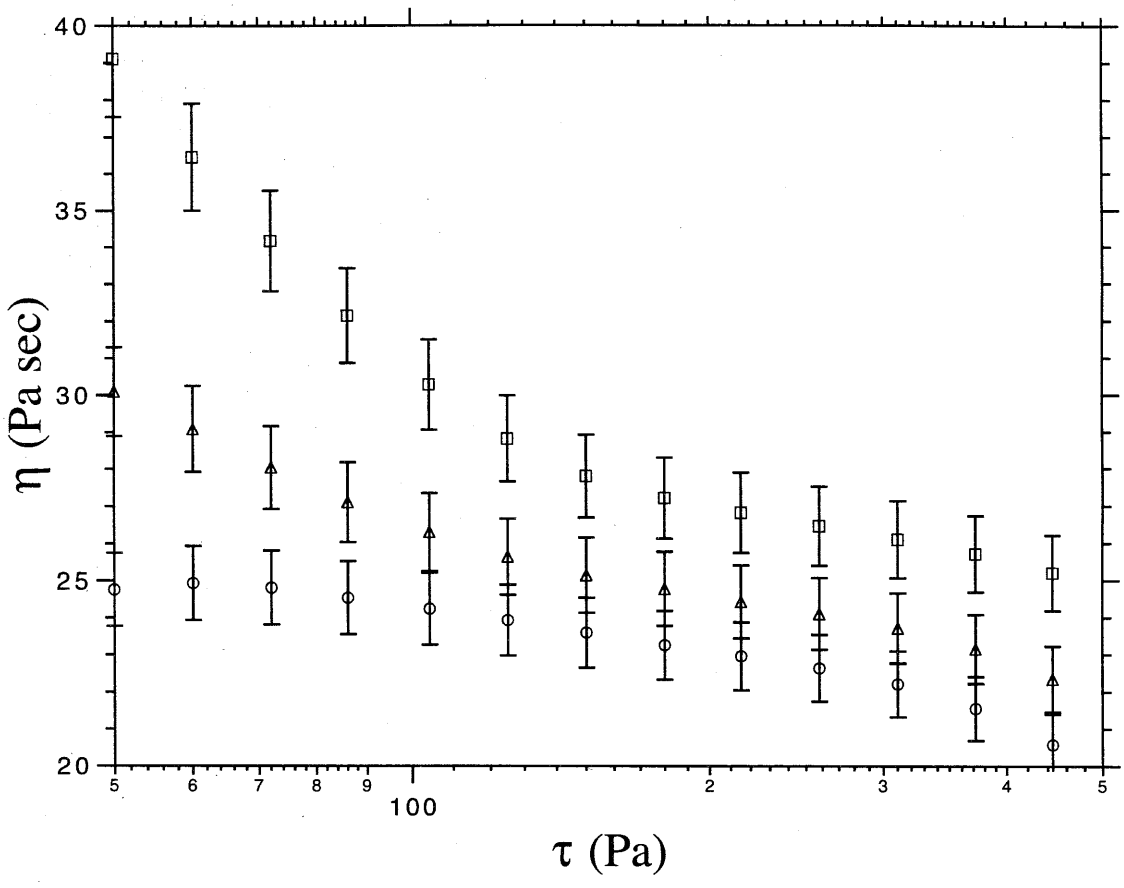

Figure 4.5: Effect of cone angle on the steady shear viscosity. Steady-state shear viscosity, η, as a function of applied stress, τ, for 40.0wt% at T=20°C using 25.0-mm diameter, aluminum cones with a cone angle of 0.04-radians (□), 0.07-radians (△), and 0.10-radians (○).

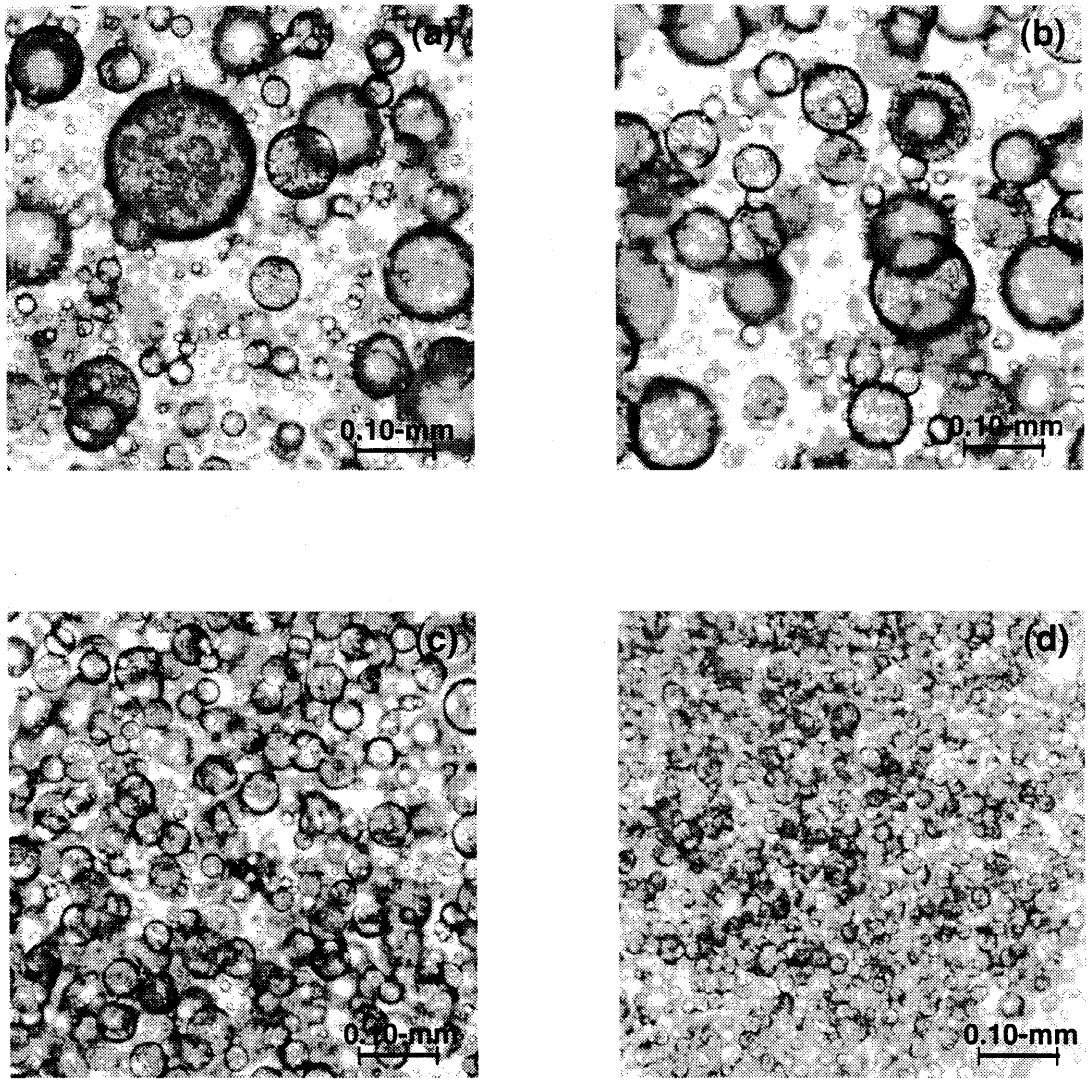

Figure 4.6: Microscopic images of droplets in an emulsion of 15.0wt% dispersed fluid at a temperature of 25.0°C. The stress sequence was started following the usual protocol and stopped after (a) 50 Pa, (b) 104 Pa, (c) 215 Pa and (d) 445 Pa to take a sample. Images of 98-μm diameter polystyrene beads (Bangs Laboratories, Inc.) were used to determine the length scale.

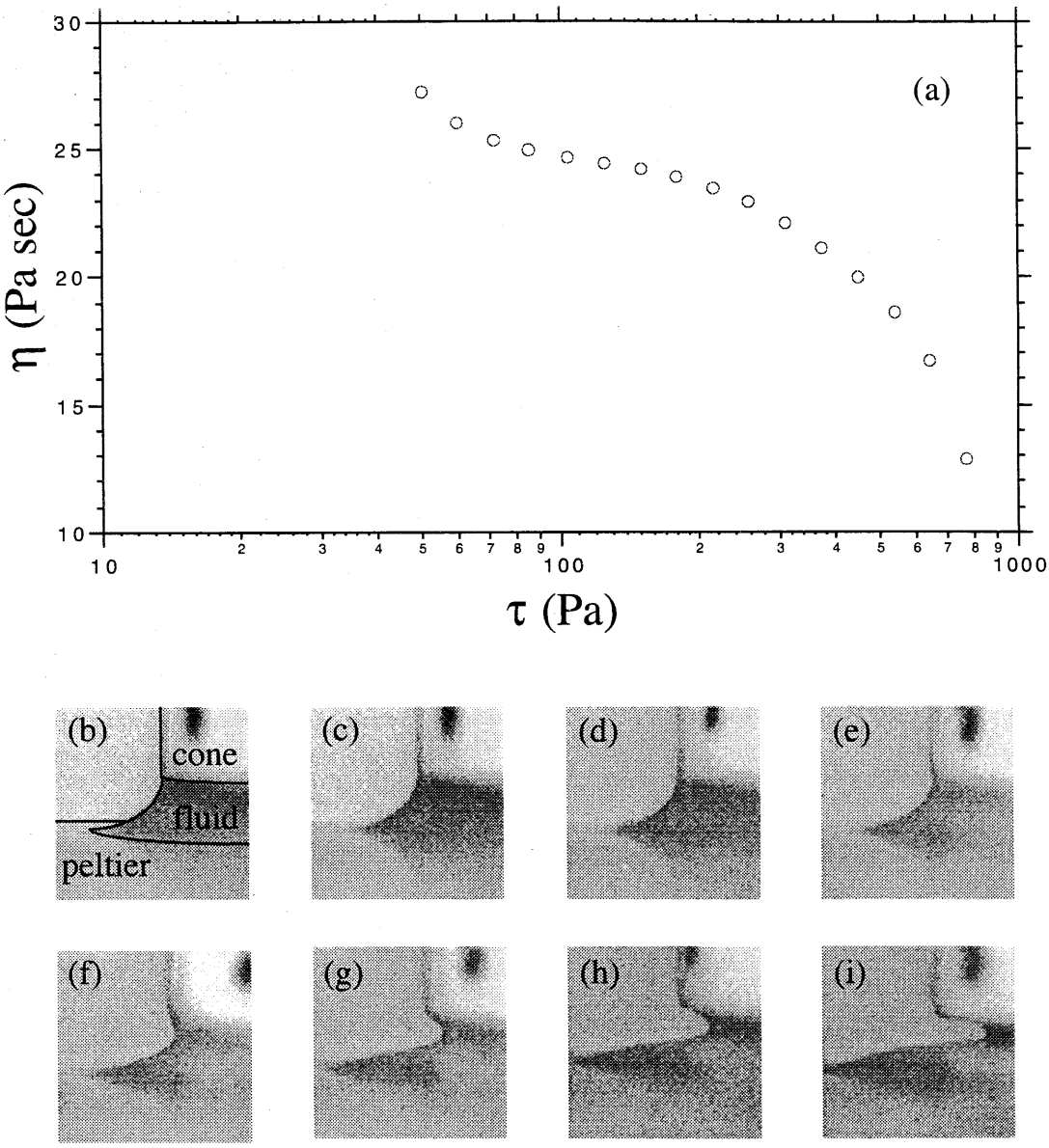

Figure 4.7: Effect of edge fracture on steady shear viscosity. (a) Steady-state shear viscosity, η, as a function of applied stress, τ, for 35.0wt% at T=20.0°C. Steady-state meniscus shape at the cone edge for (b) 0 Pa (with labels), (c) 0 Pa, (d) 125 Pa, (e) 215 Pa, (f) 310 Pa, (g) 535 Pa, (h) 640 Pa, and (i) 770 Pa.

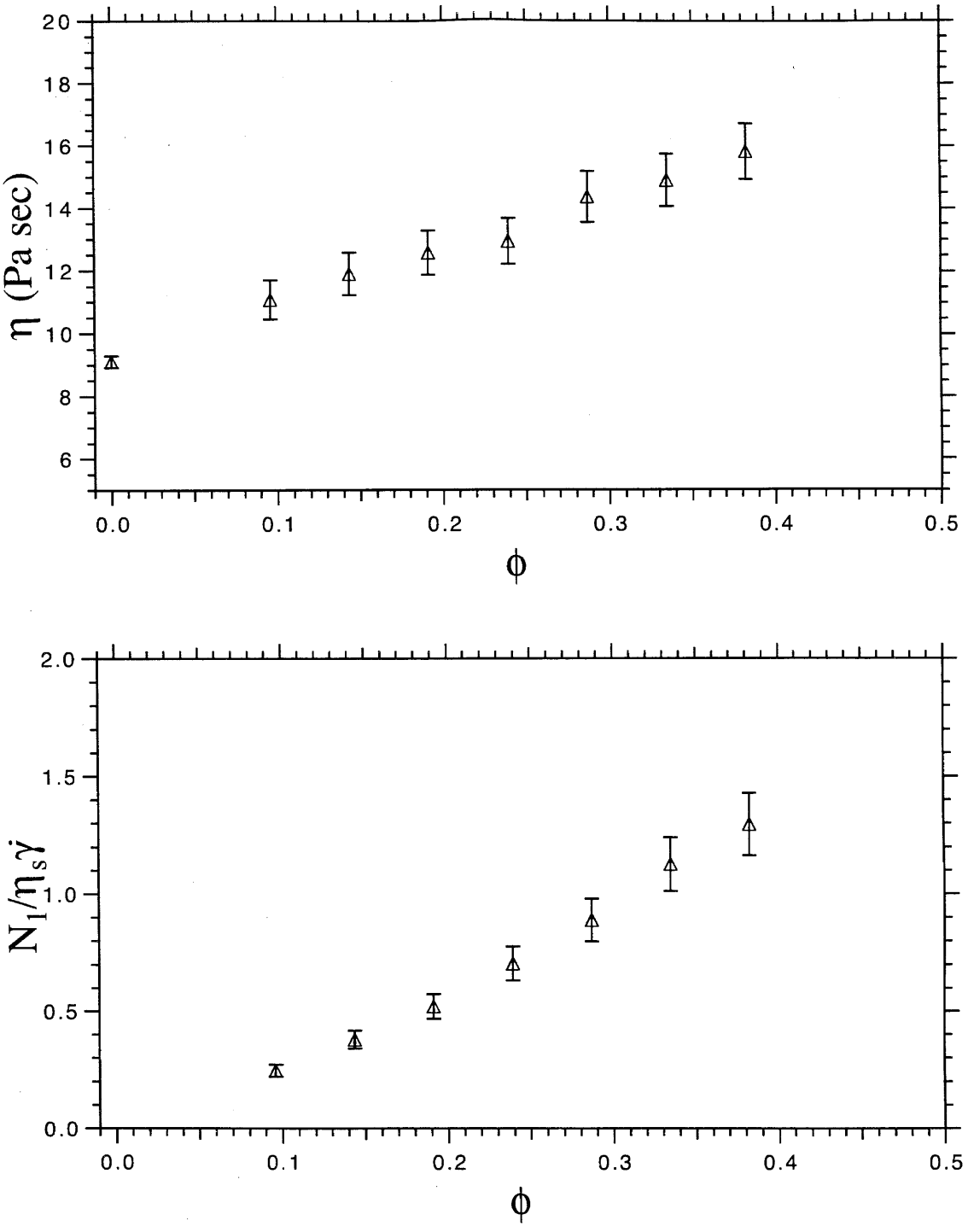

Figure 4.8: Effect of volume fraction on the contribution of the interface to the rheological properties at λ=1.55 for (a) the shear viscosity, η, and (b) the nondimensional first normal stress difference, $N_1/\eta_s\dot{\gamma}$.

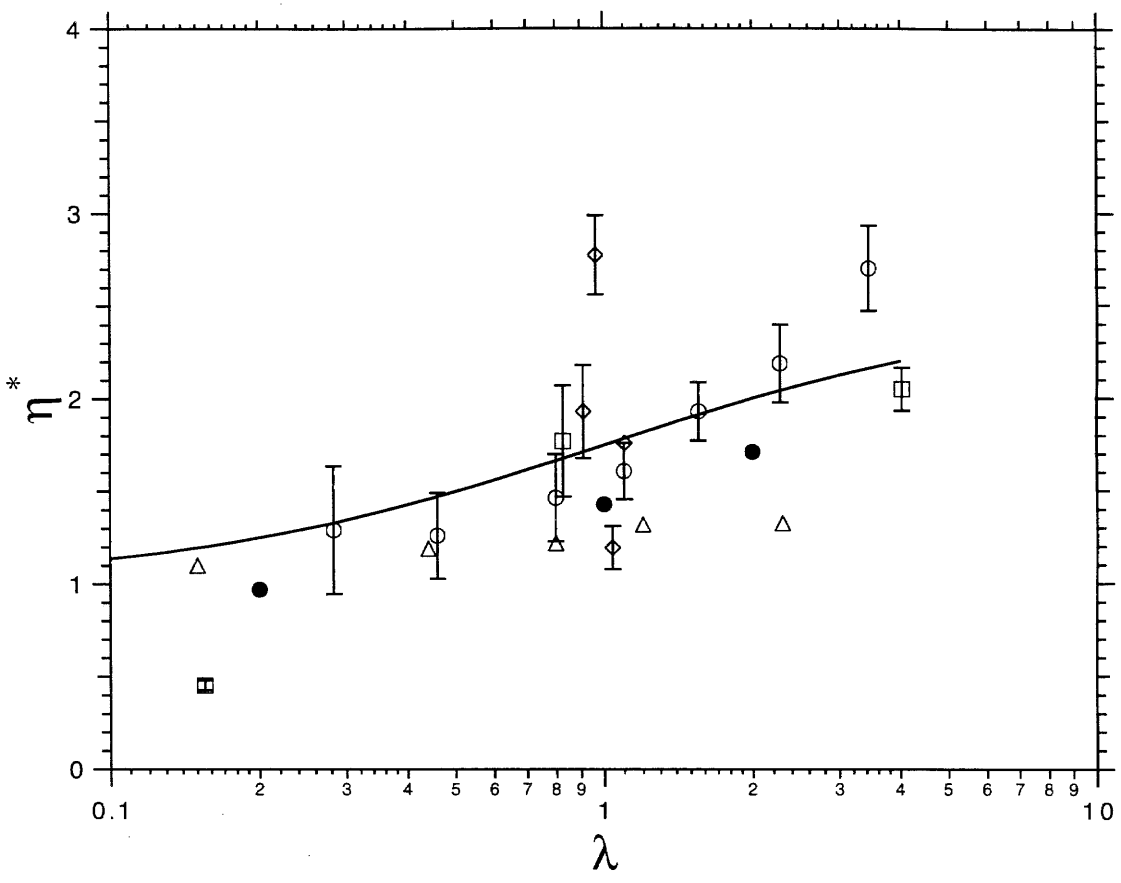

Figure 4.9: Master curve for the scaled viscosity, η^*, as a function of the viscosity ratio, λ, at the critical capillary number, Ca_c. Results of this work (○), Kitade *et al.* (1997) (□), Vinckier, Mewis & Moldenaers (1996a) for c=10wt% (△), Takahashi *et al.* (1994a, 1994b) (◇), and Loewenberg & Hinch (1996) for ϕ=0.10 (●) are shown. Small deformation theory of Taylor (1932) (solid line) is used to approximate the master curve.

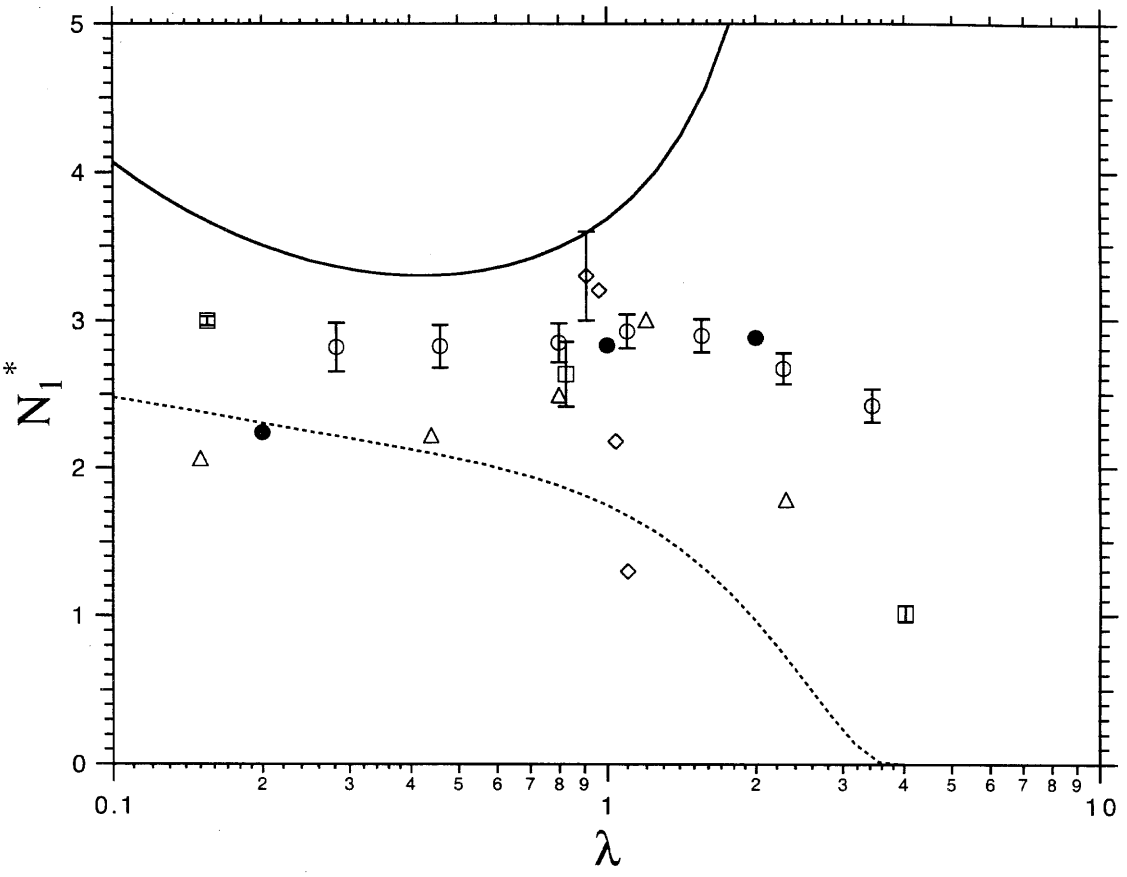

Figure 4.10: Master curve for the scaled first normal stress difference, N_1^*, as a function of the viscosity ratio, λ, at the critical capillary number, Ca_c. Results of this work (○), Kitade *et al.* (1997) (□), Vinckier, Mewis & Moldenaers (1996a) for c=10wt% (△), Takahashi *et al.* (1994a, 1994b) (◇), and Loewenberg & Hinch (1996) for ϕ=0.10 (●) are shown. Small deformation theories of Schowalter, Chaffey & Brenner (1968) (solid line) and Choi & Schowalter (1975) (dashed line) are used to approximate the master curve.

Temp (°C)	η_s (Pa sec)	η_d (Pa sec)	λ
10.0	13.51±0.337	120.56 ±4.220	8.93 ±0.394
15.0	12.16±0.376	65.74 ±1.775	5.41 ±0.222
20.0	10.99±0.429	37.82 ±1.059	3.44 ±0.165
25.0	9.98±0.389	22.69 ±0 817	2.27 ±0.121
30.0	9.10±0.191	14.14 ±0.297	1.55 ±0.046
35.0	8.33±0.192	9.15 ±0.192	1.10 ±0.034
40.0	7.68±0.276	6.15 ±0.129	0.800±0.0333
45.0	7.11±0.149	4.24 ±0.093	0.596±0.0181
50.0	6.45±0.219	2.96 ±0.115	0.458±0.0237
55.0	5.96±0.232	2.13 ±0.045	0.357±0.0158
60.0	5.54±0.138	1.56 ±0.055	0.282±0.0122
65.0	5.16±0.160	1.17 ±0.036	0.228±0.0099
70.0	4.81±0.135	0.896±0.0349	0.186±0.0089
75.0	4.50±0.112	0.694±0.0201	0.154±0.0059
80.0	4.21±0.093	0.547±0.0186	0.130±0.0053
85.0	3.94±0.114	0.435±0.0100	0.110±0.0041
90.0	3.70±0.100	0.352±0.0088	0.095±0.0035

Table 4.1: Steady-state viscosity of PDMS (η_s) and Pale 1000 (η_d) with the viscosity ratio, $\lambda = \eta_d/\eta_s$, as a function of temperature.

	Temp: 20.0°C		Temp: 25.0°C	
Stress (Pa)	Viscosity (Pa sec)	N_1 (Pa)	Viscosity (Pa sec)	N_1 (Pa)
50.0	14.35±0.0045	N/M	13.15±0.0053	N/M
60.0	14.30±0.0058	N/M	13.10±0.0090	N/M
72.0	14.23±0.0054	N/M	13.04±0.0061	N/M
86.0	14.16±0.0112	N/M	12.96±0.0029	N/M
104.0	14.06±0.0049	N/M	12.88±0.0015	N/M
125.0	13.98±0.0073	N/M	12.78±0.0039	N/M
150.0	13.88±0.0042	N/M	12.68±0.0021	N/M
180.0	13.78±0.0045	N/M	12.57±0.0044	N/M
215.0	13.69±0.0056	N/M	12.45±0.0038	N/M
258.0	13.61±0.0070	N/M	12.34±0.0042	N/M
310.0	13.53±0.0051	N/M	12.22±0.0062	N/M
372.0	13.44±0.0054	N/M	12.14±0.0048	N/M
445.0	13.38±0.0011	N/M	12.05±0.0045	82.1±3.39

Table 4.2: Viscosity and first normal stress difference, N_1, as a function of stress for c=10.0wt% at T=20.0 and 25.0°C. N/M means N_1 was not measurable.

	Temp: 30.0°C		Temp: 35.0°C	
Stress (Pa)	Viscosity (Pa sec)	N_1 (Pa)	Viscosity (Pa sec)	N_1 (Pa)
50.0	11.77±0.0076	N/M	10.51±0.0038	N/M
60.0	11.73±0.0020	N/M	10.49±0.0028	N/M
72.0	11.68±0.0032	N/M	10.46±0.0045	N/M
86.0	11.61±0.0054	N/M	10.42±0.0044	N/M
104.0	11.53±0.0048	N/M	10.36±0.0046	N/M
125.0	11.44±0.0051	N/M	10.27±0.0042	N/M
150.0	11.34±0.0042	N/M	10.18±0.0015	N/M
180.0	11.22±0.0024	N/M	10.06±0.0025	N/M
215.0	11.10±0.0040	N/M	9.95±0.0039	N/M
258.0	11.00±0.0009	N/M	9.85±0.0021	N/M
310.0	10.91±0.0044	N/M	9.79±0.0059	N/M
372.0	10.87±0.0025	N/M	9.75±0.0009	83.5±4.06
445.0	10.82±0.0051	92.1±4.96	9.71±0.0022	100.7±4.19

Table 4.3: Viscosity and first normal stress difference, N_1, as a function of stress for c=10.0wt% at T=30.0 and 35.0°C. N/M means N_1 was not measurable.

	Temp: 40.0°C		Temp: 45.0°C	
Stress (Pa)	Viscosity (Pa sec)	N_1 (Pa)	Viscosity (Pa sec)	N_1 (Pa)
50.0	9.36±0.0038	N/M	8.59±0.0039	N/M
60.0	9.34±0.0022	N/M	8.58±0.0040	N/M
72.0	9.30±0.0035	N/M	8.55±0.0036	N/M
86.0	9.26±0.0029	N/M	8.50±0.0026	N/M
104.0	9.20±0.0033	N/M	8.44±0.0028	N/M
125.0	9.13±0.0040	N/M	8.37±0.0011	N/M
150.0	9.03±0.0042	N/M	8.27±0.0066	N/M
180.0	8.93±0.0010	N/M	8.18±0.0030	N/M
215.0	8.84±0.0011	N/M	8.12±0.0030	N/M
258.0	8.79±0.0050	N/M	8.07±0.0032	N/M
310.0	8.75±0.0043	N/M	8.04±0.0029	N/M
372.0	8.72±0.0058	90.2±4.15	8.00±0.0037	92.3±4.09
445.0	8.67±0.0040	110.3±3.78	7.94±0.0039	106.0±3.68

Table 4.4: Viscosity and first normal stress difference, N_1, as a function of stress for c=10.0wt% at T=40.0 and 45.0°C. N/M means N_1 was not measurable.

	Temp: 50.0°C	
Stress (Pa)	Viscosity (Pa sec)	N_1 (Pa)
50.0	7.84±0.0057	N/M
60.0	7.82±0.0037	N/M
72.0	7.80±0.0050	N/M
86.0	7.76±0.0028	N/M
104.0	7.70±0.0013	N/M
125.0	7.63±0.0047	N/M
150.0	7.54±0.0020	N/M
180.0	7.46±0.0030	N/M
215.0	7.42±0.0043	N/M
258.0	7.38±0.0043	N/M
310.0	7.36±0.0018	N/M
372.0	7.31±0.0021	88.4±3.41
445.0	7.24±0.0042	112.0±5.78

Table 4.5: Viscosity and first normal stress difference, N_1, as a function of stress for c=10.0wt% at T=50.0°C. N/M means N_1 was not measurable.

	Temp: 20.0°C		Temp: 25.0°C	
Stress (Pa)	Viscosity (Pa sec)	N_1 (Pa)	Viscosity (Pa sec)	N_1 (Pa)
50.0	16.81±0.0082	N/M	14.40±0.0048	N/M
60.0	16.72±0.0066	N/M	14.31±0.0032	N/M
72.0	16.58±0.0078	N/M	14.19±0.0048	N/M
86.0	16.43±0.0075	N/M	14.06±0.0059	N/M
104.0	16.24±0.0060	N/M	13.88±0.0072	N/M
125.0	16.04±0.0070	N/M	13.69±0.0058	N/M
150.0	15.83±0.0068	N/M	13.48±0.0020	N/M
180.0	15.62±0.0014	N/M	13.26±0.0045	N/M
215.0	15.40±0.0072	N/M	13.05±0.0057	N/M
258.0	15.21±0.0060	N/M	12.84±0.0012	N/M
310.0	15.02±0.0009	N/M	12.68±0.0057	80.8±2.82
372.0	14.85±0.0067	N/M	12.59±0.0099	105.7±2.19
445.0	14.70±0.0071	N/M	12.54±0.0055	121.7±2.96

Table 4.6: Viscosity and first normal stress difference, N_1, as a function of stress for c=15.0wt% at T=20.0 and 25.0°C. N/M means N_1 was not measurable.

	Temp: 30.0°C		Temp: 35.0°C	
Stress (Pa)	Viscosity (Pa sec)	N_1 (Pa)	Viscosity (Pa sec)	N_1 (Pa)
50.0	13.18±0.0047	N/M	11.68±0.0035	N/M
60.0	13.11±0.0063	N/M	11.60±0.0043	N/M
72.0	13.00±0.0054	N/M	11.52±0.0045	N/M
86.0	12.88±0.0091	N/M	11.40±0.0071	N/M
104.0	12.72±0.0022	N/M	11.27±0.0058	N/M
125.0	12.54±0.0071	N/M	11.11±0.0035	N/M
150.0	12.33±0.0056	N/M	10.91±0.0011	N/M
180.0	12.10±0.0058	N/M	10.70±0.0047	N/M
215.0	11.88±0.0051	N/M	10.55±0.0015	N/M
258.0	11.71±0.0018	N/M	10.46±0.0040	N/M
310.0	11.63±0.0057	92.4±2.74	10.41±0.0043	92.2±2.23
372.0	11.57±0.0072	111.3±2.26	10.34±0.0075	116.0±2.68
445.0	11.50±0.0017	132.2±2.85	10.24±0.0049	138.7±1.86

Table 4.7: Viscosity and first normal stress difference, N_1, as a function of stress for c=15.0wt% at T=30.0 and 35.0°C. N/M means N_1 was not measurable.

	Temp: 40.0°C		Temp: 45.0°C	
Stress (Pa)	Viscosity (Pa sec)	N_1 (Pa)	Viscosity (Pa sec)	N_1 (Pa)
50.0	10.35±0.0043	N/M	9.37±0.0025	N/M
60.0	10.28±0.0054	N/M	9.31±0.0043	N/M
72.0	10.21±0.0040	N/M	9.24±0.0045	N/M
86.0	10.11±0.0035	N/M	9.15±0.0032	N/M
104.0	9.98±0.0022	N/M	9.02±0.0061	N/M
125.0	9.81±0.0017	N/M	8.86±0.0019	N/M
150.0	9.61±0.0024	N/M	8.71±0.0012	N/M
180.0	9.45±0.0040	N/M	8.61±0.0032	N/M
215.0	9.36±0.0050	N/M	8.55±0.0038	N/M
258.0	9.30±0.0048	85.8±2.10	8.51±0.0041	N/M
310.0	9.26±0.0042	102.0±2.04	8.44±0.0039	105.8±2.28
372.0	9.18±0.0037	125.7±2.55	8.34±0.0029	131.5±3.20
445.0	9.08±0.0057	155.2±1.93	8.25±0.0018	156.9±2.06

Table 4.8: Viscosity and first normal stress difference, N_1, as a function of stress for c=15.0wt% at T=40.0 and 45.0°C. N/M means N_1 was not measurable.

	Temp: 50.0°C	
Stress (Pa)	Viscosity (Pa sec)	N_1 (Pa)
50.0	8.38±0.0044	N/M
60.0	8.32±0.0036	N/M
72.0	8.24±0.0037	N/M
86.0	8.13±0.0031	N/M
104.0	8.00±0.0041	N/M
125.0	7.85±0.0028	N/M
150.0	7.76±0.0037	N/M
180.0	7.71±0.0021	N/M
215.0	7.66±0.0032	N/M
258.0	7.61±0.0042	82.6±3.04
310.0	7.55±0.0031	96.8±4.04
372.0	7.48±0.0029	131.8±2.98
445.0	7.37±0.0041	163.0±2.70

Table 4.9: Viscosity and first normal stress difference, N_1, as a function of stress for c=15.0wt% at T=50.0°C. N/M means N_1 was not measurable.

	Temp: 20.0°C		Temp: 25.0°C	
Stress (Pa)	Viscosity (Pa sec)	N_1 (Pa)	Viscosity (Pa sec)	N_1 (Pa)
50.0	18.90±0.0064	N/M	16.67±0.0075	N/M
60.0	18.68±0.0087	N/M	16.48±0.0102	N/M
72.0	18.40±0.0149	N/M	16.24±0.0072	N/M
86.0	18.09±0.0049	N/M	15.97±0.0029	N/M
104.0	17.75±0.0023	N/M	15.63±0.0072	N/M
125.0	17.39±0.0086	N/M	15.30±0.0070	N/M
150.0	17.05±0.0053	N/M	14.94±0.0027	N/M
180.0	16.73±0.0079	N/M	14.59±0.0077	N/M
215.0	16.43±0.0076	N/M	14.27±0.0063	N/M
258.0	16.15±0.0009	N/M	14.03±0.0070	82.1±1.74
310.0	15.91±0.0040	N/M	13.91±0.0062	106.5±1.82
372.0	15.72±0.0042	93.4±1.88	13.84±0.0036	119.9±3.34
445.0	15.60±0.0034	113.9±2.88	13.78±0.0039	152.3±1.64

Table 4.10: Viscosity and first normal stress difference, N_1, as a function of stress for c=20.0wt% at T=20.0 and 25.0°C. N/M means N_1 was not measurable.

	Temp: 30.0°C		Temp: 35.0°C	
Stress (Pa)	Viscosity (Pa sec)	N_1 (Pa)	Viscosity (Pa sec)	N_1 (Pa)
50.0	14.61±0.0049	N/M	12.75±0.0085	N/M
60.0	14.44±0.0061	N/M	12.61±0.0035	N/M
72.0	14.23±0.0059	N/M	12.44±0.0067	N/M
86.0	13.98±0.0062	N/M	12.22±0.0051	N/M
104.0	13.68±0.0061	N/M	11.96±0.0059	N/M
125.0	13.32±0.0046	N/M	11.66±0.0017	N/M
150.0	12.96±0.0059	N/M	11.33±0.0022	N/M
180.0	12.65±0.0070	N/M	11.10±0.0089	N/M
215.0	12.48±0.0131	N/M	11.00±0.0087	100.8±2.07
258.0	12.39±0.0092	99.8±1.99	10.94±0.0075	108.2±2.27
310.0	12.32±0.0033	119.6±2.53	10.88±0.0030	126.2±2.74
372.0	12.25±0.0037	142.2±1.66	10.79±0.0020	152.0±2.09
445.0	12.15±0.0054	171.0±2.20	10.66±0.0064	186.4±2.00

Table 4.11: Viscosity and first normal stress difference, N_1, as a function of stress for c=20.0wt% at T=30.0 and 35.0°C. N/M means N_1 was not measurable.

	Temp: 40.0°C		Temp: 45.0°C	
Stress (Pa)	Viscosity (Pa sec)	N_1 (Pa)	Viscosity (Pa sec)	N_1 (Pa)
50.0	11.31±0.0063	N/M	10.03±0.0050	N/M
60.0	11.17±0.0054	N/M	9.91±0.0029	N/M
72.0	11.01±0.0040	N/M	9.75±0.0043	N/M
86.0	10.83±0.0090	N/M	9.56±0.0075	N/M
104.0	10.58±0.0046	N/M	9.30±0.0045	N/M
125.0	10.32±0.0047	N/M	9.06±0.0043	N/M
150.0	10.07±0.0033	N/M	8.92±0.0033	N/M
180.0	9.94±0.0062	N/M	8.86±0.0023	N/M
215.0	9.93±0.0045	86.5±3.37	8.81±0.0017	84.2±2.29
258.0	9.85±0.0021	102.7±2.12	8.75±0.0059	115.2±3.35
310.0	9.74±0.0066	124.8±1.81	8.66±0.0013	136.6±3.23
372.0	9.62±0.0036	155.4±2.49	8.55±0.0006	166.0±3.29
445.0	9.46±0.0049	201.9±2.79	8.41±0.0046	204.1±2.45

Table 4.12: Viscosity and first normal stress difference, N_1, as a function of stress for c=20.0wt% at T=40.0 and 45.0°C. N/M means N_1 was not measurable.

	Temp: 50.0°C	
Stress (Pa)	Viscosity (Pa sec)	N_1 (Pa)
50.0	9.08±0.0045	N/M
60.0	8.96±0.0079	N/M
72.0	8.78±0.0069	N/M
86.0	8.58±0.0048	N/M
104.0	8.33±0.0031	N/M
125.0	8.17±0.0037	N/M
150.0	8.09±0.0040	N/M
180.0	8.04±0.0017	N/M
215.0	8.00±0.0033	92.6±3.56
258.0	7.93±0.0028	109.1±2.23
310.0	7.83±0.0025	130.6±2.56
372.0	7.71±0.0010	174.2±2.17
445.0	7.58±0.0010	222.5±1.36

Table 4.13: Viscosity and first normal stress difference, N_1, as a function of stress for c=20.0wt% at T=50.0°C. N/M means N_1 was not measurable.

	Temp: 20.0°C		Temp: 25.0°C	
Stress (Pa)	Viscosity (Pa sec)	N_1 (Pa)	Viscosity (Pa sec)	N_1 (Pa)
50.0	22.46±0.0137	N/M	18.92±0.0075	N/M
60.0	22.02±0.0124	N/M	18.61±0.0063	N/M
72.0	21.48±0.0076	N/M	18.21±0.0102	N/M
86.0	20.88±0.0067	N/M	17.72±0.0023	N/M
104.0	20.23±0.0061	N/M	17.16±0.0084	N/M
125.0	19.59±0.0076	N/M	16.56±0.0062	N/M
150.0	18.99±0.0069	N/M	15.98±0.0098	N/M
180.0	18.45±0.0068	N/M	15.55±0.0075	N/M
215.0	18.04±0.0041	N/M	15.35±0.0127	92.8±4.13
258.0	17.77±0.0049	89.2±1.69	15.27±0.0063	107.8±3.54
310.0	17.64±0.0112	106.2±2.42	15.17±0.0073	126.7±2.68
372.0	17.56±0.0049	126.9±2.34	15.05±0.0056	159.4±3.25
445.0	17.45±0.0053	151.8±2.26	14.88±0.0024	194.2±1.81

Table 4.14: Viscosity and first normal stress difference, N_1, as a function of stress for c=25.0wt% at T=20.0 and 25.0°C. N/M means N_1 was not measurable.

	Temp: 30.0°C		Temp: 35.0°C	
Stress (Pa)	Viscosity (Pa sec)	N_1 (Pa)	Viscosity (Pa sec)	N_1 (Pa)
50.0	15.83±0.0124	N/M	14.12±0.0072	N/M
60.0	15.56±0.0087	N/M	13.86±0.0072	N/M
72.0	15.21±0.0048	N/M	13.57±0.0076	N/M
86.0	14.81±0.0102	N/M	13.23±0.0093	N/M
104.0	14.30±0.0034	N/M	12.78±0.0064	N/M
125.0	13.74±0.0040	N/M	12.30±0.0037	N/M
150.0	13.29±0.0048	N/M	11.95±0.0070	N/M
180.0	13.10±0.0088	91.3±3.32	11.82±0.0099	89.5±2.02
215.0	13.02±0.0114	106.6±2.70	11.75±0.0043	108.2±2.47
258.0	12.96±0.0053	127.7±2.55	11.66±0.0057	132.7±1.88
310.0	12.87±0.0029	148.2±2.76	11.55±0.0064	149.8±3.29
372.0	12.76±0.0051	191.2±3.05	11.38±0.0038	185.0±2.15
445.0	12.58±0.0083	217.7±2.91	11.14±0.0046	232.4±2.48

Table 4.15: Viscosity and first normal stress difference, N_1, as a function of stress for c=25.0wt% at T=30.0 and 35.0°C. N/M means N_1 was not measurable.

	Temp: 40.0°C		Temp: 45.0°C	
Stress (Pa)	Viscosity (Pa sec)	N_1 (Pa)	Viscosity (Pa sec)	N_1 (Pa)
50.0	12.26±0.0088	N/M	10.67±0.0033	N/M
60.0	12.02±0.0064	N/M	10.46±0.0071	N/M
72.0	11.75±0.0040	N/M	10.19±0.0059	N/M
86.0	11.39±0.0027	N/M	9.84±0.0054	N/M
104.0	10.95±0.0039	N/M	9.50±0.0055	N/M
125.0	10.64±0.0099	N/M	9.35±0.0027	N/M
150.0	10.52±0.0050	N/M	9.29±0.0047	N/M
180.0	10.47±0.0109	84.5±2.49	9.25±0.0035	90.8±2.71
215.0	10.40±0.0046	107.9±3.36	9.18±0.0052	109.1±1.94
258.0	10.30±0.0025	127.2±2.18	9.08±0.0042	130.0±1.85
310.0	10.17±0.0033	157.3±2.55	8.93±0.0014	169.6±2.70
372.0	9.97±0.0046	198.2±2.92	8.75±0.0063	209.6±2.85
445.0	9.72±0.0059	248.0±3.72	8.50±0.0044	268.9±2.92

Table 4.16: Viscosity and first normal stress difference, N_1, as a function of stress for c=25.0wt% at T=40.0 and 45.0°C. N/M means N_1 was not measurable.

	Temp: 20.0°C		Temp: 25.0°C	
Stress (Pa)	Viscosity (Pa sec)	N_1 (Pa)	Viscosity (Pa sec)	N_1 (Pa)
50.0	26.30±0.0141	N/M	21.74±0.0076	N/M
60.0	25.47±0.0116	N/M	21.07±0.0074	N/M
72.0	24.51±0.0078	N/M	20.28±0.0066	N/M
86.0	23.54±0.0029	N/M	19.44±0.0107	N/M
104.0	22.53±0.0122	N/M	18.50±0.0070	N/M
125.0	21.62±0.0084	N/M	17.61±0.0071	N/M
150.0	20.81±0.0092	N/M	16.94±0.0087	80.1±3.06
180.0	20.13±0.0067	N/M	16.64±0.0088	94.0±3.86
215.0	19.63±0.0115	92.5±2.42	16.53±0.0092	113.7±2.76
258.0	19.40±0.0089	109.7±2.54	16.46±0.0079	137.5±3.34
310.0	19.31±0.0140	129.5±4.58	16.35±0.0080	162.7±3.31
372.0	19.20±0.0060	159.7±3.01	16.21±0.0093	188.9±3.58
445.0	19.06±0.0077	187.4±3.79	15.99±0.0048	236.7±3.08

Table 4.17: Viscosity and first normal stress difference, N_1, as a function of stress for c=30.0wt% at T=20.0 and 25.0°C. N/M means N_1 was not measurable.

	Temp: 30.0°C		Temp: 35.0°C	
Stress (Pa)	Viscosity (Pa sec)	N_1 (Pa)	Viscosity (Pa sec)	N_1 (Pa)
50.0	18.69±0.0146	N/M	15.51±0.0119	N/M
60.0	18.13±0.0052	N/M	15.09±0.0038	N/M
72.0	17.49±0.0054	N/M	14.60±0.0053	N/M
86.0	16.75±0.0137	N/M	14.03±0.0069	N/M
104.0	15.88±0.0118	N/M	13.29±0.0084	N/M
125.0	15.12±0.0043	N/M	12.65±0.0039	N/M
150.0	14.72±0.0128	83.5±2.58	12.43±0.0119	91.1±3.11
180.0	14.60±0.0096	102.2±2.25	12.36±0.0109	111.4±1.23
215.0	14.51±0.0061	120.5±3.11	12.28±0.0065	121.5±2.30
258.0	14.42±0.0098	148.2±3.29	12.20±0.0044	152.9±2.25
310.0	14.28±0.0115	167.7±3.29	12.06±0.0108	188.0±2.75
372.0	14.09±0.0122	210.6±3.49	11.86±0.0047	223.6±1.91
445.0	13.81±0.0059	255.1±3.27	11.58±0.0030	280.1±2.37

Table 4.18: Viscosity and first normal stress difference, N_1, as a function of stress for c=30.0wt% at T=30.0 and 35.0°C. N/M means N_1 was not measurable.

	Temp: 40.0°C	
Stress (Pa)	Viscosity (Pa sec)	N_1 (Pa)
50.0	13.73±0.0099	N/M
60.0	13.33±0.0052	N/M
72.0	12.84±0.0077	N/M
86.0	12.25±0.0056	N/M
104.0	11.59±0.0065	N/M
125.0	11.31±0.0119	N/M
150.0	11.23±0.0043	88.5±1.57
180.0	11.16±0.0065	103.3±2.26
215.0	11.08±0.0050	121.8±2.29
258.0	10.94±0.0064	152.3±3.13
310.0	10.73±0.0080	191.9±2.01
372.0	10.44±0.0043	243.5±1.90
445.0	10.03±0.0052	306.2±2.28

Table 4.19: Viscosity and first normal stress difference, N_1, as a function of stress for c=30.0wt% at T=40.0°C. N/M means N_1 was not measurable.

	Temp: 20.0°C		Temp: 25.0°C	
Stress (Pa)	Viscosity (Pa sec)	N_1 (Pa)	Viscosity (Pa sec)	N_1 (Pa)
50.0	30.39±0.0128	N/M	24.62±0.0311	N/M
60.0	29.07±0.0128	N/M	23.60±0.0176	N/M
72.0	27.62±0.0071	N/M	22.45±0.0103	N/M
86.0	26.21±0.0131	N/M	21.28±0.0121	N/M
104.0	24.74±0.0163	N/M	19.97±0.0093	N/M
125.0	23.38±0.0131	N/M	18.78±0.0120	N/M
150.0	22.28±0.0024	80.6±2.70	18.14±0.0115	93.1±2.72
180.0	21.58±0.0104	102.0±1.86	17.97±0.0125	118.3±2.38
215.0	21.36±0.0221	117.6±1.96	17.88±0.0075	132.3±3.49
258.0	21.26±0.0182	138.7±2.19	17.74±0.0088	156.5±1.92
310.0	21.11±0.0148	169.1±1.79	17.56±0.0121	187.0±2.59
372.0	20.92±0.0122	196.8±1.74	17.29±0.0126	227.4±3.02
445.0	20.64±0.0060	245.8±3.20	16.91±0.0020	277.8±2.62

Table 4.20: Viscosity and first normal stress difference, N_1, as a function of stress for c=35.0wt% at T=20.0 and 25.0°C. N/M means N_1 was not measurable.

	Temp: 30.0°C		Temp: 35.0°C	
Stress (Pa)	Viscosity (Pa sec)	N_1 (Pa)	Viscosity (Pa sec)	N_1 (Pa)
50.0	20.29±0.0124	N/M	17.03±0.0102	N/M
60.0	19.57±0.0113	N/M	16.40±0.0065	N/M
72.0	18.73±0.0125	N/M	15.65±0.0029	N/M
86.0	17.75±0.0030	N/M	14.74±0.0079	N/M
104.0	16.68±0.0104	N/M	13.71±0.0076	N/M
125.0	15.63±0.0110	89.6±2.70	13.30±0.0091	87.8±2.65
150.0	15.33±0.0126	111.4±2.05	13.21±0.0095	101.3±2.77
180.0	15.26±0.0101	120.9±2.26	13.14±0.0064	130.2±2.71
215.0	15.16±0.0141	149.6±3.02	13.02±0.0041	141.4±2.46
258.0	15.02±0.0078	168.9±2.95	12.84±0.0133	174.7±3.21
310.0	14.82±0.0097	206.1±3.31	12.56±0.0069	214.0±2.23
372.0	14.51±0.0081	259.2±2.94	12.13±0.0027	276.5±2.14
445.0	14.05±0.0084	306.1±3.13	11.51±0.0058	345.0±3.22

Table 4.21: Viscosity and first normal stress difference, N_1, as a function of stress for c=35.0wt% at T=30.0 and 35.0°C. N/M means N_1 was not measurable.

	Temp: 20.0°C		Temp: 25.0°C	
Stress (Pa)	Viscosity (Pa sec)	N_1 (Pa)	Viscosity (Pa sec)	N_1 (Pa)
50.0	34.38±0.0389	N/M	27.48±0.0226	N/M
60.0	32.66±0.0207	N/M	26.16±0.0167	N/M
72.0	30.80±0.0168	N/M	24.72±0.0119	N/M
86.0	28.95±0.0161	N/M	23.20±0.0110	N/M
104.0	27.07±0.0128	N/M	21.49±0.0123	N/M
125.0	25.72±0.0077	N/M	19.95±0.0550	88.7±2.77
150.0	24.32±0.0094	91.7±2.61	19.39±0.0230	117.8±1.60
180.0	23.58±0.0220	115.0±1.94	19.32±0.0248	132.5±2.38
215.0	23.40±0.0177	129.9±2.09	19.22±0.0224	152.6±2.71
258.0	23.30±0.0205	161.4±1.82	19.04±0.0078	189.1±3.79
310.0	23.08±0.0159	182.4±3.17	18.76±0.0091	216.3±3.03
372.0	22.77±0.0163	226.0±2.06	18.36±0.0110	268.3±2.36
445.0	22.34±0.0134	264.3±3.64	17.73±0.0077	321.5±1.42

Table 4.22: Viscosity and first normal stress difference, N_1, as a function of stress for c=40.0wt% at T=20.0 and 25.0°C. N/M means N_1 was not measurable.

	Temp: 30.0°C		Temp: 35.0°C	
Stress (Pa)	Viscosity (Pa sec)	N_1 (Pa)	Viscosity (Pa sec)	N_1 (Pa)
50.0	22.64±0.0315	N/M	19.18±0.0110	N/M
60.0	21.46±0.0046	N/M	18.18±0.0087	N/M
72.0	20.13±0.0097	N/M	17.07±0.0047	N/M
86.0	18.73±0.0116	N/M	15.81±0.0052	N/M
104.0	17.31±0.0174	N/M	14.68±0.0056	N/M
125.0	16.72±0.0216	95.0±2.63	14.44±0.0088	88.5±3.41
150.0	16.64±0.0189	104.6±2.14	14.36±0.0119	107.2±2.48
180.0	16.55±0.0181	131.1±2.76	14.24±0.0112	127.2±2.68
215.0	16.40±0.0062	153.5±1.88	14.06±0.0084	154.5±2.35
258.0	16.19±0.0127	187.9±2.02	13.76±0.0130	185.7±2.81
310.0	15.86±0.0099	228.4±2.41	13.30±0.0084	231.6±3.30
372.0	15.34±0.0093	285.4±2.31	12.54±0.0102	301.6±3.38
445.0	14.56±0.0068	356.8±2.52	11.00±0.0169	409.9±3.65

Table 4.23: Viscosity and first normal stress difference, N_1, as a function of stress for c=40.0wt% at T=30.0 and 35.0°C. N/M means N_1 was not measurable.

λ	τ_{min} (Pa)
3.44	2135
2.27	169
1.55	113
1.10	98
0.800	93
0.596	91
0.458	92

Table 4.24: Minimum stress required to eliminate wall effects using equations (4.14) and (4.15).

Temp (°C)	η^*	intercept (Pa sec)	slope (Pa sec)	χ^2	Q
20.0	2.70±0.228	10.85±0.387	29.30±2.246	1.163	0.9787
25.0	2.19±0.209	9.97±0.248	21.87±1.933	0.351	0.9992
30.0	1.93±0.156	9.13±0.184	17.58±1.383	0.736	0.9937
35.0	1.61±0.286	8.38±0.184	13.48±1.218	0.925	0.9883
40.0	1.47±0.234	7.72±0.258	11.32±1.786	0.181	0.9961
45.0	1.25±0.231	7.13±0.146	8.98±1.637	0.468	0.9258
50.0	1.29±0.344	6.48±0.213	8.34±2.213	0.309	0.8569

Table 4.25: Scaled viscosity, η^*, as a function of temperature. The table also includes the results for the curve fit of viscosity, η, versus volume fraction, ϕ, using a linear curve fitting program with both the slope and intercept as parameters.

Temp (°C)	N_1^* = slope	χ^2	Q
20.0	2.42±0.113	19.50	0.0000627
25.0	2.67±0.104	13.17	0.004047
30.0	2.89±0.112	7.10	0.03114
35.0	2.92±0.113	2.89	0.8224
40.0	2.85±0.130	0.417	0.9811
45.0	2.82±0.144	0.055	0.9967
50.0	2.82±0.166	0.133	0.9357

Table 4.26: Scaled first normal stress difference, N_1^*, as a function of temperature. The table also includes the results for the curve fit of the dimensionless first normal stress difference, $N_1/\eta_s\dot{\gamma}$, versus volume fraction, ϕ, using a linear curve fitting program with the intercept set to zero.

Chapter 5

Stress jumps of polymer solutions

5.1 Introduction

Polymer solutions—systems in which long-chain, flexible macromolecules are dispersed in a fluid—are, historically, one of the most studied complex fluids, but the cause of the dissipative stress and its dynamic origin in simple shear flow remain open topics. Possible causes of the dissipative stress include hydrodynamic interactions [Fuller & Leal (1981); Öttinger (1987)] and intrinsic viscosity [Osaki (1973); Fuller & Leal (1981); Allegra (1986); Manke & Williams (1987, 1992, 1993)]. There is additional experimental evidence that the dissipative stress is also affected when the continuum approximation is not satisfied—the solvent relaxation time is on the order of the relaxation time of the polymer molecule—and the solvent relaxation time is modified by the presence of the solute [Morris, Amelar & Lodge (1988); Schrag *et al.* (1991); Ngai (1991); Gisser & Ediger (1992)]. This dissipative stress can be measured by performing mechanical stress jumps in which the applied shear rate is instantaneously changed and the resulting instantaneous change in the stress is measured. Until recently, stress jumps could not be measured because of the limitations of torque transducers [Mackay, Liang & Halley (1992)]. Since the introduction of torque rebalance transducers, stress jump measurements in simple shear flow after flow cessation have been performed on semi-rigid macromolecules [Liang & Mackay (1993)], liquid crystalline polymers [Smyth & Mackay (1994); Smyth *et al.* (1995)], and colloidal dispersions [Mackay & Kaffashi (1995); O'Brien & Mackay (1996); Kaffashi *et al.* (1997)]. Stress jump measurements of polymer solutions have not yet been performed in simple shear flow, but they have been reported for cessation of extensional flow [Orr & Sridhar (1996)]. This work forms the foundation for future studies in which the strain and rate dependence of the dissipative stress of polymer solutions in simple shear flow is studied to gain a deeper understanding of the physics responsible for the dissipative stress.

In this study, stress jumps are performed at flow startup for polymer solutions of high molecular weight (M_w=18×10^6), nonionic polyacrylamide dispersed in a solvent of 70.0wt% fructose in water. A range of concentrations of dispersed polymer is

chosen so that linear viscoelastic measurements at small concentrations allow the high-frequency viscosity, η'_∞, to be determined. Since stress jumps are measured for the first time at flow startup, the relationship $\eta^+(t=0;\dot{\gamma}) = \eta'_\infty$ [Gerhardt & Manke (1994)] is confirmed, where $\eta^+(t;\dot{\gamma})$ is the viscosity associated with stress growth after flow startup, evaluated at time t and the imposed shear rate $\dot{\gamma}$.

5.2 Experiment

5.2.1 Materials

The suspending fluid is made by dissolving 70.0wt% d-fructose (Sigma, F-2543, Lot 67H10172) in double-distilled, deionized water. Water cannot be used as the solvent by itself because the viscosity of water is too low to eliminate the effects of momentum diffusivity in stress jumps [Liang & Mackay (1993)], and fructose is simply used as a viscosity thickener. Bacteria growth is hindered by adding 0.02wt% sodium azide (Sigma, S-2002, Lot 77H0079) to the fructose-water mixture. Both fructose and sodium azide are used as received. The resulting mixture is placed on a wrist action shaker (Burrel, model 75) in a sealed bottle for eight hours and then set aside for an additional eight hours to allow entrained air to escape. A single batch of fructose-water is used to make all polymer solutions.

Polymer solutions are made by adding the appropriate amount of polyacrylamide (M_w=18×10^6, Polysciences, 18522, Lot 463162) to the fructose-water mixture, and the polymer is dispersed by rotating the sealed container at approximately 10 RPM for 24 hours. The polymer solution is then placed upright for eight hours in a sealed bottle to allow entrained air to escape. All experiments for a single polymer concentration are performed within 24 hours. Polymer solutions of 0.00, 0.06, 0.09, 0.12, 0.15 and 0.18wt% polymer are made.

5.2.2 Experimental techniques

A constant rate rheometer (Rheometrics, RFS-II) outfitted with the standard bath attachment (Rheometrics), a dual-range, torque rebalance transducer (Rheometrics, 100FRT) and standard motor is used for rheological measurements. Temperature is controlled by a water circulator (Neslab; RTE-130)—there is no feedback loop between the thermocouple in contact with the lower tool and the setpoint of the circulator. The setpoint of the circulator is 15.0°C for all experiments. A 50-mm diameter titanium cone (cone angle: 0.02-radians) is used as the upper tool and a 50-mm diameter aluminum plate is used for the lower tool. A homemade Plexiglas vapor barrier, shown in Figure 5.1, is used to prevent solvent evaporation. The contribution to the torque from the fluid in the reservoir of the vapor barrier is small, but measurable, and this contribution is subtracted from the raw data.

Once the sample is loaded and the vapor barrier is attached, the torque is monitored until the load-induced stress relaxes. Linear viscoelastic measurements are completed, and then stress jump measurements are performed. Labview, a data acquisition board (National Instruments, PCI-MIO-16XE-50) and a Power Macintosh (7200/120) are used for millisecond data acquisition for stress jump measurements by sampling the unfiltered, voltage output of the torque transducer. The Labview VI is started prior to flow startup so that the no-load voltage is monitored. The rheometer motor starts, rotates for two seconds at the commanded rate and then stops, all while acquiring data in Labview. Once the motor stops, the Labview VI is also stopped and the long-time stress decay is monitored using Rheometrics software program, *Orchestrator*, to insure that the stress completely relaxes prior to the next test. These relaxation times vary with polymer concentration and are on the order of an hour for 0.18wt% polymer. This procedure for stress jumps continues until all rates have been sampled, starting with the lowest rate for which a measurable torque signal is obtained and continuing to the rate for which the high range of the transducer is reached. The rates between these two limits are chosen so that there are five rates per decade.

This experimental procedure is completed four times for every concentration of polymer except for the sample of 0.18wt% polymer for which only two replications are performed.

5.3 Results

Results for the linear viscoelastic behavior of the polymer solutions are presented in Figures 5.2–5.4. In Figure 5.2a, the loss modulus of the suspending fluid is $\sim O(\omega)$, as expected for a Newtonian fluid. At high frequency the storage modulus is $\sim O(\omega^2)$, also as expected for a Newtonian fluid. The loss modulus of low concentration polymer solutions reaches its high frequency limit, $\sim O(\omega)$, only for 0.06wt% and 0.09wt% polymer, as seen in Figures 5.2b and 5.3a; thus, the high-frequency dynamic viscosity, η'_∞, can only be measured for three different samples, c=0.00, 0.06, 0.09wt% polymer.

Typical stress jump data is shown in Figure 5.5 for one of the replications of 0.15wt% polymer solution. At low rates a single curve should be formed for the viscosity growth curve, independent of the rate [Isono *et al.* (1991)]. This behavior is *not* seen at low rates for the system shown in Figure 5.5; instead, the transient viscosity slowly approaches this single curve at low rates. This slow approach is due to a lag in the response time of the transducer caused by the large moment of inertia of the upper tool and vapor barrier and is not a function of the material itself. Experiments without the vapor barrier at low rates confirm this result. At slightly higher rates, an overshoot in the viscosity growth curve appears and the time for the peak of the overshoot appears at smaller times as the imposed rate increases. At intermediate rates, the viscosity overshoot appears at nearly the same time, and the viscosity growth curves for different rates are indistinguishable at small times. At high rates, the overshoot appears at approximately the same time, but the viscosity curve deviates from the rate-independent curve at approximately the same value of strain [Menezes & Graessley (1982); Takahashi *et al.* (1986)]. For analysis of stress jump data, only the intermediate regime of shear rates is analyzed to eliminate instrument effects at low rates and deviations from the linear viscoelastic,

rate-independent viscosity growth curve at high rates. This intermediate regime of rates includes rates for which (1) the viscosity overshoot occurs with its maximum value at times shorter than 30-ms and (2) the strain satisfies, $\gamma = \dot{\gamma}t \leq 15$. It should be noted that the ringing phenomenon seen by Liang & Mackay (1993) in stress jumps at startup is not seen here.

Once the intermediate range of shear rates is determined, the instantaneous stress jump is calculated. See Figure 5.6 for the transient viscosity curves after startup for one of the replications of a polymer solution with 0.06wt% polymer when intermediate rates are included. Figure 5.6a shows the transient viscosity for the full two seconds of the experiment, and none of the curves collapse to a single, rate-independent curve for the full duration of the experiment. But at short times, the viscosity growth curves do collapse, as seen in Figure 5.6b. There is one other important feature of Figure 5.6b—data for times less than 50-ms are eliminated. There is a characteristic time for the transducer to reach its null position after an instantaneous change in the rate. For shear startup of a 50-mm titanium cone with the vapor barrier, this characteristic time is 50-ms; thus, for times greater than 50-ms, the measured torque is caused only by the material. To calculate the value of $\eta^+(t = 0; \dot{\gamma})$, the viscosity during startup at the instant of the change in the imposed rate, the data is extrapolated. The extrapolation is performed using a linear curve fit since [Attané, Pierrard & Turrel (1985); Takahashi *et al.* (1986)]

$$\eta^+(t; \dot{\gamma}) \sim tG_0 \tag{5.1}$$

for short times, where

$$G_0 = G(t = 0), \tag{5.2}$$

and $G(t)$ is the linear viscoelastic relaxation modulus. The curve fit [Press *et al.* (1992)] is performed over the range of 50-ms to 100-ms.

This procedure for stress jump analysis is completed for all 22 samples of this study. Data for one replication for 0.09, 0.12, 0.15 and 0.18wt% polymer are shown in Figures 5.7, 5.8, 5.9, and 5.10, respectively. The results for $\eta^+(t = 0; \dot{\gamma})$ and $G(t = 0)$

for each concentration are then averaged over the replications, and these averaged results are shown in Figures 5.11 and 5.12, respectively. In Figure 5.11, there is excellent agreement between the results for $\eta^+(t=0;\dot{\gamma})$ and η'_∞ at low concentration, where both quantities are measured; thus, the relationship

$$\eta^+(t=0;\dot{\gamma}) = \eta'_\infty \tag{5.3}$$

derived by Gerhardt & Manke (1994) using linear viscoelastic fluid theory is confirmed. At higher concentrations the high-frequency dynamic viscosity cannot be measured since the relaxation time increases with volume fraction and the region where $G'' \sim O(\omega)$ occurs at higher values of ω, outside of the range of the rheometer. It's no surprise that $\eta^+(t=0;\dot{\gamma}) = \eta'_\infty$ since both measurements contain information regarding the hydrodynamic contribution to the viscosity associated with the equilibrium microstructure.

5.4 Conclusions

Stress jump and linear viscoelastic measurements are performed for polymer solutions at startup of simple shear flow. The relationship derived by Gerhardt & Manke (1994) for a general viscoelastic fluid is confirmed for polymer solutions, $\eta^+(t=0;\dot{\gamma}) = \eta'_\infty$. Since both η'_∞, the high-frequency viscosity, and $G(t=0)$, the linear viscoelastic relaxation modulus at $t=0$, can both be measured by stress jump measurements, stress jumps at startup provide two pieces of useful information when testing theoretical models.

Since stress jump measurements can be performed for polymer solutions, the strain and rate dependence of the dissipative stress can be studied by performing stress jumps after shear cessation. If intrinsic viscosity is the dominant dissipative mechanism, the hydrodynamic contribution to the viscosity should change as a function of strain for a given rate since the relative velocity of the two beads of the dumbbell changes as the molecule stretches and orients with the flow. In addition, these

experiments are instrumental in determining the cause of shear thickening in some polymer solutions [Kishbaugh & McHugh (1993)].

The fact that stress jump measurements can be accurately performed at startup is also important for other complex fluids. For example, the scaling theory of Brady (1993) relies on knowledge of the high-frequency dynamic viscosity, η'_∞, to scale both the shear rate and rheological properties. Unfortunately, η'_∞ of concentrated dispersions cannot typically be measured on conventional rheometers because of their limited frequency range in dynamic experiments, but stress jumps at startup can instead be measured to yield the same information. Stress jump measurements at startup can also be performed on emulsions. If an emulsion is composed of two immiscible Newtonian fluids with spherical droplets and droplet interactions are treated in a self-consistent way similar to the Lorentz sphere method, the high-frequency dynamic viscosity is [Palierne (1990); Graebling, Muller & Palierne (1993)],

$$\eta'_\infty = \eta_s \frac{10(\lambda+1) + 3\phi(5\lambda+2)}{10(\lambda+1) - 2\phi(5\lambda+2)}, \tag{5.4}$$

where η_s is the viscosity of the suspending fluid, λ is the viscosity ratio of the dispersed and suspending fluids, and ϕ is the volume fraction of the dispersed phase.

Acknowledgements

Michael Mackay suggested that I perform stress jumps of polymer solutions at the end of my stay at The Univeristy of Queensland, where I performed preliminary work on Separan 273 in maltose-water and on the momentum diffusivity of Newtonian fluids in parallel disk flow. He kindly allowed me to continue similar work at Caltech on my own.

References

Allegra, G., "Internal viscosity in polymer chains: A critical analysis." J. Chem. Phys. **84**, 5881–5890 (1986).

Attané, P., J.M. Pierrard & G. Turrel, "Steady and transient shear flows of polystyrene solutions. II. Shear-rate dependence of nondimensional viscometric functions: Characteristic relaxation times." J. Non-Newt. Fluid Mech. **18**, 319–333 (1985).

Brady, J.F., "The rheological behavior of concentrated colloidal dispersions." J. Chem. Phys. **99**, 567–581 (1993).

Fuller, G.G. & L.G. Leal, "The effects of conformation-dependent friction and internal viscosity on the dynamics of the nonlinear dumbbell model for a dilute polymer solution." J. Non-Newt. Fluid Mech. **8**, 271–310 (1981).

Gerhardt, L.J. & C.W. Manke, "Relationships among shear stress jumps and high-frequency dynamic viscosity of viscoelastic fluids." J. Rheol. **38**, 1227–1234 (1994).

Gisser, D.J. & M.D. Ediger, "Local polymer and solvent dynamics in Aroclor solutions: Implications for solvent modification." Macromolecules **25**, 1284–1293 (1992).

Graebling, D., R. Muller & J.F. Palierne, "Linear viscoelastic behavior of some incompatible polymer blends in the melt. Interpretation with a model of emulsion of viscoelastic liquids." Macromolecules **26**, 320–329 (1993).

Isono, Y., H. Kawaura, T. Komiyatani & T. Fujimoto, "Differential dynamic modulus of polyisobutylene with high molecular weight. 3. Stress development after the onset of steady shear flow." Macromolecules **24**, 4437–4440 (1991).

Kaffashi, B., V.T. O'Brien, M.E. Mackay & S.M. Underwood, "Elastic-like and viscous-like components of the shear viscosity for nearly hard-sphere, Brownian suspensions." J. Coll. & Int. Sci. **187**, 22–28 (1997).

Kishbaugh, A.J. & A.J. McHugh, "A rheo-optical study of shear-thickening and structure formation in polymer solutions. Part I: Experimental." Rheol. Acta **32**, 9–24 (1993).

Liang, C.-H. & M.E. Mackay, "The stress jump of a semirigid macromolecule after shear: Steady-state results." J. Rheol. **37**, 149–174 (1993).

Mackay, M.E., C.-H. Liang & P.J. Halley, "Instrument effects on stress jump measurements." Rheol. Acta **31**, 481–489 (1992).

Mackay, M.E. & B. Kaffashi, "Stress jumps of charged colloidal suspensions, measurement of the elastic-like and viscous-like stress components." J. Coll. & Int. Sci. **174**, 117–123 (1995).

Manke, C.W. & M.C. Williams, "Stress jump at the inception of shear and elongational flows of dilute polymer solutions due to internal viscosity." J. Rheol. **31**, 495–510 (1987).

Manke, C.W. & M.C. Williams, "Stress jumps predicted by the internal viscosity model with hydrodynamic interactions." J. Rheol. **36**, 1261–1274 (1992).

Manke, C.W. & M.C. Williams, "Comparison of a new internal viscosity model with other constrained-connector theories of dilute polymer solution rheology." Rheol. Acta **32**, 418–421 (1993).

Menezes, E.V. & W.W. Graessley, "Nonlinear rheological behavior of polymer systems for several shear-flow histories." J. Polym. Science: Polym. Physics Ed. **20**, 1817–1833 (1982).

Morris, R.L., S. Alemar & T.P. Lodge, "Solvent friction in polymer solutions and its relation to the high frequency limiting viscosity." J. Chem. Phys. **89**, 6523–6537 (1988).

Ngai, K.L., "Coupling scheme applied to solvent relaxation modified by dissolved polymer molecules." J. Polym. Science: Part B: Polym. Phys. **29**, 867–876 (1991).

O'Brien, V.T. & M.E. Mackay, "Stress components and shear thickening of hard sphere suspensions." personal communication (1996).

Orr, N.V. & T. Sridhar, "Stress relaxation in uniaxial extension." J. Non-Newt. Fluid Mech. **67**, 77–103 (1996).

Osaki, K., "Viscoelastic properties of dilute polymer solutions." Adv. Polym. Sci. **12**, 1–64 (1973).

Öttinger, H.C., "A model of dilute polymer solutions with hydrodynamic interactions and finite extensibility. I. Basic equations and series expansions." J. Non-Newt. Fluid Mech. **26**, 207–246 (1987).

Palierne, J.F., "Linear rheology of viscoelastic emulsions with interfacial tension." Rheol. Acta **29**, 204–214 (1990).

Press, W.H., S.A. Teukolsky, W.T. Vetterling & B.P. Flannery, *Numerical recipes in Fortran: The art of scientific computing.* (Cambridge University Press, 2nd edition, 1992).

Schrag, J.L., *et al.*, "Local modification of solvent dynamics by polymeric solutes." J. Non-Cryst. Solids **131–133**, 537–543 (1991).

Smyth, S.F. & M.E. Mackay, "The viscous stress contribution to lyotropic hydroxypropylcellulose solutions in the biphasic and liquid-crystalline regions." J. Rheol. **38**, 1549–1558 (1994).

Smyth, S.F., C.-H. Liang, M.E. Mackay & G.G. Fuller, "The stress jump of a semirigid macromolecule after shear: Comparison of the elastic stress to the birefringence." J. Rheol. **39**, 659–672 (1995).

Takahashi, T., Y. Isono, I. Noda & M. Nagasawa, "Transient viscoelastic properties of linear polymer solutions." Macromolecules **19**, 1217–1222 (1986).

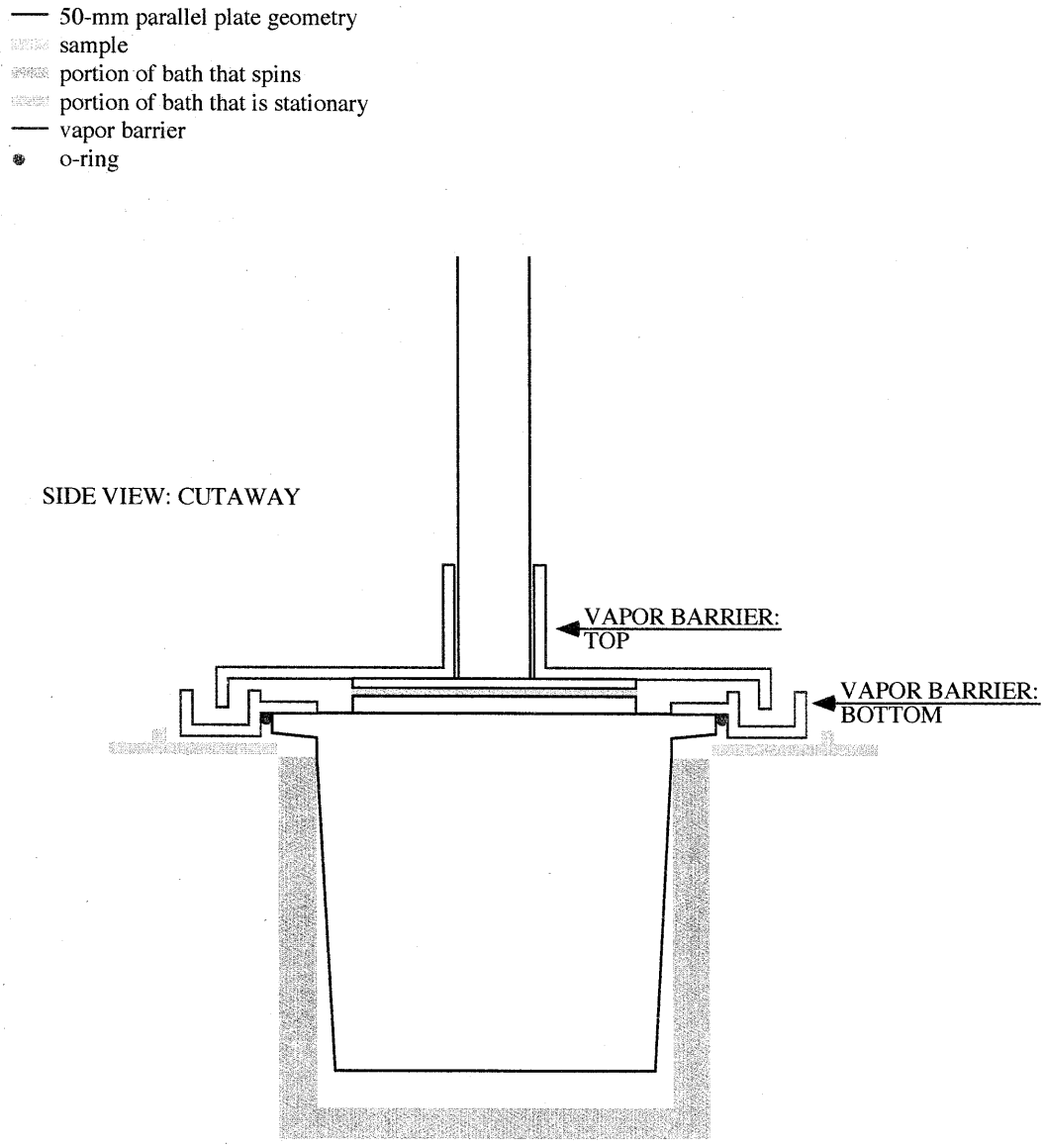

Figure 5.1: A seal is formed between the lower portion of the vapor barrier and the lower tool by using vacuum grease, and an o-ring is used as a secondary seal. The two upper pieces of the vapor barrier are attached to the upper tool and to each other with vacuum grease. Additionally, a small cable tie is used around the neck of the two upper pieces to keep them attached. Finally, 10-ml of low viscosity silicone oil is added to the reservoir to complete the seal.

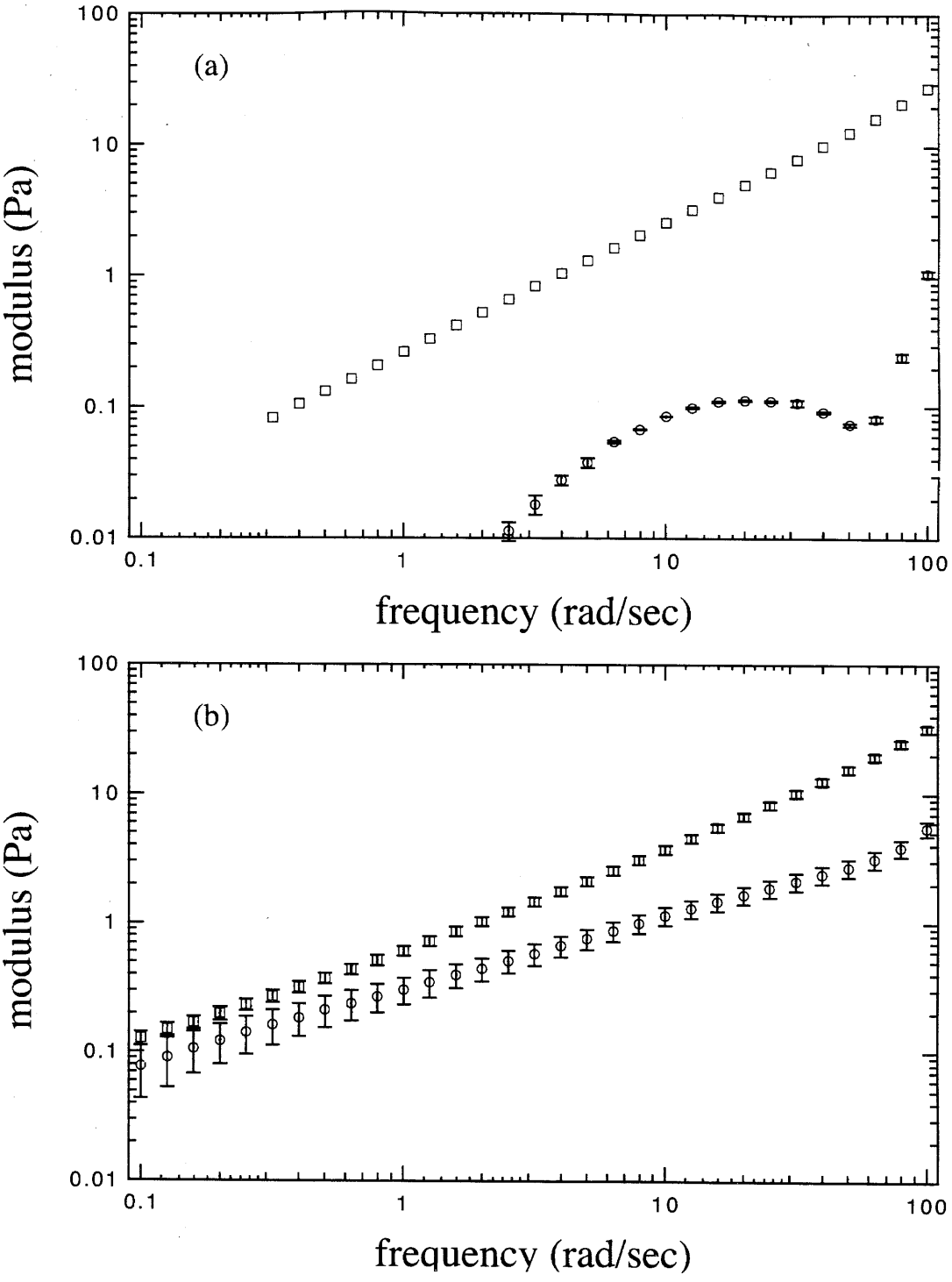

Figure 5.2: Results for storage modulus, G' (○), and loss modulus, G'' (□), as a function of frequency, ω, for (a) pure suspending fluid and (b) c=0.06wt%.

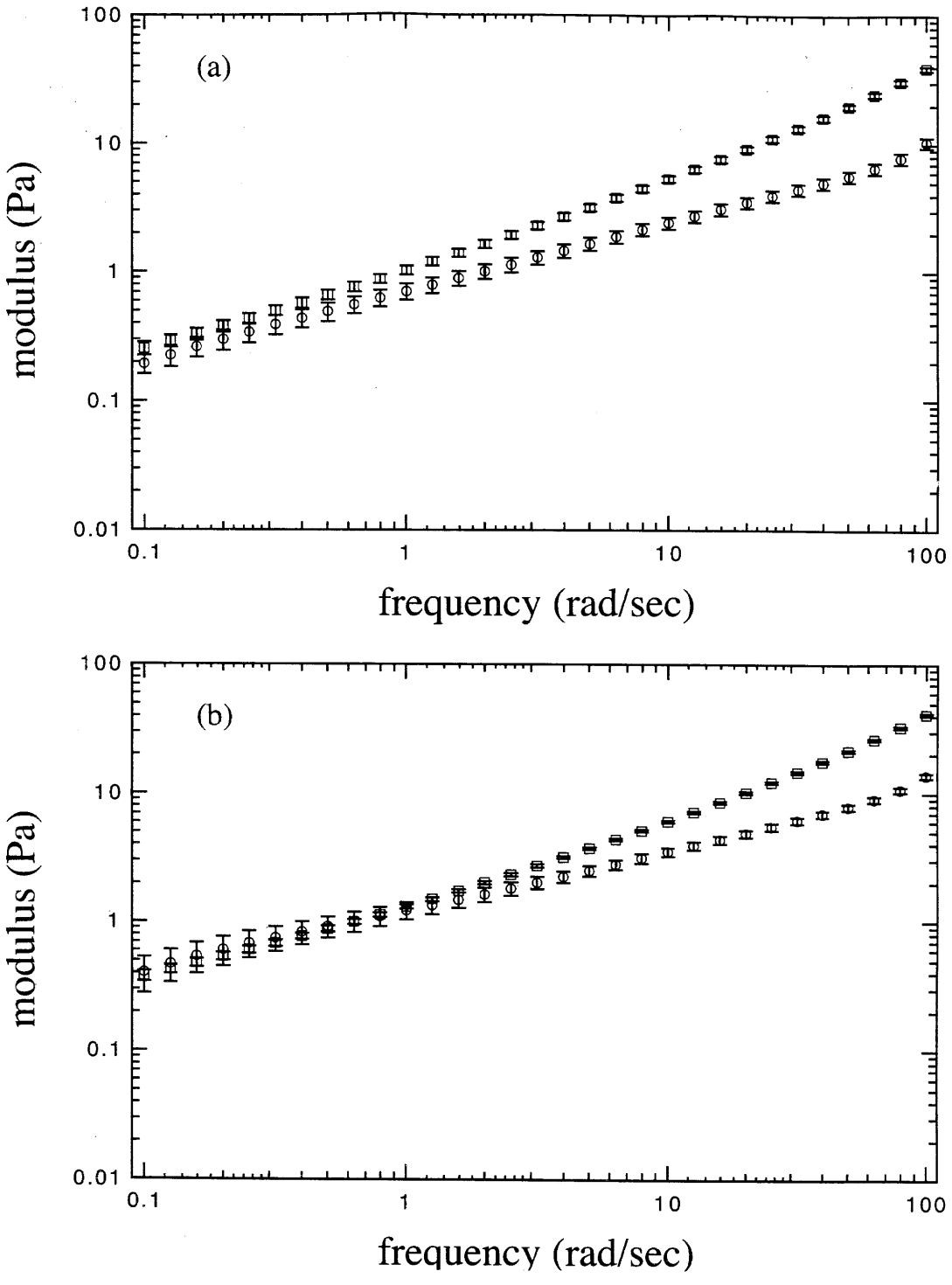

Figure 5.3: Results for storage modulus, G' (o), and loss modulus, G'' (□), as a function of frequency, ω, for (a) c=0.09wt% and (b) c=0.12wt%.

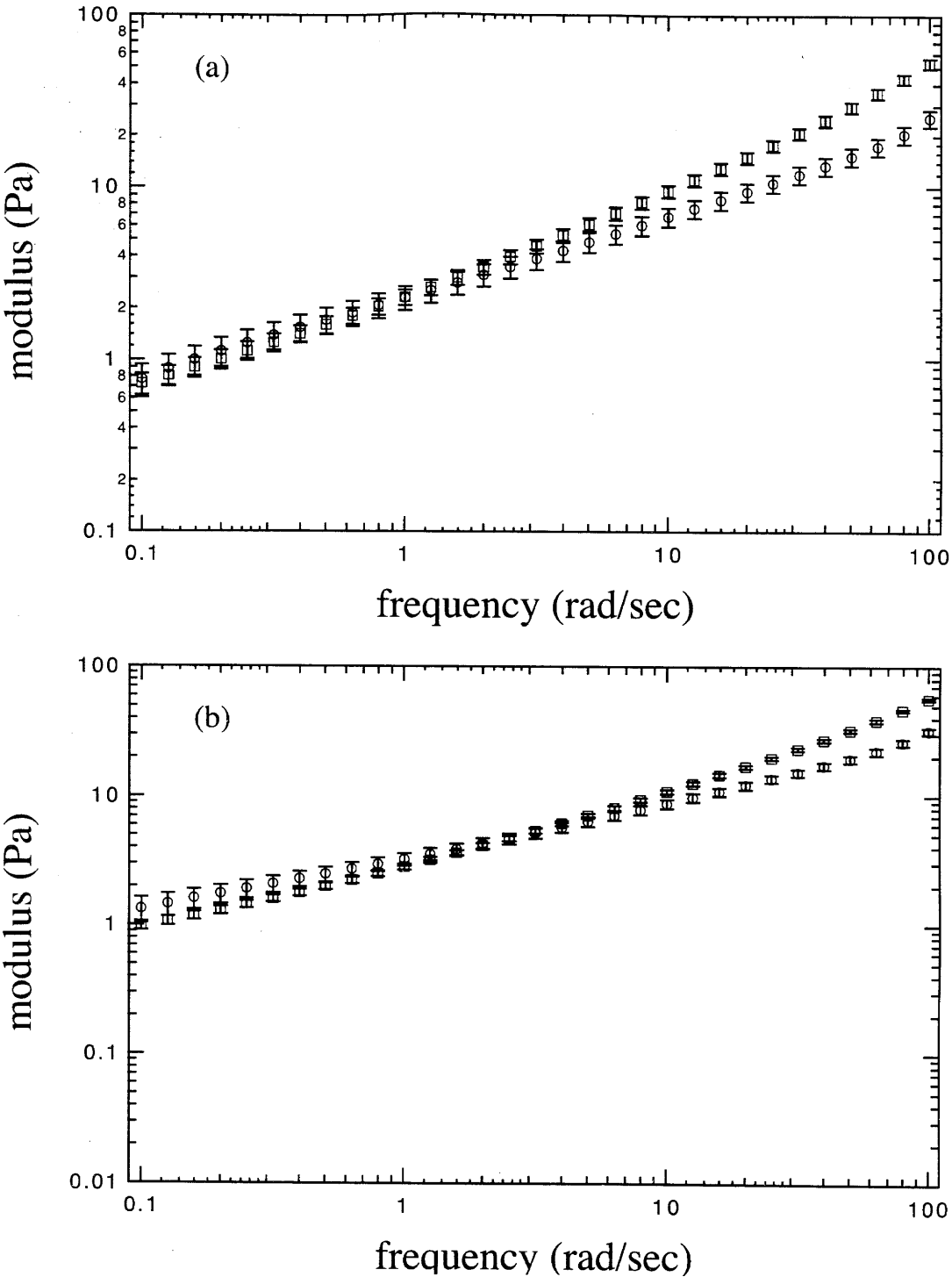

Figure 5.4: Results for storage modulus, G' (○), and loss modulus, G'' (□), as a function of frequency, ω, for (a) c=0.15wt% and (b) c=0.18wt%.

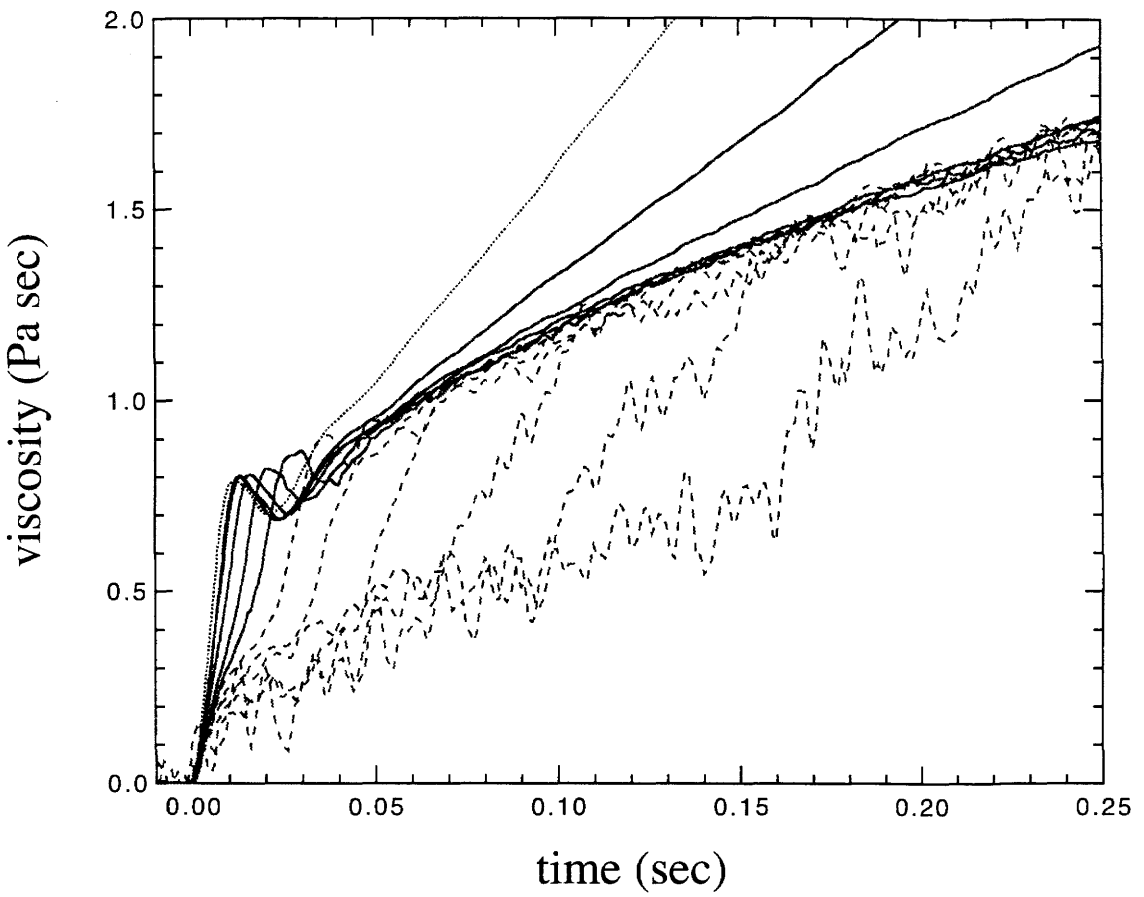

Figure 5.5: Results for shear viscosity growth in startup flow for a polymer solution with 0.15wt% polymer over a range of shear rates. At low rates (dashed line), the transducer does not respond immediately and there is a lag in the stress jump caused by the large moment of inertia of the tool when using the vapor barrier. At high rates (dotted line), deviations from linear viscoelastic behavior occur at times smaller than 50-ms after startup, the characteristic time scale for the response of the transducer. Data from both cases are eliminated from the stress jump analysis.

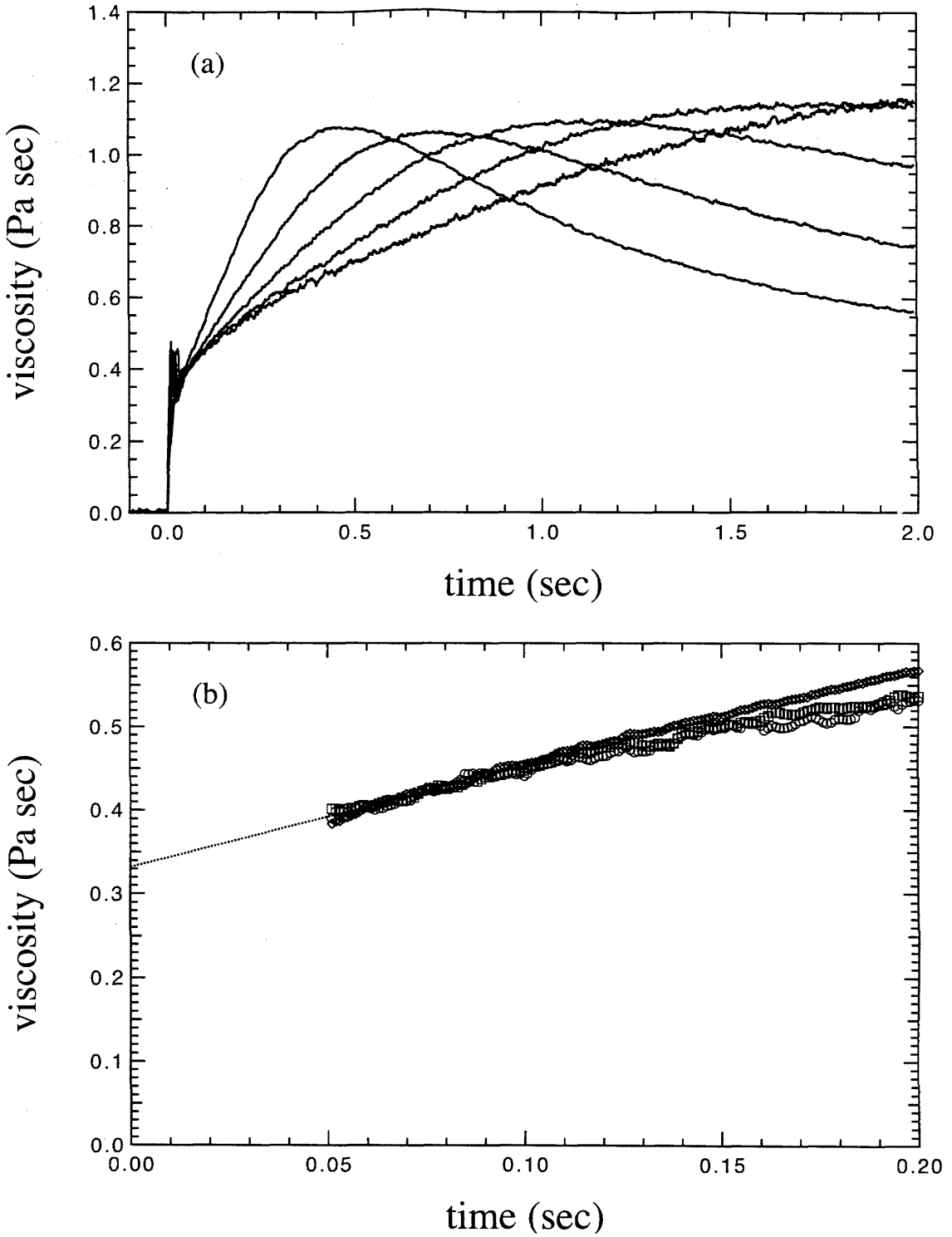

Figure 5.6: Results for shear viscosity growth in startup flow for a polymer solution with 0.06wt% polymer over a range of shear rates (10.0 ($\circ$), 15.8 ($\square$), 25.1 ($\diamond$), 39.8 ($\times$), and 63.1 sec^{-1} ($+$)) when the system is initially at equilibrium. Data is taken for a total of (a) two seconds but only the first (b) 100 milliseconds is used in the stress jump analysis, where the dotted line is the extrapolation to $t = 0$.

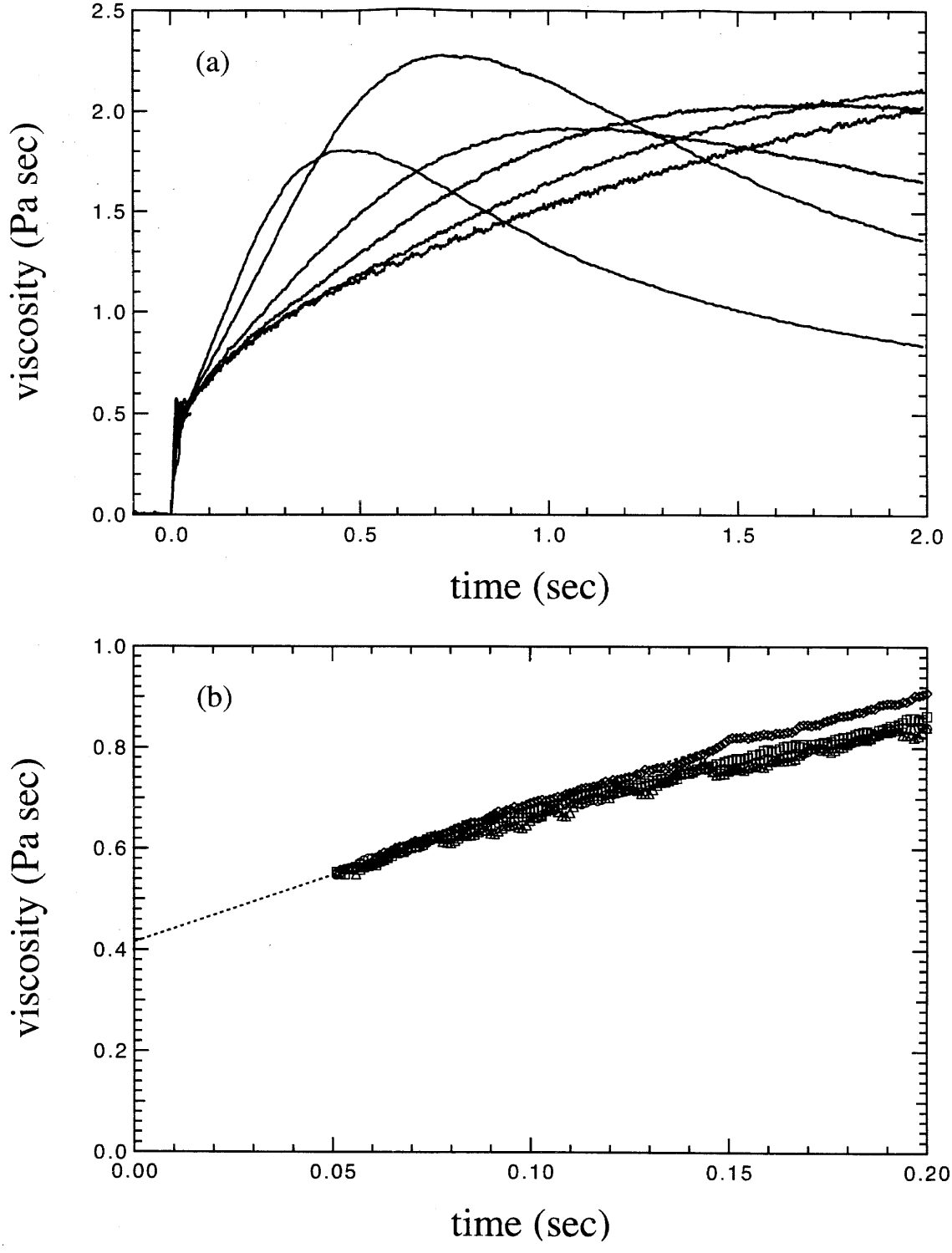

Figure 5.7: Results for shear viscosity growth in startup flow for a polymer solution with 0.09wt% polymer over a range of shear rates (6.31 ($\triangle$), 10.0 ($\circ$), 15.8 ($\square$), 25.1 ($\diamond$), 39.8 ($\times$), and 63.1 $\sec^{-1}$ ($+$)) when the system is initially at equilibrium. Data is taken for a total of (a) two seconds but only the first (b) 100 milliseconds is used in the stress jump analysis, where the dotted line is the extrapolation to $t = 0$.

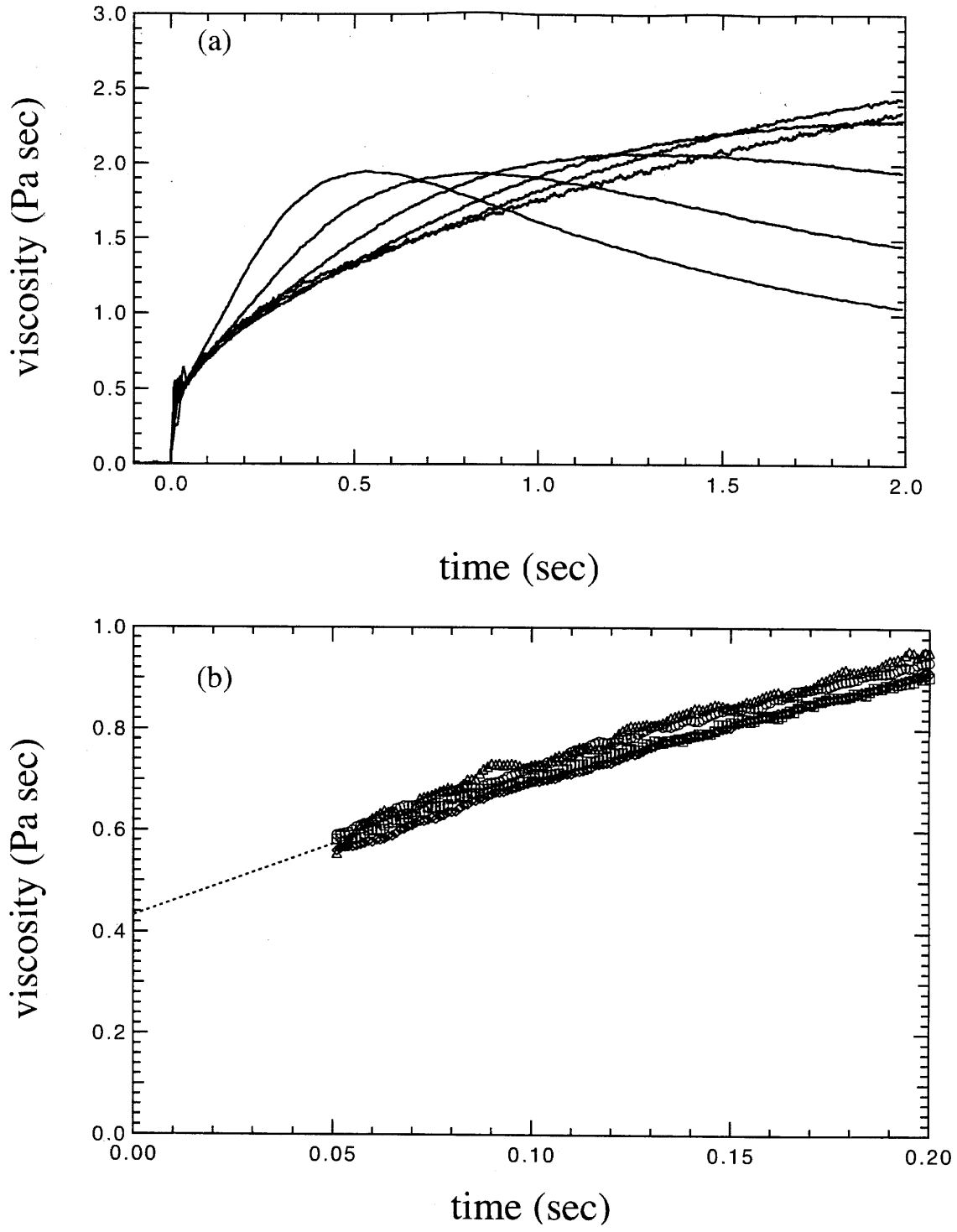

Figure 5.8: Results for shear viscosity growth in startup flow for a polymer solution with 0.12wt% polymer over a range of shear rates (6.31 ($\triangle$), 10.0 ($\circ$), 15.8 ($\square$), 25.1 ($\diamond$), 39.8 ($\times$), and 63.1 $\sec^{-1}$ ($+$)) when the system is initially at equilibrium. Data is taken for a total of (a) two seconds but only the first (b) 100 milliseconds is used in the stress jump analysis, where the dotted line is the extrapolation to $t = 0$.

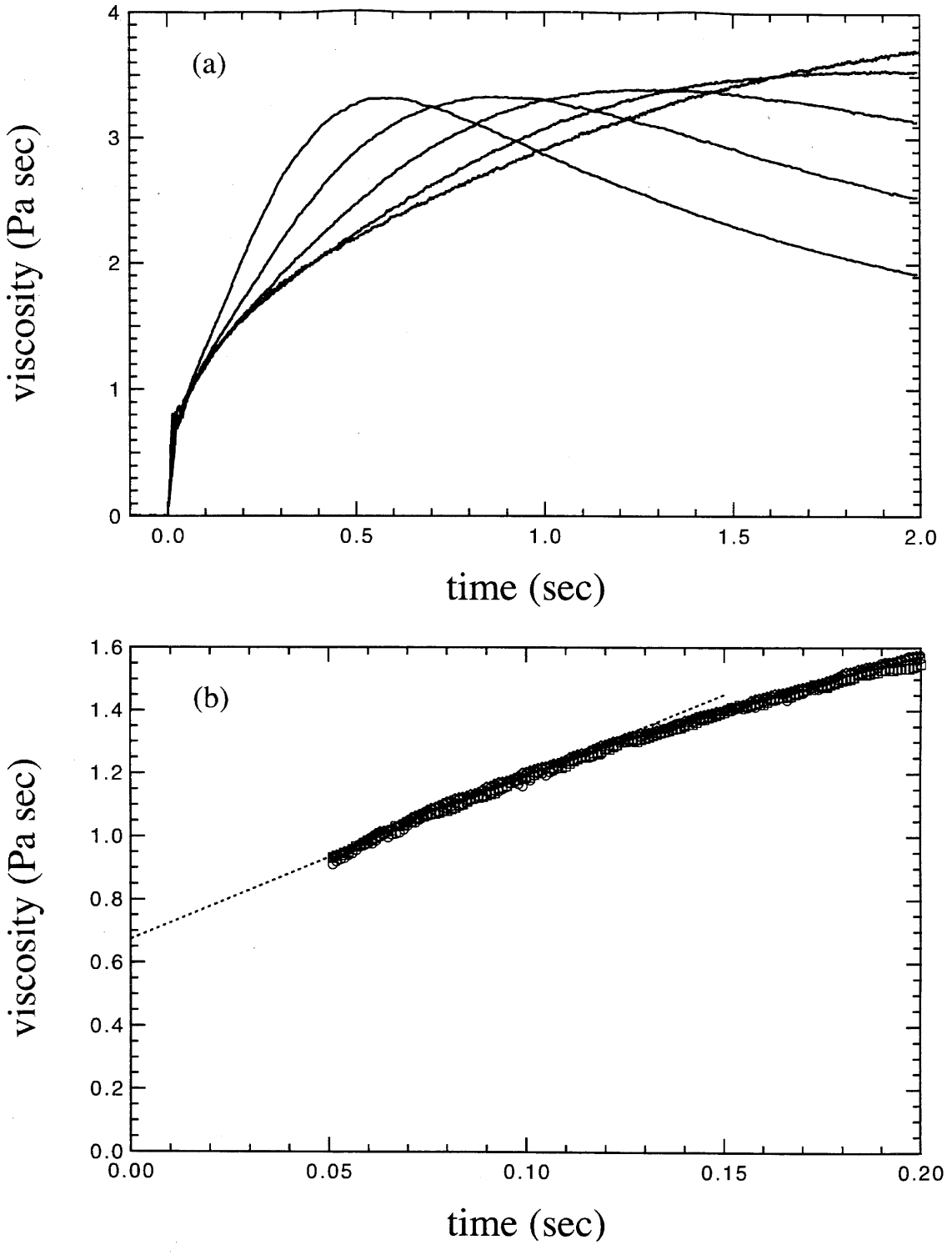

Figure 5.9: Results for shear viscosity growth in startup flow for a polymer solution with 0.15wt% polymer over a range of shear rates (10.0 ($\circ$), 15.8 ($\square$), 25.1 ($\diamond$), 39.8 ($\times$), and 63.1 sec^{-1} ($+$)) when the system is initially at equilibrium. Data is taken for a total of (a) two seconds but only the first (b) 100 milliseconds is used in the stress jump analysis, where the dotted line is the extrapolation to $t = 0$.

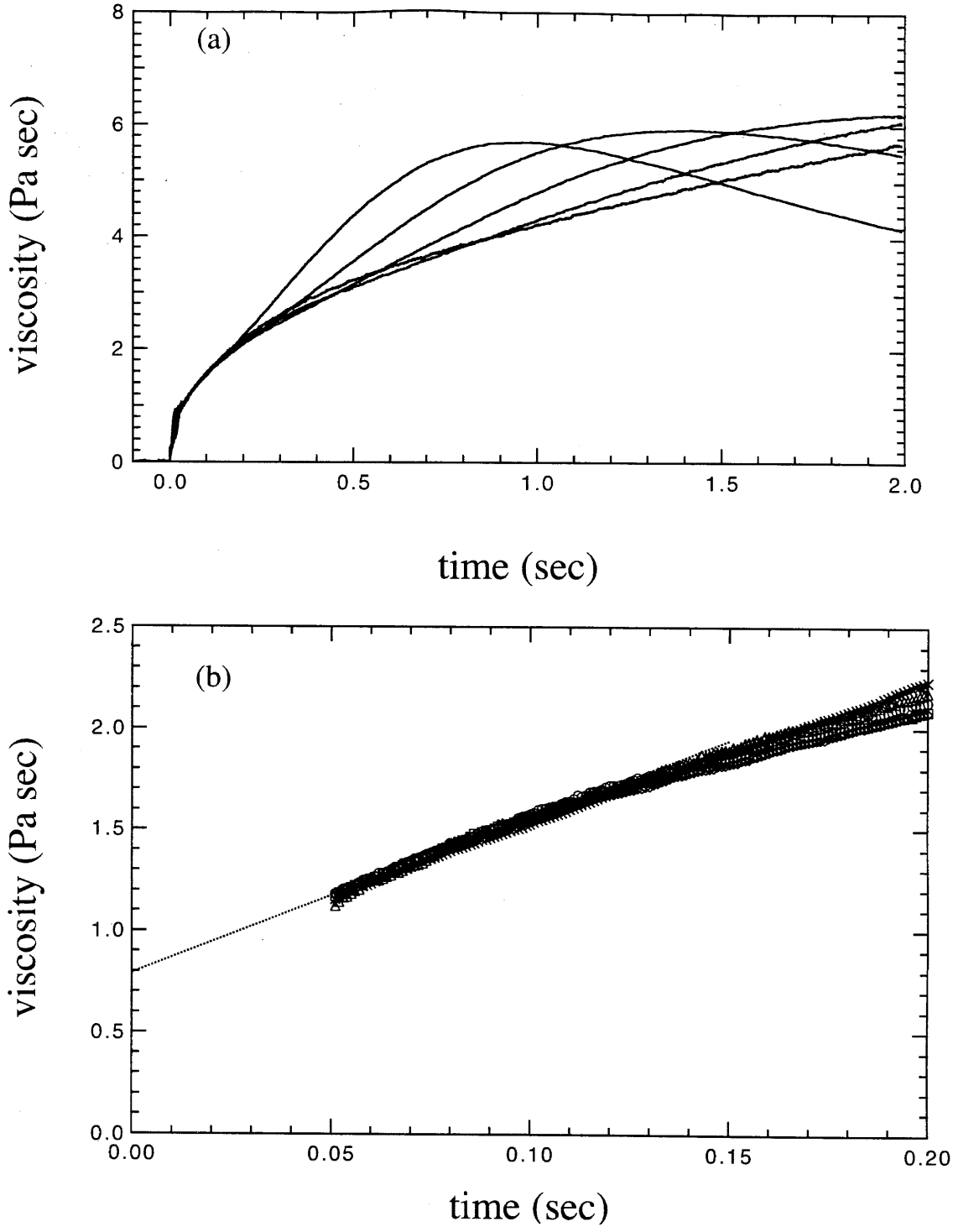

Figure 5.10: Results for shear viscosity growth in startup flow for a polymer solution with 0.18wt% polymer over a range of shear rates (6.31 ($\triangle$), 10.0 ($\circ$), 15.8 ($\square$), 25.1 ($\diamond$), and 39.8 ($\times$)) when the system is initially at equilibrium. Data is taken for a total of (a) two seconds but only the first (b) 100 milliseconds is used in the stress jump analysis, where the dotted line is the extrapolation to $t = 0$.

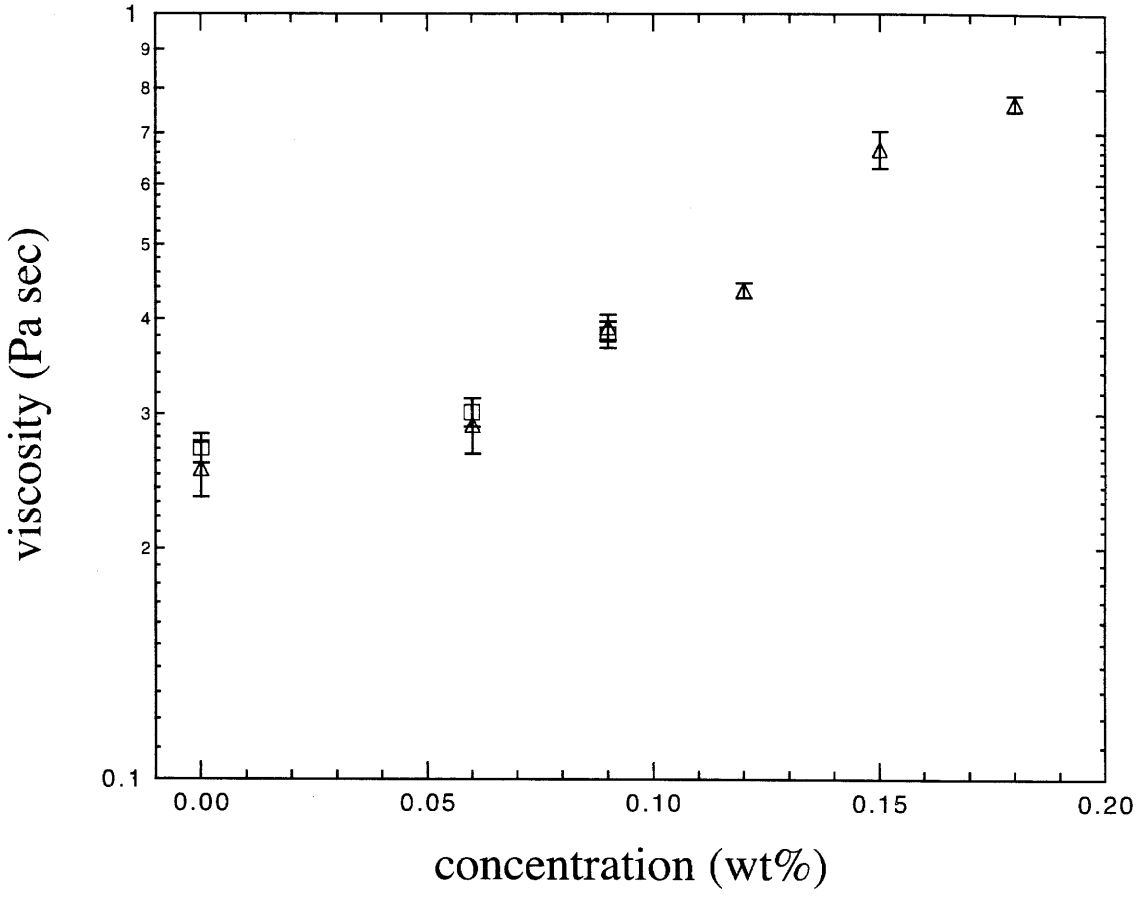

Figure 5.11: Results for the startup viscosity, $\eta^+(t=0)$ ($\triangle$), and the high-frequency dynamic viscosity, η'_∞ ($\square$), as a function of polymer concentration for nonionic polyacrylamide (M_w=18×10^6) in a solvent of 70.0wt% fructose-water.

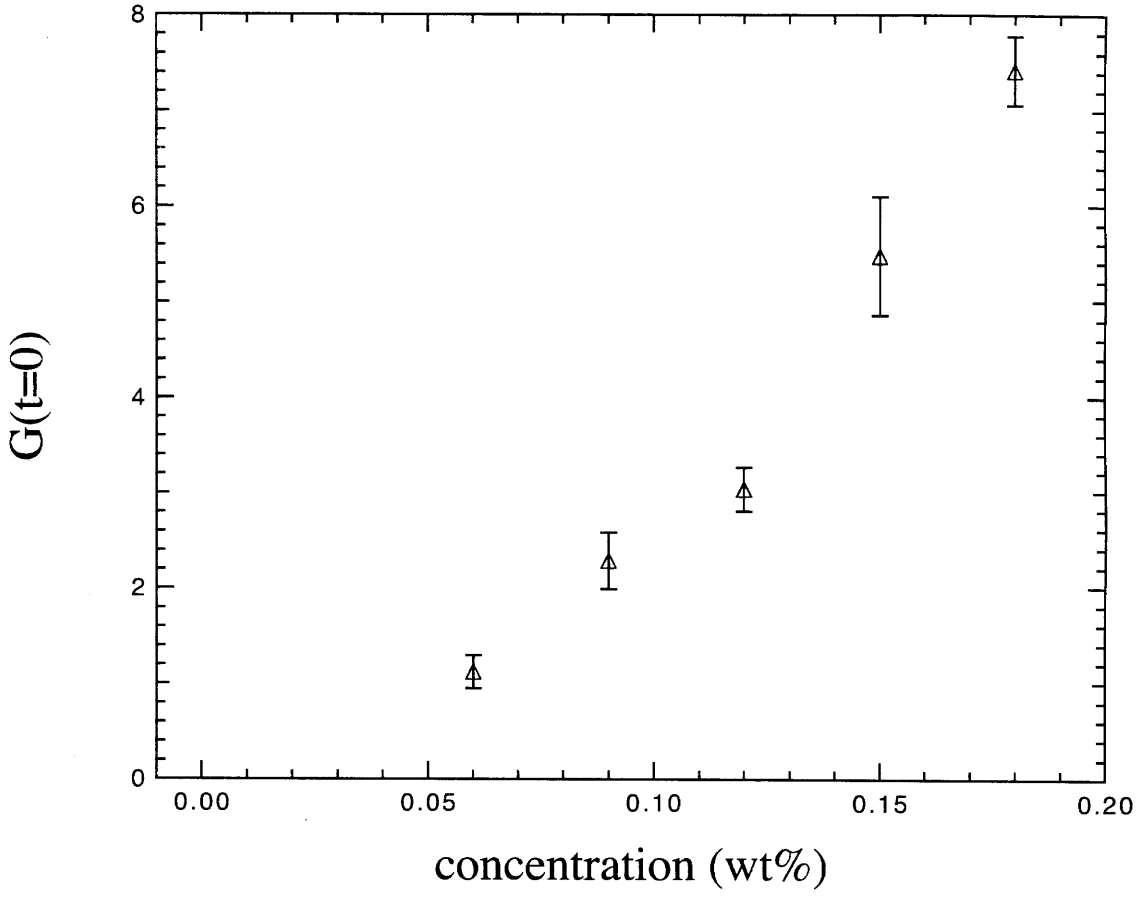

Figure 5.12: Results for the linear viscoelastic relaxation modulus at $t = 0$, $G(t = 0)$, as a function of polymer concentration for nonionic polyacrylamide (M_w=18×10^6) in a solvent of 70.0wt% fructose-water. $G(t = 0)$ is simply the slope of the linear viscoelastic, viscosity growth curve at short times in stress jump measurements.

Chapter 6

Concluding remarks

The relationship between macroscopic rheological properties and the underlying microstructure of complex fluids is explored for colloidal dispersions, emulsions and polymer solutions. For colloidal dispersions in simple shear flow, the two-particle Smoluchowski equation is solved and the resulting microstructure is used to calculate rheological properties as a function of dimensionless shear rate. Scaling arguments and experiments are used to show that rheological properties are linear in volume fraction for an emulsion at the critical capillary number in simple shear flow if the size, shape and orientation of the droplets are weak functions of volume fraction for a given shear rate. Finally, stress jumps at startup and dynamic measurements are performed on polymer solutions to show that $\eta^+(t=0;\dot{\gamma}) = \eta'_\infty$, where $\eta^+(t;\dot{\gamma})$ is the viscosity growth function after shear startup at time t for shear rate $\dot{\gamma}$, and η'_∞ is the high-frequency dynamic viscosity. The fact that these two quantities are equal makes physical sense since both methods measure the viscous contribution to the viscosity associated with the equilibrium microstructure.

The methods used to predict the rheology and microstructure of colloidal dispersions are quite general and can be used for other systems and/or flows. In all cases, the particles in the system must be spherical, but the two particles can have different sizes or be fluid droplets instead of hard spheres. In addition, the particles can interact with an interparticle force other than a hard sphere interaction, such as a square-well potential or a Hookean force. Finally, other rheologically significant flows, such as planar or uniaxial extensional flows, can be studied instead of simple shear flow.

For emulsions at the critical capillary number, it is shown that rheological functions are linear in volume fraction for dilute to moderately-concentrated systems. There are two terms that contribute to these rheological properties. The first term is the anisotropy tensor and the second term is related to the rate of strain within the droplets. Neither the scaling arguments nor the experiments of this work can determine the relative contribution of these two terms to emulsion viscosity, but mechanical stress jumps can provide such a measurement. Upon flow cessation, the rate of strain within the droplets instantly vanishes, and there is only a single contribution

to the stress through the anisotropy tensor since the droplets have not yet relaxed from their steady size, shape and orientation.

Finally, stress jumps at flow startup are performed on polymer solutions in shear flow, and it is shown that stress jumps exist that are different from the solvent viscosity. These experiments form the foundation for analysis of the strain and rate dependence of the hydrodynamic viscosity to shed light on the mechanism for the dissipative stress and the cause of shear thickening in polymer solutions. Furthermore, stress jumps at startup yield two quantities, η'_∞ and $G(t=0)$, that can be used to test rheological models for $G(t)$, where $G(t)$ is the linear viscoelastic relaxation modulus.